

Hedvig Åstebøl

Stability analysis of an olivine quarry at Åheim, Western Norway

Master's thesis in Tekniske geofag

Supervisor: Charlie Chunlin Li

June 2020

NTNU
Norwegian University of Science and Technology
Faculty of Engineering
Department of Geoscience and Petroleum

Hedvig Åstebøl

Stability analysis of an olivine quarry at Åheim, Western Norway

Master's thesis in Tekniske geofag
Supervisor: Charlie Chunlin Li
June 2020

Norwegian University of Science and Technology
Faculty of Engineering
Department of Geoscience and Petroleum





MASTEROPPGAVEN

Kandidatens navn: Hedvig Åstebøl

Oppgavens tittel: Stability analysis of an olivine quarry at Åheim, Western Norway

Norsk tittel: Stabilitetsanalyse av et olivinbrudd på Åheim i Møre og Romsdal

Utfyllende tekst: The task of the master thesis is to perform a stability analysis of the back wall in Sibelco Nordic's open pit mine at Åheim. The work will be carried out by continuum numerical modelling using software RS2. In addition, the stability of some wedges observed in the current slope will be analysed by the limit equilibrium method using Swedge. The field mapping data and laboratory testing results carried out during the Project work, provide input data for the stability analysis. The stability of the current slope will first be studied in representative profiles. The numerical models of profiles in the current wall will be calibrated by observational data, and they are then used to study the stability of the slope when the pit develops to lower levels.

The thesis is written in cooperation with Sibelco Nordic. The contact person in Sibelco Nordic is Senior Geologist Mannie Mehu.

Ansvarlig faglærer og hovedveileder for oppgaven er Charlie Chunlin Li, Institutt for geovitenskap og petroleum.

Studieretning: Tekniske geofag

Hovedprofil: Mineralproduksjon

Tidsrom: 15.01.2020-10.06.2010

Faglærer

03 juni 2020

Abstract

This thesis presents an analysis of the stability of Sibelco Nordic's olivine quarry at Åheim. The analysis was carried out by investigating the stability of the current back wall in the quarry and the planned final back wall at life of mine. The analysis was performed by numerical modelling of the back wall, limit equilibrium analysis of wedges, and evaluation of observations and measurements from field mapping. The input parameters in the computer analysis were determined from estimations and measurements in the field and the laboratory, carried out as the authors Project work autumn 2019.

The numerical analysis was performed by continuum method finite element modelling (FEM) using the software RS2 Rocscience (2019b). The analysis was carried out by modelling sections perpendicular to the current and final back wall. One section of the current back wall was used to calibrate joint shear strength by reproducing a plane failure. The analysis by numerical modelling was performed using two different methods. One analysis was performed using the shear strength reduction method (SSR) on a model without joint network. The second analysis was performed by creating models including a joint network and analyse the stability with the input parameters determined from field mapping and laboratory testing. The flow of water in the rock mass was not included in the analyses. The analysis of wedges was carried out by investigating the stability of four wedges observed in the quarry during field mapping. The analysis was performed for dry and completely water filled joints.

Calibration of plane failure went beyond the limitations of FEM. The numerical analysis by the SSR method gave CSRF equal to 5.62 for the current back wall and 2.97 for the final back wall. The wall become unstable at CSRF by rock mass failure at the bottom of the slope. The rock mass at the bottom of the wall has a high weathering rate, and the depth of weathering after long term exposure will determine the risk of global failure in the final back wall. The numerical models did not indicate any risk structural failure or instability in the benches in the current and the final wall, but plane failure along the bench faces were observed during field mapping. The plane failure occurs due to undercutting of benches.

The identified wedges had a factor of safety $FS > 5$ for dry conditions. Analysis with water filled joints gave a $FS < 1$ for one of the wedges. The dip and dip direction of the discontinuities forming the wedges result in a low dip of the intersection line resulting in a low risk of instability.

There was not identified any risk of global failure in the current back wall. The risk of global failure in the final back wall will depend on the depth of weathering at the bottom of the wall. There is a risk of structural instability along the bench face in the uppermost part of the current and the final back wall. The planned mine design can be used as long as undercutting of the foliation is avoided. An analysis using discontinuum numerical modelling can be performed to give a better understanding of the influence of the foliation on the stability.

Sammendrag

Denne oppgaven presenterer en stabilitetsanalyse av Sibelco Nordics olivinbrudd på Åheim. Analysen undersøkte stabiliteten til dagens bakvegg og bakveggen i det endelige bruddet. Analysen ble utført ved bruk av numerisk modellering av bakveggen, likevektanalyse av kiler og ved å evaluere observasjoner og målinger fra feltkartlegging. Inngangsparametrene til de dataprosesserte analysene ble bestemt fra estimeringer og målinger som ble foretatt i felt og i laboratoriet i forbindelse med arbeidet med forfatterens prosjektoppgave høsten 2019.

Den numeriske analysen ble utført med den kontinuerlig metode endelig elementmetode (FEM) ved bruk av programmet RS2 (). Analysen ble utført ved å modellere snitt vinkelrett på dagens bakvegg og den endelige bakveggen. Et snitt av dagens bakvegg ble brukt til å kalibrere skjærstyrken til en sprekkeoverflate ved å gjenskape et plant brudd. Den numeriske analysen ble utført ved å bruke to ulike analysemetoder. Den ene analysen ble utført ved å bruke metoden for redusering av skjærstyrke (Shear strength reduction (SSR)). Den andre analysen ble utført med modeller som inkluderer sprekkesett og analysere stabiliteten til modellen med inngangsparameterene fra feltkartlegging og laboratorietesting. Vannstrømning i bergmassen ble ikke inkludert i analysen. Analysen av kiler ble gjennomført ved å undersøke stabiliteten av fire kiler som ble observert i dagbruddet under feltkartlegging. Analysen ble utført med tørre sprekker og vannfylte sprekker.

Kalibreringen av plane brudd gikk utenfor anvendelsesområdet til FEM. Den numeriske analysen ved bruk av SSR metoden ga CSRF lik 5.62 for dagens bakvegg og 2.97 for den endelige bakveggen. Bakveggen ble ustabil ved CSRF som følge av brudd i bergmassen i nedre del av veggen. Bergmassen i nedre del av bakveggen forvitrer raskt, og forvitningsdybden etter lang tids eksponering vil bestemme faren for at et stort ras kan skje. De numeriske modellene indikerte ingen fare for strukturelt bestemte brudd eller ustabiliteter i pallene i dagens bakvegg eller den endelige bakveggen, men under feltkartlegging ble plane brudd observert enkelte steder langs pallfronten. Plane brudd forekommer som følge av underkutting av paller.

De identifiserte kilene har en sikkerhetsfaktor $F > 5$ ved tørre forhold. Analysen utført med vannfylte sprekker ga $F < 1$ for en av kilene. Fallet og fallretningen til sprekken som danner kiler, gir skjæringslinja mellom sprekken en lav vinkel som resulterer i liten fare for ustabiliteter.

Det ble ikke identifisert fare for et stort ras i dagens bakvegg. Faren for et stort ras i den endelige bakveggen vil avhenge av forvitningsdybden i den nedre delen av veggen. Den planlagte utformingen av dagbruddet kan bli brukt dersom underkutting av foliasjon unngås. En analyse ved bruk av ikke-kontinuerlig numerisk modellering kan bli utført for å få en bedre forståelse av foliasjonens betydning for stabiliteten.

Acknowledgment

This master's thesis was written as the final part of my master's degree in Mineral production at the Department of Geoscience and Petroleum at Norwegian University of Science and Technology. The thesis was written in cooperation with Sibelco Nordic at Åheim.

First, I would like to thank my supervisor Charlie Chunlin Li for guidance throughout the whole process, from the beginning of my Project work with field mapping to the completion of the thesis. I would also like to thank Mannie Mehu at Sibelco Nordic. I am very grateful for that you shared your knowledge of the quarry and gave me valuable support during my field work at Åheim and while I was working on my thesis. I very much appreciate all the help I got from the employees at Sibelco Nordic at Åheim. A special thanks to Anders Bakkebø and Jermund Rekkedal for making sure I stayed safe in the quarry and giving me useful contributions to my work. I must also thank Roar Sandøy for giving valuable input to the task and answering all my question.

I would also like to thank Jon Runar Drotningshaug at the Rock Mechanics Laboratory at NTNU. I am grateful for all your help with performing laboratory test.

At the end, I wish to thank my dad for reviewing the thesis and giving me valuable comments.

Trondheim, 03.06.2020

Hedvig Åstebøl

Table of Contents

Table of Contents	xii
List of Tables	xviii
List of Figures	xxxi
1 Introduction	1
1.1 Location and geological setting	1
1.2 The aim of the thesis	4
1.3 The structure of the thesis	6
2 Theory	7
2.1 Instability of a rock slope	7
2.1.1 External factors influencing the rock slope stability	7
2.1.2 Failure modes	8
2.2 Failure rriterions	9
2.2.1 Hoek-Brown Criterion	9
2.2.2 Mohr-Coulomb criterion	11
2.2.3 Barton-Bandis criterion	13
2.3 Approaches for stability analyses of a rock slope	14
2.3.1 Limit equilibrium method	14
2.3.2 Empirical methods	15

2.3.3	Numerical modelling	15
2.3.4	Shear Strength Reduction method (SSR)	16
2.4	Rock Mass Classification Systems	17
2.4.1	Geological Strength Index (GSI)	17
2.4.2	Q-system	18
2.4.3	From Q-value to The Hoek-Brown Failure Criterion	19
3	Field mapping and laboratory testing	21
3.1	Methods for field mapping	21
3.1.1	Dip and dip direction	22
3.1.2	Q-value	23
3.1.3	Apparent friction angle	24
3.1.4	Joint Roughness Coefficient	26
3.1.5	Joint Wall Compressive Strength	27
3.1.6	Laboratory testing of uniaxial compressive strength and sound velocity	28
3.1.7	Laboratory testing of free swelling	32
3.1.8	Uncertainties of measurements and estimations in the field and laboratory testing	32
3.1.9	Studying of drill cores	34
3.2	Results from field mapping	36
3.2.1	Dip and dip direction of joint sets and weakness zone	36
3.2.2	Q-values for area section 1, 2, and 3	39
3.2.3	Apparent friction angle, JRC, and JCS for joint wall surfaces	39
3.3	Results from laboratory testing	41
3.3.1	UCS-testing of core specimen	41

3.3.2	P-wave velocity testing of core specimen	42
3.3.3	Free swelling test of clay	42
3.4	Results from core logging	43
3.4.1	Weakness zones related to point Z1-Z5	43
3.4.2	Contact zone by the gneiss boundary	44
3.4.3	Zones with eclogite and amphibolite	45
4	Methods for stability analysis	46
4.1	Rock mass data and determination of strength parameters	46
4.1.1	Rock mass strength parameters	46
4.1.2	Weakness zones in the numerical models	48
4.1.3	Properties of joint sets	49
4.2	Estimation of the stability of wedges	50
4.2.1	Input parameters for wedge analysis	50
4.2.2	Method for analysing wedges	52
4.2.3	Potential wedges	54
4.2.4	Uncertainties related to the input in the analysis of wedges	55
4.3	Numerical Modelling for Stability analyses	55
4.3.1	Selection of sections for stability analyses	56
4.3.2	Establishment of a finite element model	56
4.3.3	Computation and analysis	64
4.3.4	Method for stability analysis	64
4.3.5	Uncertainties and simplifications in the numerical models	65
4.4	The numerical models for stability analysis	67

4.4.1	Description of the numerical models	68
4.4.2	The sizes of the finite elements in the numerical models	72
4.5	Calibration of joint strength parameters	72
4.5.1	Establish the numerical model for calibration	73
4.5.2	Defining finite elements in the calibration model	74
4.5.3	The calibration process	76
4.5.4	Alternative methods for calibration	77
5	Analysis and discussion	79
5.1	Input data for wedge analysis and numerical modelling	79
5.1.1	Input parameters for rock mass strength	79
5.1.2	Start parameters for the joint set in each of the area sections 1,2, and 3.	80
5.2	Stability analysis of wedges	81
5.2.1	Input parameters	81
5.2.2	Stability of wedges in the current back wall	83
5.2.3	Stability of wedges in the final back wall	85
5.3	Numerical stability analysis of the current back wall	90
5.3.1	Calibration	90
5.3.2	The general stability of the current wall along section S3	93
5.4	Stability analysis of the current back wall along section S2	94
5.4.1	Stability analysis of section S2 using analysing method 1	94
5.4.2	Stability analysis of section S2 using method 2	97
5.5	Stability analysis of the final back wall	99
5.5.1	Stability analysis using method 1	99

5.5.2	Stability analysis using method 2	108
5.6	Discussion - the stability of the current and the final back wall	115
5.6.1	Global stability	115
5.6.2	Local stability	116
5.6.3	Limitations and uncertainties in the analysis	119
6	Conclusion and further investigations	121
	Bibliography	125
	Appendix	130
A	Field Mapping	132
A.1	Measurements of dip and dip direction	132
A.1.1	Data of dip and dip direction from Sibelco Nordic	134
A.2	Q-value	138
A.2.1	Area section 1	138
A.2.2	Section 2	139
A.2.3	Section 3	140
A.3	Shear strength of joints	140
A.3.1	Tilttesting	140
A.3.2	Joint Roughness Coefficient (JRC)	142
A.3.3	Joint Compressive Strength (JCS)	146
B	Lab testing	152
B.1	Uniaxial Compressive Strength (UCS) Testing	152

B.1.1	Typical failure modes of UCS-tested cores	152
B.1.2	The complete data from UCS-testing	152
B.1.3	Graphical representation of the results from UCS-testing	154
B.2	P-wave velocity testing	156
B.3	Free Swelling Test	158
C	Core logging	159
C.1	Weakness zone Z1-Z5	159
C.2	Contact zone at the gneiss boundary	160
C.3	Eclogite and amphibolite zones	163
C.4	Data from core logs by Sibelco Nordic	164
C.4.1	Drill core GU-D2010-039	164
C.4.2	Drill core GU-D2010-040	165
C.4.3	Drill core GU-D2010-041	166
C.4.4	Drill core GU-D2010-042	167
C.4.5	Drill core GU-D2010-043	168
C.4.6	Drill core GU-D2010-047	169
C.4.7	Drill core GU-D2013-054	170
D	Rock Mass Classification	171
D.1	Barton-Bandis failure criterion	171
D.1.1	Determination of JCS from rebound value	171
D.1.2	Determination of JRC from roughness profiles	172
D.2	Geological Strength Index	173

D.3	Q-value	174
E	Input parameters for numerical modelling	180
E.1	Input rock mass parameters	180
E.1.1	Calculation of Q'-value and GSI	180
E.2	Input joints strength parameters	182
E.2.1	Input parameters for calculation of joint stiffness	182
F	Wedges	183
F.1	Determination of the geometry defining the wedges	183
F.1.1	Sections of identified wedges in the current back wall	186
F.1.2	Sections of identified wedges in the final back wall	188
G	Numerical modelling	191
G.1	Calibration	191
G.1.1	The numerical model used for calibration	191
G.1.2	Data used for plotting of displacement along joint surface	192
G.2	Stability analysis of the current back wall along section S2	193
G.2.1	Analysis using method 1	193
G.2.2	Analysis using method 2	194
G.3	Stability analysis of the final back wall	195
G.3.1	Analysis using method 1	195
G.3.2	Analysis using method 2	199
G.3.3	Elevation profiles	203
G.3.4	Data for plotting from the numerical models for analysing method 1	205

G.3.5 Data used in graphs from analysing method 2 209

H Risk analysis **228**

List of Tables

3.1	The four different block samples collected in the quarry and their sample name, modified after Aasteboel (2019).	28
3.2	Uncertainties related to the methods used for measurements and estimation of parameters in the field and in the laboratory.	33
3.3	The drill cores studied through core logs from Sibelco Nordic and examination of cores. The cores are named with the names used by Sibelco Nordic.	34
3.4	The parameters registered from core logs and from studying of cores for the weakness zones of interest.	35
3.5	Dip and strike of weakness zones in section 1. Location given by the points Z1-Z8, see figure 3.2.	38
3.6	Average Q-value for section 1,2 and 3 estimated by field mapping in the quarry.	39
3.7	Average measured friction angle, JRC, and basic friction angle of each surface category present in area section 1. Both average and median value of JCS of the surfaces were calculated.	39
3.8	Average measured friction angle, JRC, and basic friction angle of the surface category present in area section 2. Both average and median value of JCS of the surface were calculated.	40
3.9	Average measured friction angle, JRC, and basic friction angle of the surface category present in area section 3. Both average and median value of JCS of the surface were calculated.	40
3.10	Average UCS, E-modulus, Poisson’s ration and fracture angle for sample No. 1,2,3 and 4 from UCS-testing, after Aasteboel (2019).	41
3.11	P-wave velocity and density for each sample No. 1,2,3 and 4 from p-wave testing.	42
3.12	Readings and calculated FS value from free swelling test on material from weakness zone Z4, see figure 3.2 and table 3.5.	42

3.13	Registered values of parameters for the weakness zones evaluated to be related to the weakness zone Z1-Z5 observed in the quarry.	43
3.14	Registered parameters of the contact zone by the gneiss boundary from core logging. . .	44
3.15	Registered parameters of the contact zone by the gneiss boundary from core logging. . .	45
4.1	Input parameters used to determine the rock mass strength in the numerical models from the Hoek-Brown criterion.	47
4.2	Input parameters used to determine the rock mass strength in the numerical models from the Barton-Bandis criterion.	49
4.3	Input parameters used to investigate if wedges are formed and the stability of occurring wedges.	51
4.4	Uncertainties related to the input in the analysis of wedges.	55
4.5	The defined properties for the rock material in the numerical models.	62
4.6	The defined properties for the joint set following the foliation in the numerical models. .	62
4.7	The allowed direction of movement of the finite elements along different parts of the external boundaries.	64
4.8	Uncertainties related to the input in the numerical models.	66
4.9	The defined length of the finite elements in each area 1,2,3, and 4. The lengths were used for analyses with method 1.	72
4.10	Trials of finite element sizes and joint spacing in the numerical model for calibration. The lengths of the finite elements in the table define the maximum allowed length of the elements in the model.	75
5.1	Input parameters for the strength of rock mass used in the numerical models.	79
5.2	Input parameters used for the foliation in the different rock types in area section 1. . . .	80
5.3	Input parameters used for foliation in the chlorite banded dunite in area section 2.	80
5.4	Input parameters used for the foliation in the dunite in area section 3.	81

5.5	Input strength parameters for the joints defining the potential wedges. The two discontinuities defining each potential wedge are named after which discontinuity is located furthest to the east and west. All the discontinuities are named joints.	81
5.6	Input parameters used to define the geometry of the slope and the bench where the wedges are located.	82
5.7	The factor of safety for the wedges that can be formed from the two joints in consideration in wedge 1 within the geometry of the current back wall.	83
5.8	The factor of safety for the wedges that can be formed from the two joints in consideration in wedge 2 within the current slope geometry.	84
5.9	The factor of safety for the wedges that can be formed from the two joints in consideration in wedge 3 within the geometry of the current back wall.	85
5.10	The factor of safety for the wedges that can be formed from the two discontinuities in consideration in wedge 1 within the geometry of the final back wall.	86
5.11	The factor of safety for the wedges that can be formed from the two discontinuities in consideration in wedge 2 within the geometry of the final back wall.	87
5.12	The factor of safety for the wedges that can be formed from the two joints in consideration in wedge 3 within the geometry of the final back wall.	88
5.13	The factor of safety for the of wedges that can be formed from the two discontinuities in consideration in wedge 4 within the geometry of the final back wall.	89
5.14	The parameters used in each round 1-5 to calibrate the joint strength of the serpentized surface.	90
5.15	The critical strength reduction factor (CSRf) for the analysis of the stability of the current back wall along section 2 using method 1.	94
5.16	The critical strength reduction factor (CSRf) for each of the sections in the final back wall.	99
A.1	All results from measurements of dip and dip direction for area section 1, 2, 3, and 4. The locations indicated in the table are shown in the map in figure 3.2.	133

A.2	Measurements of dip and dip direction in area section 1 and 2 from Sibelco Nordic. The measurements were used to make the rose diagrams in section 3.2.1. The names of the measurements are given by the names used by Sibelco Nordic.	137
A.3	Values of the estimated parameters for calculation of Q-value in area section 1. The locations for estimation indicated in the table are shown in the map in figure 3.3.	139
A.4	Values of the estimated parameters for calculation of Q-value in area section 2. The locations for estimation indicated in the table are shown in the map in figure 3.3.	140
A.5	Values of the estimated parameters for calculation of Q-value in area section 3. The locations for estimation indicated in the table are shown in the map in figure 3.3.	140
A.6	The measured apparent friction angle for tilt tested blocks. The locations for testing indicated in the table are shown in the map in figure 3.5.	141
A.7	Estimated JRC-values for different surfaces in the quarry. The locations for testing indicated in the table are shown in the map in figure 3.6.	146
A.8	Measured rebound values, and the corresponding JCS-values for surfaces in the quarry. The locations for testing indicated in the table are shown in the map in figure 3.6.	151
B.1	Results from UCS-testing of the cores from block No. 1,2, 3 and 4., after Aasteboel (2019).	154
B.2	Results from p-wave velocity test of the cores from block No. 1,2, 3 and 4., after Aasteboel (2019).	157
C.1	The data of drill core GU-D2010-039 from the core logs by Sibelco Nordic used to study the core.	164
C.2	The data of drill core GU-D2010-040 from the core logs by Sibelco Nordic used to study the core.	165
C.3	The data of drill core GU-D2010-041 from the core logs by Sibelco Nordic used to study the core.	166
C.4	The data of drill core GU-D2010-042 from the core logs by Sibelco Nordic used to study the core.	167
C.5	The data of drill core GU-D2010-043 from the core logs by Sibelco Nordic used to study the core.	168

C.6	The data of drill core GU-D2010-047 from the core logs by Sibelco Nordic used to study the core.	169
C.7	The data of drill core GU-D2010-054 from the core logs by Sibelco Nordic used to study the core.	170
E.1	Values of parameters used for calculation of Q'-value and GSI, and the final GSI value. The locations for estimation indicated in the table are shown in the map in figure 3.3. . .	181
E.2	The input parameters used to calculate the joint stiffness for joints in area section 1. . .	182
E.3	The input parameters used to calculate the joint stiffness for the joints in area section 2. .	182
E.4	The input parameters used to calculate the joint stiffness for the joints in area section 3. .	182
G.1	The data used to create the graphs in figure 5.10 showing the shear displacement along the joints used for calibration at different locations (given by the y-coordinate).	192
G.2	Data of displacement in point 1-7 for increasing SRF. The data was used to create the graph in section 5.5.1 for stability analysis of the final back wall along section S1.	205
G.3	Data of displacement in point 1-7 for increasing SRF. The data was used to create the graph in section 5.5.1 for stability analysis of the current back wall along section S2. . .	206
G.4	Data of displacement in point 1-7 for increasing SRF. The data was used to create the graph in section 5.5.1 for stability analysis of the final back wall along section S2.	207
G.5	Data of displacement in point 1-7 for increasing SRF. The data was used to create the graph in section 5.5.1 for stability analysis of the final back wall along section S3.	207
G.6	Data of displacement in point 1-7 for increasing SRF. The data was used to create the graph in section 5.5.1 for stability analysis of the current back wall along section S4. . .	208
G.7	Data of shear displacement along joint 1,2, and 3 for increasing SRF. The data was used to create the graph in section 5.5.2 for stability analysis of the final back wall along section S1.	212
G.8	Data of shear displacement along joint 1,2, and 3 for increasing SRF. The data was used to create the graph in section 5.5.2 for stability analysis of the current back wall along section S2.	216

G.9 Data of shear displacement along joint 1,2, and 3 for increasing SRF. The data was used to create the graph in section 5.5.2 for stability analysis of the final back wall along section S2. 219

G.10 Data of shear displacement along joint 1,2, and 3 for increasing SRF. The data was used to create the graph in section 5.5.2 for stability analysis of the final back wall along section S3. 222

G.11 Data of shear displacement along joint 1,2, and 3 for increasing SRF. The data was used to create the graph in section 5.5.2 for stability analysis of the final back wall along section S4. 227

H.1 Risk analysis of potential risks during field mapping and laboratory testing based on risk matrix by Aasteboel (2019) used for the field work in the quarry and the laboratory testing.228

List of Figures

1.1	The location of the quarry is marked with the red square in the right figure. The figure is modified after a map of Norway from Maps (2009). The left figure displays a map of the area around the quarry from Høydedata (Kartverket, 2020), showing the placement of the quarry along the hill.	1
1.3	Geological map of the quarry with the differentiation of dunites and serpentinite after Osland (1998). The map is modified after a geological map from Sibelco Nordic.	3
1.4	Foliation structures characteristic for the rock mass in the quarry. The benches are approximately 15m high.	3
1.5	Photo of parts of an eclogite boudin in the quarry.	4
1.6	Sketch of the planned geometry of the benches in the final back wall.	5
1.7	Model of the current and the final pit.	5
2.1	The four main failure modes, modified after Hoek and Bray (1977). From above: rotational failure, plane failure, wedge failure and toppling failure.	9
2.2	Rock mass properties depending on the scale in consideration, modified after Hoek and Marinos (2007). The Hoek-Brown failure criterion is applicable for intact rock, rock mass with many joints and heavily jointed rock mass.	10
2.3	Figure of triaxial loading of a core specimen with failure along a plane. The stresses σ_n and τ acting along the failure plane, and the fracture angle θ (or β) are indicated.	11
2.4	Illustration of the Mohr-Coulomb criterion, modified after Li (2018). Equation 2.4 defining the Mohr-Coulomb criterion, is drawn in a Mohr diagram. Mohr circles tangent to the line, express combinations of σ_1 and σ_3 at failure.	12
2.5	Strength envelopes, modified after Hammah et al. (2005), for the shear strength defined by the Hoek-Brown criterion as a function of σ_n , before and after strength reduction by safety factor F.	16

3.1	Plan of the quarry from Aasteboel (2019) showing the division of the quarry into section 1,2, and 3. The plan is modified after a model of the quarry by Sibelco Nordic,	22
3.2	Plan of the quarry, modified after Aasteboel (2019), showing the locations for measurements of dip and dip-direction of joints (indicated by the points P1-P55) and weakness zones (indicated by the points Z1-Z8). The green and the blue line indicate the main strike of the back wall. The plan was created from a model of the current quarry by Sibelco Nordic.	23
3.3	Plan of the quarry, modified after Aasteboel (2019), showing the locations for Q-value estimation, indicated by the points P1-P36. The plan was created from a model of the quarry by Sibelco Nordic.	24
3.4	Performance of tilttesting.	25
3.5	Plan of the quarry from Aasteboel (2019), showing the locations for tilttesting indicated by the points T1-T23. The plan was created after a model of the quarry by Sibelco Nordic.	26
3.6	Plan of the quarry from Aasteboel (2019), modified after Sibelco Nordic, showing the locations for estimation of JRC and JCS indicated by the points P1-P34. The black lines display the boundaries of the area sections.	27
3.7	28
3.8	Plan of the quarry showing the locations for collection of the four blocks used for UCS testing (B1: Dunite, B2: Serpentinised dunite 2, B3: Chlorite banded dunite, B4: Serpentinised Dunite 1. Soil for free swelling test was collected by point C1. The plan is modified after a model of the current quarry by Sibelco Nordic.	29
3.9	Photos of weathering of chlorite banded dunite.	29
3.10	The apparatus used for UCS testing and the sound velocity test.	31
3.11	Plan of the quarry showing where each of the cores are drilled. The plan is created after a model of the current quarry by Sibelco Nordic.	34
3.12	Rose diagram showing the distribution of strike for measured joints in area section 1, modified after Aasteboel (2019). The main strikes of the final back wall are indicated by the green and the blue lines (see figure 3.2 in section 3.1 for the direction of the lines in the quarry.)	36

3.13	Rose diagram showing the distribution of strike for measured joints in area section 2, modified after Aasteboel (2019). The main strike of the final back wall in the section is indicated by the green line (see figure 3.2 in section 3.1 for the direction of the lines in the quarry).	37
3.14	Rose diagram showing the distribution of strike for measured joints in area section 3, modified after Aasteboel (2019). The main strike of the final back wall in the section is indicated by the blue line (see figure 3.2 in section 3.1 for the direction of the lines in the quarry).	37
3.15	Plan of the quarry showing weakness zones observed during field mapping. The strike and the dip of the observed zones are indicated. The plan is modified after a model of the current quarry by Sibelco Nordic.	38
4.1	Plan of the quarry showing the locations of the four analysed potential wedges 1,2,3,4 marked in green, after model of the current quarry from Siblco Nordic. The shape and the size of the marks is based on the spacing of the discontinuities forming the wedge. They do not indicate the exact shape of the wedges.	52
4.2	Sketch of geometries used in the stability analyses of wedges. 50 is the defined width in meters of the surface at the top of the quarry, used to delimit the size of the wedge that can be formed	53
4.3	Photo of the analysed wedges. The position of the wedges are marked by the yellow lines.	54
4.4	A vertical load were added to the model with magnitude approximately equal to the weight of the overburden above the surface. A gravity stress field were defined with $\sigma_h = 1.5\sigma_v$, and ground surface at the height of the top of the hill.	58
4.5	Stress distribution of σ_v (σ_{yy}) induced by the vertical load.	58
4.6	Stress distribution of σ_h (σ_{xx}) induced by the vertical load.	59
4.7	The model includes the slope up to the hill above the quarry. A gravity stress field were defined with $\sigma_h = 1.5\sigma_v$, and ground surface at the top of the hill.	59
4.8	Stress distribution of σ_v (σ_{yy}).	60
4.9	Stress distribution of σ_h (σ_{xx}).	60
4.10	The figure shows the background for the placement of the external boundaries in the numerical models.	61

4.11	Plan of the quarry showing the location of the sections S1,S2,S3, and S4. The grey lines indicate the area sections 1,2, and 3 defined during field mapping. The plan is modified after a model of the quarry from Sibelco Nordic,	67
4.12	The geological section used to define the geology of the the model from section S1. The geometry of the final back wall is indicated by the black line. The brown line indicate the planned geometry of the wall from a simplified quarry design model. The geological section is modified after a section from Sibelco Nordic.	68
4.13	Geological section used to define the geology of the models from section S2. The geometry of the model of the current and the final back wall is indicated by the black lines. The brown line indicate the planned geometry of the final back wall from a simplified model of the quarry design. The geological section is modified after a section from Sibelco Nordic.	69
4.14	Geological section used to define the geology of the models from section S3. The geometry of the model of the current and the final back wall is indicated by the black lines. The brown line indicate the planned geometry of the final back wall from a simplified quarry design model. The geological section is modified after a section from Sibelco Nordic.	70
4.15	Geological section used to define the geology of the model by section S4. The geometries of the model of the current back wall and the final back wall are indicated by the black lines. The geological section is modified after a section from Sibelco Nordic.	71
4.16	The mesh set up used for calibration, showing the areas 1,2,3, and 4.	72
4.17	Photo of the plane failure used to calibrate the joint strength parameters of a serpentinized surface. The bench is about 15m high.	73
4.18	Section of geology from Sibelco Nordic used for the calibration model. The geometry of the back wall today is marked in black. The geometry of the final back wall is marked in brown.	74
4.19	The figures show the sizes of the finite elements and the foliation spacing for each trial 1-5 in the area of model showing the rock failure. The figures also show how the undercutting of the bench by the failure is included in the model. The finite elements in the models differ from the defined size when smaller elements are required to mesh details in the model and to obtain a gradual transition in the element sizes.	76

4.20	A sketch showing the rock failure used for the calibration process, represented by a block sliding down a surface. W = weight of block, N = Normal force from the block on the foliation surface, T = Shear force from the block on the foliation surface, l = length of the block, w = width of the block and h = height of the block.	77
5.1	Figures of the identified wedges in the current back wall formed by the discontinuities in wedge 1. The figures are constructed by Swedge.	83
5.2	Figures of the identified wedges in the current back wall formed by the discontinuities in wedge 2. The figures are constructed by Swedge Rocscience Inc (2019c).	84
5.3	Figure of the wedge formed when the tension crack is defined by a foliation crack and bench width. The wedge is located in the uppermost bench, and the bench top is the surface at the top of the quarry. The figures are constructed by the software Swedge. . . .	85
5.4	Figures of the identified wedges in the final back wall formed by the discontinuities in wedge 1. The figures are constructed by the software Swedge.	86
5.5	Figures of the identified wedges in the final back wall formed by the discontinuities in wedge 2. The figures are constructed by the software Swedge Rocscience Inc (2019c). . .	87
5.6	Figure of the wedge formed when the tension crack is defined by a foliation crack and bench width. The wedge is located in the uppermost bench, and the bench top is the surface at the top of the quarry. The figures are constructed by the software Swedge. . . .	88
5.7	Figures of the identified wedges in the final back wall formed by the discontinuities in wedge 4. The figures are constructed by the software Swedge Rocscience Inc (2019c). . .	89
5.8	The figure show the distribution of maximum shear strain in the back wall with the input parameters defined in Round 1 during calibration. The location of the failure surface in the numerical model is marked with a red line.	91
5.9	The graph displays the shear displacement along the failure surface, for the different joint strength parameters defined in Round 1-5. Negative shear displacement in the graph defines that the couple shear forces along the joint give a clockwise rotation to an element. The left side of the joint is in sliding down.	92
5.10	The figure show the location and the magnitude of the largest displacements in the wall with the input parameters from round 1.	93

5.11	Graph showing the maximum displacement in the back wall for increasing strength reduction factors (SRF). Green points indicate SRF where the model is stable. The red points indicate SRF where the model has become unstable. The critical SRF (CSRF) is indicated by the first red point along the graph in the model.	95
5.12	The figure indicates the points used to examine the deformation of the rock mass at different places in the back wall. The figure also shows the distribution of shear strain in the back wall when SRF equals 1.	96
5.13	Graph showing the displacement for increasing SRF at different places in the rock mass in the back wall. Blue curves are used for points located in rock mass typical for area section 2. Brown and yellow curves are used for points located in rock mass typical for area section 1.	96
5.14	The distribution of maximum shear strain in the current back wall along section S2 when SRF equals 6.11. The colours show different values of shear strain and indicate the location of the failure when the wall becomes unstable.	97
5.15	The figure indicate the joints where shear displacement was analysed in the current back wall in section S2.	98
5.16	The graph displays the shear displacement along three joints with different surface types in the current back wall in section S2.	98
5.17	Graph showing the maximum displacement in the back wall for increasing strength reduction factors (SRF). Green points indicate SRF where the model is stable. The red points indicate SRF where the model has become unstable. The critical SRF (CSRF) is indicated by the first red point along the graph in the model.	100
5.18	The figure indicates the points along section S1 used to examine the deformation of the rock mass at different places in the back wall.	101
5.19	Graph showing the maximum displacement for increasing SRF at different places in the rock mass in the back wall. Blue curves are used for points located in rock mass typical for area section 2. Brown and yellow curves are used for points located in rock mass typical for area section 1.	101
5.20	The figure indicates the points used to examine the deformation of the rock mass at different places in the back wall.	102

5.21	Graph showing the maximum displacement for increasing SRF at different places in the back wall. Blue curves are used for points located in rock mass typical for area section 2. Brown and yellow curves are used for points located in rock mass typical for area section 1.	103
5.22	The figure indicates the points used to examine the deformation of the rock mass at different places in the back wall.	104
5.23	Graph showing the maximum displacement for increasing SRF at different places in the rock mass in the back wall. Blue curves are used for points located in rock mass typical for area section 2. Brown and yellow curves are used for points located in rock mass typical for area section 1.	104
5.24	The figure indicates the points used to examine the deformation of the rock mass at different places in the back wall.	105
5.25	Graph showing the maximum displacement for increasing SRF at different places in the rock mass in the back wall. Green curves are used for the points located in rock mass typical for area section 2. Brown and yellow curves are used for the point located in rock mass typical for area section 1.	106
5.26	The figure shows the contours of maximum strain along the four sections S1, S2, S3, and S4 for the highest SRF values used in the analysis of each section. The colours are used to show the location of the global failure along each section, and the colour of the strain in the different figures should not be compared.	106
5.27	The figure indicates the joints used in the analysis of shear displacement. The coordinates are used to show the location of the displacements along the joints given in graph 5.28. The coordinates are defined relative to the location of the bottom of the wall in the numerical model of the section.	108
5.28	The graph displays the shear displacement along three joints with different surface types in the final back wall in section S1. The coordinates give the location of the displacement relative to the bottom of the wall in the numerical model of the section. The location of the joints are shown in figure 5.27.	109
5.29	The figure indicates the joints used in the analysis of shear displacement. The coordinates are used to show the location of the displacements along the joints given in graph 5.30. The coordinates are defined relative to the location of the bottom of the wall in the numerical model of the section.	110

5.30	The graph displays the shear displacement along three joints with different surface types in the final back wall in section S2. The coordinates give the location of the displacement relative to the bottom of the wall in the numerical model of the section. The location of the joints are shown in figure 5.29.	110
5.31	The figure indicates the joints used in the analysis of shear displacement. The coordinates are used to show the location of the displacements along the joints given in graph 5.32. The coordinates are defined relative to the location of the bottom of the wall in the numerical model of the section.	111
5.32	The graph displays the shear displacement along three joints with different surface types in the final back wall in section S3. The coordinates give the location of the displacement relative to the bottom of the wall in the numerical model of the section. The location of the joints are shown in figure 5.31.	112
5.33	The figure indicates the joints used in the analysis of shear displacement. The coordinates are used to show the location of the displacements along the joints given in graph 5.34. The coordinates are defined relative to the location of the bottom of the wall in the numerical model of section S4.	113
5.34	The graph displays the shear displacement along three joints with different surface types in the final back wall in section S4. The coordinates give the location of the displacement relative to the bottom of the wall in the numerical model of the section. The location of the joints are shown in figure 5.33	113
5.35	The plan of the quarry show the locations where the foliation has been measured to have a dip below 70 ° (marked in red). The names of the points used in the results from field mapping are indicated. The plan also shows (in purple) the area with eclogite boudins. The plane failure used for calibration occurred by point P12. The plan is modified after a model of the quarry by Sibelco Nordic.	118
6.1	The figure shows a plan of the current quarry with the location of risk zone 1. The zone is drawn after a map of geology from Sibelco Nordic (see fig 1.3) and observations of eclogite boudins during field mapping. The plan of the quarry is modified after a model of the quarry by Sibelco Nordic.	123

6.2	The figure shows a plan of the quarry at life of mine with location of risk zone 1 and 2. Risk zone 1 is drawn after map of geology from Sibelco Nordic (see fig 1.3) and observations from field mapping. Risk zone 2 is drawn as an approximation of the area in the final back wall that will consist of chlorite banded dunite and blastogranular dunite after geology sections of S1, S2, S3, and S4. The plan of the quarry is modified after a model of the quarry by Sibelco Nordic.	124
A.1	Roughness profiles drawn during field mapping to estimate JRC.	142
A.2	Roughness profiles drawn during field mapping to estimate JRC.	142
B.1	The photos by Aasteboel (2019) show typical failure modes of cores from block No.1, 2, 3 and 4 during UCS-testing.	152
B.2	Graphical representation, after Aasteboel (2019), of the relationship between stress and strain during UCS-testing of five cores from block No. 1.	154
B.3	Graphical representation, after Aasteboel (2019), of the relationship between stress and strain during UCS-testing of six cores from block No. 2.	155
B.4	Graphical representation, after Aasteboel (2019), of the relationship between stress and strain during UCS-testing of seven cores from block No. 3.	155
B.5	Graphical representation, after Aasteboel (2019), of the relationship between stress and strain during UCS-testing of five cores from block No. 4.	156
B.6	Photo, after Aasteboel (2019), of clay from weakness zones Z4 after 24 hours of swelling in free swelling test.	158
C.1	Photo of the core with the weakness zones evaluated to be related to the weakness zone Z1-Z5 observed in the quarry.	159
C.2	Photos of the areas in the studied cores evaluated to correspond to the contact zone at the gneiss boundary observed in the quarry at point Z8.	160
C.2	Photos of the areas in the studied cores evaluated to correspond to the contact zone at the gneiss boundary observed in the quarry at point Z8.	161
C.2	Photos of the areas in the studied cores evaluated to correspond to the contact zone at the gneiss boundary observed in the quarry at point Z8.	162

C.3	Photos of weathering of chlorite banded dunite.	163
D.1	Chart by Deere and Miller (1966) used to determine JCS based on measured Schmidtness hardness SH and the density of measured rock.	171
D.2	Chart of roughness profiles used to determine the JRC value after Barton and Choubey (1977).	172
D.3	Chart after Marinos and Hoek (2000) for determination of the Geological Strength Index (GSI).	173
D.4	Table after Norges Geotekniske Institutt (2015) for determination of RQD.	174
D.5	Table after Norges Geotekniske Institutt (2015) for determination of Jn.	174
D.6	Table after Norges Geotekniske Institutt (2015) for determination of Jr.	175
D.7	Table after Norges Geotekniske Institutt (2015) for determination of Ja.	176
D.8	Table after Norges Geotekniske Institutt (2015) for determination of Jw.	177
D.9	Table after Norges Geotekniske Institutt (2015) for determination of SRF.	178
D.10	Continuation of table after Norges Geotekniske Institutt (2015) for determination of SRF.	179
F.1	Wedge 1	183
F.2	Geometry of the current slope and the slope defined in the life of mine model, by wedge 2.	184
F.3	Wedge 3	184
F.4	Wedge 4	185
F.5	Sections of the identified wedges in the final back wall formed by the discontinuities in wedge 1. The sections are constructed by the software Swedge (Rocscience Inc, 2019c).	186
F.6	Sections of the identified wedges in the final back wall formed by the discontinuities in wedge 2. The sections are constructed by the software Swedge (Rocscience Inc, 2019c).	187
F.7	Section of the wedge formed when the tension crack is defined by a foliation crack and bench width. The wedge is located in the uppermost bench, and the bench top is the surface at the top of the quarry. The section are constructed by the software Swedge (Rocscience Inc, 2019c).	188

F.8	Sections of the identified wedges in the final back wall formed by the discontinuities in wedge 1. The sections are constructed by the software Swedge (Rocscience Inc, 2019c).	188
F.9	Sections of the identified wedges in the final back wall formed by the discontinuities in wedge 2. The sections are constructed by the software Swedge (Rocscience Inc, 2019c).	189
F.10	Section of the wedge formed when the tension crack is defined by a foliation crack and bench width. The wedge is located in the uppermost bench, and the bench top is the surface at the top of the quarry. The sections are constructed by the software Swedge (Rocscience Inc, 2019c).	190
F.11	Sections of the identified wedges in the final back wall formed by the discontinuities in wedge 2. The sections are constructed by the software Swedge (Rocscience Inc, 2019c).	190
G.1	The numerical model used to perform the calibration of joint strength parameters for the serpentized surface.	191
G.2	The numerical model used to perform the calibration divided into finite elements.	191
G.3	The figure show the calculated total displacement in the numerical model used for calibration in Round 1.	192
G.4	The numerical model of section S2 used to perform the stability analysis of the current back wall using method 1.	193
G.5	The numerical model of section S2 showing the division of the model into finite elements. The model was used to perform the stability analysis of the current back wall using method 1.	193
G.6	The numerical model of section S2 used to perform the stability analysis of the current back wall using method 2 with the division of the model into finite elements.	194
G.7	The numerical model of section S2 showing the division of the model into finite elements. The model was used to perform the stability analysis of the current back wall using method 2.	194
G.8	The numerical model of section S1 used to perform the stability analysis of the final back wall using method 1.	195
G.9	The numerical model of section S1 showing the division of the model into finite elements. The model was used to perform the stability analysis of the current back wall using method 1.	195

G.10	The numerical model of section S2 used to perform the stability analysis of the final back wall using method 1.	196
G.11	The numerical model of section S2 showing the division of the model into finite elements. The model was used to perform the stability analysis of the current back wall using method 1.	196
G.12	The numerical model of section S3 showing the division of the model into finite elements. The model was used to perform the stability analysis of the current back wall using method 1.	197
G.13	The numerical model of section S3 showing the division of the model into finite elements. The model was used to perform the stability analysis of the current back wall using method 1.	197
G.14	The numerical model of section S4 used to perform the stability analysis of the final back wall using method 1.	198
G.15	The numerical model of section S4 showing the division of the model into finite elements. The model was used to perform the stability analysis of the current back wall using method 1.	198
G.16	The numerical model of section S1 used to perform the stability analysis of the final back wall using method 2.	199
G.17	The numerical model of section S1 showing the division of the model into finite elements. The model was used to perform the stability analysis of the current back wall using method 1.	199
G.18	The numerical model of section S2 used to perform the stability analysis of the final back wall using method 2.	200
G.19	The numerical model of section S2 showing the division of the model into finite elements. The model was used to perform the stability analysis of the current back wall using method 2.	200
G.20	The numerical model of section S3 used to perform the stability analysis of the final back wall using method 2.	201
G.21	The numerical model of section S3 showing the division of the model into finite elements. The model was used to perform the stability analysis of the current back wall using method 2.	201

G.22 The numerical model of section S4 used to perform the stability analysis of the final back wall using method 2.	202
G.23 The numerical model of section S2 showing the division of the model into finite elements. The model was used to perform the stability analysis of the current back wall using method 2.	202
G.24 The figure show the elevation profile used to draw the hill slope above the quarry in the numerical model of section S1. The profile show the elevation along the orange line. "Høyde i Meters" define meters above sea level. "Avstand in Meters" define the distance from the start of the line in meters The elevation profile is made by Høydedata (Kartverket, 2020).	203
G.25 The figure show the elevation profile used to draw the hill slope above the quarry in the numerical model of section S2. The profile show the elevation along the orange line. "Høyde i Meters" define meters above sea level. "Avstand in Meters" define the distance from the start of the line in meters The elevation profile is made by Høydedata (Kartverket, 2020).	203
G.26 The figure show the elevation profile used to draw the hill slope above the quarry in the numerical model of section S3. The profile show the elevation along the orange line. "Høyde i Meters" define meters above sea level. "Avstand in Meters" define the distance from the start of the line in meters The elevation profile is made by Høydedata (Kartverket, 2020).	204
G.27 The figure show the elevation profile used to draw the hill slope above the quarry in the numerical model of section S4. The profile show the elevation along the orange line. "Høyde i Meters" define meters above sea level. "Avstand in Meters" define the distance from the start of the line in meters The elevation profile is made by Høydedata (Kartverket, 2020).	204

1. Introduction

This thesis presents a stability analysis of an olivine quarry located at Åheim, in Møre og Romsdal county in western Norway, see figure 1.1 for location. The quarry is the world's largest producer of olivine. The olivine quarry is operated by Sibelco Nordic with an annual production of approximately 2 million tons. The production has an estimated life of mine of 120 years.

1.1 Location and geological setting

The quarry is situated along a hillside striking approximately east-west, with the back wall following the hillside, see figure 1.1. The top of the hill lies about 570 m.a.s.l. (meters above sea level). The lowest level in the quarry is placed 90 m.a.s.l. and the top level is 350 m.a.s.l. This also defines the bottom and top level in the life of mine plan of the quarry.

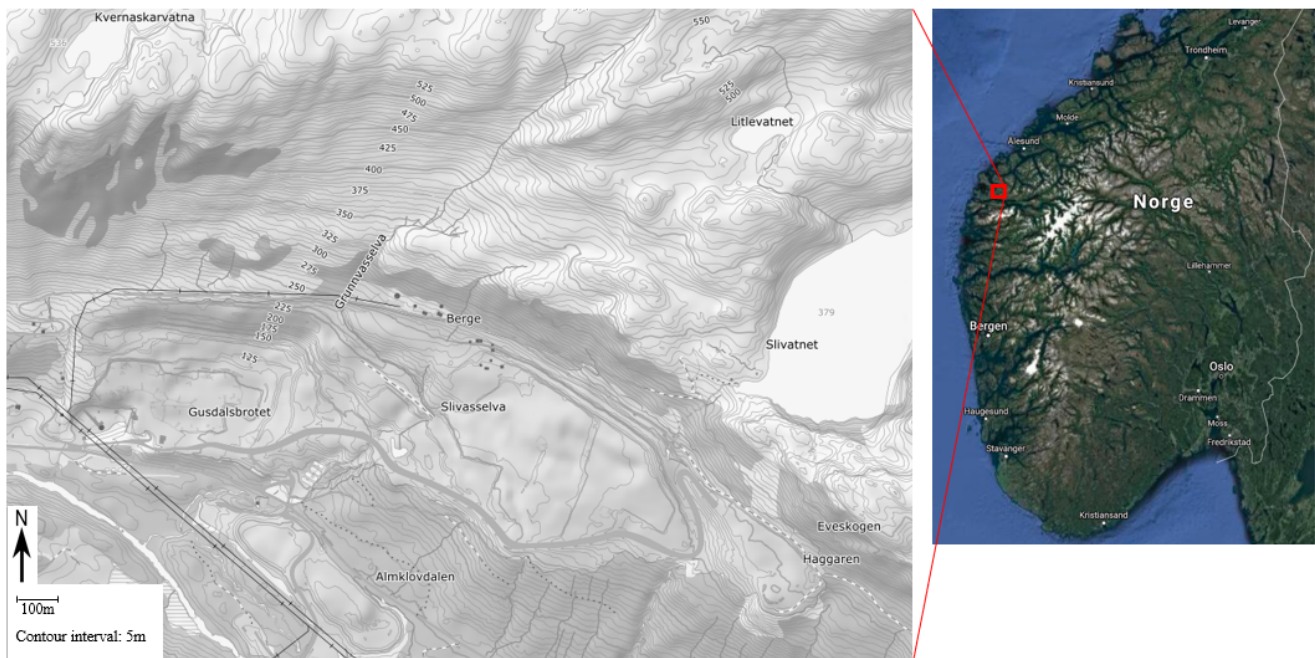
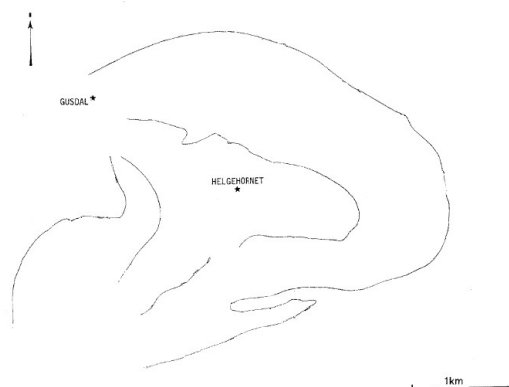
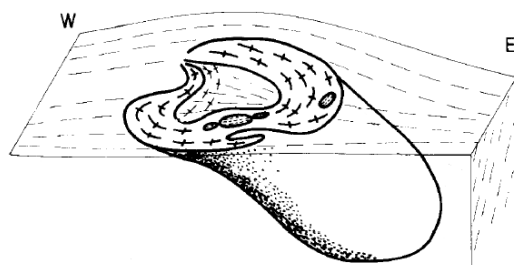


Figure 1.1: The location of the quarry is marked with the red square in the right figure. The figure is modified after a map of Norway from Maps (2009). The left figure displays a map of the area around the quarry from Høydedata (Kartverket, 2020), showing the placement of the quarry along the hill.

The olivine quarry is situated in an ultramafic lense (Lappin, 1966). In the middle of the lense, is a mountain of gneiss, and the lense is surrounded by gneiss on all sides. Olivine has been produced from different places in the lense. The quarry in operation today, is situated in the northern part of the lense. The shape of the lense below the surface is uncertain. Cordellier et al. (1981) proposed that the ultramafic lense has a synform cone-shape, extending under the gneiss in S-E direction, as shown in figure 1.2a and 1.2b. Different formation mechanisms have been proposed for the lense. The protoliths have possibly been deformed during the Svecofennian orogeny, the Sveconorwegian orogeny, and the Caledonian orogeny. According to a structural analysis by Cordellier et al. (1981), most of the structural forming deformation happened during the Svecofennian orogeny. The ultramafic lense may originate from the upper part of the mantel, and was emplaced into the lower crust during the orogeny. Later in the orogeny, the lense sank into the gneiss due to gravity sinking, resulting in the synform shape of the lense.



(a) Figure modified after Cordellier et al. (1981), showing a sketch of the shape of the ultramafic lense at the surface.



(b) Figure modified after Cordellier et al. (1981), showing the proposed cone shape of the ultramafic lense extending in South-East direction.

The ultramafic lense consists of different types of dunite. A serpentine-gneiss contact zone surrounds the dunite. There is a gradual transition between the different layers of dunite and the serpentinised zone, and a large part of the dunite is serpentinized (Osland, 1998). Sibelco Nordic defines the varieties of dunite and serpentine after the proposed division by Osland (1998). The dunite and serpentinite are divided into different varieties based on their petrochemistry and structure. The defined types are dunite, blastogranular dunite, chlorite-banded dunite, chlorite-veined dunite, chlorite-amphibole dunite, serpentinized dunite, and serpentinite, see figure 1.3. The variations of dunites and serpentinite are mainly distinguished by the degree of serpentinisation, the size of the olivine grains, and the chlorite content. All the presented varieties of rocks will be present in the final back wall of the pit.

The varieties of dunite have a layered structure with boundaries striking parallel to the serpentine-gneiss contact zone in the north. The layers have a subvertical dip. The lense is characterised by a strong foliation dipping parallel to the gneiss-serpentine contact and the dunite boundaries (Lappin, 1966),(Osland, 1998). The foliation structure is defined by chlorite bands and a foliation-parallel joint set, see figure 1.4. In the northern part of the lense is a layer with eclogite boudin. According to Cordellier

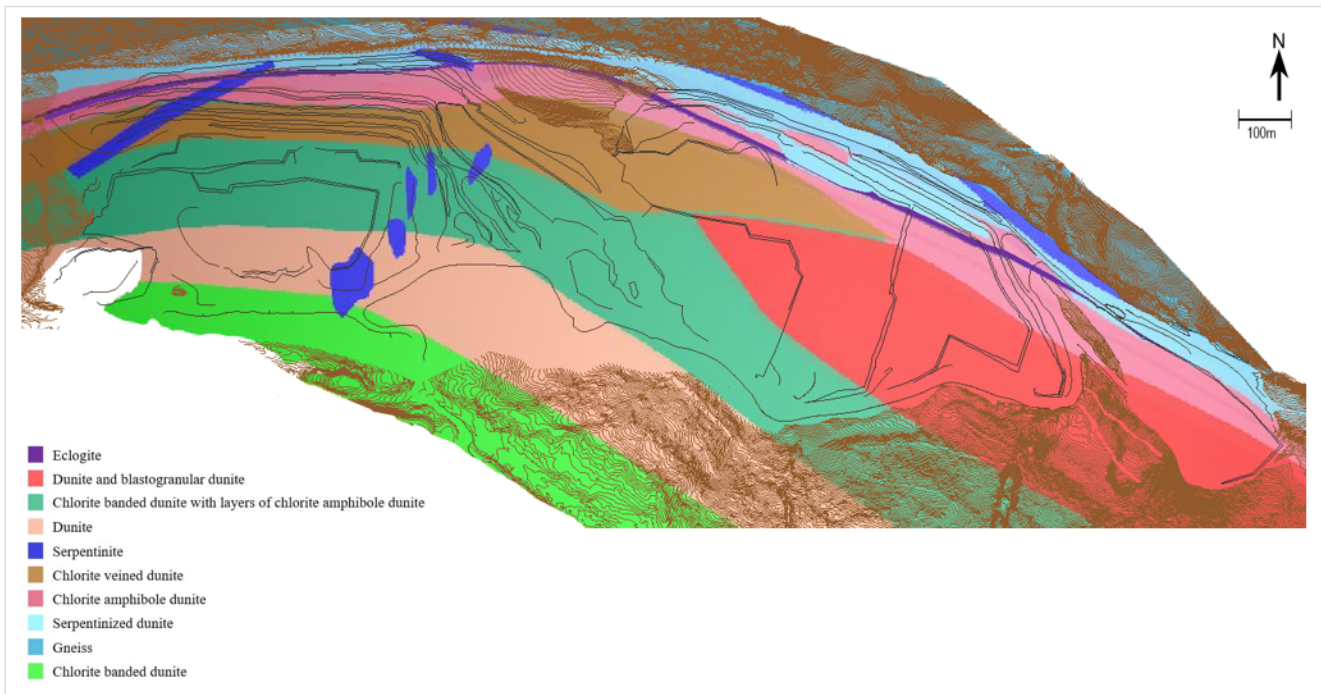


Figure 1.3: Geological map of the quarry with the differentiation of dunites and serpentinite after Osland (1998). The map is modified after a geological map from Sibelco Nordic.

et al. (1981), the eclogite was emplaced into the crust by the same processes as the dunite lense. The eclogite boudins are up to 10m long with a thickness of maximum 1m. The longest axis of the boudins strike parallel to the chlorite foliation. The core of the boudins consists of unaltered eclogite, while the outer parts of the boudins are retrograded, and the rock is close to amphibolite. Figure 1.5 show a photo of an eclogite boudin. The dunite close to the boudins is serpentinized. The eclogite boudins are also associated with areas of garnet-peridotite.



(a) Chlorite banded dunite at level 90.



(b) Serpentinised dunite at level 225.

Figure 1.4: Foliation structures characteristic for the rock mass in the quarry. The benches are approximately 15m high.



Figure 1.5: Photo of parts of an eclogite boudin in the quarry.

1.2 The aim of the thesis

The entire quarry is located in dunite with the top of the back wall at the gneiss boundary, see figure 1.3, and there is low production of waste rock. Due to the shape of the quarry and the gneiss boundary, the slope of the back wall has a high influence on the degree of exploitation of the olivine resource and the stability of the quarry (Contreras, 2015). A steep slope angle will allow more dunite to be produced. A smaller slope angle will result in less dunite production. The slope angle of the quarry is determined to balance maximum exploitation and safety (Deliveris et al., 2016) within the boundaries of the dunite. In 1995 a master thesis analysed the stability of the current planned slope design (Schönborn, 1995). The thesis concluded the current wall to be stable, but the risk of instability could increase when the quarry is being developed at lower levels. As the production in the quarry has continued, the plan for mine design has been developed. The current plan for the geometry of the benches and the slope in the final back wall is displayed in figure 1.6. The plan gives the design for the quarry at life of mine. A model of the current quarry and the quarry at life of mine is shown in figure 1.7.

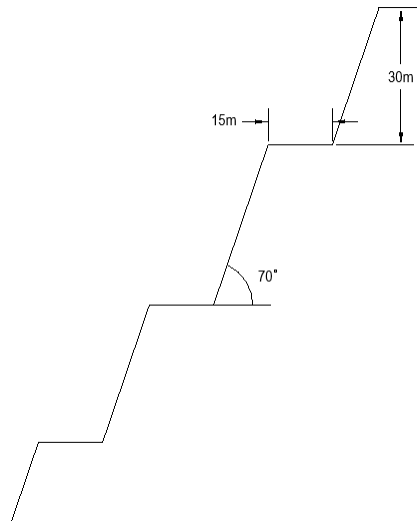
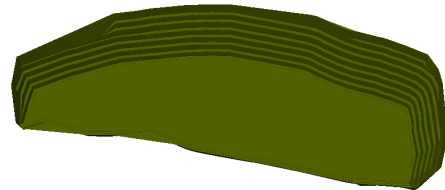


Figure 1.6: Sketch of the planned geometry of the benches in the final back wall.



(a) Model of the pit today constructed in Microstation (Bentley Systems, 2018), after a model of the current quarry from Sibelco Nordic.



(b) Model of the final pit constructed in Microstation (Bentley Systems, 2018), after a model of the current quarry from Sibelco Nordic.

Figure 1.7: Model of the current and the final pit.

The aim of this thesis is to analyse the stability of the current back wall and the back wall as the quarry develops to lower levels with the geometry of the life of mine plan. The analysis will investigate the local stability in terms of the stability of benches, and the global stability in terms of the stability of the entire wall. The following methods will be used to investigate the stability:

- Continuum numerical modelling of sections of the current back wall and the planned final back wall at life of mine. The numerical modelling will be performed using the software RS2 by Rocscience (2019b).
- Analysis of wedges observed in the quarry using the limit equilibrium method. The analysis of wedges will be performed using the software Swedge by Rocscience Inc (2019c).
- Measurements and observations from field mapping.

The input data in the analyses are provided by results from field mapping and laboratory testing. The field mapping and laboratory testing were performed as the author's project work autumn 2019 and the results were presented in an unpublished report (Aasteboel, 2019).

1.3 The structure of the thesis

The results from field mapping and laboratory testing had influence on the performance of the numerical and the limit equilibrium analyses. After a theory overview in chapter 2, the methods applied for field mapping and laboratory testing and the following results are therefore presented first, in chapter 3. The methods used for the numerical analysis of the wall and the analysis of wedges are described in chapter 4. The results from the analysis will be displayed and discussed in chapter 5. The last chapter will present the conclusion on the stability of the wall.

2. Theory

This chapter presents theory applied in this thesis regarding instability of rock slopes. The first section outlines factors that can induce instability in a rock slope. The main types of rock slope failures is described. The second section describes common failure criteria that can be used to determine the strength of the rock mass and joints. The third section outlines commonly used methods to analyse the stability of a rock slope. The section focus on the methods that is used in the stability analysis of the quarry. The last section describes different rock mass classification systems that are used to define the rock mass quality. The classification system Q-system was used during field mapping, and the section focuses on how the Q-system can be used to determine the rock mass strength.

2.1 Instability of a rock slope

Instability of a rock slope is related to rock mass properties and external factors. The properties of the rock mass will determine the resistance of the rock mass to failure and the potential failure mode. External factors can contribute to instability or trigger a slope failure (Varnes, 1978).

2.1.1 External factors influencing the rock slope stability

The external factors contributing to instability can be divided into two main categories (Varnes, 1978):

- Factors increasing the shear stress in the rock mass.
- Factors reducing the shear strength in the rock mass.

Increased shear stress in a slope can be a result of removed support in front of, or at the toe of the slope, caused by erosion, rock mass failure or excavation. The shear stress will also increase when an extra load is added to the top surface of a slope. This can be in terms of water, snow, man-made piles and constructions. The presence of water can also contribute to increased pressure in joints and swelling of clay, inducing swelling pressure. In addition, blasting, machinery and seismic events will cause vibrations in the rock mass, giving acceleration to the slope (Raghuvanshi, 2019). If the magnitude of the shear stress becomes higher than the shear strength, slope failure will be induced. The shear strength of the rock mass can be reduced by weathering and alteration of the rock material and discontinuities.

2.1.2 Failure modes

There are four main modes of rock slope failure (Kliche, 2018), see figure 2.1.

- Rotational failure

Rotational failure is also called circular failure. Rotational failure in rock slopes is most common in very jointed rock mass, constructed rock fillings or in highly weathered rock mass. The rock mass fails by sliding along a curved surface (Kliche, 2018). The shape of the sliding surface is determined by the discontinuities in the rock mass.

- Plane failure

Plane failure describes failure along a discontinuity surface. Failure can occur where a discontinuity is striking parallel or approximately parallel to the slope face, and have a dip greater than the friction angle and smaller than the dip of the slope surface (Hoek and Bray, 1977). Plane failure also requires release surfaces, and a joint or free surface at the top of the rock mass volume in consideration.

- Wedge failure

A wedge is produced when two discontinuities strike across the slope face and intersect in a line (Hoek and Bray, 1977). If the line of intersection dip into the slope face with an angle greater than the friction angle, the wedge can slide along the intersection line and cause wedge failure.

- Toppling failure

Toppling failure is failure due to rotation of block about it's base (Hoek and Bray, 1977). Toppling failure occur in slopes were open joints form blocks with small width compared to height, or where the slope surface is very steep. The blocks lean against each other downwards, and exert a thrust force at the toe of the slope (Goodman, 2013). The thrust force can cause deformation at the toe of the slope, which cause the blocks to become unstable and fall.

In addition to the main slope failure modes, smaller rock falls called ravelling, may occur. The rock failure happens due to a combination of mechanisms, and is often associated with freezing and thawing of water in cracks and fissures (Hoek and Bray, 1977).

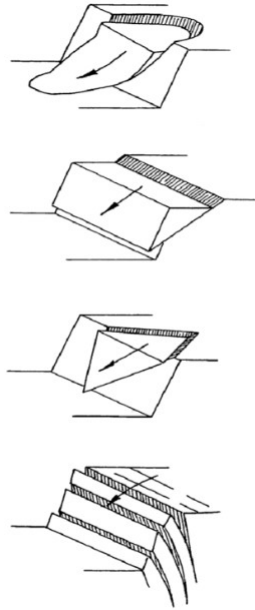


Figure 2.1: The four main failure modes, modified after Hoek and Bray (1977). From above: rotational failure, plane failure, wedge failure and toppling failure.

2.2 Failure criteria

Rock mass strength depends on the strength of intact rock, joints, and the surface conditions of the joints (Marinos and Hoek, 2000). Different failure criteria have been developed to estimate the strength properties of rock mass. The Barton-Bandis failure criterion is used to investigate the shear strength of joints properties and potential sliding along joint surfaces (Barton and Bandis, 1990). The Hoek-Brown criterion and the Mohr-Coulomb criterion are used to investigate the strength of isotropic rock mass, and the potential for failure in the rock mass as a whole (Hoek and Brown, 1988).

2.2.1 Hoek-Brown Criterion

The Hoek-Brown criterion is an empirical, non-linear failure criterion (Hoek and Brown, 1980). The empirical criterion was developed due to the difficulty of establishing a mechanistic criterion. The criterion can be used to describe the strength of rock mass which behaves as an isotropic material, see figure 2.2. The criterion can be applied to problems related to small rock mass volumes, like laboratory testing of intact rock (Hoek and Brown, 1988). It can also be used to estimate the strength of heavily jointed rock mass. For rock mass with low density of discontinuities compared to the scale of the slope, the strength of the discontinuities should be evaluated separately (Hoek, 2007).

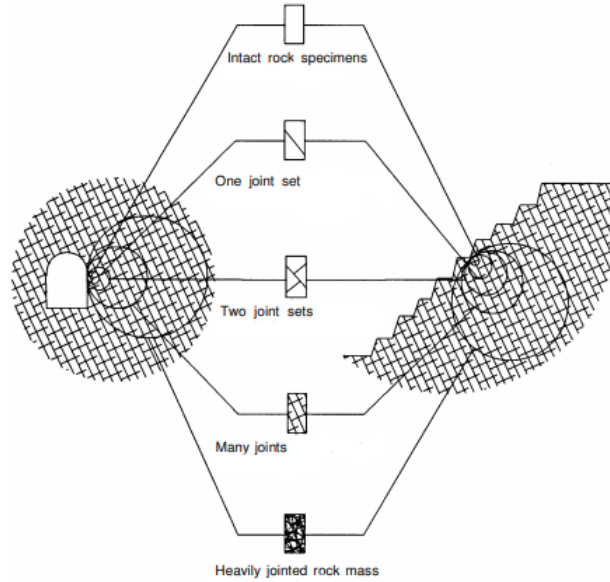


Figure 2.2: Rock mass properties depending on the scale in consideration, modified after Hoek and Marinos (2007). The Hoek-Brown failure criterion is applicable for intact rock, rock mass with many joints and heavily jointed rock mass.

The generalised Hoek-Brown failure criterion is expressed by equation 2.1. The criterion is defined by six different parameters: major and minor effective principle stress, σ_1' and σ_3' , uniaxial compressive strength of intact rock σ_{ci} and the constant m_b , s and a describing the properties of the rock mass.

$$\sigma_1' = \sigma_3' + \sigma_{ci} \left(m_b \frac{\sigma_3'}{\sigma_{ci}} + s \right)^a \quad (2.1)$$

The criterion considers the intermediate principle stress to be insignificant for potential rock mass failure. The uniaxial compressive strength (UCS) defines the contribution of strength of intact rock, to the rock mass strength (Hoek and Brown, 1988). The UCS of intact rock is found by UCS-testing of a 50 mm core, tested normal to any discontinuities (Hoek et al., 1995). Constant m_b is a material constant and depends on the degree of fracturing of the rock mass before the rock mass was disturbed. The constants a and s are used to describe the properties of the rock mass. Constant s is related to the tensile strength between particles and the interlocking of the particles. Joints in the rock mass give blocks more freedom to move, and lower the value of a and s .

The Hoek-Brown Criterion can also be described by the shear stress τ and the normal stress σ_n on a discontinuity surface. τ and σ_n can be expressed by the major and minor principal stress, σ_1 and σ_3 by equation 2.2 and 2.3 after Hoek et al. (1973).

$$\tau = (\sigma'_1 - \sigma'_3) \left(\frac{\sqrt{1 + am_b \left(m_b \frac{\sigma'_3}{\sigma_{ci}} + s \right)^{a-1}}}{2 + am_b \left(m_b \frac{\sigma'_3}{\sigma_{ci}} + s \right)^{a-1}} \right) \quad (2.2)$$

$$\sigma'_n = \frac{\sigma'_1 + \sigma'_3}{2} - \frac{\sigma'_1 - \sigma'_3}{2} \cdot \left(\frac{1 + am_b \left(m_b \frac{\sigma'_3}{\sigma_{ci}} + s \right)^{a-1} - 1}{1 + am_b \left(m_b \frac{\sigma'_3}{\sigma_{ci}} + s \right)^{a-1} + 1} \right) \quad (2.3)$$

It is difficult to estimate the rock mass strength, and further the constants m , s and a , on the scale of the excavations and slopes considered in rock mechanical problems (Hoek and Brown, 1980). Equations have been developed to relate the material constants to rock mass characterisation systems, see section 2.4.

2.2.2 Mohr-Coulomb criterion

The Mohr-Coulomb criterion is a linear criterion, defining the stress conditions that will cause failure of intact rock (Li, 2018). The failure criterion is based on the theory that failure along a plane in intact rock, is caused by shear stress along the plane (Jaeger et al., 2007). The failure plane will have an orientation with an angle relative to the direction of the main principle stress σ_1 , given by the fracture angle θ , see figure 2.3. (The fracture angle can also be described in terms of the angle between the direction of σ_1 and the normal stress on the failure plane σ_n by angle β .)

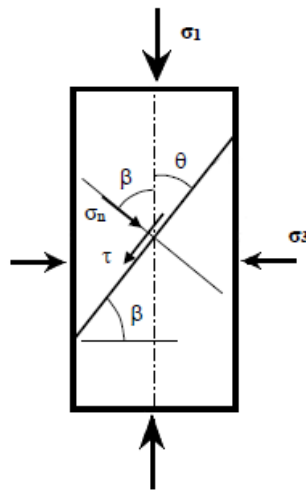


Figure 2.3: Figure of triaxial loading of a core specimen with failure along a plane. The stresses σ_n and τ acting along the failure plane, and the fracture angle θ (or β) are indicated.

The Mohr-Coulomb criterion looks at the combination of the major and the minor principal stress on the rock, and ignores the impact of the intermediate principal stress. Failure occurs when the shear stress on the plane is higher than the shear strength. The shear strength of intact rock is described by equation 2.4. The shear strength is considered to be a function of σ_n , internal cohesion c and internal friction, described by an internal friction angle ϕ .

$$\tau = c + \sigma_n \tan(\phi) \quad (2.4)$$

The internal friction angle ϕ is related to the fracture angle θ by equation 2.5.

$$\theta = \frac{\pi}{4} + \frac{\phi}{2} \quad (2.5)$$

The internal cohesion represents a cohesive force in the rock. The internal friction can be regarded as friction working along an imaginary surface in the intact rock before failure. Right before failure, the failure plane in the intact rock consists of areas with micro cracks and intact areas, along the imaginary surface (Savage et al., 1996). The internal friction is due to the frictional forces along the micro cracks in the plane.

Equation 2.4 forms a straight line in the σ, τ plane (Li, 2018). Mohr's circle for a stress relationship between the strength of the rock σ_1 and the confining stress σ_3 at failure, will be tangent to this straight line, and the equation form the failure envelope of the Mohr-Coulomb criterion. This is illustrated in figure 2.4.

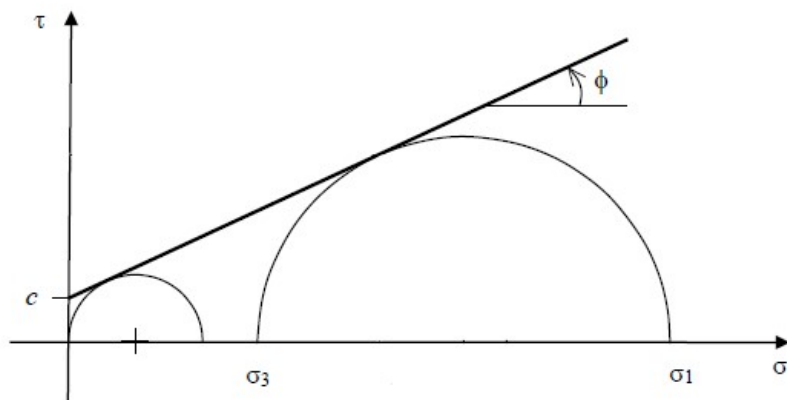


Figure 2.4: Illustration of the Mohr-Coulomb criterion, modified after Li (2018). Equation 2.4 defining the Mohr-Coulomb criterion, is drawn in a Mohr diagram. Mohr circles tangent to the line, express combinations of σ_1 and σ_3 at failure.

On entirely separated joint surfaces, the cementation causing cohesion is broken, and $c = 0$ (Barton, 2012). Based on equation 2.4, the shear strength of a rock joint with no filling, can be described in terms

of normal stress and the friction of the joint surfaces, by Coulomb's law, see equation 2.6 (Li, 2018).

$$\tau = \sigma_n \tan(\phi) \quad (2.6)$$

ϕ is the apparent friction angle of the joint surface, and describes the frictional conditions on the surface. The apparent friction angle ϕ is a joint characteristic defined by the basic friction angle ϕ_b and the dilation angle i by equation 2.7.

$$\phi = \phi_b + i \quad (2.7)$$

ϕ_b is describing the material properties of the rock and i describes the roughness of the surface, before any asperities have been sheared off. The Barton-Bandis failure criterion can be used to determine the dilation angle, and estimate the shear strength of the joints surface.

2.2.3 Barton-Bandis criterion

The Barton-Bandis failure criterion gives an estimate of the shear strength of rock joints without filling. The criterion is non-linear and based on empirical data. The shear strength of joints after is expressed by equation 2.8 by Barton and Bandis (1990). The equation propose an expression for the apparent friction angle defined in the Mohr-Coulomb criterion for joints (see equation 2.6). In the Barton-Bandis criterion, the frictional resistance of a joint is defined by the normal stress σ_n acting across the joint, the joint wall compressive strength (JCS), the joint roughness coefficient (JRC), and the residual friction angle ϕ_r .

$$\tau = \sigma_n \tan\left(JRC \log\left(\frac{JCS}{\sigma_n}\right) + \phi_r\right) \quad (2.8)$$

The magnitude of σ_n depends on the weight of overlying rock and the angle of the joint. JCS describes the compressive strength of a joint surface (Barton, 1976). When σ_n is small, there is little contact between the walls on each side of the joint, resulting in low confinement along the joint. The JCS of an unweathered joint surface can therefore be estimated to be equal to the UCS of intact rock. In most cases, the joint wall has experienced some degree of weathering and JCS is less than UCS. If σ_n is very small compared to JCS, none of the asperities will be sheared off. When σ_n is much larger than JCS, all the roughness of the surfaces will be sheared off (Li, 2018). The field of application for the Barton-Bandis criterion is therefore assigned to be surfaces where the value of σ_n is equal to or between 0.1JCS and 1.0JCS.

Field measurements are used to estimate the unknown parameters JCS, JRC, and ϕ . JCS can be estimated

in the field by using a Schmidt Hammer. The Schmidt Hammer releases a piston against the joint wall surface and measures the rebound value when the piston bounces back. The rebound value is used to determine the JCS for the wall, by using the chart by Deere and Miller (1966) for correlation between rebound value, density of rock, and UCS, see figure D.1 in appendix D. JRC describes the roughness of a joint wall surface by the dilation angle i . JRC is found by comparing a profile of the asperities on the joint wall, with the roughness profiles by Barton and Choubey (1977), see figure D.2 in appendix A. The profiles are used to assign a dilation angle i between 0-20 degrees to the surface. When the asperities on the surface have been sheared off, $i = 0$ and the value of ϕ is called the residual friction angle ϕ_r . Equation 2.7 give that ϕ_r is approximately equal to ϕ_b . ϕ can be found by tilttesting of blocks and be used to estimate ϕ_b .

Alterations on the joint surface influencing JCS, JRC, and ϕ_b , will change the shear strength of the joints. The conditions on the joints will also influence the importance of the parameters in equation 2.8 for the shear strength. σ_n is in general the parameter with highest influence on the shear strength (Barton, 1973). Equation 2.8 shows that when σ_n is low, JCS is of high importance for the shear strength of rough surfaces (Barton, 1976). Low JCS makes the asperities easier to shear off, and reduces the shear strength. The presence of water and other weathering mechanisms may cause reduction of JCS. The magnitude of JCS have less influence on the shear strength of planar surfaces. The basic friction angle ϕ_b has high influence on the frictional resistance of planar surfaces. On planar surfaces, the presence of water can affect the friction angle by altering the crystal structure of the minerals on the surface (Coulson, 1970). Planar surfaces of minerals with a massive crystal structure, will get increased friction, while the friction on planar surfaces of layer lattice structure will decrease. The presence of water has little effect on ϕ_b of rough surfaces. For both rough and planar surfaces, water in joints will decrease the shear strength, by reduction of the effective normal stress σ'_n .

2.3 Approaches for stability analyses of a rock slope

Different methods have been developed to compare the stress and the strength in the rock mass, in order to determine the rock slope stability. Methods that are commonly used for stability calculations are limit equilibrium, empirical, and numerical methods (Nilsen, 2016).

2.3.1 Limit equilibrium method

Limit equilibrium method analyses the forces acting on a sliding plane. According to the method, failure will occur when the driving forces are equal to or higher than the stabilising forces. This happens when the forces on the failure surface reach the state of limit equilibrium (Nilsen, 2016). The limit equilibrium method is typically used for slope failure caused by rock sliding along discontinuity surfaces, like plane

failure and wedge failure. The method can be used to calculate a factor of safety (FS), describing the risk of sliding for a given block or rock mass volume. FS is defined by equation 2.9.

$$FS = \frac{\textit{stabilising forces}}{\textit{driving forces}} \quad (2.9)$$

2.3.2 Empirical methods

Empirical analysis of rock slope stability is performed by comparing the slope to be analysed with other slopes in the area with similar rock mass characteristics. (Nilsen, 2016). These slopes are used to create an indication of the stability of slopes with different combination of height and slope angle. This is compared with the height and the slope angle of the slope in consideration. The method is mainly used to get a indication of possibilities and limitations in the beginning of a rock mechanic project.

2.3.3 Numerical modelling

Numerical modelling is used to model the complexity of rock mass when handling rock mechanic problems (Nikolić et al., 2016). The model expresses the behaviour of rock mass by mathematical terms (Jones and Brischke, 2017). The model divides the rock mass into elements with a certain size, and each element gets assigned material properties (Nilsen, 2016). The elements are used to calculate stress distribution and deformation of the rock mass in the rock mechanic problem. Several numerical methods have been developed for analyses of different types of deformation and failure. The main numerical methods are continuum, discontinuum and a hybrid of continuum and discontinuum. Continuum methods consider the rock mass as a continuous material with continuity between all the elements. The elements follow the same general rules for geological features (Sinha and Walton, 2019). The continuum method is often used for analyses of deformations in the rock mass as a whole. In discontinuum modelling, each element has their own rule. The method can be used to investigate the movement of a defined body, like a block.

Finite element modelling (FEM) is a type of continuum modelling (Nikolić et al., 2016). FEM allows the model to treat among other things, the heterogeneity of rock mass, plastic deformation, in-situ stress, boundary conditions, and shear strength of joints (Jings and Hudson, 2002). The finite elements meet in nodes, where the deformations are calculated (Nilsen, 2016). The equations representing the finite elements, are combined and solved simultaneously, in order to find the response of the whole system.

2.3.4 Shear Strength Reduction method (SSR)

The Shear Strength Reduction Method (SSR) is a finite element modelling technique for stability analyses of soil and rock mass (You et al., 2017). The technique can be used to evaluate the risk of slope failure. The method is especially useful for analyses of failure triggered by the occurring stress conditions (Hammah et al., 2005). The method uses stress-strain analyses to calculate a safety factor called shear strength reduction factor (SRF) (Souza and Nelson, 2018). The safety factor is determined by reducing the strength parameters along a sliding surface, by an increasing SRF until the model reach limit equilibrium, see figure 2.5. The value of SRF at limit equilibrium is called the critical SRF (CSR), and defines the safety factor of the slope. The critical SRF is defined equally the factor of safety (FS) calculated in the equilibrium method (Rocscience, n.d.i).

The SSR method can be used for models where the rock mass strength is defined by the Hoek-Brown criterion (Hammah et al., 2005). Shear strength reduction of rock mass defined by the Hoek-Brown Criterion, can be done by dividing the equation for shear stress 2.2 by factor F, see equation 2.10.

$$\tau^{red} = \frac{\tau^{orig}}{F} \quad (2.10)$$

τ^{orig} define the calculated shear strength by the Hoek-Brown criterion. τ^{red} is the shear strength reduced by a factor F.

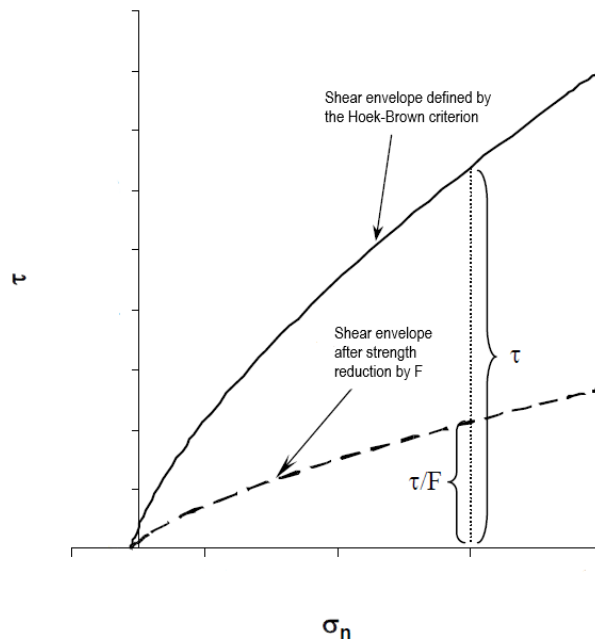


Figure 2.5: Strength envelopes, modified after Hammah et al. (2005), for the shear strength defined by the Hoek-Brown criterion as a function of σ_n , before and after strength reduction by safety factor F.

2.4 Rock Mass Classification Systems

The strength of rock mass depends on different parameters (Khatik and Nandi, 2018). Rock mass classification systems have been developed in order to classify the rock mass quality based on observations of rock mass characteristics (Harrison and Hudson, 2000). Rock mass classification systems quantify the quality of important factors influencing the strength. Classification systems have been used to estimate the strength parameters applied in the Hoek-Brown failure criterion. Hoek (1994) established a relationship between the failure criterion, and the classification systems Q-system and Geological Strength Index (GSI). GSI can also be estimated from the Rock Mass Rating system (RMR) (Hoek, 1994).

2.4.1 Geological Strength Index (GSI)

The Geological Strength Index (GSI) is used to estimate the constants m_b , s and a from field observations (Hoek et al., 1995). The index system was developed from RMR, aiming to make a simple rock mass classification system for estimation of the rock mass strength compared to the strength of the intact rock (Hoek, 2007). GSI is used for rock mass where the density of discontinuities is high compared to the scale of the project in consideration. The index gives rock mass a value between 10-100, where 10 indicates very poor rock mass and 100 is intact rock. GSI for blocky rock mass is determined by evaluation of the structure of discontinuity sets and the surface conditions of the rockmass, using the chart by (Marinos and Hoek, 2000), see figure D.3 in appendix D. Marinos and Hoek (2000) proposed another chart to be used for heterogeneous rock masses. Blasting will cause disturbance in the rock mass. When GSI is estimated from on a damaged surface, a factor D is used to correct the relationship between GSI and the Hoek-Brown constants (Hoek et al., 1973). D is 0 for undisturbed rock mass and is 1 for heavily disturbed rock mass. D equals 1 for production blasting, where special measures for control has not been taken. Hoek et al. (1973) defined the relationship between GSI and m_b , s and a for disturbed rock mass by equation 2.11, 2.12 and 2.13.

$$m_b = m_i \exp\left(\frac{GSI - 100}{28 - 14D}\right) \quad (2.11)$$

$$s = \exp\left(\frac{GSI - 100}{9 - 3D}\right) \quad (2.12)$$

$$a = \frac{1}{2} + \frac{1}{6} (e^{-GSI/15} - e^{-20/3}) \quad (2.13)$$

2.4.2 Q-system

The Q-system relates the rock mass quality defined by a value Q, and required permanent support for the stability of underground excavations (Barton et al., 1974). The classification system is developed from analysis of different rock mechanical projects. The Q-value is a number between 0,001 for very poor rock mass and 1000 for very good rock mass. The system calculates a Q-value based on evaluation of the following six parameters, defined by Barton et al. (1974):

- Rock quality designation, RQD
- Joint set number, Jn
- Joint roughness number, Jr
- Joint alteration number, Ja
- Joint water reduction factor, Jw
- Stress reduction factor, SRF

Each of the parameters are evaluated and given a value using tables developed by Barton et al. (1974), see section D.3 in appendix D. The Q-value is calculated from the six parameters by equation 2.14.

$$Q = \frac{RQD}{J_n} \cdot \frac{J_r}{J_a} \cdot \frac{J_w}{SRF} \quad (2.14)$$

RQD was introduced by Deere et al. (1967) as a rock mass quality index based on the spacing of discontinuities. RQD is estimated from core logging and defined as the percentage of the pieces in a drill core that is equal to or longer than 100 mm, and is calculated by equation 2.15 .

$$RQD = \frac{\sum x_i}{L} \cdot 100 \quad (2.15)$$

Only natural joints are considered when calculating RQD (Deere and Deere, 1988). Rock pieces divided during handling of cores, are treated as one piece. Jn is determined by the number of joint sets in the rock mass (Barton et al., 1974). Joints which don't belong to a parallel system of joints, are defined as random joints. RQD/Jn represents the block size in the rock mass. The value of Jr is chosen by examination of the roughness on the joint surface of the most unfavourable joint set. The same joint set is used to determine Ja by examination of the joint filling. Jr/Ja represents the shear strength of the joints. Jw is found by evaluating the water conditions in the rock mass. SRF is determined by evaluation of factors that influence the stress conditions in the rock mass, compared with the strength of the intact rock (Norges Geotekniske Institutt, 2015). Jw/SRF defines what Barton et al. (1974) call "active stress".

2.4.3 From Q-value to The Hoek-Brown Failure Criterion

An estimated Q-value can be used to estimate GSI. To calculate GSI, the parameters J_w and SRF are set equal to 1, corresponding to a dry rock mass and favourable stress conditions (Hoek et al., 1995). These parameters influence the stress conditions in the rock mass, and are accounted for in the Hoek-Brown failure criterion. The other parameters included in the Q-value, are estimated as usual. The resulting formula for Q'-value is given by equation 2.16 (Hoek, 1994).

$$Q' = \frac{RQD}{J_n} \cdot \frac{J_r}{J_a} \quad (2.16)$$

The Q' value is used in formula 2.17 to calculate the GSI for the rock mass.

$$GSI = 9\text{Log}_e(Q') + 44 \quad (2.17)$$

3. Field mapping and laboratory testing

Properties of rocks and rock mass in the quarry were studied by field mapping, laboratory testing and studying of drill cores. Each test procedure used for field mapping and laboratory testing was described in the unpublished report Aasteboel (2019), and is reproduced in the descriptions of the methods for measuring and testing.

3.1 Methods for field mapping

The field mapping consisted of measurements and estimation of dip and dip-direction of discontinuities, Q-value, apparent friction angle, JRC, and JCS at different places in the quarry. The uncertainties related to the measurement and estimation of each parameter is given in section 3.1.8. In the beginning of the field mapping the variations of dunite were divided into four types of dunite based on the characteristics of the rocks.

During field mapping, the variations of dunite and serpentinite with similar characteristics were divided into three main types of dunite:

- Chlorite banded dunite: Chlorite banded dunite and chlorite veined dunite
- Dunite: Dunite and blastogranular dunite
- Serpentinized dunite: Serpentinized dunite, serpentinite, and chlorite amphibole dunite

After this division, the quarry was divided into three different area sections, section 1, 2, and 3 depending on the observed rock type and rock mass quality.

- Area section 1: Serpentinized dunite
- Area section 2: Chlorite banded dunite
- Area section 3: Dunite

The sections are indicated in figure 3.1. Measurements and estimations were performed in each section to determine the rock mass quality of the sections. The field mapping was performed with respect to potential risks related to the mapping procedure. The risk analysis for the field work is shown in table H.1 in appendix H.

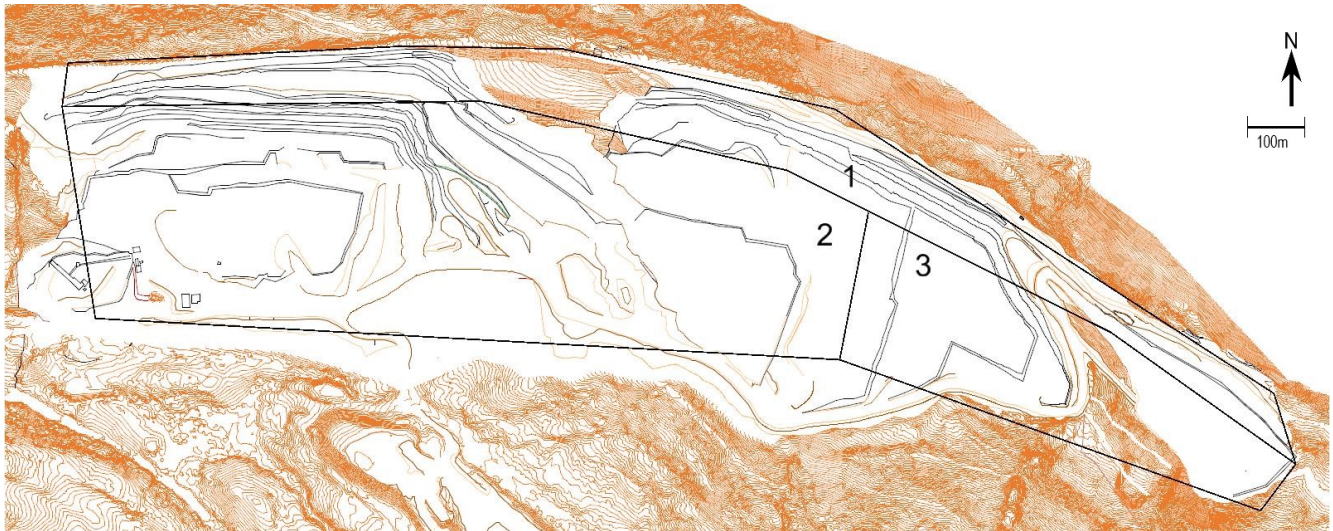


Figure 3.1: Plan of the quarry from Aasteboel (2019) showing the division of the quarry into section 1,2, and 3. The plan is modified after a model of the quarry by Sibelco Nordic,

3.1.1 Dip and dip direction

Dip and dip direction of joints and weakness zones was measured using the compass Breithaupt Gekom Pro Basic Stratum Compass:

The dip was measured with respect to the horizontal with angles between 0-90°. The dip direction was measured with respect to north [clockwise], with angles between (...) 0 and 360°. When the compass was adjusted in the right position, dip and dip direction was read at a glance. The measurements of joints were used to construct a rose diagram for section 1,2 and 3 to display the main joint sets in each section (Aasteboel, 2019, p. 5).

Dip and dip direction for weakness zones were displayed in a table. Registrations of the filling and the thickness of the weakness zones were made in parallel with the measuring, and were included in the table. Measurements of dip and dip direction were taken at the locations indicated in figure 3.2.

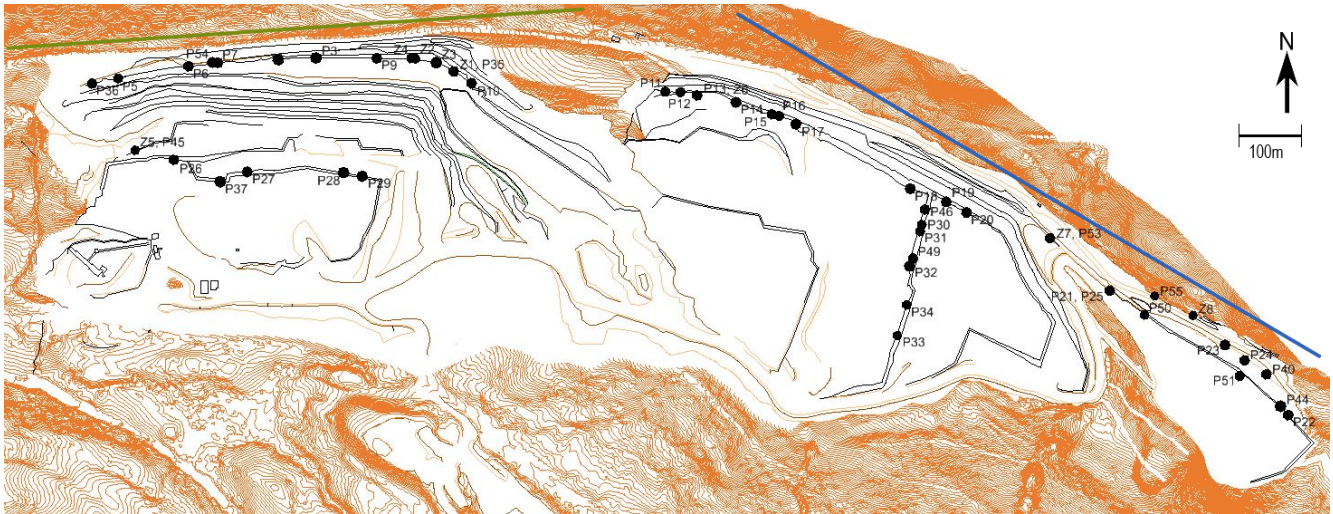


Figure 3.2: Plan of the quarry, modified after Aasteboel (2019), showing the locations for measurements of dip and dip-direction of joints (indicated by the points P1-P55) and weakness zones (indicated by the points Z1-Z8). The green and the blue line indicate the main strike of the back wall. The plan was created from a model of the current quarry by Sibelco Nordic.

3.1.2 Q-value

Q-values were estimated for the rock mass by the locations shown in figure 3.3. The values were estimated by following the handbook for estimation of Q-value by Norges Geotekniske Institutt (2015):

RQD value for the rock mass, was calculated from the mean value of the estimated RQD for the horizontal and vertical direction, and the direction going into the wall. The RQD for each direction was estimated (...) [by manual inspection]. Where only a few joints were visible in the same direction, the joint set were [*sic*] defined as random for determination of J_n . The joint set following the foliation was considered to be the least favourable joint set for the stability of the wall, and were [*sic*] examined for determination of J_r and J_a . The value for J_w was determined based on the assumption that the area has regular occurrence of rainfall, meaning that the rock mass is frequently exposed to water.

After field mapping, one Q-value was determined for each section 1, 2 and 3. In order to get a representative value for the section, both median and average Q-value was [*sic*] calculated due to a large span in Q-values (Aasteboel, 2019, p. 5-6).

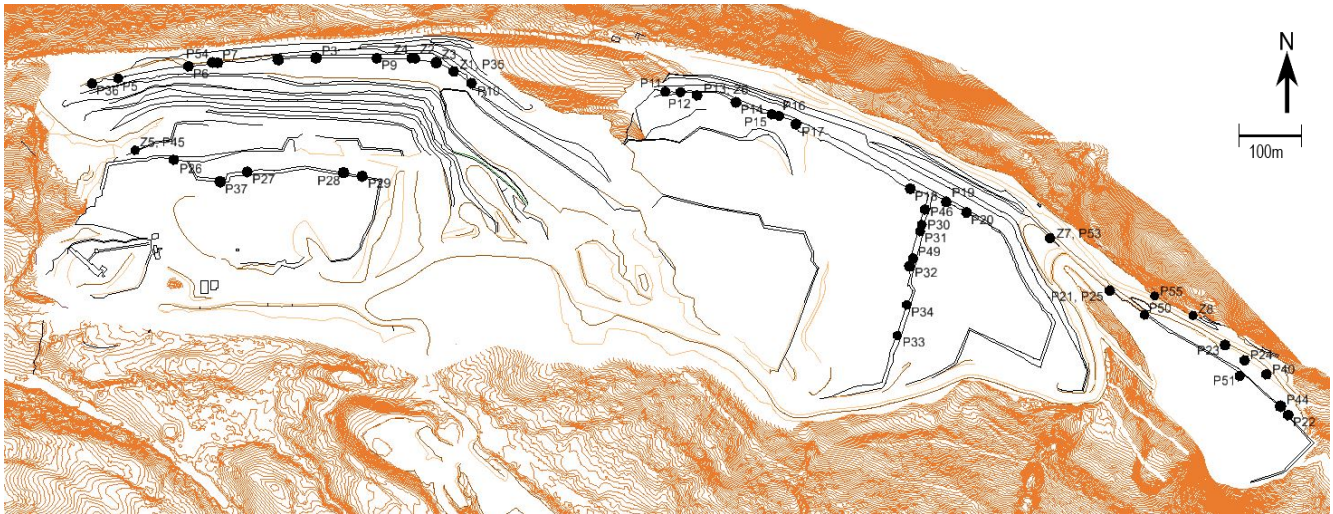


Figure 3.3: Plan of the quarry, modified after Aasteboel (2019), showing the locations for Q-value estimation, indicated by the points P1-P36. The plan was created from a model of the quarry by Sibelco Nordic.

3.1.3 Apparent friction angle

Measurements of the apparent friction angle ϕ of discontinuity surfaces, were carried out by tilt testing blocks with surfaces typical for the discontinuities in the quarry. The locations of the tilt tests are shown in figure 3.5:

The tilt test was carried out using a tilting platform for field work, from Rock Mechanics Laboratory at NTNU, see figure (...) [3.4a], and the procedure suggested by Alejano et al. (2018) for tilt testing. The method described by Alejano et al. (2018) is based on laboratory testing of freshly cut surfaces and gives the basic friction angle ϕ_b . In this case (...), [the tests were] performed in the field, and was carried out using blocks collected in the quarry. Blocks with surface similar to the surface of typical rock joints were selected (Aasteboel, 2019, p.6).

Five different types of discontinuity surfaces typical for the rock mass in the quarry were defined (Aasteboel, 2019):

- Slickensided surface
- Serpentinized surface
- Rough, slightly weathered surface
- Talk, chlorite, and mica coated surface

- Rough, sandy surface

A pair of blocks with the same defined surface type was placed on top of each other on the tilting platform, see figure 3.4a and 3.4b. The platform was tilted until the top block started to slide and the tilting angle was registered. The tilting angle was noted as the apparent friction angle ϕ for the surface type. It was noted that the testing facilities would have influence on the measured apparent friction angle:

The tilt testing were [*sic*] carried out in the field, and the conditions during testing could not be controlled. The testing conditions were divided into two categories, "dry" and "wet". "Dry" indicated that the test was carried [out] on days with with no rainfall. "Wet" was used when regular rainfall occurred on the day of testing. In addition, the rotational-velocity could not be determined, and the platform was tilted with a velocity resulting in sliding after approximately 30 seconds. The test was repeated five times for each pair of blocks. The final apparent friction angle for the pair was calculated from the median of the tests, as recommended by Alejano et al. (2018). The apparent friction angle for each surface category, was calculated as the average value of the median for each pair of blocks representative for the category (Aasteboel, 2019, p.8).



(a) Photo from Aasteboel (2019) of the tilting platform used for tilt testing.



(b) Photo from Aasteboel (2019) of a pair of blocks to be tested on the tilting platform.

Figure 3.4: Performance of tilttesting.

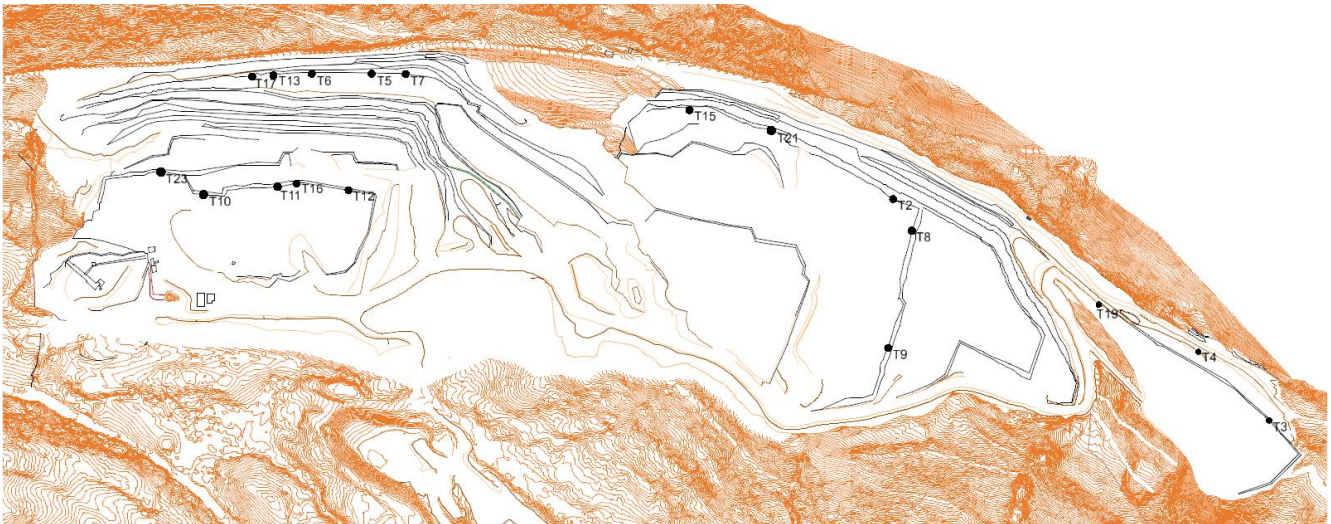


Figure 3.5: Plan of the quarry from Aasteboel (2019), showing the locations for tilttesting indicated by the points T1-T23. The plan was created after a model of the quarry by Sibelco Nordic.

3.1.4 Joint Roughness Coefficient

Roughness profiles of joint wall surfaces were drawn for the five defined surface types, to estimate the joint roughness coefficient (JRC). The JRC was estimated for joint surfaces by the locations shown in figure 3.6:

The joint roughness coefficient JRC was estimated by taking imprint of the surface roughness of joint walls. The imprint was taken by a 15 centimeters long steel profile gauge, see figure (...) [3.7a]. The profile gauge was pressed against the wall to followed [*sic*] the shape of the surface. The profile of the imprint was drawn on paper and compared against the roughness profiles by Barton and Choubey (1977), see figure (...) [D.2 in appendix D], to determine the JRC- value of the surface. On each surface, an imprint was taken in the vertical and the horizontal direction. The resulting JRC- value for a given joint wall was calculated as the average of the vertical and the horizontal value.

(...) Each drawn joint wall surface (...) [was] correlated with the corresponding defined surface categories in section (...) [3.1.3]. The JRC values calculated for different joint walls in section 1,2 and 3, were used to calculate an average JRC value for the surface categories present in the section (Aasteboel, 2019, p. 8-9).

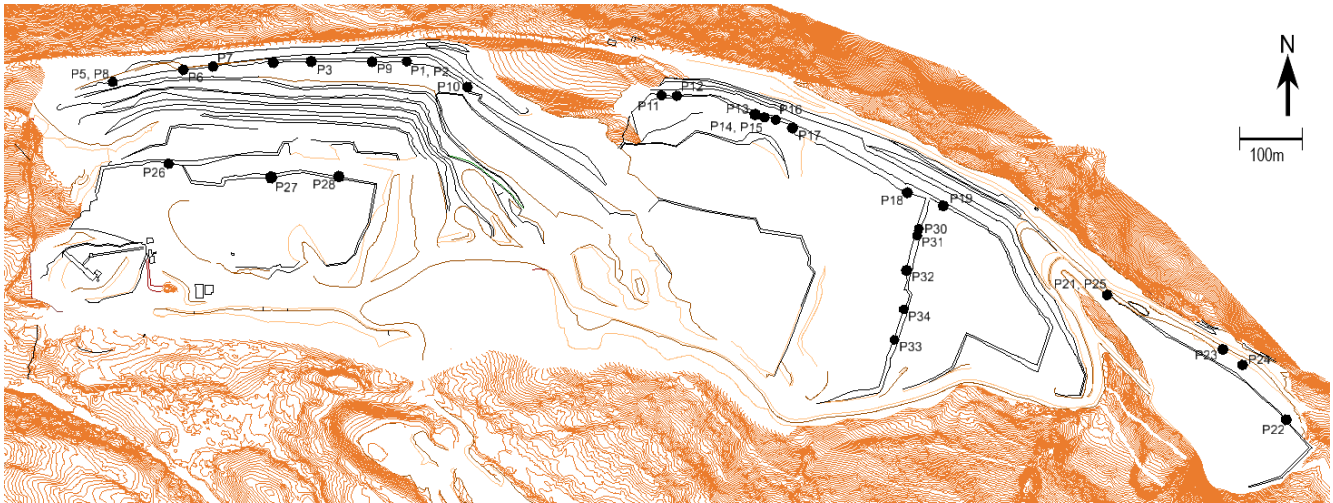


Figure 3.6: Plan of the quarry from Aasteboel (2019), modified after Sibelco Nordic, showing the locations for estimation of JRC and JCS indicated by the points P1-P34. The black lines display the boundaries of the area sections.

3.1.5 Joint Wall Compressive Strength

Measurements using a Schmidt Hammer were taken to find the JCS of joint walls. The measurements were taken on the joint surfaces where JRC had been estimated, see figure 3.6:

JCS of joint surfaces was determined using the Schmidt hammer Proceq Betonprüfhammer N/L, see figure (...) [3.7b]. The Schmidt hammer measurements were carried out following the procedure given by the ISRM standard (Schmidt, 1978). 10 readings were taken at each area on the wall (11 readings were taken when the quality of a reading was uncertain). The measurements were carried out at one area, or two different areas on the wall of the discontinuity, depending on the risk of standing at the bottom of a bench (...). Measurements at two different areas give the data a higher reliability.

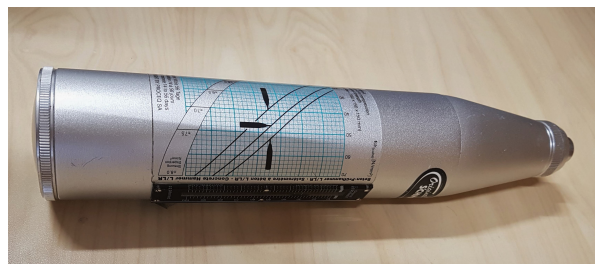
For each set of measurement [*sic*], the direction of the hammer in position were [*sic*] noted. The direction was described as vertical or diagonal down, vertical or diagonal upwards or horizontal. The mean rebound value for each set of readings were [*sic*] calculated by ignoring the highest and the lowest value and calculating the mean. The mean value was used to find JCS using the chart by Deere and Miller (1966), see figure (...) [D.1 in appendix D]. The chart requires information about the density of the joint wall rock. The density of each tested wall was set equal to the density of the corresponding sample block used for laboratory testing, see section (...) [3.1.6].

(...) Like for determination of JRC, each tested joint surface, were [*sic*] correlated with the corresponding surface defined by the surface categories in section (...) [3.1.3]. The JCS calculated for the different joint walls in section 1,2 and 3 were used to calculate an average

JRC value for the surface categories present in the section (Aasteboel, 2019, p.9).



(a) Photo after Aasteboel (2019) of the steel profile gauge used to take imprint of surface roughness of joint walls.



(b) Photo after Aasteboel (2019) Schmidt Hammer used to measure rebound value of joint walls for estimation of JCS.

Figure 3.7

3.1.6 Laboratory testing of uniaxial compressive strength and sound velocity

Uniaxial compressive strength (UCS) test and sound velocity test were performed on cores prepared from four different blocks from the quarry. The tests were performed in the Rock Mechanics Laboratory at NTNU. The uncertainties related to the laboratory testing is given in section 3.1.8. The blocks used for testing were collected at different places in the quarry, and were selected to represent the rock types in the final back wall (Aasteboel, 2019). The locations where the four blocks were collected are indicated in figure 3.8. The four blocks represents four rock types with different behaviour: Dunite, chlorite banded dunite and two varieties of serpentinitised dunite.

Block	Rock
B1	Dunite
B2	Serpentinitised dunite 2 (called massive dunite in Aasteboel (2019))
B3	Chlorite banded dunite
B4	Serpentinitised dunite 1

Table 3.1: The four different block samples collected in the quarry and their sample name, modified after Aasteboel (2019).

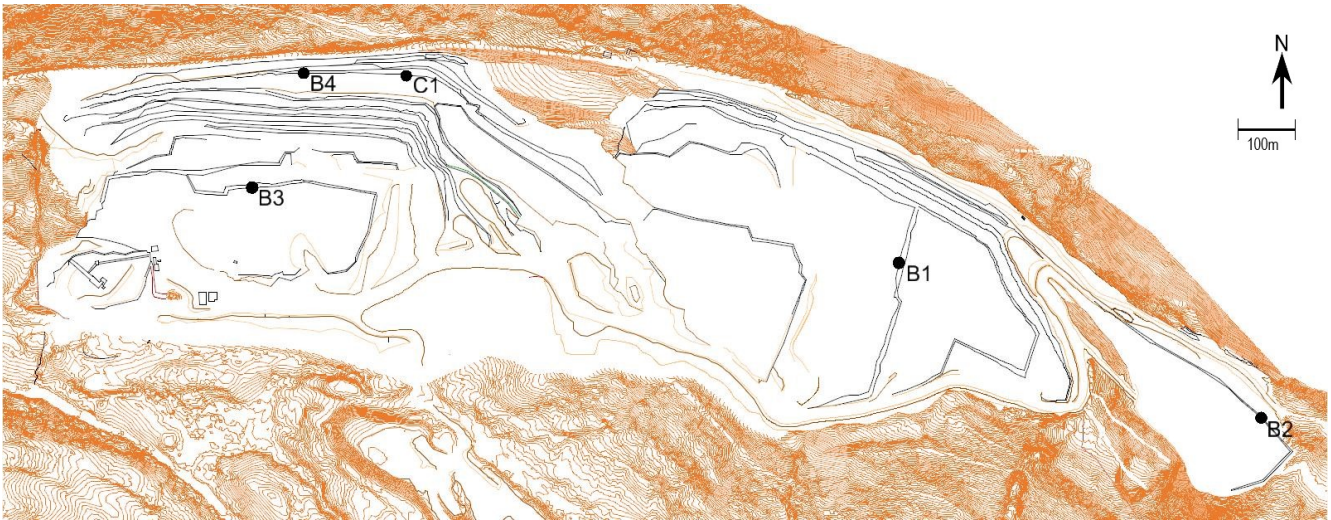


Figure 3.8: Plan of the quarry showing the locations for collection of the four blocks used for UCS testing (B1: Dunite, B2: Serpentinised dunite 2, B3: Chlorite banded dunite, B4: Serpentinised Dunite 1. Soil for free swelling test was collected by point C1. The plan is modified after a model of the current quarry by Sibelco Nordic.

The blocks were loosened by production blasting. Block sample B3 displayed granular disintegration due to weathering, but was still tested. The chlorite banded dunite in the quarry has a high weathering rate when exposed to water and air. Figure 3.9 show examples of weathered chlorite banded dunite in the quarry. The weathering was considered to have a high influence on the strength of the rock mass of this rock type.



(a) Photo taken during field mapping showing weathering of a bench of chlorite banded dunite.



(b) Photo taken during field mapping of weathered chlorite banded dunite crumbling after a light hammer blow.

Figure 3.9: Photos of weathering of chlorite banded dunite.

The blocks were prepared in the laboratory before testing:

The test specimen were [sic] prepared following the ISRM-standard for UCS-testing (International Society for Rock Mechanics, 1979). The axial direction [sic] of the cores were aimed to be perpendicular to the foliation. (Aasteboel, 2019, p. 11)

After the cores were prepared, the cores with the fewest discontinuities were used for testing:

The UCS-test was carried out following the ISRM suggested method for UCS testing (International Society for Rock Mechanics, 1979). The test was performed on dry cores with height to diameter ratio of 2.5-2.8. The cores from the sample blocks No. B1 and B2 had a diameter of approximately 50mm. The cores from sample No. B3 and B4 were prepared with 40mm diameter due to a smaller sample blocks. The UCS-test was performed using GCTS RTR-4000 Rapid Triaxial Rock Testing System, see figure (...) [3.10]. During each test, the apparatus continuously applied load on the core while measuring the corresponding radial and axial strain. The applied load and the resulting strain values were monitored by using the software GCTS C.A.T.S. Advanced (GCTS Testing Systems, n.d.). For each sample block, at least five cores were tested. If the cores had fractures before testing, more tests were performed.

After testing, Young's modulus E , [and] Poisson's ratio ν was [sic] calculated. Young's modulus E was calculated from the stress equal to 50% of UCS and the corresponding strain, and Poisson's ratio was calculated as the ratio between E and the radial strain at 50% UCS. In addition, the fracture angle θ was estimated for the test specimens that failed by shear failure. The angle was found by measuring the length of the opposite and the adjacent side of the fracture angle, and calculating the tangent of the angle. After all the cores from a sample block were tested, an average UCS, E , ν and θ value for the block was calculated (Aasteboel, 2019, p.12).

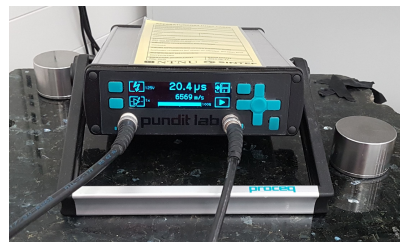
The sound velocity test were [sic] carried out on the cores prepared for UCS-testing. The measurements of the velocity were used to calculate get an indication of the porosity of the rocks. P-waves were used for the test:

[The] p-wave velocity (...) [tests] were performed following the method given by International Society for Rock Mechanics (1978) for testing with high frequency ultrasonic pulse. Before the test was carried out, the weight of each core was measured, to be able to investigate the correlation between the density ρ of the core and the p-wave velocity v_p . The sound test was

carried out using Proceq Pundit Lab Ultrasonic Instrument, see figure (...) [3.10]. Prior to testing, a thin layer of ultrasound gel was applied on each side of the core to prevent the wave from going through air between the core and the transmitter, and the core and the receiver. After each test, the travel time of the p-wave through the core specimen was registered, and v_p was calculated. An average ρ and v_p for each block were determined, after all the cores were tested (Aasteboel, 2019, p.12-13).



(a) Photo after Aasteboel (2019) of the apparatus used to test uniaxial compressive strength.



(b) Photo after Aasteboel (2019) of the apparatus used to perform the sound velocity test. The apparatus measure the p-wave velocity.

Figure 3.10: The apparatus used for UCS testing and the sound velocity test.

3.1.7 Laboratory testing of free swelling

A free swelling test was performed on clay from a collected sample of soil from weakness zone Z4 in the quarry. (The location of the zone is shown in figure 3.2 in section 3.1.1.) The weakness zone is situated in an area with other weakness zones with similar characteristics. These weakness zone are indicated in figure 3.2 by point Z1-Z5. The soil sample was prepared to accumulate the clay in the soil before testing:

The test material for free swelling test was prepared following Statens Vegvesen Handbook R210 for Laboratory Testing (Vegdirektoratet, 2016) with a few changes. The material was wet sieved on a 1mm sieve before continuing with the finer sieves as given in the handbook. The material was dried at 40 °[C] (Aasteboel, 2019, p.11).

When the clay material was dry, the swelling test was performed:

The free swelling test was carried out by following the procedure given by Statens Vegvesen Handbook R210 for Laboratory Testing (Vegdirektoratet, 2016). According to the handbook, the glass cylinder containing the clay material and distilled water shall be turned upside down to dissolve clumps. When performing the test, the material was instead sprinkled slowly onto the water surface, so the clay particles could sediment separately and further avoid clumps. The sedimented particles was left to swell for 24 hours. Free swelling, FV was calculated from volume of added clay material V_t and sedimented volume V_1 (Aasteboel, 2019, p.13).

3.1.8 Uncertainties of measurements and estimations in the field and laboratory testing

Table 3.2 show uncertainties that will arise in the results from the measurements and estimations of parameters in the field and in the laboratory. The uncertainties will be dominated by the qualitative uncertainties. Quantitative uncertainties related to the apparatus used for measurements is therefor not evaluated. To decrease the degree of uncertainty related the results, several measurements were made of each parameter, as suggested by Joughin (2018).

Field mapping		
Method	Obtained parameter	Uncertainties
Compass measurements	Dip and dip direction of the main joint sets	The obtained trend in dip and dip direction will depend on the number of measurements made of each joint set.
Estimation of Q-value	Rock mass quality	<ul style="list-style-type: none"> - The estimations will be based on exposed rock mass which can have different characteristics than the rock mass at depth. - Rock mass influenced by blasting used for estimation. - Estimation often based on the characteristics on one side of the rock mass.
Tilttesting	Apparent friction angle, ϕ	<ul style="list-style-type: none"> - Representativity of the tested blocks for the defined surface type. - The performance of the testing.
Drawing of roughness profile	JRC	<ul style="list-style-type: none"> - Representativity of the drawn surface for the defined surface type. - The accuracy of the imprint and the drawing. - The comparison of drawn profile with the appropriate roughness profile.
Measurements with Schmidt Hammer	JCS	<ul style="list-style-type: none"> - The representativity of the used surface for the defined surface type. - The degree of weathering of the used surface. - The accuracy of the noted angle of the apparatus.
UCS-testing	UCS	<ul style="list-style-type: none"> - The representativity of the rock sample for the rock in the quarry. - Anisotropy in the cores used for testing. - Fissures and fractures in the cores.
Sound velocity testing	<ul style="list-style-type: none"> - Density - P-wave velocity 	<ul style="list-style-type: none"> - The representativity of the rock sample for the rock in the quarry. - The performance of testing.
Free swelling test	Free swelling	<ul style="list-style-type: none"> - The representativity of the clay sample for the clay in the weakness zone. - Loss of clay during the preparation.

Table 3.2: Uncertainties related to the methods used for measurements and estimation of parameters in the field and in the laboratory.

3.1.9 Studying of drill cores

Drill cores from the quarry were studied after field mapping, to get an indication and overview of the conditions of weakness zones observed in the quarry at depth. Detailed investigation and interpretation of the geology at depth were considered outside the scope of this study. The drill cores had been logged by Sibelco Nordic, and information from the cores for the project was collected by reading the core logs and by examination of cores. Seven drill cores that had been drilled out from the rock mass, were used for the analysis. The name of the drill cores is shown in table 3.3. The origin of the drill cores is displayed in figure 3.11.

Drill cores used for analysis
GU-D2010-039
GU-D2010-040
GU-D2010-041
GU-D2010-042
GU-D2010-043
GU-D2010-47
GU-D2013-54

Table 3.3: The drill cores studied through core logs from Sibelco Nordic and examination of cores. The cores are named with the names used by Sibelco Nordic.

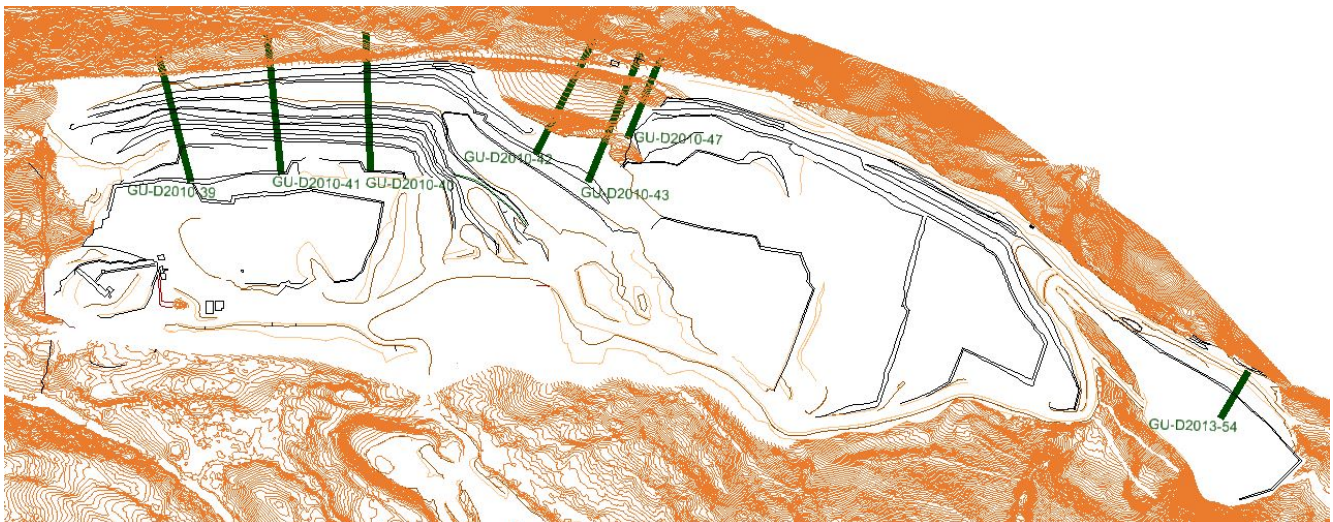


Figure 3.11: Plan of the quarry showing where each of the cores are drilled. The plan is created after a model of the current quarry by Sibelco Nordic.

Three types of weakness zones registered during field mapping were searched for in the drill cores: A zone of fragmented rock in chlorite banded dunite (Z1-Z5, see table 3.5 in section 3.2.1), a contact zone at the gneiss boundary in the north (Z8), and eclogite and amphibolite zones. The parameters registered for the weakness zones of interest are given in table 3.4.

Parameter registered	Purpose	Comment
Location of the zone in consideration	To investigate if the logged zone corresponds to the zones observed at the surface.	From core logs and study of the cores.
Length of the zone	To get an indication of the extension of the zone at depth.	From core logs and study of the cores.
Rock type in the zone	To see if the zone is located by the same rocks at depth, as observed at the surface.	From core logs and study of the cores.
Description of the fracturing of the zone.	To use together with observations in the field to determine the GSI of the zone for the numerical modelling, see section 4.1.	From study of the cores.

Table 3.4: The parameters registered from core logs and from studying of cores for the weakness zones of interest.

The size of eclogite and amphibolite zones registered in the core logs, was noted and used to find the maximum registered size of the eclogite boudins at depth in the studied cores. The drill cores were studied to determine the fracturing of the eclogite amphibole zones. RQD was not used to characterize the fracturing of any of the weakness zones since the weakness zones had varying length.

3.2 Results from field mapping

The results from field mapping were presented in Aasteboel (2019), and are reproduced in the sections below. All measurements, estimations and observation from field mapping were made between 19th August and 11th September in 2019.

3.2.1 Dip and dip direction of joint sets and weakness zone

The dip and dip directions of joints measured in area section 1,2, and 3 are presented in rose diagrams, see figure 3.12, 3.13 and 3.14 made by using Dips 7.0 by Rocscience Inc (2019a). Data of dip and dip direction measurements from Sibelco Nordic for area section 1 and 2 were also included in the rose diagram, to get a more reliable indication of the dip and dip direction for the main joint sets. The data from measurements by Sibelco Nordic is given in table A.2 in appendix A. The measured dip and dip direction for weakness zones and the filling and thickness of the zones are shown in table 3.5. The strike and the dip of registered weakness zones are displayed in figure 3.15. All measurements of dip and dip direction of joints taken during field mapping, are displayed in table A.1 in appendix A.

Area section 1

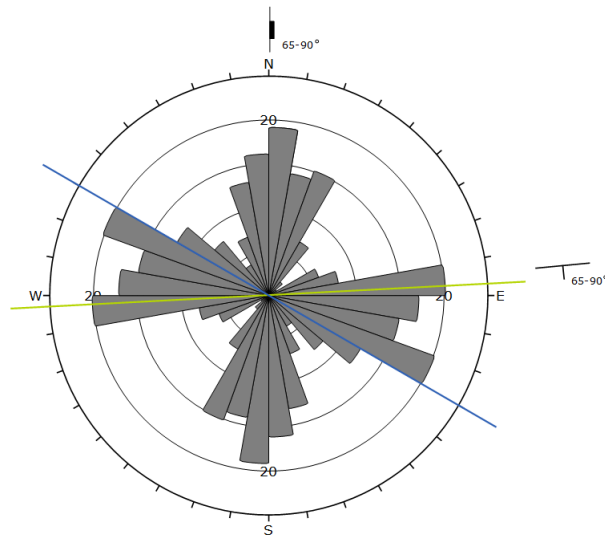


Figure 3.12: Rose diagram showing the distribution of strike for measured joints in area section 1, modified after Aasteboel (2019). The main strikes of the final back wall are indicated by the green and the blue lines (see figure 3.2 in section 3.1 for the direction of the lines in the quarry.)

Area section 2

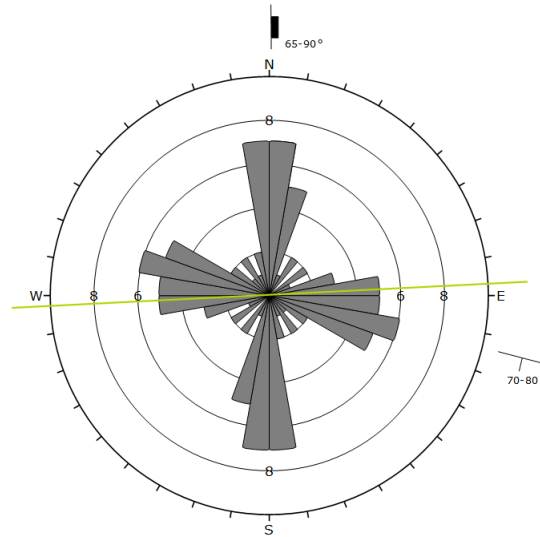


Figure 3.13: Rose diagram showing the distribution of strike for measured joints in area section 2, modified after Aasteboel (2019). The main strike of the final back wall in the section is indicated by the green line (see figure 3.2 in section 3.1 for the direction of the lines in the quarry.).

Area section 3

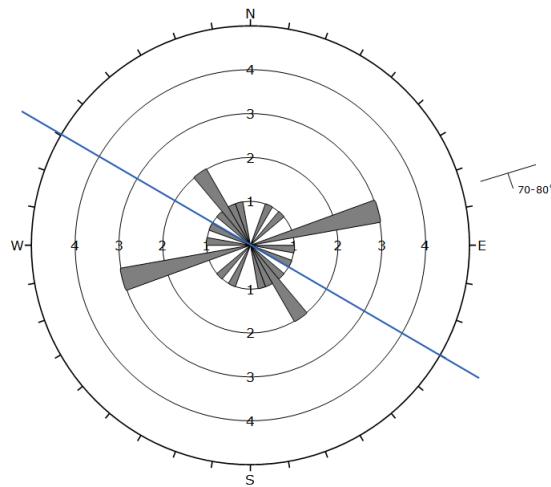


Figure 3.14: Rose diagram showing the distribution of strike for measured joints in area section 3, modified after Aasteboel (2019). The main strike of the final back wall in the section is indicated by the blue line (see figure 3.2 in section 3.1 for the direction of the lines in the quarry.).

Weakness zones

Point	Dip	Dip direction	Filling	Grain size	Thickness (cm)
Z1	71	152	Chlorite, mica, pyroxen and amphiboles	From clay to block	20
Z2	40	156	Chlorite, mica, pyroxen and amphiboles	From clay to block	10
Z3	74	158	Chlorite, mica, pyroxen and amphiboles	From clay to block	100
Z4	75	170	Chlorite, mica, pyroxen and amphiboles	From clay to block	40
Z5	72	159	Chlorite, mica, pyroxen and amphiboles	From clay to block	5-15
Z6	65	191	Retrograded eclogite	From clay to block	5-100
Z7	69	331	Chlorite, mica, pyroxen and amphiboles	From clay to block	30-100
Z8	81	195	Sheared dunite	From clay to block	100-300

Table 3.5: Dip and strike of weakness zones in section 1. Location given by the points Z1-Z8, see figure 3.2.

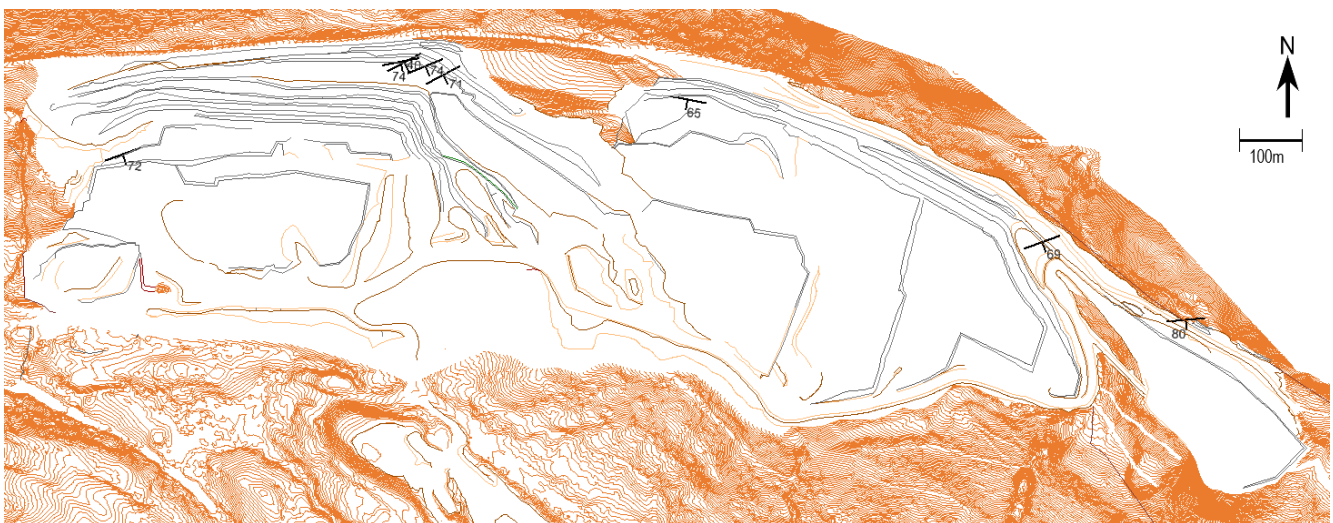


Figure 3.15: Plan of the quarry showing weakness zones observed during field mapping. The strike and the dip of the observed zones are indicated. The plan is modified after a model of the current quarry by Sibelco Nordic.

3.2.2 Q-values for area section 1, 2, and 3

Table 3.6 gives the calculated average and median Q-value for area section 1,2, and 3. All estimated Q-values for each section are given in table A.2 in appendix A.

Area section	Average Q-value	Median Q-value	Q-value spectrum
1	6.0	5.8	2-11
2	12.9	10.9	6-23
3	8.4	6.9	2-8

Table 3.6: Average Q-value for section 1,2 and 3 estimated by field mapping in the quarry.

3.2.3 Apparent friction angle, JRC, and JCS for joint wall surfaces

Table 3.7, 3.8, and 3.9 give the calculated average values of apparent friction angle ϕ , JRC, and JCS and the median value of JCS for the defined surface types in each area sections. The basic friction angle ϕ_b for the surfaces is calculated from the average value of ϕ and JRC, as described in section 3.1.

Area section 1

Surface Category	Apparent friction angle ϕ (°)	JRC	Average value JCS (MPa)	Median value JCS (MPa)	Basic friction angle ϕ_b (°)
Rough, slightly weathered surface	31.0	8	63	60	23
Serpentinised surface	28.0	5	47	42	23
Slickensided surface	22.6	8	137	170	14.6
Talk, chlorite and mica coated surface	28.9	9	53	56	19.9

Table 3.7: Average measured friction angle, JRC, and basic friction angle of each surface category present in area section 1. Both average and median value of JCS of the surfaces were calculated.

Area section 2

Surface Category	Apparent friction angle ϕ ($^{\circ}$)	JRC	Average value JCS (MPa)	Median value JCS (MPa)	Basic friction angel ϕ_b
Rough, sandy surface	37.8	5	60	55	32.5

Table 3.8: Average measured friction angle, JRC, and basic friction angle of the surface category present in area section 2. Both average and median value of JCS of the surface were calculated.

Area section 3

Surface Category	Apparent friction angle ϕ ($^{\circ}$)	JRC	Average value JCS (MPa)	Median value JCS (MPa)	Basic friction angel ϕ_b
Rough, sandy surface	35.0	7	59	50	28.0

Table 3.9: Average measured friction angle, JRC, and basic friction angle of the surface category present in area section 3. Both average and median value of JCS of the surface were calculated.

3.3 Results from laboratory testing

The results from laboratory testing were presented in Aasteboel (2019), and are reproduced in the sections below.

3.3.1 UCS-testing of core specimen

Table 3.10 display the calculated average values of UCS, Young's Modulus, Poisson's ratio, and fracture angle. Block No. 1 and 3 failed by shear failure and the average fracture angle was only calculated for these two blocks. Examples of the failure modes of the cores from the four different blocks are shown in figure B.1 in appendix B. The stress-strain curve for the tested cores was plotted for each block to show the behaviour of the rock as the stress increase. The curves are displayed in figure B.2, B.3, B.4, and B.5 in appendix B. All the results from UCS-testing are shown in table B.1 in appendix B.

The UCS-testing was performed 1st and 5th November 2019 (Aasteboel, 2019).

Sample block No.	Rock	UCS (MPa)	Young's Modulus, E (GPa)	Poisson's ratio, ν	Fracture angle, θ ($^{\circ}$)
B1	Dunite	85.1	55.78	0.45	20.0
B2	Massive Dunite	130.1	59.99	0.35	-
B3	Chlorite Banded Dunite	81.8	35.45	0.35	21.8
B4	Serpentinised Dunite	87.8	53.98	0.27	-

Table 3.10: Average UCS, E-modulus, Poisson's ration and fracture angle for sample No. 1,2,3 and 4 from UCS-testing, after Aasteboel (2019).

3.3.2 P-wave velocity testing of core specimen

The p-wave velocity test was performed 1st and 5th November 2019. Table 3.11 show the calculated average values of p-wave velocity and density from the p-wave velocity test. All the results from the p-wave test are displayed in table B.2.

The p-wave velocity test was performed 1st and 5th November 2019.

Sample block No.	Rock	v_p (m/s)	Density (g/mm^3)
B1	Dunite	2525.14	3.23
B2	Massive dunite	5717.07	2.63
B3	Chlorite banded dunite	1179.02	3.17
B4	Serpentinised dunite	5474.82	2.87

Table 3.11: P-wave velocity and density for each sample No. 1,2,3 and 4 from p-wave testing.

3.3.3 Free swelling test of clay

Table 3.12 show the results from the free swelling test of sample C1 from weakness zone Z4. Figure B.6 in appendix B.6 show the clay and water in the cylinder when V_1 was read off.

The free swelling test was carried out 26th November 2019.

V_t (ml)	V_1 (ml)	FS (%)	Aktivitet
10	11.5	115	Lite aktiv (definert etter kategoriseringen av aktivitet fra (Vegdirektoratet, 2016)).

Table 3.12: Readings and calculated FS value from free swelling test on material from weakness zone Z4, see figure 3.2 and table 3.5.

3.4 Results from core logging

The sections below show the registered values from examination and studying of drill cores for the weakness zone related to point Z1-Z5, the contact zone, and zones with eclogite and amphibole. Photos of the zones in the cores are displayed in section C.1, C.2, and C.3 in appendix C.

3.4.1 Weakness zones related to point Z1-Z5

Drill core	Length of core (m)	Location of the zone (m)	Length of the zone (m)	Rock	Quality of rock mass	Comment
GU-D2010-039	220	80.8-83	2.2	Serpentinite	Highly fractured rock mass	

Table 3.13: Registered values of parameters for the weakness zones evaluated to be related to the weakness zone Z1-Z5 observed in the quarry.

3.4.2 Contact zone by the gneiss boundary

Drill core	Length of core (m)	Location of the zone (m)	Length of the zone (m)	Rock	Quality of rock mass	Comment
GU-D2010-039	220	200.6-205.9	5.3	Serpentinite and gneiss	From intact rock to soil*	
GU-D2010-040	231	194 - 231	37	Serpentinite and gneiss	From intact rock to high degree of fracturing*	
GU-D2010-041	238	188-212	24	Serpentinite	From intact rock to soil*	
GU-D2010-042	221	178-221	43	Serpentinized dunite, serpentinite, gneiss	From intact rock to high degree of fracturing*	
GU-D2010-043	235	200-217.1	17.1	Serpentinite and gneiss	From intact rock to soil*	
GU-D2010-47	155	135.8-137.4	1.6	Serpentinite and gneiss		Information only from core logs
GU-D2013-54	88	86.8-87.75	0.95	Serpentinized dunite		Information only from core logs

*Defined as intact rock when a core piece was >0.2m.

Table 3.14: Registered parameters of the contact zone by the gneiss boundary from core logging.

3.4.3 Zones with eclogite and amphibolite

Drill core	Length of core (m)	Location of the zone (m)	Length of the zone (m)	Rock	Quality of rock mass	Comment
GU-D2010-039	220	200.6-205.9	5.3	Serpentinite and gneiss	From intact rock to soil*	
GU-D2010-040	231	194 - 231	37	Serpentinite and gneiss	From intact rock to high degree of fracturing*	
GU-D2010-041	238	188-212	24	Serpentinite	From intact rock to soil*	
GU-D2010-042	221	178-221	43	Serpentinized dunite, serpentinite, gneiss	From intact rock to high degree of fracturing*	
GU-D2010-043	235	200-217.1	17.1	Serpentinite and gneiss	From intact rock to soil*	
GU-D2010-47	155	135.8-137.4	1.6	Serpentinite and gneiss		Information only from core logs
GU-D2013-54	88	86.8-87.75	0.95	Serpentinized dunite		Information only from core logs

*Defined as intact rock when a core piece was >0.2m.

Table 3.15: Registered parameters of the contact zone by the gneiss boundary from core logging.

4. Methods for stability analysis

This chapter presents the methods used to perform the stability analysis of the current and the final back wall. The first section describes how the collected data from field mapping and laboratory testing were used in the numerical models and the models of wedges. This section also presents how unknown strength parameters were defined. In the next section, the stability analysis of discontinuities forming potential wedges is described. In the end of the sections, uncertainties related to the input parameters in the analysis is considered. The third section describes the methods, evaluations and simplifications used for the numerical modelling. The section presents the software used for the modelling, how the numerical models were established, and describes the methods used to analyse the models. Uncertainties and simplification made in the numerical models is evaluated. The fourth section gives a detailed description of each established numerical model. The last section presents the numerical model used for calibration of strength parameters, and the calibration process. Alternative methods for calibration is also presented.

4.1 Rock mass data and determination of strength parameters

The results from field mapping and laboratory testing were combined to define the input parameters for rock mass strength and joint strength in the numerical models. The input parameters for joint strength were also used for the analysis of wedges. Strength parameters that had not been estimated in the field or in the laboratory, were determined using tables for rock mass data from the software RocData (Rocscience Inc, 2019b). Uncertainties related to the input parameters when used in the numerical models and the wedge analysis, are given in section 4.3.5 and section 4.2.4.

4.1.1 Rock mass strength parameters

The rock mass strength was estimated by the Generalized Hoek-Brown criterion. The Hoek-Brown criterion was used due to the ability of the criterion to give a reliable estimation of strength for both near surface rock mass, and rock mass at larger depth (Li, 2018). It was still noted that only one joint set were observed in most parts of the quarry during estimation of Q-value, and the characteristics of the rock mass could be close to the limit of the Hoek-Brown criterion, see section 2.2.1 (see table A.3, A.4, and A.5 for the determined number of joints sets from estimation of Q-value). The input parameters required to define the rock mass strength by the Generalized Hoek-Brown criterion in RS2 (Rocscience, 2019b) and the method for determination of the values are shown in table 4.1.

Strength parameter	Basis for determination of value	Comment
Compressive strength, σ_{ci}	Measured by laboratory testing	
Young's Modulus, E	Measured by laboratory testing	
Poisson's ratio, ν	Measured by laboratory testing	
mb	Calculated by equation 2.11.	For the equation, see section 2.4.1.
s	Calculated by equation 2.12.	For the equation, see section 2.4.1.
a	Calculated by equation 2.13	For the equation, see section 2.4.1.
GSI	Calculated from the median Q'-value for the rock type. The Q'-value was derived from the estimation of Q-values, using equation 2.16.	The median Q'-value were used due to a large span in the Q-values. See table E.1 in appendix E for the calculated Q'-values.
mi	From table in RocData (Rocscience Inc, 2019b). The mean value for peridotite were used.	
Disturbance factor, D	Determined from the guidelines by Hoek et al. (1973).	

Table 4.1: Input parameters used to determine the rock mass strength in the numerical models from the Hoek-Brown criterion.

The laboratory measurements, were used by correlating the sample blocks B1-B4 and the rock types in the quarry defined by Osland (1998), see section 1.1. Rocks with similar characteristics were correlated.

- Block B1, dunite: Used for blastogranular dunite and dunite.
- Block B2, serpentinitised dunite 1: Used for chlorite amphibole dunite, serpentinitised dunite and serpentinite.
- Block B3, chlorite banded dunite: Used for chlorite banded dunite and chlorite veined dunite.
- Block B4, serpentinitised dunite 2: Used for serpentinitised dunite in the eastern part of the quarry.

Rock mass properties of gneiss were only characterised in the field, and unknown strength parameters were estimated using RocData (Rocscience Inc, 2019b). σ_{ci} , Young's modulus and, m_i were determined

by the mean value for gneiss in RocData. ν and unit weight were determined from the database of gneiss in RocData. The unit weight and Poisson's ratio were defined equal to the values for the gneiss with Record ID 65, after Dorren and Seijmonsbergen (2003).

4.1.2 Weakness zones in the numerical models

Three major types of weakness zones were observed in the quarry. The weakness zones were included in two different ways in the numerical models, based on the character of the weakness zone and the surrounding rock. Based on the observations from field mapping and studying of drill core, the contact zone and the weakness zone by point Z1-Z5 were included as a zone with weaker rock mass. Eclogite boudins were included in the models by defining an area in serpentinitized dunite with serpentinitized joints surfaces. The contact zone between gneiss and serpentinite was included in the all the models. The width of the zone were determined to 10m in the model, based on data from the study of cores, see section 3.4. The width of the zone was assigned with an approximate value since a more detailed determination of the width would require a study of geology outside the scope of this project. The zone was assumed to have a dip equal to the dip of the gneiss-serpentinitised dunite boundary in the geology sections used for modelling.

Rock mass with similar characteristics to the weakness zones observed at point Z1-Z5 was observed in the westernmost of the studied drill cores, see section 3.4. Based on the measured dip direction of the weakness zones at the surface and the location of the zone in the drill core, the weakness zone was only included in the analysis of the back wall in a numerical model of a section crossing weakness zone Z3, see section 4.4. The dip of the weakness zone was determined by the dip of Z3. In order to analyse the stability for the worst case scenario, the maximum width of the zone estimated in the field was used to define the width of the zone.

The locations of the eclogite boudins influence the area with the strongly serpentinitized joint surfaces, as mentioned in section 1.1. In the analysed core logs, see section 3.4, the zones of eclogite were observed to have a maximum width of 1.5m, with a large variation in rock mass quality. Based on these considerations, the importance of the eclogite zone was evaluated to mainly be the serpeninization of joints surfaces. Also in the area where the rock mostly consisted of serpentinitized dunite 2, the rock around the eclogite boudins was evaluated to have characteristics more similar to serpentinitized dunite 1. As a result, the areas with eclogite were modelled as serpentinitized dunite 1 with serpentinitized surface on the joints. This interpretation was used in all the numerical analyses in the areas where eclogite was indicated in geological sections, see section 4.3.2.

The strength parameters for weakness zones were determined by altering the GSI for the host rock to the rock mass conditions in the zone. The GSI was altered based on the fracturing of the rock mass in weakness zones registered during core logging, see section 3.4. The other strength parameters were

defined equal to the values for the host rock.

4.1.3 Properties of joint sets

The software RS2 used for the numerical modelling (for information about the program see section 4.3) defines the properties of joints from shear strength and stiffness. The Barton-Bandis failure criterion was used to determine the strength of the joint set following the foliation. The Barton-Bandis criterion was also used to determine the strength of discontinuities forming wedges, see section 4.2. The input parameters required to define the joint strength by the criterion in RS2 and for analysis of wedges are shown in table 4.2. The table also shows the method used for determination of the values of the parameters.

Parameter	Basis for determination of value	Comment
JRC	Measured in the field.	Used the average value for the surface type in the relevant area section.
JCS	Measured in the field	Used the average value for the surface type in the relevant area section.
ϕ_r	Set equal to ϕ_b	Used the average value for the surface type in the relevant area section.
ϕ_b	Calculated from the measured friction angle by equation 2.7.	Used the average value for the surface type in the relevant area section. For the equation, see section 2.2.3.

Table 4.2: Input parameters used to determine the rock mass strength in the numerical models from the Barton-Bandis criterion.

The joint stiffness was calculated using equation 4.1 for normal stiffness and 4.2 for shear stiffness, modified after (Barton, 1972), as suggested by Rocscience (n.d.d).

$$k_n = \frac{E_i E_m}{L(E_i - E_m)} \quad (4.1)$$

$$k_s = \frac{G_i G_m}{L(G_i - G_m)} \quad (4.2)$$

To perform the calculation of k_n and k_s , the parameters rock mass modulus E_{rm} , intact rock shear modulus G_i and rock mass shear modulus G_m were calculated for the host rock. E_{rm} were calculated using equation 4.3 by Hoek and Diederichs (2006)

$$E_{rm} = E_i \left(0.02 + \frac{1 - D/2}{1 + e^{((60+15D-GSI)/11)}} \right) \quad (4.3)$$

G_i and G_m were calculated by equation 4.4 and 4.5 after Myrvang (2001).

$$G_i = \frac{E_i}{2(1 + \nu)} \quad (4.4)$$

$$G_m = \frac{E_{rm}}{2(1 + \nu)} \quad (4.5)$$

4.2 Estimation of the stability of wedges

Discontinuities forming potential wedges were observed in the quarry during field mapping. These discontinuities were analysed to examine whether wedges were formed, and to estimate the stability of occurring wedges. All the wedges were located on benches in area section 1 with geometry similar to the bench geometry planned in the final back wall. The stability of the potential wedges was therefore analysed for both the current wall and the final back wall. The software SWedge (Rocscience Inc, 2019c) was used to examine potential wedges. Swedge uses the limit equilibrium method to calculate a safety factor for a wedge sliding along planar discontinuity surfaces (Rocscience, 2019c). The following input parameters are used to identify wedges and calculate the safety factor:

Swedge uses the orientation of the discontinuities, and not the location, to determine if a wedge is formed and the size of the wedge (Rocscience, n.d.). Swedge searches for the largest wedge that can be formed at the given slope with the defined joint orientations. If the wedge identified in Swedge was smaller than the wedge that potentially could be formed by the discontinuities due to their location, the discontinuities were concluded to not form a wedge. If the wedge identified was larger than the wedge that potentially could be formed, the size of the wedge was scaled down to find the size of the real wedge and the correct safety factor. The calculated factor of safety (FS) was rounded down to one decimal place.

4.2.1 Input parameters for wedge analysis

The input parameters used to analyse the potential wedges are displayed in table 4.3

Input parameters		Basis for determination of value
Dip and dip direction of slope		Derived from a model of the current quarry by and the life of mine model by Sibelco Nordic, using Microstation.
Bench height and bench width		Derived from a model of the current quarry and the life of mine model by Sibelco Nordic, using Microstation.
Dip and dip direction of upper face		The upper face was defined as horizontal.
Dip of tension crack		Defined equal to the measured dip of the foliation by the discontinuities.
Dip direction of tension crack		Defined equal to the measured dip direction of the foliation by the discontinuities.
Dip of joints		Measured in the field when the discontinuities were accessible for measurements. Measured from photos when the discontinuities were inaccessible for measurements.
Dip direction of discontinuities		Measured in the field when the discontinuities were accessible for measurements. Estimated at distance when the discontinuities were inaccessible for measurements.
Shear strength of discontinuities defined by the Barton-Bandis criterion.	JRC	Derived from roughness profile of the discontinuity surface, when the surface was accessible. Determined by the average value for the surface type in area section 1, when the surface was inaccessible for measurements.
	JCS	Derived from measurement on the discontinuity surface, when the surface was accessible. Determined by the average value for the surface type in area section 1, when the surface was inaccessible for measurements.
	ϕ_b	Measured by blocks from the discontinuity when blocks were available. Determined by the average value for the surface type in area section 1, when the surface was inaccessible for measurements.
Unit weight of rock		Determined from the laboratory tested rock sample of serpentinized dunite 1.

Table 4.3: Input parameters used to investigate if wedges are formed and the stability of occurring wedges.

Due to the frequent rainfall in the area, the factor of safety for identified wedges was determined with and without water pressure in the joints. The water pressure was determined by defining the discontinuities to be completely filled with water. This conditions imitate the water pressure after extreme rainfall (Rocscience, n.d.e), and were used to obtain an indication of the stability of the wedges in a worst case scenario. The water pressure was determined to be zero at the surface and be largest along the intersection line. The joints following the foliation were regarded to behave as tension cracks. These joints had an average spacing of approximately 0.2m. There were no other observed joints that could form tension cracks. It was still noted that there could be tension cracks on the benches that were not observed since some areas not were accessible for field mapping, and the top of benches were covered by loose material.

4.2.2 Method for analysing wedges

The stability of four potential wedges in the quarry was analysed. The locations of the wedges are indicated in figure 4.1.

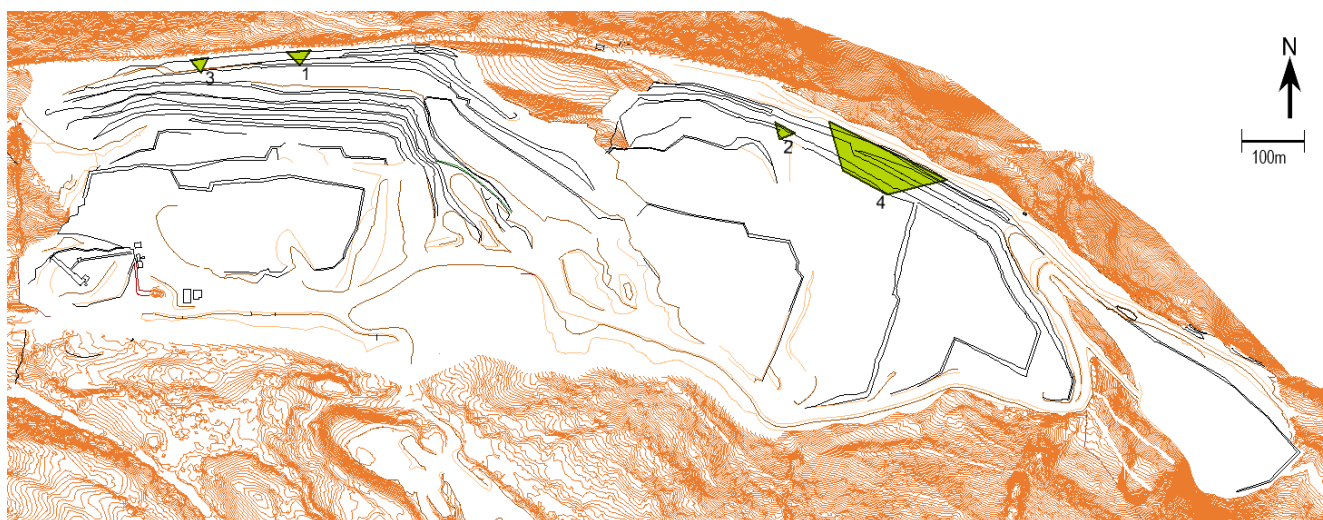


Figure 4.1: Plan of the quarry showing the locations of the four analysed potential wedges 1,2,3,4 marked in green, after model of the current quarry from Siblco Nordic. The shape and the size of the marks is based on the spacing of the discontinuities forming the wedge. They do not indicate the exact shape of the wedges.

First the wedges were identified and analysed inside the geometry of the bench, where the discontinuity were located. In addition, analyses were used investigate the possibility of wedges extending up to the surface at the top of the quarry. The geometry of the slope up to the surface was simplified by defining the height and the overall slope angle from the bench with the discontinuities and up to the top, see figure 4.2. The analysis were carried out with and without a tension crack. Four analyses were performed for each potential wedge for both the current wall and the final back wall, defining different boundaries that wedges could be formed within. These analyses were carried out to investigate how wedges could be formed, and the associated risk of rock failure. The four analyses were:

- Foliation: The wedge is delimited by a tension crack located 0.2m from the bench face, and the geometry of the bench.
- Bench: The wedge is delimited by a tension crack located at the innermost part of the bench, and the geometry of the bench. This analysis takes into account that the wedge can extend across several foliation planes.
- To the top of the quarry: The wedge is delimited by the geometry of the slope up to the top of the quarry, and a tension crack at the surface. (The tension crack was determined to be located maximum 50m from the crest of the top bench. This distance were regarded to allow the wedge size to be large enough to capture the risk of a large wedge failure.)
- To the top of the quarry - without tension crack: The wedge is delimited by the geometry of the slope up to the top of the quarry. The analysis consider the possibility that the wedge is only formed by the two discontinuities.

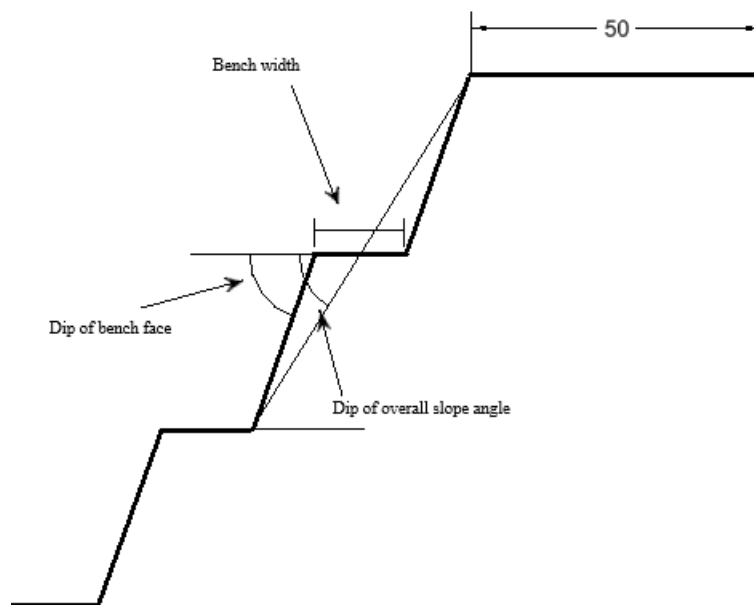


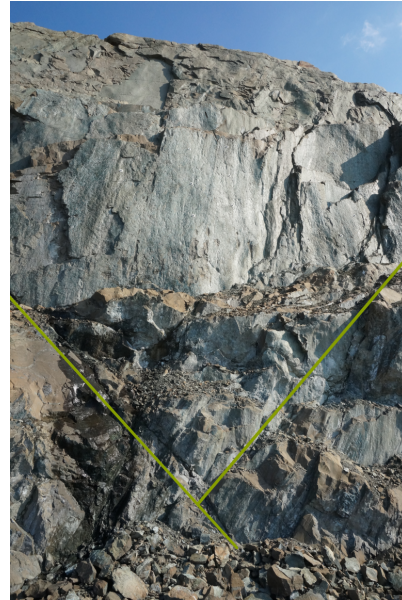
Figure 4.2: Sketch of geometries used in the stability analyses of wedges. 50 is the defined width in meters of the surface at the top of the quarry, used to delimit the size of the wedge that can be formed

4.2.3 Potential wedges

The potential wedges are shown in figure 4.3. There are three parallel joints on the west (left) side of the potential wedge 1. Either of these parallel joints was considered to potentially form the left side of the wedge. Wedge 3 and 4 were observed from distance.



(a) Photo of wedge 1.



(b) Photo of wedge 2.



(c) Photo of wedge 3.



(d) Photo of wedge 4.

Figure 4.3: Photo of the analysed wedges. The position of the wedges are marked by the yellow lines.

4.2.4 Uncertainties related to the input in the analysis of wedges

Like in the numerical models, simplifications and interpretations are made to perform the analysis. Uncertainties related to the input in the analysis are given in figure 4.4.

Input	Uncertainties
Dip and dip direction of joints	- The dip can vary. - Estimation of the dip and dip direction from photo and distance.
Surface strength of joints	- Will inherit the uncertainties from field mapping and laboratory testing. - The applicability of the Barton-Bandis criterion to the surface conditions along the discontinuities. - The surface type of discontinuities observed from distance.
Tension cracks	Location and existense of a tension crack.
Water pressure	The true worst case water pressure is unknown.

Table 4.4: Uncertainties related to the input in the analysis of wedges.

4.3 Numerical Modelling for Stability analyses

The numerical modelling program RS2 (Rocscience, 2019b) was used to create numerical models for the stability analysis. RS2 is a 2D finite element (FEM) analysis software program (Rocscience, 2019a). The program can analyse the stress distribution in a rock mass and the resulting deformation. The program uses three steps to perform an analysis (Rocscience, n.d.g):

- Establishment of a finite element model

The numerical model in RS2 is built as a 2D model of the project in consideration. The model includes information about the geometry of the project, the characteristics of the relevant rock mass, the in-situ stress and the distribution of water. When all the desired information is included in the model, the model is meshed into finite elements (Rocscience, n.d.f). The accuracy of the calculated deformation will depend on the size of the elements. A finer mesh gives a more accurate description of the displacement in a given point. At the same time will a finer mesh require more computer resources and processing time.

- Computation of the model

A numerical solution is calculated in each node of the finite elements by iterating until the solution for the elements converges (Rocscience, n.d.a), (Nikolić et al., 2016). The computation for the model will converge when the rock mass in the model is stable. RS2 calculate the displacements that will occur in the rock mass before it stabilises. When the model doesn't converge, the model will not become stable for any displacement of the rock mass. RS2 proposes three different convergence criterion that can be used to determine when the iterated solution is close enough. This value is determined by a defined tolerance value.

- Interpretation of the results

After computation, the deformations in the rock mass required for the model to become stable are visualised, and the analysis of stability can be performed.

4.3.1 Selection of sections for stability analyses

Numerical modelling was used to perform stability analysis at four different places in the quarry. The models were created from four sections cutting the back wall perpendicularly: S1, S1, S3 and S4. The sections are shown in the plan of the quarry in figure 4.11 in section 4.4. The four sections were chosen based on the three section areas 1,2, and 3 defined during field mapping. The three section areas consist of three types of rock mass with different behaviour. The modeled sections were chosen to represent different combinations of these three types of rock mass in the back wall, and potential failure related to each of them. S2 and S3 were used to analyse the stability of the current wall and the final back wall. S1 and S4 were only used to analyse the stability of the final back wall. The models created from S1, S2, S3, and S4 are described in detail in section 4.4.

After the sections for the models were determined, evaluations were made to establish the finite element model. The finite element models were established with regards to give a reliable reproduction of the conditions in the back wall, while at the same time consider the complexity of the model. A more complex model requires more computing power and computer memory, which further increase the processing time of the model.

It can be noted that the analyses were performed on well equipped personal computers.

4.3.2 Establishment of a finite element model

Geometry and the stress distribution

The geometry of the numerical models was defined by drawing external boundaries. The geometry of

the boundaries will influence the computed stress distribution in the model. The geometry of the current wall, was drawn after sections from the model of the quarry from the autumn 2019 by Sibelco Nordic. The geometry of the final back wall, was drawn after sections from the life of mine model from 2016 by Sibelco Nordic. (The sections were made from the models using the software MicroStation Bentley Systems (2018).) The models were tested with different geometries and loading around the drawn back wall, to get the most correct stress distribution in the model. The topography around the quarry was used to determine the expected stress conditions in the rock mass in the wall. The hillside above the quarry, acts as a large overburden to the back wall and induce vertical stress, σ_v . σ_v vary linearly with depth below surface, as described by equation 4.6, where ρ is the density of the overburden, g is the gravitational acceleration and h is depth below the ground surface.

$$\sigma_v = \rho gh \quad (4.6)$$

The shape of the quarry results in low confinement on the sides of the quarry, and a higher confinement in the middle part. The horizontal confinement was considered to be lowest in the eastern part of the back wall due to a valley located east of the quarry. Stress related geological conditions will also influence the stress distribution. Since RS2 creates a 2D numerical model, the horizontal stress in the model is defined by two components, horizontal stress in plane σ_h , and out of plane σ_z . From the considerations of the stress distribution, the relationship between σ_v , σ_h and σ_z in the back wall was evaluated to be given as expressed by equation 4.7 in most parts of the quarry.

$$\sigma_h = \sigma_z = 1.5\sigma_v \quad (4.7)$$

On the eastern most part of the quarry, the relationship between σ_v and σ_z were considered to be given as expressed by equation 4.8.

$$\sigma_z = 1.3\sigma_v \quad (4.8)$$

To achieve this stress distribution in the numerical models, two different geometries and loading around the slope were tested. The numerical model established for the calibration process, were used for the testing:

Trial 1

Trial 1 for geometry of model and loading is shown in figure 4.4. The model only includes the benches relevant for the calibration analysis. The achieved stress distribution was incorrect, see figure 4.5 and 4.6.

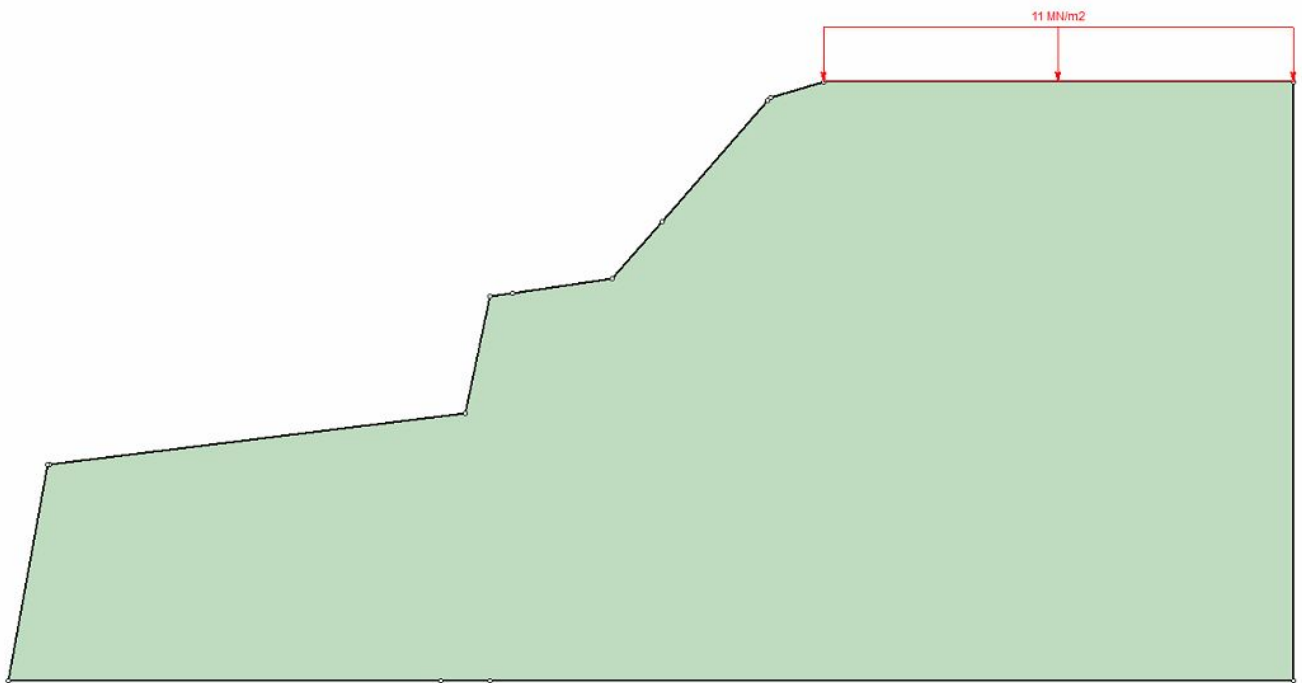


Figure 4.4: A vertical load were added to the model with magnitude approximately equal to the weight of the overburden above the surface. A gravity stress field were defined with $\sigma_h = 1.5\sigma_v$, and ground surface at the height of the top of the hill.

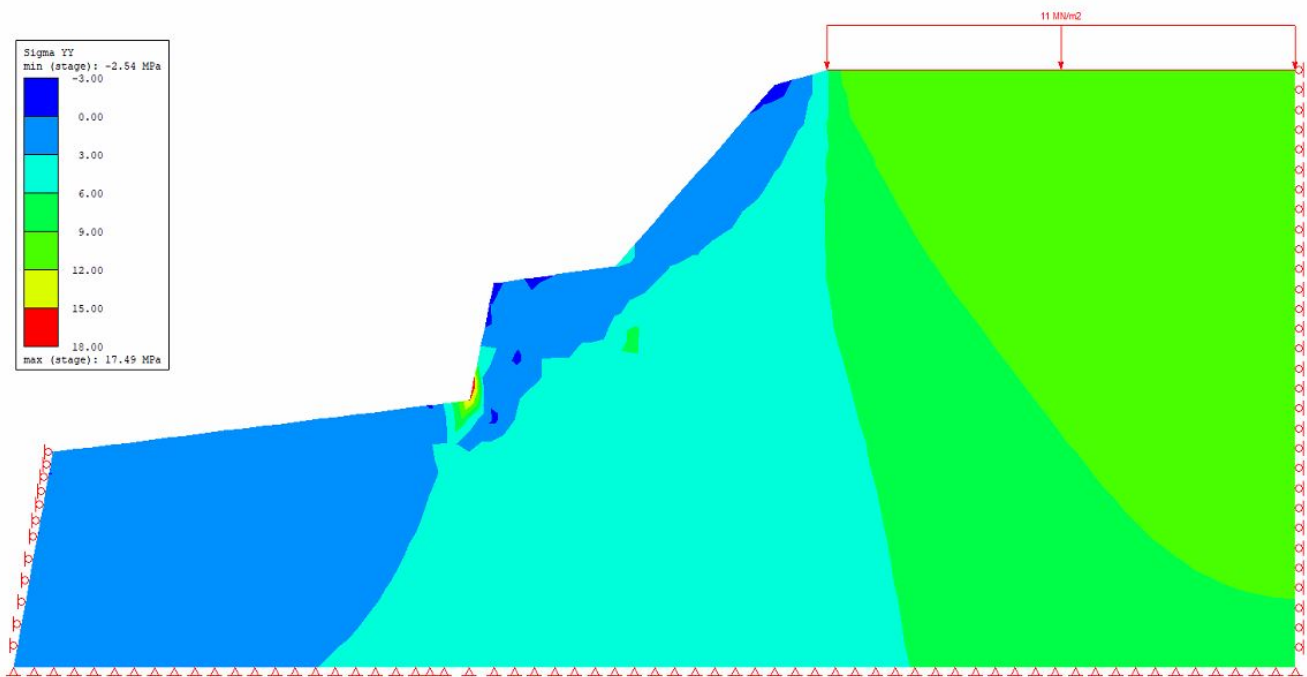


Figure 4.5: Stress distribution of σ_v (σ_{yy}) induced by the vertical load.

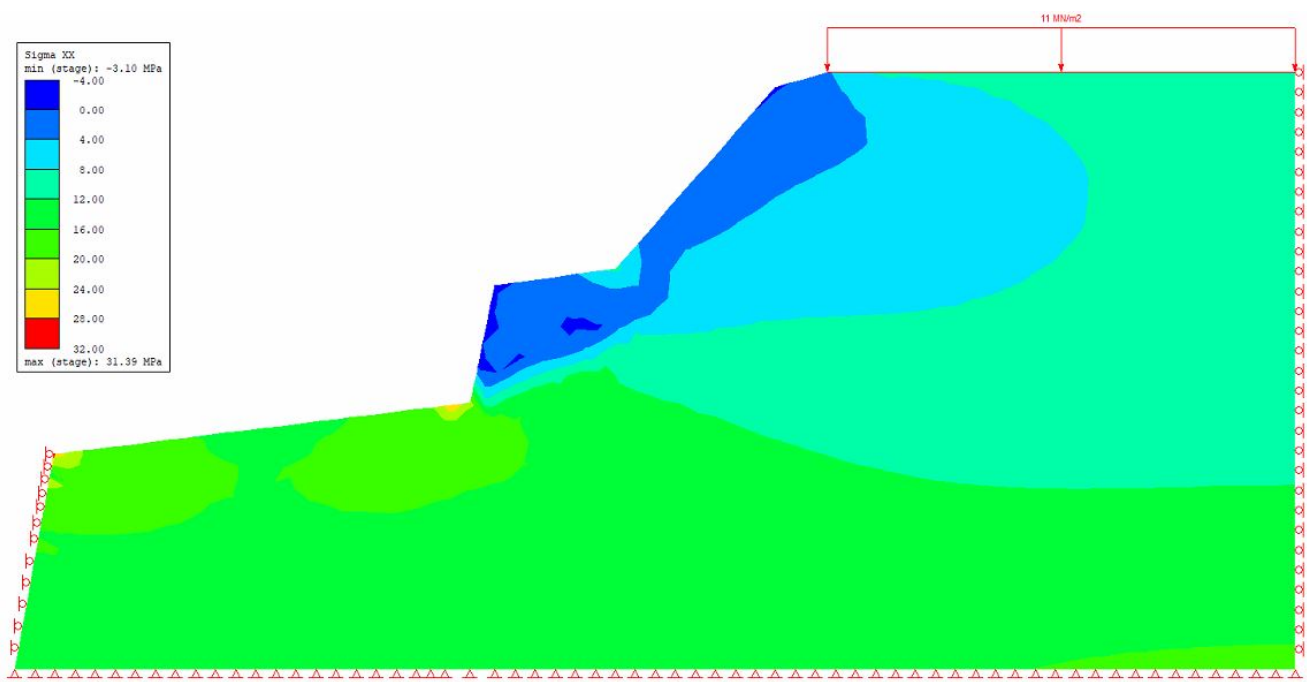


Figure 4.6: Stress distribution of σ_h (σ_{xx}) induced by the vertical load.

Trial 2

Trial 2 for geometry of model and loading is shown in figure 4.7. The model includes the slope up to the top of the hill above the quarry. The achieved stress distribution is similar to the considered stress conditions in the rock mass, see figure 4.8 and 4.9.

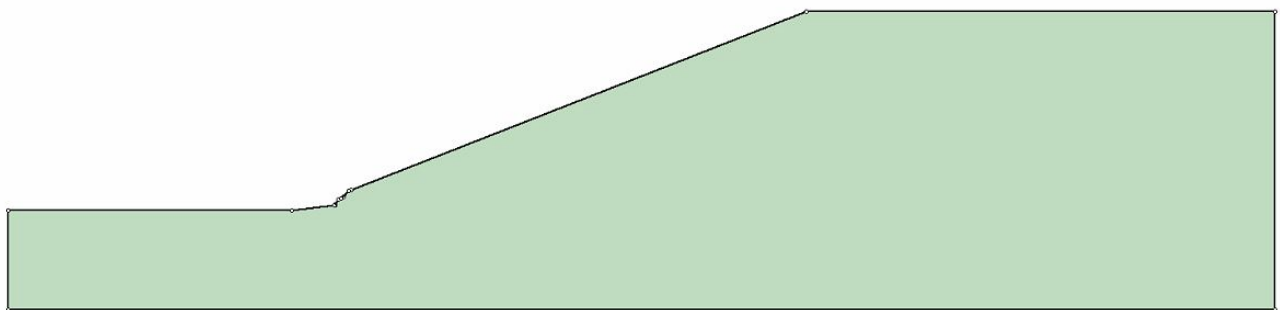


Figure 4.7: The model includes the slope up to the hill above the quarry. A gravity stress field were defined with $\sigma_h = 1.5\sigma_v$, and ground surface at the top of the hill.

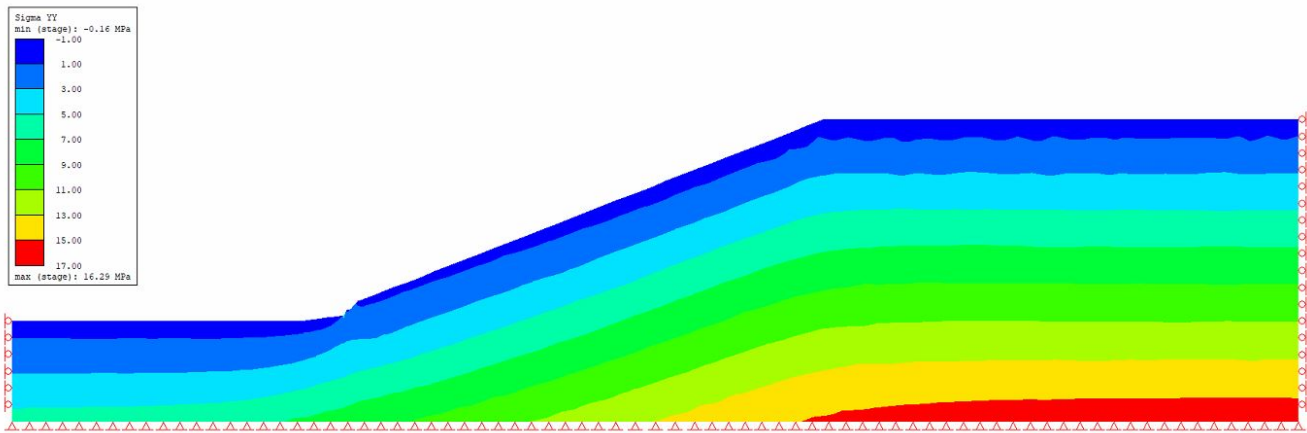


Figure 4.8: Stress distribution of σ_v (σ_{yy}).

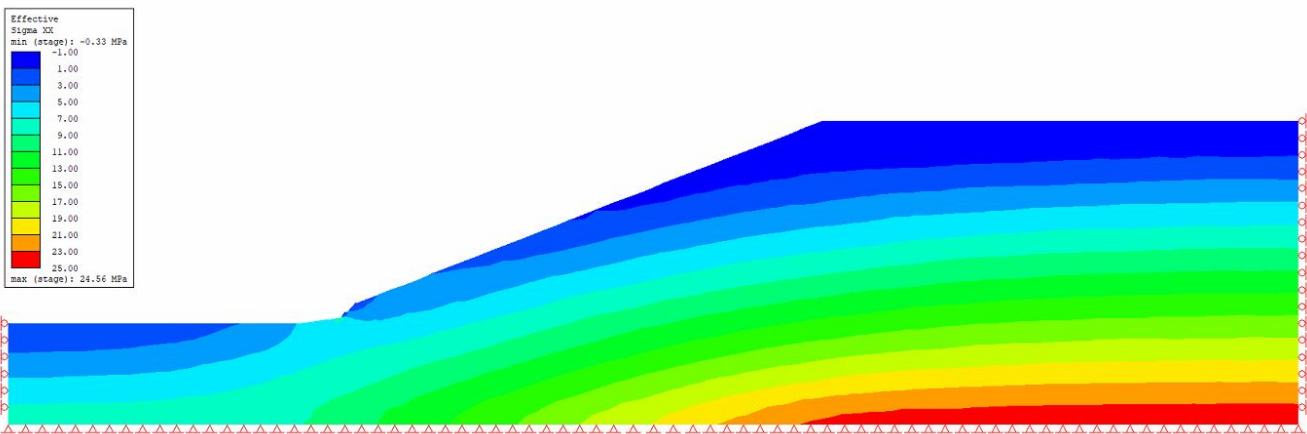


Figure 4.9: Stress distribution of σ_h (σ_{xx}).

The model with the hill slope included, gave the stress distribution most similar to the evaluations of stress above. This model was used even though the size of the model would increase the processing time of computations and require more computer resources. The geometry of the hill slope was simplified by a straight line with an angle to the horizontal equal to the angle from the top of the pit to the top of the hill. The angle and the height to the top of the hill were determined based on elevation profiles from Kartverket (2020). The elevation profiles for the modelled sections are shown in figure G.24, G.25, G.26, and G.27, in appendix G.2. The density of the overburden in the numerical models were set equal to the determined unit weight for gneiss, see section 4.1.

Boundary conditions

Considerate drawing of the geometry of the numerical models is also important to avoid disturbance of the stress and deformation analysis of the back wall. The dimensions of the external boundaries outside the area of the slope were determined based on the recommendations by Wyllie and Mah (2004), shown in figure 4.10. Only the part of the slope in the model representing the back wall is of interest in the analysis. The width behind the slope where therefore allowed to be $2/3W$ to reduce the required computer resources. The external boundary at the bottom of the slope surface was given a length of 350 m.

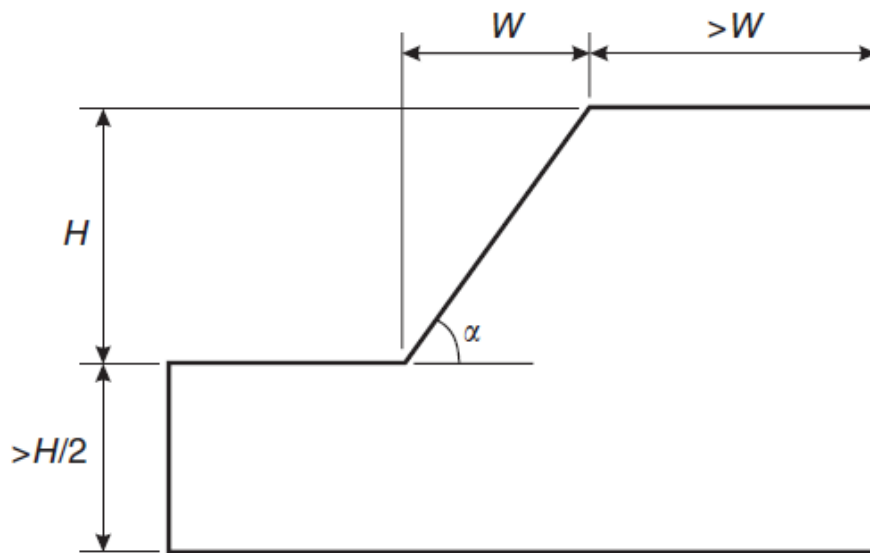


Figure 4.10: The figure shows the background for the placement of the external boundaries in the numerical models.

Characterisation of the rock mass

The characterisation of the rock mass in the quarry was included in the numerical models by defining the behaviour of the rock material, the strength of the rock mass and the properties of the joints sets. The distribution of the different rock types in the back wall, was determined in the numerical models after sections of geology from Sibelco Nordic. The strength of the rock mass within the different rock types was defined by the process described in section 4.1. The material properties of the rocks was defined as described in table 4.5 for all the different rock types in the quarry.

Defined material properties	Comment
Isotropic behaviour	It was noted that many of the rocks have chlorite bands or veins following the foliation.
Dry rock mass	Defined as dry even though the area is exposed to frequent rainfall.
Plastic	The rocks were evaluated to behave as an elastic-plastic material from the stress-strain curve obtained from laboratory testing, see figure B.2, B.3, B.4 and B.5 in appendix B (Li, 2018).
Residual strength defined equal to the peak strength	Recommended by Rocscience (n.d.) for elastic-plastic materials.

Table 4.5: The defined properties for the rock material in the numerical models.

The 2D numerical model will only include the joint sets with a strike crossing the modelled section. The foliation was the only joint set included in the numerical models. This was also the main joint set in the quarry. The foliation is a distinct feature of the rock mass in the quarry, and a reproduction of the joint set was considered important to give a reliable characterisation of the rock mass behaviour in the models. The properties of the foliation were defined as shown in table 4.6. The strength of the joint surfaces was determined as described in section 4.1.

Defined joint properties	Comment
Parallel deterministic joint network model	The joint set was observed to have an approximately fixed spacing and dip within a rock type. The spacing and the dip were determined from registrations during field mapping.
Infinite length	The joints were observed to be persistent.
Joint ends open at surface contacts	The joints were observed to be open at the surface.
Joint ends closed at material contacts	The dip of the joint set had a small variation in the different rock types and the joints evaluated to not be persistent between the different rock types.

Table 4.6: The defined properties for the joint set following the foliation in the numerical models.

The density of joints in a model will influence the sizes of the required finite elements, which further will have impact on the required computing resources and processing time, see the section below. The calibration model was the first model to be created and analysed. The calibration model was used to evaluate the spacing of the joints with respect to the real joint spacing and computation time, see section 4.5.

Definition of finite elements

When the external boundaries of the model and the behaviour of the rock mass were defined, the model was divided into finite elements. The sizes of the finite elements was determined by aiming to get the desired accuracy of the analysis within the limits of the available computer power and memory. The sizes of the finite elements were essential for the analysis and were defined with care. The finite elements were constructed from 6 noded triangles. For the elements to represent the stress conditions and deformation at a given point most accurately in both x- and y- direction, the width and the height of the elements were aimed to be similar. A high accuracy of the stress and deformation analysis was desired in the part of the model representing the back wall, and this part was modelled with the finest mesh. The rock mass on each side of the back wall was allowed a lower accuracy, and was modelled with larger finite elements. A gradual transition in element size was used between the areas with the finest and the larger mesh. The determination of appropriate element size was performed during the establishment of the numerical models for the stability analysis of the back wall and calibration model, see section 4.4.2 and 5.1.

Restraining movement

The displacement of the finite elements along the external boundaries has to be restrained to represent the possible deformation of the rock mass in that area in the model. The allowed displacement of the elements along the external boundaries, was defined as suggested by Chugh (2003) for 2D continuum models, see table 4.7.

External boundary	Allowed direction of deformation	Restrained direction in the numerical model
Ground surface	All directions	Free *
Slope	All directions	Free *
Right edge	Vertical deformation	x-direction
Left edge	Vertical deformation	x-direction
Bottom edge	No deformation	x- and y-direction
Bottom corners	No deformation	x- and y-direction
*”Free” is used in RS2 for a surface free to deform in all directions.		

Table 4.7: The allowed direction of movement of the finite elements along different parts of the external boundaries.

4.3.3 Computation and analysis

After the model had been established and divided into finite elements, the computation of the numerical model was performed. The default settings for computation of a stress analyses was used. A maximum of 500 iterations were allowed for each step in the computation (Rocscience, n.d.k). The convergence criteria were ”Absolute Force and Energy”, and the tolerance for convergence were set to 0.001.

4.3.4 Method for stability analysis

The computed numerical models were analysed by examination of the stress distribution and the following deformations in the rock mass. Two different types of numerical methods available in RS2 were used to perform the analysis:

1. The shear strength reduction method (SSR)
2. An analysis of the deformation in the rock mass with the determined input parameters. There is no change in the strength of rock mass or joints.

The SSR method was used to look at how far the rock mass in the wall is and will be from failure with the given input parameters, and how the deformation in the rock mass can evolve with decreased rock mass strength. The SSR method requires high computing power and computing memory. The power and memory required depends on the complexity of the model. Dense joint networks in the model increase the complexity of the model (see section 4.5), and the necessary computer resources to perform the SSR analysis with joints networks in the model was not available. The SSR method can't include the strength of joints defined by the Barton-Bandis criterion in the model, which was the strength criterion used in the field and for the numerical modelling, see section 4.1 (Rocscience, n.d.b). The strength of joint surfaces can also be defined by the Mohr-Coulomb criterion with a known apparent friction angle, see section 2.2.2. The apparent friction angle will vary with the normal stress σ_n on the surface (Nilsen, 2000). With a defined σ_n , the strength of the joints can be converted from the non-linear Barton-Bandis criterion to the linear Mohr-Coulomb criterion (Rocscience, n.d.c). There will be large variations in σ_n on the joint surfaces in the final back wall. The conversion was therefore not considered to be relevant. Based on these considerations, the SSR analysis were performed on models without the joint network following the foliation. The estimated Q-values from field mapping were used to include the properties of the joints in the rock mass strength in the model, see section 4.1. The SSR analysis was only carried out on the part of the numerical model forming the back wall to reduce the processing time.

The second method for analysing was used to investigate the influence of the dip and the strength of the foliation on the stability of the wall. The method also proposes a simple method to consider if the wall in the model is stable. The analysis will determine if the computation of the model converges, and the potential displacement before the rock mass is stable. The method required less computer resources and the set and joint strength were included in the model. The foliation was included in only the part of the model which represents the back wall, to achieve a high accuracy in the analysis of the wall within the limits of the computer resources available. The numerical model used for calibration was only analysed by this method. The other analyses were performed with both methods.

4.3.5 Uncertainties and simplifications in the numerical models

In the numerical model, simplifications of the rock mass conditions and conditions in the quarry are made. Several simplifications have been defined above to define a reliable numerical model within the available computer resources. The modeled conditions in the rock mass were determined from input parameters based on measurements and estimations from field mapping and laboratory testing. The uncertainties related to these methods are inherited in the numerical models. In addition, interpretations of the parameters in order to include them in the model will contribute to new uncertainties. Different uncertainties that accompanied the input in the numerical models are given in table 4.8.

Numerical modelling	
Input	Uncertainties
Rock mass strength	<ul style="list-style-type: none"> - Will inherit the uncertainties from field mapping and laboratory testing. - The applicability of the Hoek-Brown criterion to the rock mass in the quarry.
Joint strength	<ul style="list-style-type: none"> - Will inherit the uncertainties from field mapping and laboratory testing. - The applicability of the Barton-Bandis criterion to the surface conditions in the quarry. - The surface conditions below the surface. - The consistency of surface strength along a joint surface.
Joint networks	<ul style="list-style-type: none"> - Will inherit the uncertainties from field mapping and laboratory testing. - The persistence of the joints. - The conditions of the joints on the boundaries.
Geology	<ul style="list-style-type: none"> - Location of rock types. - Location and size of weakness zones.
Geometry	<ul style="list-style-type: none"> - The geometry of the benches in the quarry compared to the planned design.

Table 4.8: Uncertainties related to the input in the numerical models.

Rock mass failures that have already occurred, can be used to calibrate measured strength parameters. The rock mass failures observed in the quarry were mainly due to plane failure of slabs along the serpentinized joints following the foliation. A rock fall due to plane failure were used to calibrate joint strength parameters for a surface type. Since other rock failure was not observed to have occurred in the quarry, only plane failure was used for calibration. The calibration process is described in section 4.5. The uncertainties in the strength parameters were also accounted for by using the SSR to evaluate the consequence of a weaker or stronger rock mass than given by the field and laboratory measurements. The rock mass was considered to be dry and a potential decrease in rock mass strength due to water in the pores in rock was also included through the SSR analysis. The movement of the ground water in the rock mass was not investigated in the field and were not included in the numerical models. This simplification was considered when evaluating the stability of the rock mass.

4.4 The numerical models for stability analysis

The numerical models created from S1,S2,S3, and S4 were used to analyse the stability of the quarry. The location of the models are indicated in figure 4.11. The characteristics of the rock mass in each section and the purpose of the models are described in section 4.4.1. The division of the models into finite elements is described in section 4.4.2.

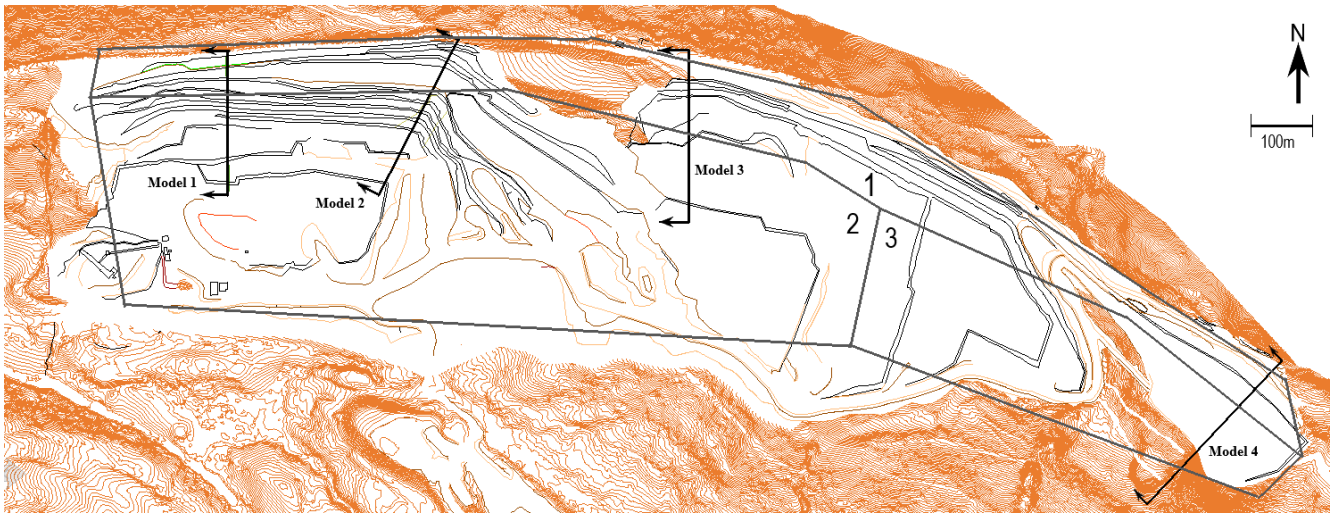


Figure 4.11: Plan of the quarry showing the location of the sections S1,S2,S3, and S4. The grey lines indicate the area sections 1,2, and 3 defined during field mapping. The plan is modified after a model of the quarry from Sibelco Nordic,

4.4.1 Description of the numerical models

Section S1

Section S1 was used to create a numerical model to analyse the stability of the lowest part of the final back wall. The benches in the final back wall will consist of chlorite banded dunite, rock mass typical for area section 2, see figure 4.12. The upper benches will consist of serpentized dunite, rock mass typical for area section 1.

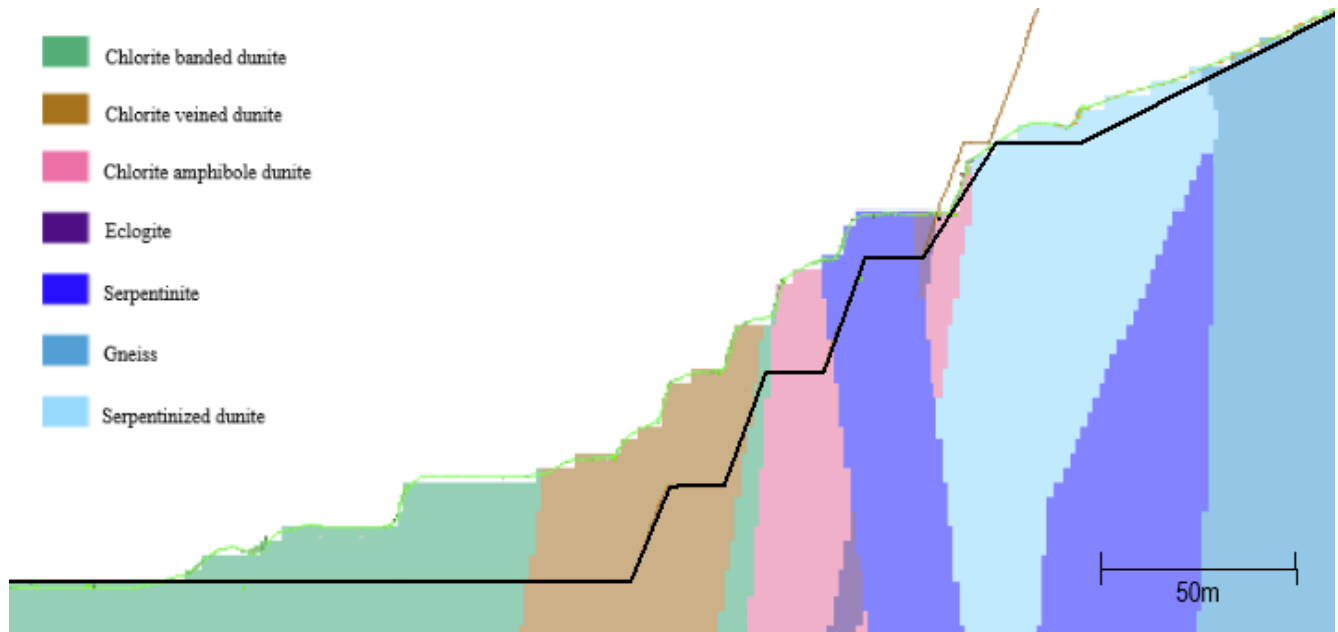


Figure 4.12: The geological section used to define the geology of the the model from section S1. The geometry of the final back wall is indicated by the black line. The brown line indicate the planned geometry of the wall from a simplified quarry design model. The geological section is modified after a section from Sibelco Nordic.

Section S2

The section was used to perform two different analyses: One analysis of the current back wall, and one analysis of the final back wall. The section is cutting the back wall in the most developed part of the present quarry. The stability analysis of the current quarry was performed by creating a model of this section of the current back wall. The model was created to investigate the response of the rock mass to the stress conditions in the high slope today. The benches of the current wall along the section, consist mainly of chlorite banded dunite at the lower levels, see figure 4.13, and have characteristics typical for area section 2. The stability of the section was analysed with focus on the rock mass of chlorite banded dunite.

Along section S2 in the final back wall, the rock mass will mainly consist of serpentized dunite, with

rock mass characteristics typical for area section 1. The model was used to analyse the response of this type of rock mass to the stress conditions that will be present in the final back wall. The model was also used to examine the response of the chlorite banded dunite at the lowest bench in a slope that is higher than the slope by section S1. In addition, the analyses of the current back wall and the final back wall were used to analyse the influence the weakness zone observed at point Z1-Z5 on the stability. The inclusion of the weakness zone in the model is described in section 4.1.2.

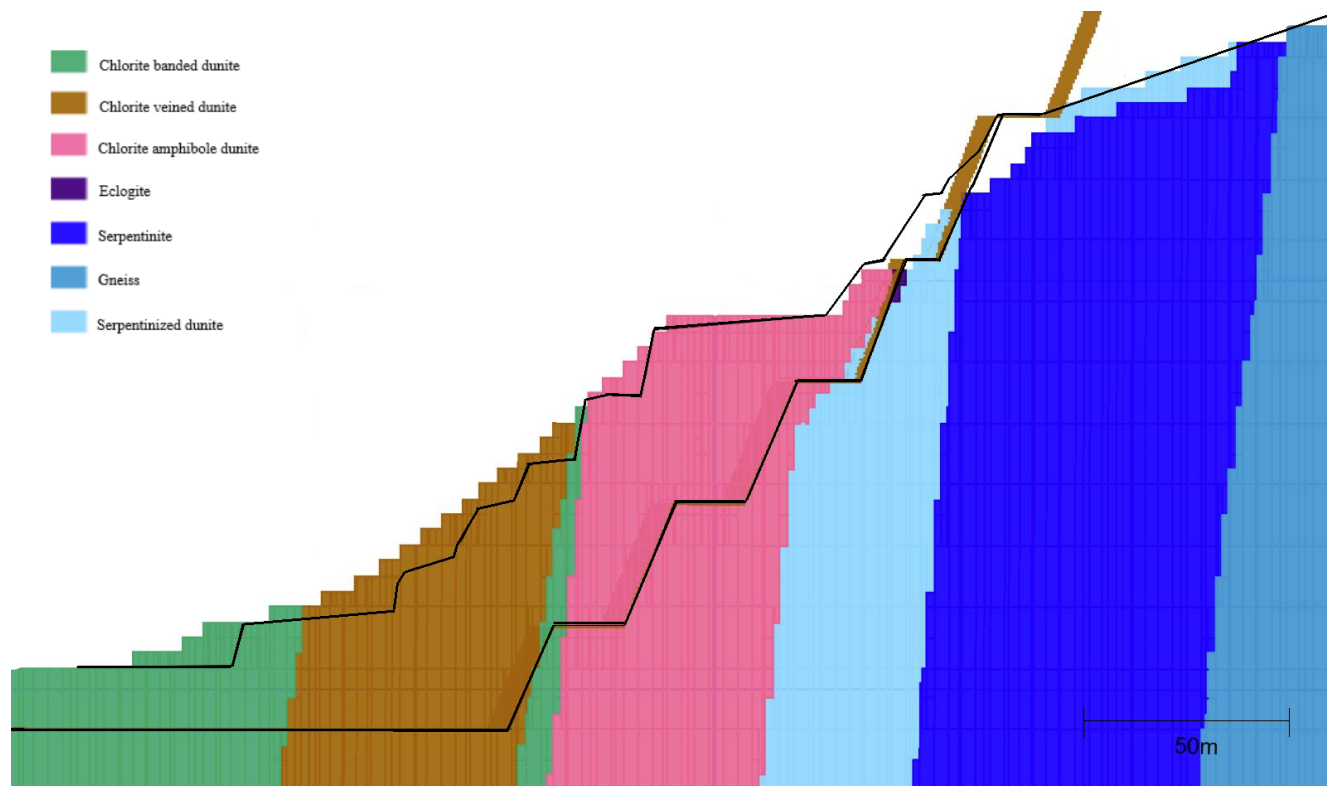


Figure 4.13: Geological section used to define the geology of the models from section S2. The geometry of the model of the current and the final back wall is indicated by the black lines. The brown line indicate the planned geometry of the final back wall from a simplified model of the quarry design. The geological section is modified after a section from Sibelco Nordic.

Section S3

The section was used to create a numerical model of the current back wall and the final back wall. The section is cutting the wall where the plane failure used for calibration was observed, see section 4.5, and is located in a less developed part of the current quarry, see figure 4.11. The section was used to create a model to perform the calibration of the serpentinized joint surface, and to analyse the stability of the benches by the plane failure in the current back wall. The model of the final back wall was used to investigate the stability of the planned wall in this area, and to examine how the serpentinized surface will affect the stability of the final wall.

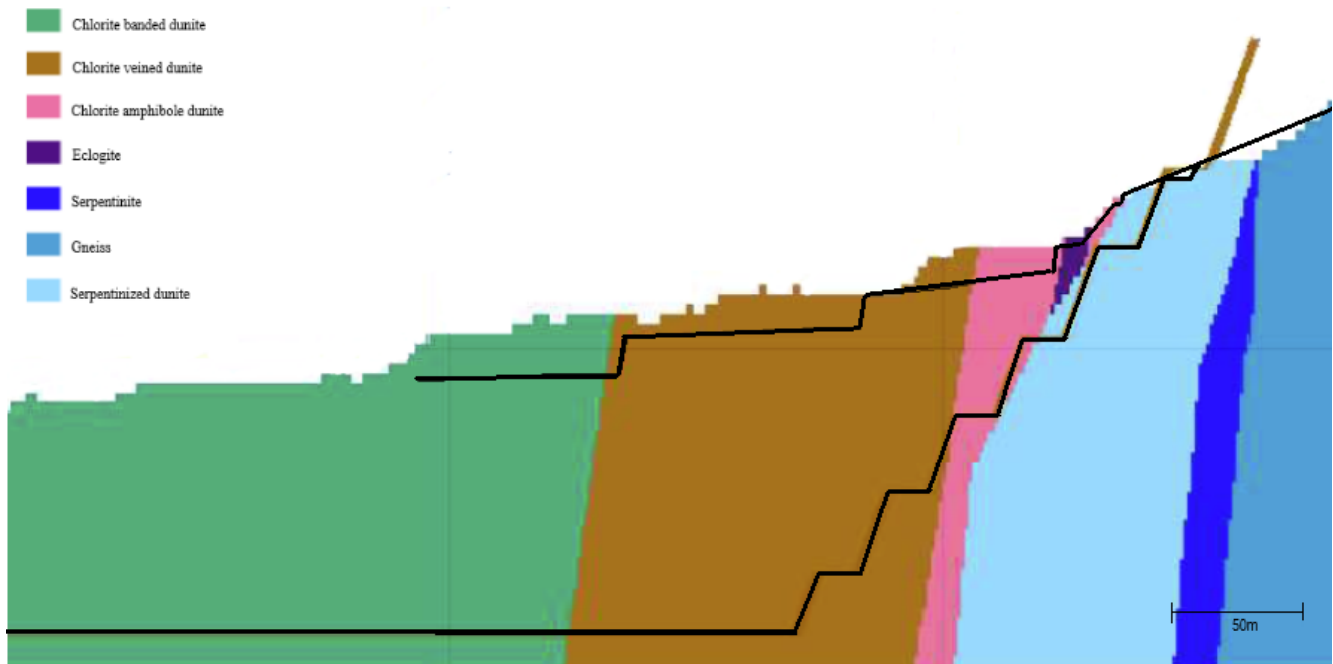


Figure 4.14: Geological section used to define the geology of the models from section S3. The geometry of the model of the current and the final back wall is indicated by the black lines. The brown line indicate the planned geometry of the final back wall from a simplified quarry design model. The geological section is modified after a section from Sibelco Nordic.

Section S4

The section was used to create a numerical model to analyse the stability of the final wall when most of the benches in the wall will consist of blastogranular dunite, rock mass type typical for section 3. In this part of the back wall, the horizontal stress out of plane σ_z was evaluated to be defined by equation 4.8 (for the equation, see section 4.3).

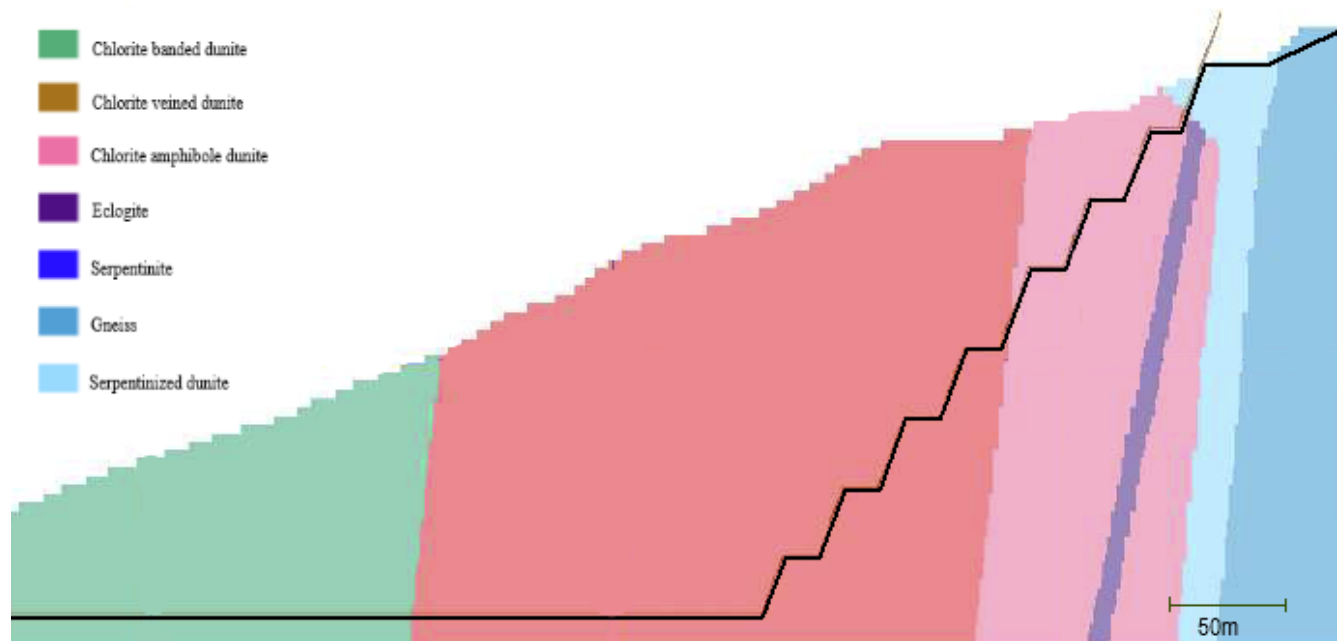


Figure 4.15: Geological section used to define the geology of the model by section S4. The geometries of the model of the current back wall and the final back wall are indicated by the black lines. The geological section is modified after a section from Sibelco Nordic.

4.4.2 The sizes of the finite elements in the numerical models

The sizes of the finite elements in the different parts of the model, was defined by dividing the numerical model into four different areas: area 1, 2, 3, and 4, see figure 4.16.

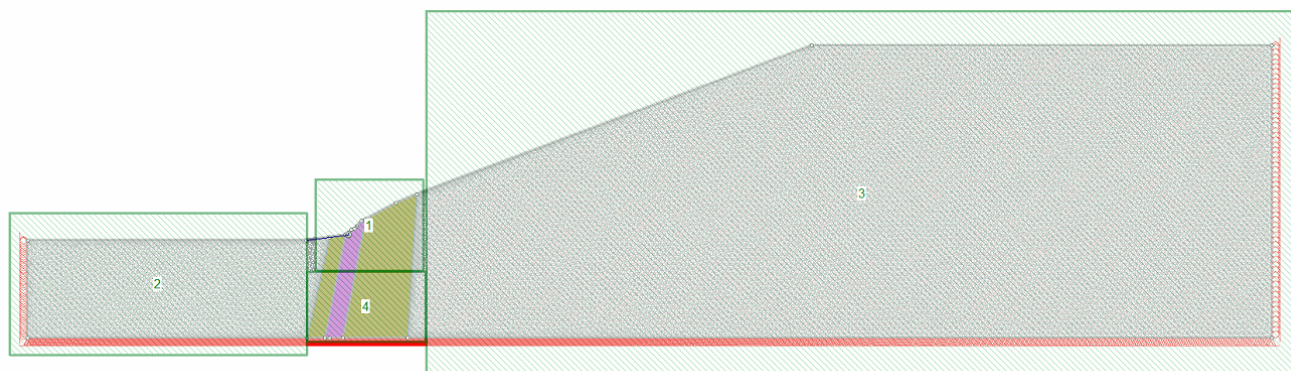


Figure 4.16: The mesh set up used for calibration, showing the areas 1,2,3, and 4.

The benches in the back wall were located in area 1, and required the highest accuracy of the calculation. Larger elements were used in area 2,3, and 4. The desirable size of the larger elements was investigated with focus on avoiding disturbance of the stress conditions by the rock failure. The sizes of the elements were defined differently for the two methods used for numerical analysis, described in 4.3.4. The defined sizes of the finite elements in method 1 are given in table 4.9. The defined sizes of the elements in method 2 were determined during the establishment of the numerical model for calibration, and is given in section 4.5.2. The other input parameters in the models were defined as described in section 4.1.

Area	Length of finite elements (m)
1	2
2,3	30
4	5

Table 4.9: The defined length of the finite elements in each area 1,2,3, and 4. The lengths were used for analyses with method 1.

4.5 Calibration of joint strength parameters

The numerical model for the calibration was the first established model in this project. The model was therefore used to determine some of the input to be used in all the numerical analysis of the back wall. Figure 4.17 shows the rock failure used for calibration. The failure was located along section S3, see

figure 4.11. The rock failure observed was caused by a block sliding along a serpentinized foliation surface. This type of rock failure was observed in several places in section 1, often in zones close to the eclogite boudins. Due to the frequency of this failure in section 1, the strength of the serpentinized surface was regarded to be important for the stability of the back wall. The goal of the numerical analysis was to calibrate the joint strength of the serpentinized surface. The rock failure shown in figure 4.17 was used for the calibration since the failure surface was available for measurements of strength parameters. The established numerical model was also used to investigate the stability of the benches in the current back wall in the section of serpentinized dunite.



Figure 4.17: Photo of the plane failure used to calibrate the joint strength parameters of a serpentinized surface. The bench is about 15m high.

4.5.1 Establish the numerical model for calibration

Observations of the rock failure were used to establish the geometry and the geology in the numerical model. The photo of the failure shows an undercutting of the bench. The block was evaluated to be able to slide due to the undercutting, and the undercutting was included in the model, see figure 4.19. The input data of the rock mass and joints were defined and determined as described in section 4.3 and 4.1. The geology along the section is displayed in figure 4.18. The failure occurred in an rock mass of serpentinized dunite (termed serpentinized dunite 1 in 4.1).

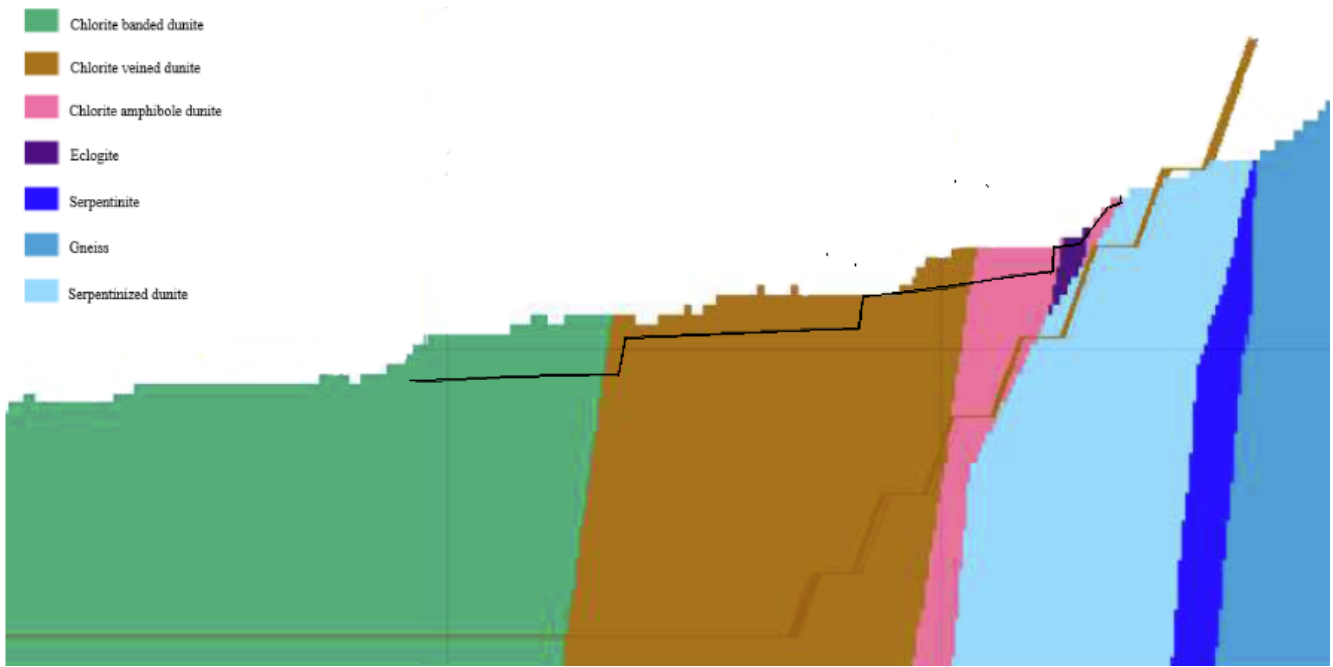


Figure 4.18: Section of geology from Sibelco Nordic used for the calibration model. The geometry of the back wall today is marked in black. The geometry of the final back wall is marked in brown.

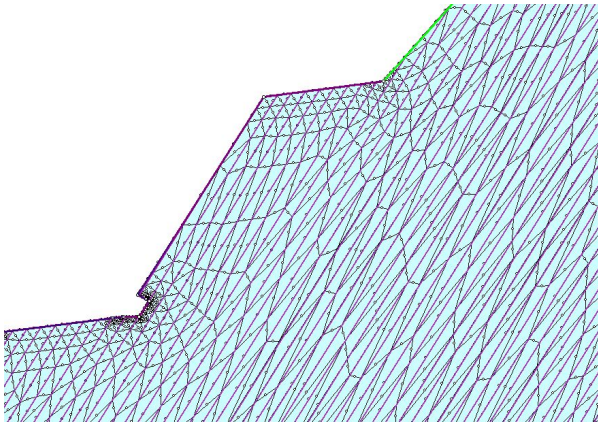
4.5.2 Defining finite elements in the calibration model

The model of the rock failure was divided into finite elements based on the evaluations made in section 4.3.2. The established calibration model was used to investigate in detail the most appropriate division of finite elements for the numerical models for analysis method 2. The sizes of the finite elements had to make a reliable reproduction of the characteristics of the joint set following the foliation, within the limits of the computer resources available. The most favourable sizes of the finite elements in the model were investigated for the four different mesh areas defined in section 4.4.2: area 1, 2, 3, and 4, see figure 4.16. The foliation in the rock mass was only included in the area around the rock failure (area 1 and 4), since a reliable representation of the conditions along the foliation requires small elements. The sizes of the elements in the foliation area was determined with by taking into account the foliation spacing in the quarry, and the relationship between the width and the height of the elements. The spacing between the joints following the foliation was measured in the quarry to be approximately 0.2m.

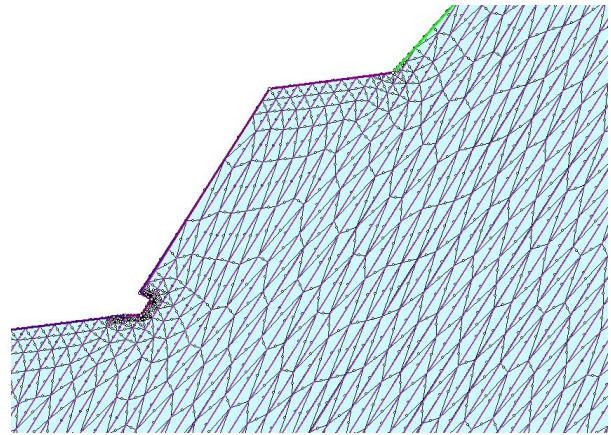
Table 4.10 shows different combinations of spacing and lengths of finite elements proposed for the calibration model. The sizes of the finite elements in the area of failure for each trial is shown in figure 4.19.

Trial	Spacing (m)	Length of finite elements (m)		
		Area 1	Area 2,3	Area 4
1	0.5	5	20	5
2	0.5	3	20	3
3	0.5	2	30	2
4	0.2	2	20	2
5	0.5	1	20	2

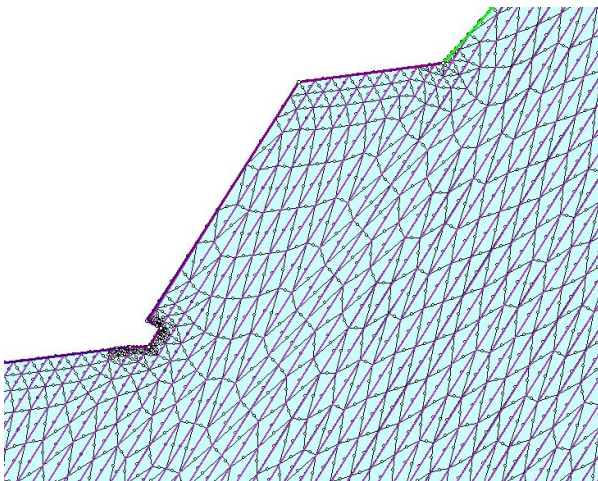
Table 4.10: Trials of finite element sizes and joint spacing in the numerical model for calibration. The lengths of the finite elements in the table define the maximum allowed length of the elements in the model.



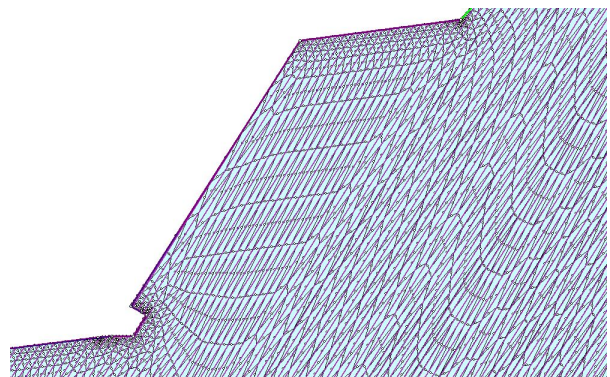
(a) The size of the finite elements in mesh area 1 in trial 1.



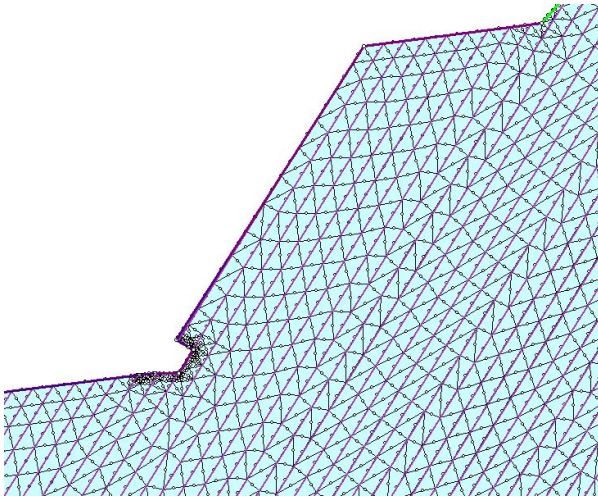
(b) The size of the finite elements in mesh area 1 in trial 2.



(c) The size of the finite elements in mesh area 1 in trial 3.



(d) The size of the finite elements in mesh area 1 in trial 4.



(e) The sizes of the finite elements in mesh area 1 in trial 5.

Figure 4.19: The figures show the sizes of the finite elements and the foliation spacing for each trial 1-5 in the area of model showing the rock failure. The figures also show how the undercutting of the bench by the failure is included in the model. The finite elements in the models differ from the defined size when smaller elements are required to mesh details in the model and to obtain a gradual transition in the element sizes.

The combination of element sizes used in trial 5 was used for the calibration model and all the other numerical models for analysing method 1. The combination of element sizes in area 1 and joint spacing was considered to give a model which expresses the dense foliation structure in the rock mass, and at the same time limits the processing time. The element sizes proposed in area 2,3 and 4 were considered to not disturb the conditions by the rock failure in the model.

4.5.3 The calibration process

The calibration was performed by analysing the failure area using analysing method 2, with the start input parameters defined as described in section 4.1. The results of an analysis was evaluated by investigating if there was deformation along the failure surface in the model with the given strength parameters. If the first analysis showed no deformation along the joint surface, the values of the strength parameters JRC, JCS and ϕ_b of the serpentinized surface were decreased until deformations along the failure plane occurred. If the first analysis showed deformation, the values of the strength parameters were increased until the deformation stopped, to find the upper limit of the strength. The measurements of other serpentinized surfaces were used to determine the alteration of the parameters. Low and high values of the strength parameters, compared to the start values, were also used to find the upper and lower boundaries of the values for the strength parameters surface.

4.5.4 Alternative methods for calibration

The calibration of strength parameters can also be performed by back calculation of a rock failure. One method for back calculation is to use the Coulomb's law in combination with the Barton-Bandis criterion as expressed in equation 2.8 in section 4.5, to determine an unknown shear strength parameters of a joint surface. The rock failure used for calibration can be represented as a block sliding down a surface, as shown in figure 4.20. The back calculation is performed by finding the values of the strength parameters at limit equilibrium. Limit equilibrium is obtained when the shear stress along the surface is equal to the shear strength.

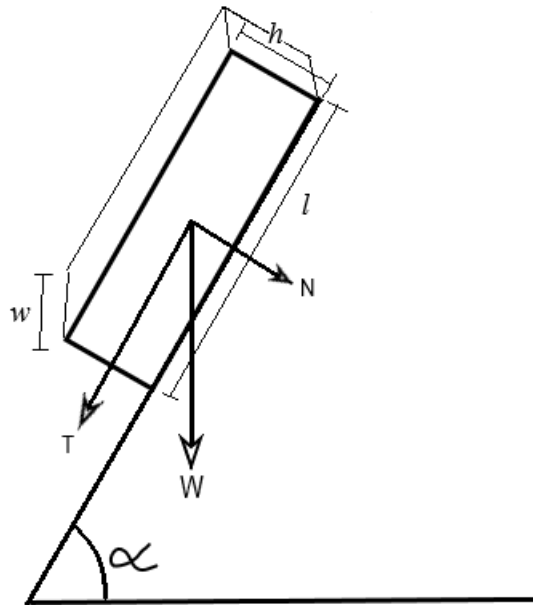


Figure 4.20: A sketch showing the rock failure used for the calibration process, represented by a block sliding down a surface. W = weight of block, N = Normal force from the block on the foliation surface, T = Shear force from the block on the foliation surface, l = length of the block, w = width of the block and h = height of the block.

The back calculation can be used to find the value of one unknown parameter. The measurements of JCS was considered to be the values with the largest uncertainties of the parameters measured in the field. JCS was therefore treated as the unknown parameter. JRC and ϕ_r were considered known. The normal stress on the surface from the block can be expressed by 4.9, where W is the weight of the block. W is given by equation 4.10.

$$\sigma_n = \frac{N}{l \cdot w} = \frac{W \cos \alpha}{l \cdot w} \quad (4.9)$$

W is the weight of the block and is given by equation 4.10, where V is the volume of the block, ρ is the

density and g is the gravitational acceleration.

$$W = l \cdot w \cdot h \cdot \rho \cdot g \quad (4.10)$$

The shear stress along the surface was considered to only be induced by the weight of block, and was expressed by equation 4.11.

$$\tau = \frac{T}{l \cdot w} = \frac{W \sin \alpha}{l \cdot w} \quad (4.11)$$

5. Analysis and discussion

This chapter presents the analyses of wedges, the numerical models, and the evaluation of the stability of the current and the final back wall. The input parameters used in the analyses are given in the first section. The next section presents the determined safety factors for each of the four potential wedges in the current and the final back wall. The stability indicated by the safety factors is evaluated. The third section presents the results and interpretations made from numerical analysis of the current and the final back wall. The calibration analysis is included in the consideration of the stability of the current back wall. At the end of this chapter, the stability of the current and the final back wall based on the results from the analyses are discussed. The stability is evaluated by looking at the risk of global and local failure in the wall.

5.1 Input data for wedge analysis and numerical modelling

5.1.1 Input parameters for rock mass strength

Table 5.1 presents the determined input parameters for rock mass strength to be used in the analyses of wedges and the numerical models.

Rock/ rock mass	Compressive strength, σ_{ci} (MPa)	Young's Modulus, E (MPa)	Poisson's ratio, ν	Unit weight (MN/m^3)	GSI	m_i	m_b	s	a
Dunite	85.1	55780	0.45	0.032	72	25	5.368	0.017	0.5
Serpentinized dunite 1	87.8	53980	0.287	0.029	67	25	4.078	0.008	0.5
Chlorite banded dunite	81.8	35450	0.35	0.032	69	25	4.552	0.011	0.5
Serpentinized dunite 2	130.1	59990	0.35	0.026	71	25	5.081	0.015	0.5
Gneiss	175	91875	0.37	0.029	72	28	6.012	0.017	0.5
Contact zone by the gneiss boundary	87.8	53980	0.287	0.029	35	25	0.703	0.000081	0.5
Weakness zone related to point Z1-Z5	81.8	35450	0.35	0.032	30	25	0.534	0.000040	0.5

Table 5.1: Input parameters for the strength of rock mass used in the numerical models.

5.1.2 Start parameters for the joint set in each of the area sections 1,2, and 3.

The joint set parameters are defined for each area section 1,2, and 3. The input parameters for the joint set in the numerical models of section S1,S2,S3, and S4 are given in table 5.2, 5.3, and 5.4. The rock types and the surface types used in the different models are displayed in appendix G.2.

Section 1

Rock	Surface type	JRC	JCS (MPa)	ϕ_b (°)	Normal stiffness, k_n (MPa/m)	Shear stiffness, k_s (MPa/m)	Dip of joints used in the models (°)	
							S1,S2, S3	S4
Serpentinized dunite 1	Rough, slightly weathered surface	8	63	23	84435	32803	75	80
Serpentinized dunite 1	Serpentinized	5	47	23	84435	32803	75	80
Serpentinized dunite 2	Rough, slightly weathered surface	8	63	23	143023	52971	-	80

Table 5.2: Input parameters used for the foliation in the different rock types in area section 1.

Section 2

Rock	Surface type	JRC	JCS (MPa)	ϕ_b (°)	Normal stiffness, k_n (MPa/m)	Shear stiffness, k_s (MPa/m)	Dip of joints used in the models (°)
Chlorite banded dunite	Rough, sandy surface	5	60	32	96446	35721	75

Table 5.3: Input parameters used for foliation in the chlorite banded dunite in area section 2.

Section 3

Rock	Surface type	JRC	JCS (MPa)	ϕ_b (°)	Normal stiffness, k_n (MPa/m)	Shear stiffness, k_s (MPa/m)	Dip of joints used in the models (°)
Dunite	Rough, sandy surface	7	59	28	161784	55788	75

Table 5.4: Input parameters used for the foliation in the dunite in area section 3.

5.2 Stability analysis of wedges

5.2.1 Input parameters

The input parameters of joint strength used in the stability analysis of each wedge are shown in table 5.5. The input parameters defining the geometry of the analysed wedges are given in table 5.6.

Wedge No.	Joint	Dip (°)	Dip direction (°)	Surface type	JRC	JCS	ϕ_r	Comment
1	Joint west	78	78	Serpentinized	7	28	22	
	Joint east	60	297	Serpentinized	7	28	22	
2	Joint west	59	138	Rough surface, slightly weathered	2.5	120	27	
	Joint east	58	302	Talk, chlorite, mica	11	82	11	
3	Joint west	65	81	Rough surface, slightly weathered	8	63	22	Average values for the surface type was used.
	Joint east	57	261	Rough surface, slightly weathered	8	63	22	Average values for the surface type was used.
4	Joint west	34	116	Rough surface, slightly weathered	8	63	22	
	Joint east	42	296	Rough surface, slightly weathered	8	63	22	

Table 5.5: Input strength parameters for the joints defining the potential wedges. The two discontinuities defining each potential wedge are named after which discontinuity is located furthest to the east and west. All the discontinuities are named joints.

Wedge No.	Point			Dip (°)	Dip direction (°)	Height (m)	Upper bench width (m)	Comment
1	P3		Tension crack	82	178			
		Current slope	Slope bench	55	178	30	50	The joints are located in the uppermost bench so the analysis of the wedge up to the surface is performed within the geometry of the bench.
		Slope - final back wall	Slope bench	70	178	43	50	
2	P17		Tension crack	74	192			
		Current slope	Slope bench	74	192	21	14	
			Slope up to the top of the quarry	61	192	52	50	
		Slope - final back wall	Slope bench	74	206	35	14	
Slope up to the top of the quarry	53		206	66	50			
3	P7		Tension crack	86	182			
		Slope - final back wall	Slope bench	51	172	19	50	The bench top is the surface at the top of the quarry
			Slope up to the top of the quarry	51	172	30	50	The current wall have the same dip and dip direction as the final back wall
4	Area wedge 4		Tension crack	75	211			The foliation is not available for measurements. Use the measurements by P18 for reference (location of P18 is given figure 3.2).
		Slope - final back wall	Slope bench	73	208	30	13	Can't be sure where the wedge starts.
			Slope up to the top of the quarry	57	208	110	50	The whole wedge is not exposed in the current back wall so the wedge is only analysed for the final back wall.

Table 5.6: Input parameters used to define the geometry of the slope and the bench where the wedges are located.

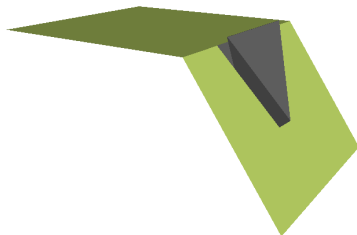
5.2.2 Stability of wedges in the current back wall

The calculated factor of safety and figures of the identified wedges in the current back wall are displayed for each wedge below. The factor of safety and the stability of the current back wall is shortly evaluated at the end of the section. Sections of the wedges are shown in figure F.5, F.6, and F.7 in appendix F.

Wedge 1

Boundary of the wedge	Factor of safety		Comment
	Without water pressure	With water pressure	
Foliation	Infinitely stable	2.4	
Bench width	Infinitely stable	Infinitely stable	
To the top of the quarry - without tension crack	No wedge formed	-	

Table 5.7: The factor of safety for the wedges that can be formed from the two joints in consideration in wedge 1 within the geometry of the current back wall.



(a) Figure of the wedge formed when the tension crack is defined by the closest foliation joint.



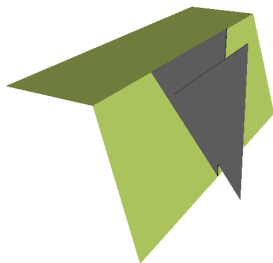
(b) Figure of the wedge formed when the tension crack is defined by the foliation located at the innermost part of the bench.

Figure 5.1: Figures of the identified wedges in the current back wall formed by the discontinuities in wedge 1. The figures are constructed by Swedge.

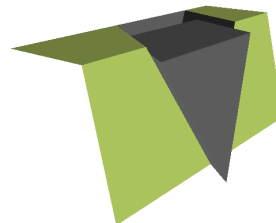
Wedge 2

Boundary of the wedge	Factor of safety		Comment
	Without water pressure	With water pressure	
Foliation	6	0.11	
Bench width	6	3.2	
Up to surface	5.5	3.7	
To the top of the quarry - without tension crack	No wedge formed	-	The wedge formed in Swedge is smaller than the wedge that can be defined by the discontinuities.

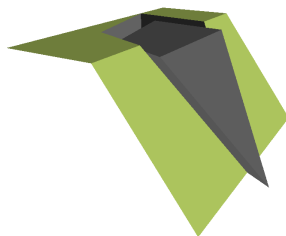
Table 5.8: The factor of safety for the wedges that can be formed from the two joints in consideration in wedge 2 within the current slope geometry.



(a) Figure of the wedge formed when the tension crack is defined by the closest foliation joint.



(b) Figure of the wedge formed when the tension crack is defined by the foliation located at the innermost part of the bench.



(c) Figure of the wedge formed when the discontinuities extend up to the top of the quarry and there is no tension crack.

Figure 5.2: Figures of the identified wedges in the current back wall formed by the discontinuities in wedge 2. The figures are constructed by Swedge Rocscience Inc (2019c).

Wedge 3

Boundary of the wedge	Factor of safety		Comment
	Without water pressure	With water pressure	
Foliation	-	-	The wedge formed in Swedge is smaller than the wedge that can be defined by the joints.
Bench width	Infinitely stable	17.3	
To the top of the quarry - without tension crack	No wedge formed	-	

Table 5.9: The factor of safety for the wedges that can be formed from the two joints in consideration in wedge 3 within the geometry of the current back wall.

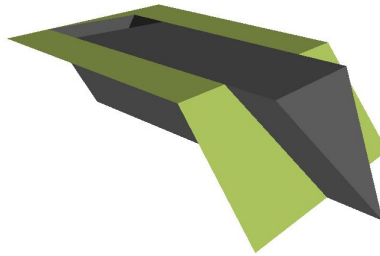


Figure 5.3: Figure of the wedge formed when the tension crack is defined by a foliation crack and bench width. The wedge is located in the uppermost bench, and the bench top is the surface at the top of the quarry. The figures are constructed by the software Swedge.

For dry conditions the calculated factor of safety for the wedge is so high that there is no risk of a wedge failure, if the input parameters are considered to be correct. When water pressure is included in the model, the factor of safety for wedge 2 indicate high instability for the wedge limited by the closest foliation. The other wedges continues to have a factor of safety above 2.

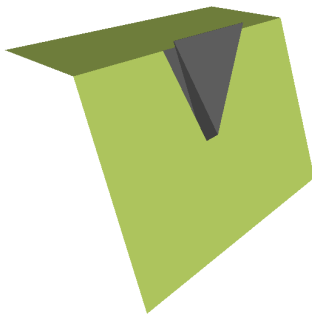
5.2.3 Stability of wedges in the final back wall

The calculated factor of safety and figures of the identified wedges in the final back wall are displayed for each wedge below. A short evaluation of the stability of the wedges in the final back wall are made at the end of the section. Sections of the wedges are shown in figure F.8, F.9, F.10, and F.11 appendix F.

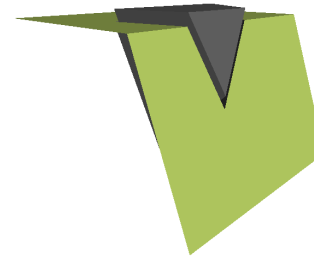
Wedge 1

Boundary of the wedge	Factor of safety		Comment
	Without water pressure	With water pressure	
Foliation	Infinitely stable	15.5	
Bench width	Infinitely stable	Infinitely stable	The wedge formed in Swedge is smaller than the wedge that can be defined by the joints.
To the top of the quarry - without tension crack	No wedge formed	-	To the wedge formed in swedge is smaller than wedge that can be defined by joints.

Table 5.10: The factor of safety for the wedges that can be formed from the two discontinuities in consideration in wedge 1 within the geometry of the final back wall.



(a) Figure of the wedge formed when the tension crack is defined by the closest foliation joint.



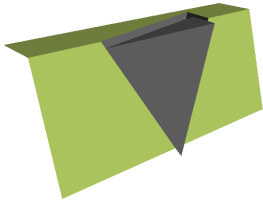
(b) Figure of the wedge formed when the tension crack is defined by the foliation located at the innermost part of the bench.

Figure 5.4: Figures of the identified wedges in the final back wall formed by the discontinuities in wedge 1. The figures are constructed by the software Swedge.

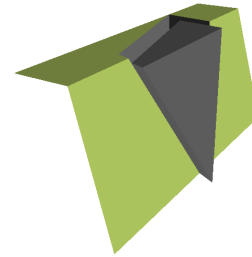
Wedge 2

Boundary of the wedge	Factor of safety		Comment
	Without water pressure	With water pressure	
Foliation	5.7	0.67	
Bench width	5.7	1.28	
To the top of the quarry	5.4	3.0	
To the top of the quarry - without tension crack	No wedge formed	-	The wedge formed in Swedge is smaller than the wedge that can be defined by the joints.

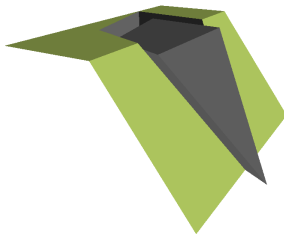
Table 5.11: The factor of safety for the wedges that can be formed from the two discontinuities in consideration in wedge 2 within the geometry of the final back wall.



(a) Figure of the wedge formed when the tension crack is defined by the closest foliation joint.



(b) Figure of the wedge formed when the tension crack is defined by the foliation located at the innermost part of the bench.



(c) Figure of the wedge formed when the discontinuities extend up to the top of the quarry and there is no tension crack.

Figure 5.5: Figures of the identified wedges in the final back wall formed by the discontinuities in wedge 2. The figures are constructed by the software Swedge Rocscience Inc (2019c).

Wedge 3

Boundary of the wedge	Factor of safety		Comment
	Without water pressure	With water pressure	
Foliation	-	-	The wedge formed in Swedge is smaller than the wedge that can be defined by the joints.
Bench width	Infinitely stable	15.1	
To the top of the quarry - without tension crack	No wedge formed	-	

Table 5.12: The factor of safety for the wedges that can be formed from the two joints in consideration in wedge 3 within the geometry of the final back wall.

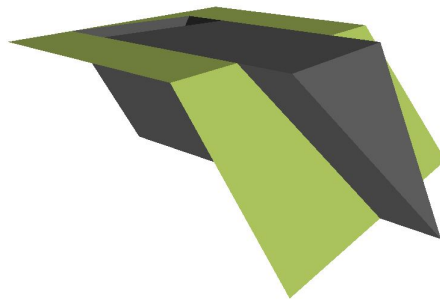
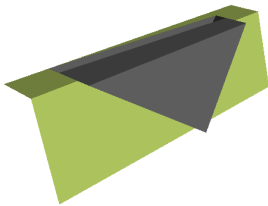


Figure 5.6: Figure of the wedge formed when the tension crack is defined by a foliation crack and bench width. The wedge is located in the uppermost bench, and the bench top is the surface at the top of the quarry. The figures are constructed by the software Swedge.

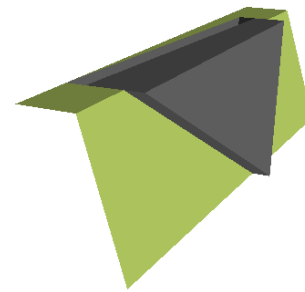
Wedge 4

Boundary of the wedge	Factor of safety		Comment
	Without water pressure	With water pressure	
Foliation	-	-	The wedge formed in Swedge is smaller than the wedge that can be defined by the joints.
Bench width	Infinitely stable	2.4	
Up to surface	Infinitely stable	2.8	
To the top of the quarry - without tension crack	No wedge formed	-	

Table 5.13: The factor of safety for the of wedges that can be formed from the two discontinuities in consideration in wedge 4 within the geometry of the final back wall.



(a) Figure of the wedge formed when the tension crack is defined by the foliation located at the innermost part of the bench at the bottom of the wedge.



(b) Figure of the wedge formed when the discontinuities extend up to the top of the quarry and the foliation crack is located 50m from the crest of the wall.

Figure 5.7: Figures of the identified wedges in the final back wall formed by the discontinuities in wedge 4. The figures are constructed by the software Swedge Rocscience Inc (2019c).

When the rock mass is dry, the wedges formed by the discontinuities in the final back wall will be stable. High water pressure in the discontinuities of wedge 2 lower the factor of safety to below 1.3 for the wedges formed within the geometry of the bench. This indicates that a wedge failure must be expected for completely water filled joints.

5.3 Numerical stability analysis of the current back wall

5.3.1 Calibration

Five rounds of analysis were performed to calibrate the serpentinized surface. Table 5.14 shows the strength values used in each round. The values in Round 1 represent the start input parameters. The numerical model used to perform the analysis is shown in figure G.1 and G.2 in appendix G.

Round No.	JRC	JCS (MPa)	ϕ_b (°)
1	5	47	23
2	5	47	16
3	10	47	23
4	10	67	23
5	10	100	35

Table 5.14: The parameters used in each round 1-5 to calibrate the joint strength of the serpentinized surface.

The shear displacement along the serpentinized surface in consideration was plotted for each round to find the strength values that would cause plane failure. The plots are displayed in figure 5.10. The stability of the wall was also considered by evaluating the location and magnitude of the maximum shear strain in the wall, see figure 5.8. Negative shear displacement in the graph defines that the couple shear forces along the joint give a clockwise rotation to an element. The left side of the joint is sliding down.

The shear strain in the numerical can often indicate the location of failure (Rocscience, n.d.h). The distribution of maximum shear strain in the failure area in round 1 shows that the largest shear strain is located on each side of the area with serpentinized surfaces. Since the maximum shear strain is located outside the failure area, the strain was only investigated in round 1. The calibration process was analysed with focus on displacement along the failure surface.

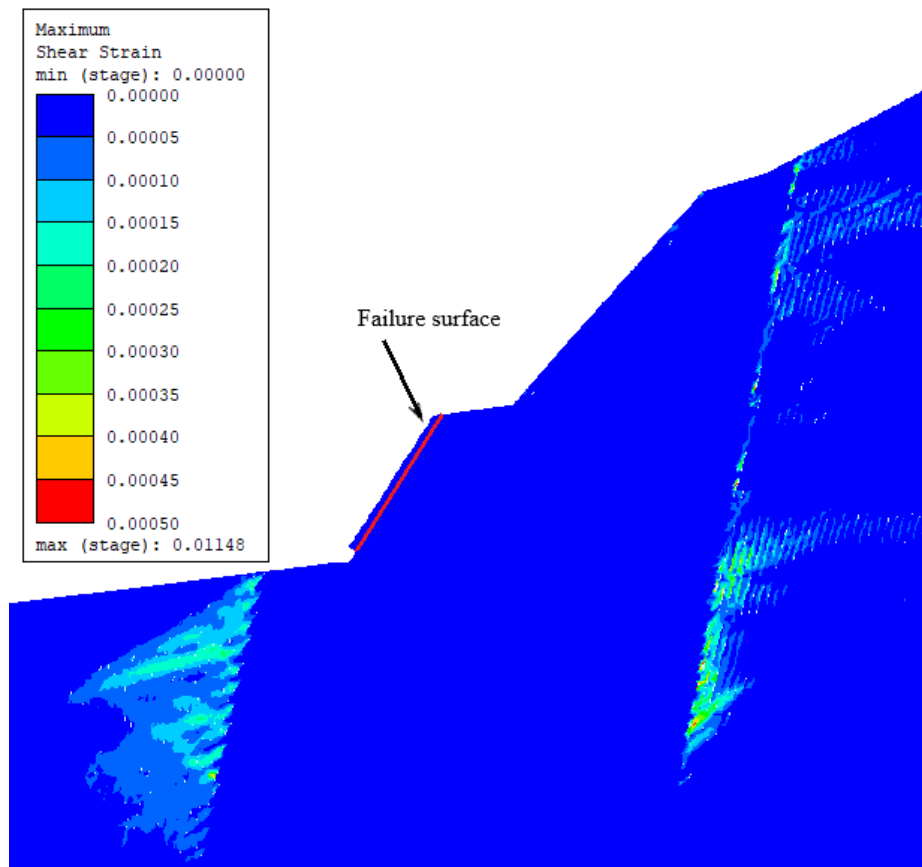


Figure 5.8: The figure show the distribution of maximum shear strain in the back wall with the input parameters defined in Round 1 during calibration. The location of the failure surface in the numerical model is marked with a red line.

The plots show that the displacement is below 0.3mm with movement in both downward and upward direction along this joint surface. The graph also show that the displacement is almost equal for the different strength values. This can indicate that the analysis is not able to display a relationship between the defined strength of the surface and displacement along the surface for a single block. The calibration of the rock failure by the numerical method used in this project, go beyond the limitations of the continuum finite element modelling. Continuum modelling won't consider the failure of only one block, but the deformation of the rock mass as a whole (Hammah et al., 2008). It was therefore evaluated to be impossible to make a reliable evaluation of the strength of the serpentinized surface by calibration with the numerical model.

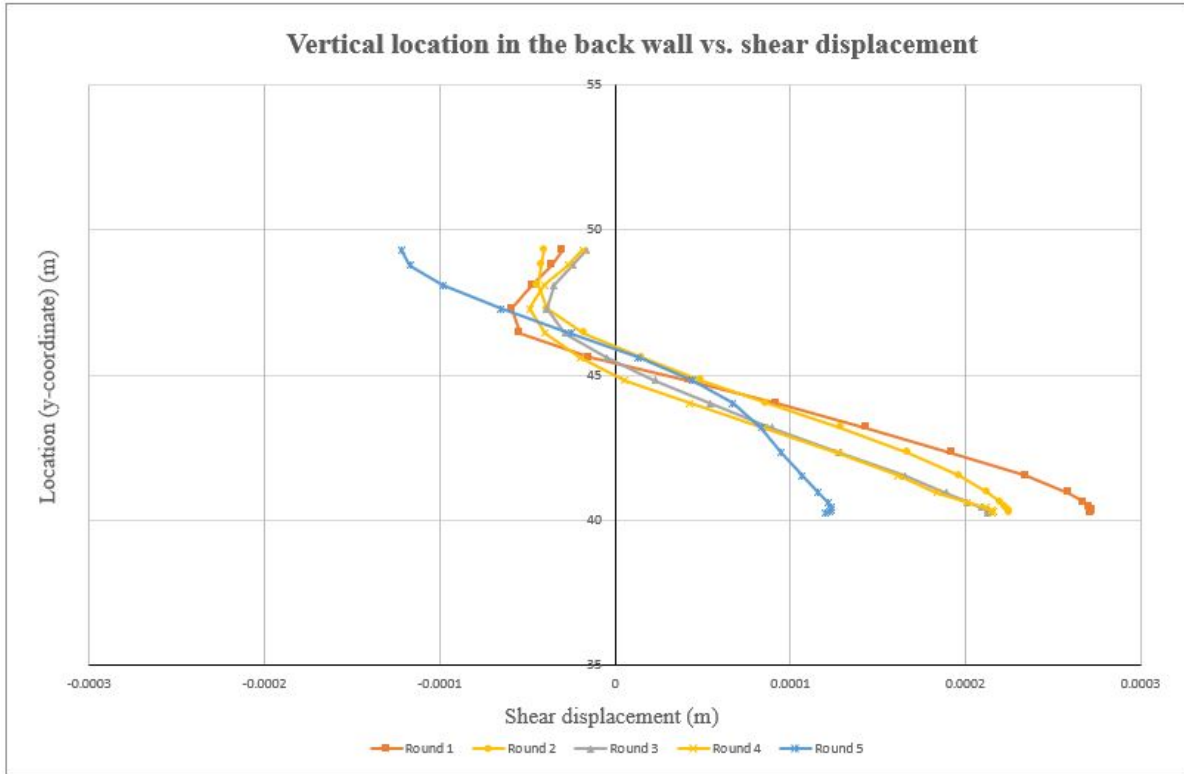


Figure 5.9: The graph displays the shear displacement along the failure surface, for the different joint strength parameters defined in Round 1-5. Negative shear displacement in the graph defines that the couple shear forces along the joint give a clockwise rotation to an element. The left side of the joint is in sliding down.

Calibration of the serpentinized surface can also be performed by back calculation, as described in section 4.5. To perform the back calculation, the value of σ_n must be calculated. The block used to represent the rock failure in figure 4.20 was given the following input parameters: $l = 2\text{m}$, $w = 1\text{m}$, $h = 0.5\text{m}$, density = 2870 kg/m^3 (equal to the density of serpentinized dunite 1), and the gravitational acceleration, $g = 9.81 \text{ m/s}^2$. The value of σ_n is then given by equation 5.1.

$$\sigma_n = \frac{2 \cdot 1 \cdot 0.5 \cdot 2870 \cdot 9.81 \cdot \cos(\alpha)}{2 \cdot 0.5} = 14.08 \text{ kPa} \quad (5.1)$$

The value of JCS of the surface was measured in the field to have the magnitude of a whole number of Mega Pascal. This means that the calculated value of σ_n is at least 0.001JCS. The Barton-Bandis failure criterion is applicable for $\sigma_n = 1-0.1\text{JCS}$ (Li, 2018). The criterion was therefore considered to be unsuitable for back calculation of the strength of the failure surface.

Outside the field of application for the Barton-Bandis criterion, Coulomb's law can be used to find the apparent friction angle ϕ of the surface when the shear stress and the normal stress along the surface is known. The shear stress along the surface can be expressed using equation 4.11 in section 4.5.4. This results in equation 5.2:

$$\frac{W \sin \alpha}{L \cdot W} = \frac{W \cos \alpha}{L \cdot W} \tan(\phi) \quad (5.2)$$

By rearranging the equation, the apparent friction angle can be expressed by equation 5.3:

$$\tan(\alpha) = \tan(\phi) \quad (5.3)$$

The equation expresses that the apparent friction angle would be equal to the rock slope angle α , also if the angle of the rock slope change. This can not be the case, and indicates that there is cohesion on the surface. The cohesion is the factor that keeps most of the blocks from sliding. The cohesion of separated joints is 0 (Barton, 2012). If the joints have cohesion, it means that the joints are not entirely separated. Weathering of the cohesion can reduce the cohesive force and cause the blocks to slide.

5.3.2 The general stability of the current wall along section S3

The location of the maximum strain in the model can indicate where a failure can occur in the model (Rocscience, n.d.h). The distribution of maximum strain shown in 5.8 does not indicate a failure area for the given input parameters in the back wall. The stability of the current wall can also be considered by looking at the locations of the total displacement in the numerical model.

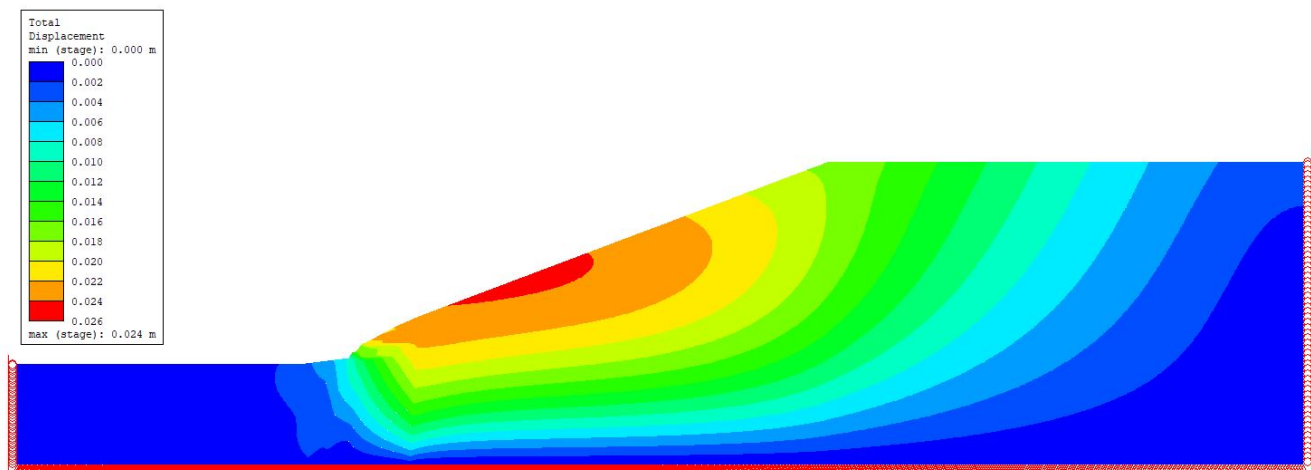


Figure 5.10: The figure show the location and the magnitude of the largest displacements in the wall with the input parameters from round 1.

The largest displacements are located in the hill above the quarry. The hill above the quarry is modelled with a highly simplified geometry, and a reliable detailed analysis of the hill slope can not be performed with the model. The displacement model also shows that there is displacement of about 0.02m in the back

wall. The model converged during computation and is therefore considered stable by the calculations in RS2 (see section 4.3 for explanation of computation and convergence of model). This means that there might be small movements in the rock mass, before the rock mass stabilises again. The quarry is little developed along section S3, and the risk of failure along the section is related to local failures, like the plane failures observed in area section 1.

5.4 Stability analysis of the current back wall along section S2

Results from the numerical modelling of the current back wall along section S2 using method 1 and 2 are presented and evaluated in the sections below.

5.4.1 Stability analysis of section S2 using analysing method 1

Analysing method 1 calculated the factor of safety given in table 5.15 for the current back wall along section S2.

Section	CSRF
S2: Current back wall	5.62

Table 5.15: The critical strength reduction factor (CSRF) for the analysis of the stability of the current back wall along section 2 using method 1.

The high factor of safety indicates that if the model of the rock mass without joints is representative for the conditions in the back wall, the wall has a high degree of stability. This will also be the case if the input parameters for the rock mass strength are inaccurate. Due to uncertainty related to the reliability of the input parameters, the stability of the section was analysed by looking at the change in displacements in the rock mass as the rock mass strength is reduced by an increased SRF. Figure 5.11 show the size of the maximum displacement with different SRF.

The graph shows that the displacements in the rock mass are about 5cm before the rock mass stabilises again. When the rock mass strength is reduced by CSRF, there is an abrupt change in the size of the displacement. The displacements in the rock mass were also examined at different points in the back wall to investigate if the rock mass in different parts of the wall behave differently when the shear strength is reduced. Figure 5.13 shows the displacement at eight different points in the rock mass as the SRF increases. The locations of the points in the rock mass are indicated in figure 5.15. The points investigated were chosen to represent different types of rock mass and areas in the wall with various stress conditions. Point 1-4 where chosen to represent the conditions at the bottom of the wall. Point 5 is located higher up in the the wall in rock mass typical for area section 2. Point 6 and 7 represent the

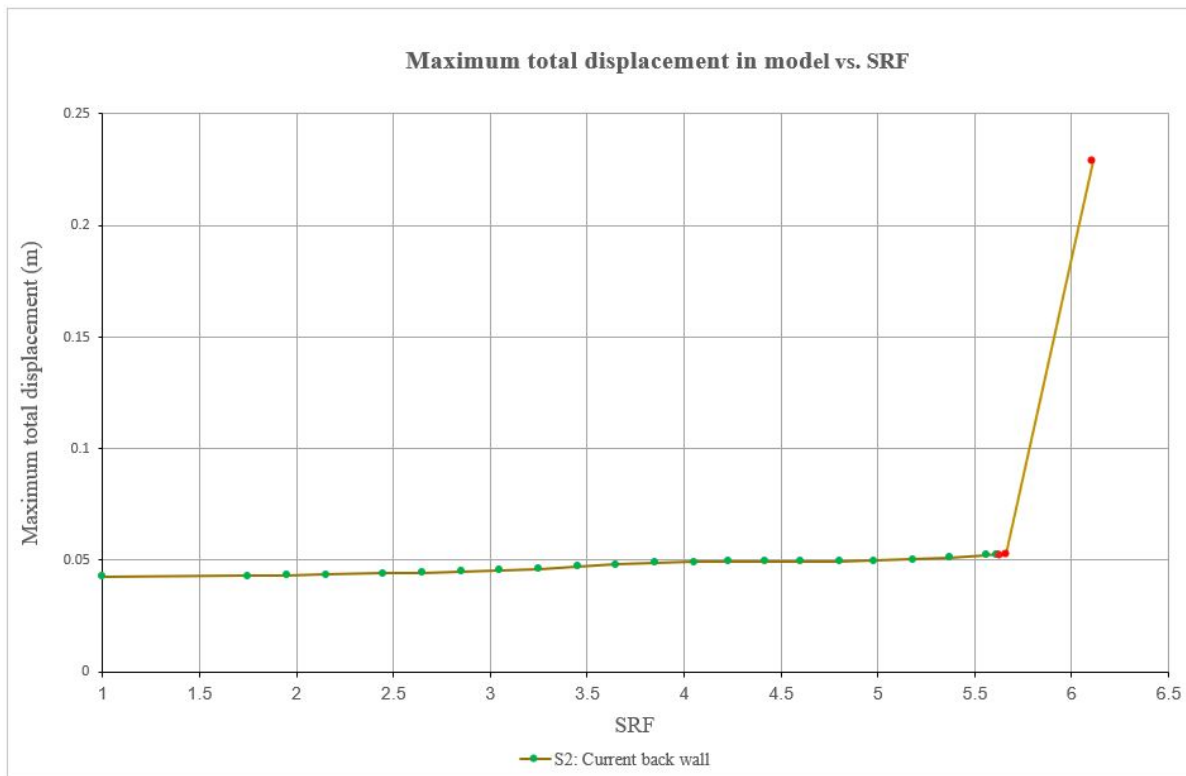


Figure 5.11: Graph showing the maximum displacement in the back wall for increasing strength reduction factors (SRF). Green points indicate SRF where the model is stable. The red points indicate SRF where the model has become unstable. The critical SRF (CSRF) is indicated by the first red point along the graph in the model.

displacements in rock mass typical for area section 1 in areas with differencing stress conditions. Point 8 is located at the contact zone by the gneiss boundary.

The curves show that the behaviour of the rock mass is similar in the different parts of the wall until the strength is reduced with a value past CSRF and the wall becomes unstable. The rock mass in the upper part of the back wall shows large and abrupt deformations, while the displacements at the bottom remain low. Even though the maximum displacements given in figure 5.11 after CSRF are small, the model does not converge for this SRF, which means that the wall is unstable, and a larger failure will occur. Figure 5.14 shows the contours of maximum strain when SRF equals 6.11. The contours indicate that the wall will fail by a global rotational failure induced by failure at the bottom of the slope. The contact zone along the gneiss boundary, will form the back of the failure area. When the failure occur, the wall will slide down, resulting in the largest displacements at the top of the wall. The analysis indicates that the weakness zone by Z1-Z5 have little influence on the stability of the current back wall. Even though method 1 gives a high factor of safety to the wall, the model does not include the risk of failures along the foliation and other discontinuities. This type of failure is evaluated by using analysis method 2 and by analysing wedges. The numerical model used for the analysis with method 1 is shown in figure G.4 and G.5 in appendix G.

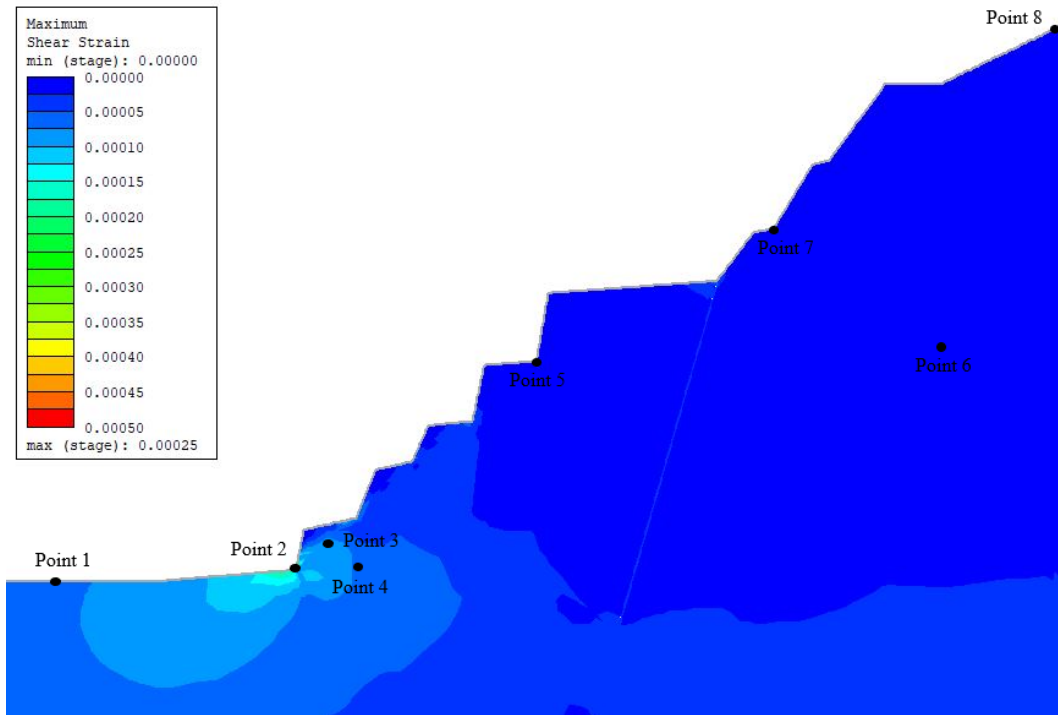


Figure 5.12: The figure indicates the points used to examine the deformation of the rock mass at different places in the back wall. The figure also shows the distribution of shear strain in the back wall when SRF equals 1.

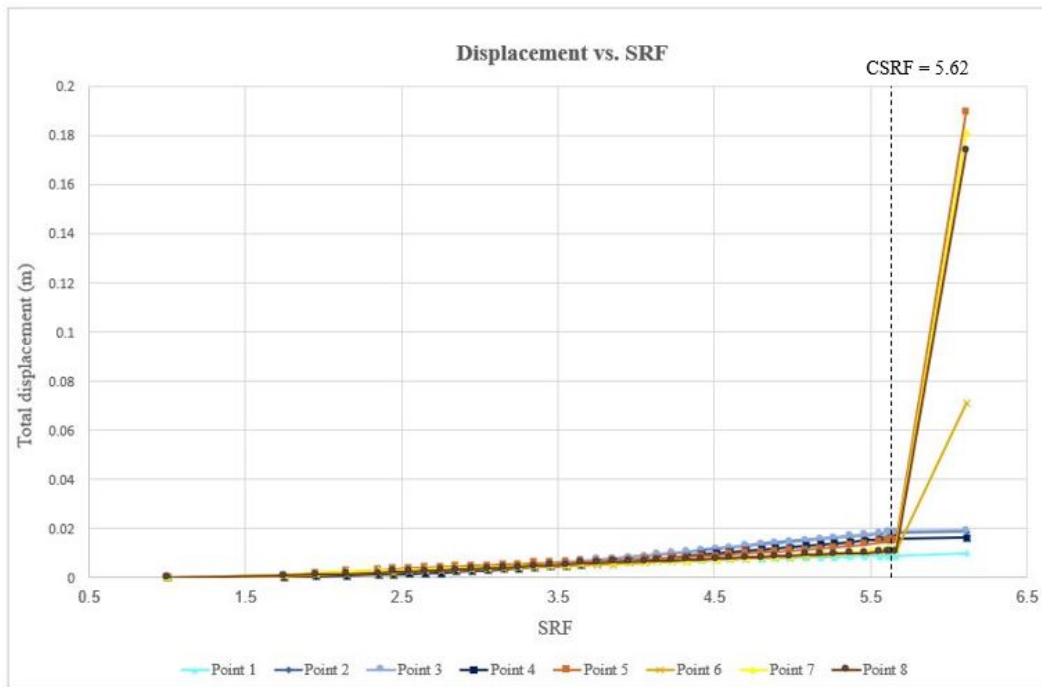


Figure 5.13: Graph showing the displacement for increasing SRF at different places in the rock mass in the back wall. Blue curves are used for points located in rock mass typical for area section 2. Brown and yellow curves are used for points located in rock mass typical for area section 1.

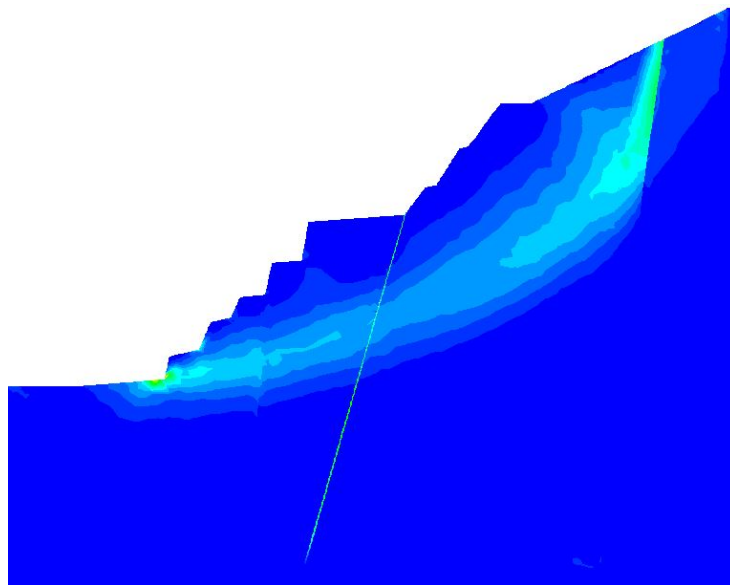


Figure 5.14: The distribution of maximum shear strain in the current back wall along section S2 when SRF equals 6.11. The colours show different values of shear strain and indicate the location of the failure when the wall becomes unstable.

5.4.2 Stability analysis of section S2 using method 2

The models were analysed by looking at shear displacement along joints, as done for calibration analysis in section 5.3.1. Shear displacement was plotted against location in the back wall (given by the y-coordinate in the model), see figure 5.16. The locations of the examined joints are shown in figure 5.15 along with the maximum shear strain in the model. Three joints were chosen to investigate the deformation along the three different types of joint surfaces present in the wall along section S2. The joints are plotted for different locations since the joints stop at boundary contacts.

Figure 5.15 displays that the shear strain in the model is located at the bottom of the wall with the same magnitude as in the analysis from method 1. At the same time is the analysis including the joints showing more shear strain in the lower bench. The graph of shear displacement shows that the displacements along the joints are smaller than 0.7mm for the three analysed joints. The displacements along the serpentinized surface in section S2 are of the same size as the movement along the other joints with higher surface strength. This can indicate that there is little room for movements in the rock mass. The similar movement can also be due to that the defined strength for the serpentinized surface is too high for any movement to occur. The largest displacements are located at the height of the second lowest bench.

The numerical model used for the analysis using method 2 is shown in figure G.4 and G.5 in appendix G.

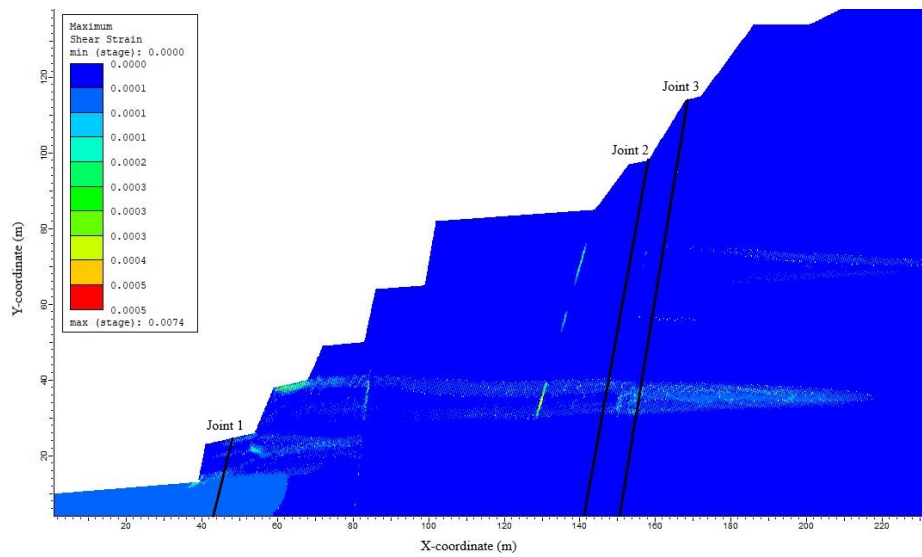


Figure 5.15: The figure indicate the joints where shear displacement was analysed in the current back wall in section S2.

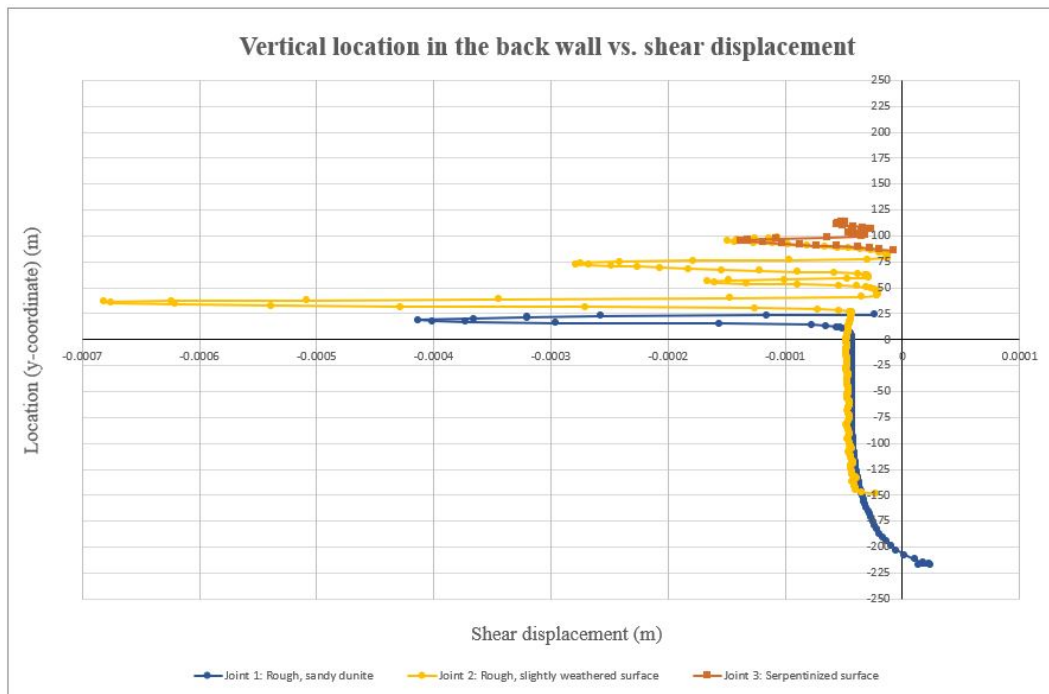


Figure 5.16: The graph displays the shear displacement along three joints with different surface types in the current back wall in section S2.

5.5 Stability analysis of the final back wall

The two next sections present results and evaluations of the analysis by numerical modelling of the final back wall.

5.5.1 Stability analysis using method 1

Calculated CSRFB for the analysed sections S1-S4 in the final back wall are given in table 5.16.

Section	CSRFB
S1: Final back wall	4.08
S2: Final back wall	3.31
S3: Final back wall	2.97
S4: Final back wall	4.06

Table 5.16: The critical strength reduction factor (CSRFB) for each of the sections in the final back wall.

The CSRFB shows that the final back wall along all the analysed sections is stable when the structure of the foliation is not considered in the model. The sections on each sides of the quarry have the highest stability. In figure 5.17, the maximum displacement in the rock mass for the four different section is plotted against SRF.

The plots show that for rock mass strength of SRF lower than CSRFB, the deformations in the rock mass is about 5 cm in the final back wall. When the rock mass is reduced above the CSRFB, the displacements in the wall will vary. The graph show that the most abrupt and largest displacements are found along section S1 and S2. The character of the deformations in the rock mass was investigated by looking at the displacement at different points in the wall as the rock mass strength is reduced. The resulting graph for the points is shown for each section S1, S2, S3 and S4 below. The figures of the locations of the point also show the distribution of shear strain in the model when SRF is equal to 1. Figure 5.26 shows the distribution of maximum shear strain in each section for the highest value of SRF used in each analysis.

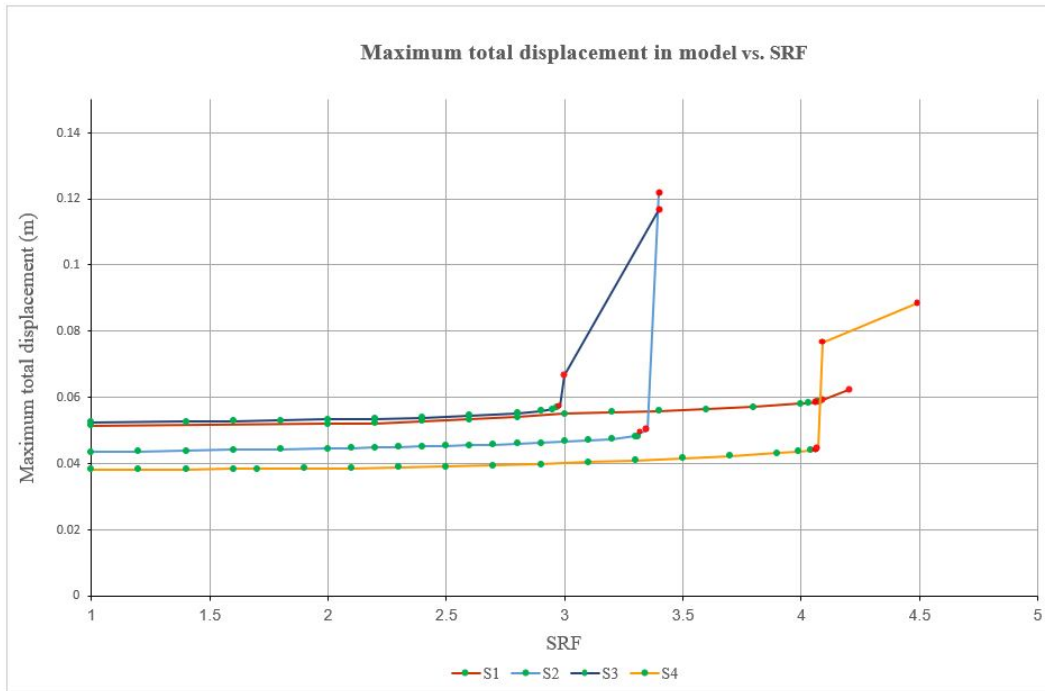


Figure 5.17: Graph showing the maximum displacement in the back wall for increasing strength reduction factors (SRF). Green points indicate SRF where the model is stable. The red points indicate SRF where the model has become unstable. The critical SRF (CSRF) is indicated by the first red point along the graph in the model.

Section S1

The location of the analysed points along section S1 is displayed in figure 5.20. The graph in figure 5.19 shows that there is a gradual increase in the displacements in the entire back wall as the SRF increase. The displacements before the wall becomes unstable are below 2cm for the given points. The displacements are largest in the lowermost bench before and after failure. After failure the most abrupt increase in the displacement is located in the outermost part of the back wall. This indicates that the failure causing instability at CSRF is a shallow failure. This can also be observed in figure 5.26a which shows the distribution of max shear strain in the wall when $SRF = 4.2$ (the highest value of SRF shown in the graph in figure 5.19). The figure shows a concentration of strain in three different areas. Due to the low displacements in the back of the wall, the model is considered to become unstable due to failure along the two uppermost areas with the highest shear strain.

The numerical model used for the analysis of section S1 is shown in figure G.8 and G.9 in appendix G

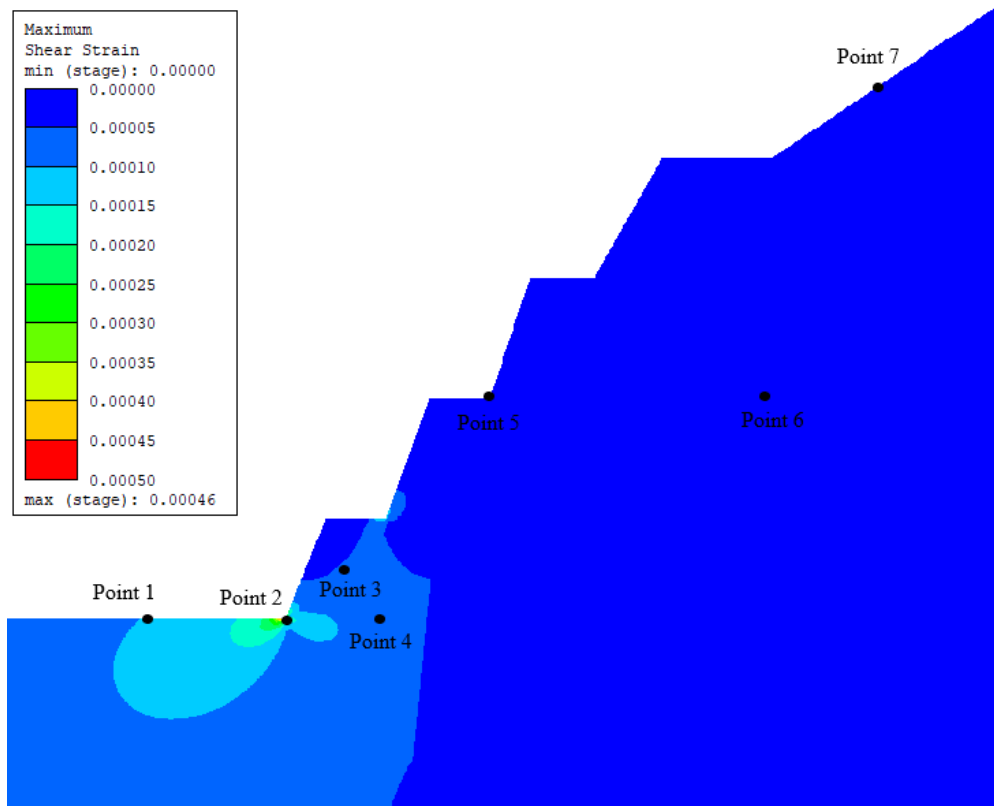


Figure 5.18: The figure indicates the points along section S1 used to examine the deformation of the rock mass at different places in the back wall.

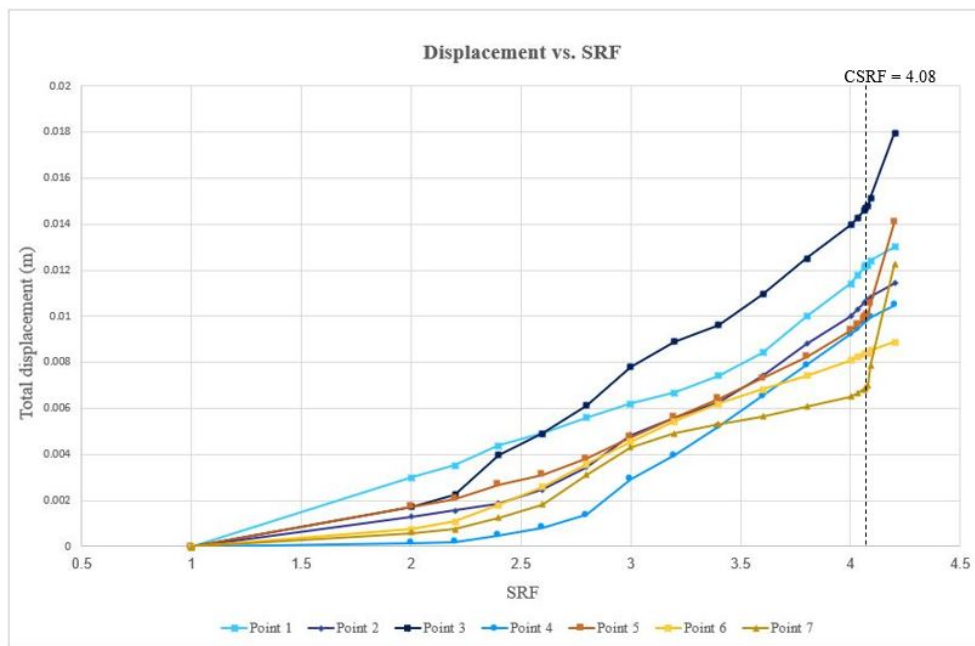


Figure 5.19: Graph showing the maximum displacement for increasing SRF at different places in the rock mass in the back wall. Blue curves are used for points located in rock mass typical for area section 2. Brown and yellow curves are used for points located in rock mass typical for area section 1.

Section S2

The location of the analysed points along section S2 is displayed in figure 5.20. The graph in figure 5.21 shows small displacements in all areas of the back wall before the wall becomes unstable. When the back wall becomes unstable, there is a fast increase in the displacements in the upper parts of the wall. The abrupt change in displacement in point 6 shows that there is more movement at the back of the wall along section S2 than along section S1. There is very little displacement in front of wall and at the toe of the wall. Figure 5.26b indicates the location of the failure surface.

The numerical model used for the analysis of the current back wall along section S2 is shown in figure G.10 and G.11 in appendix G

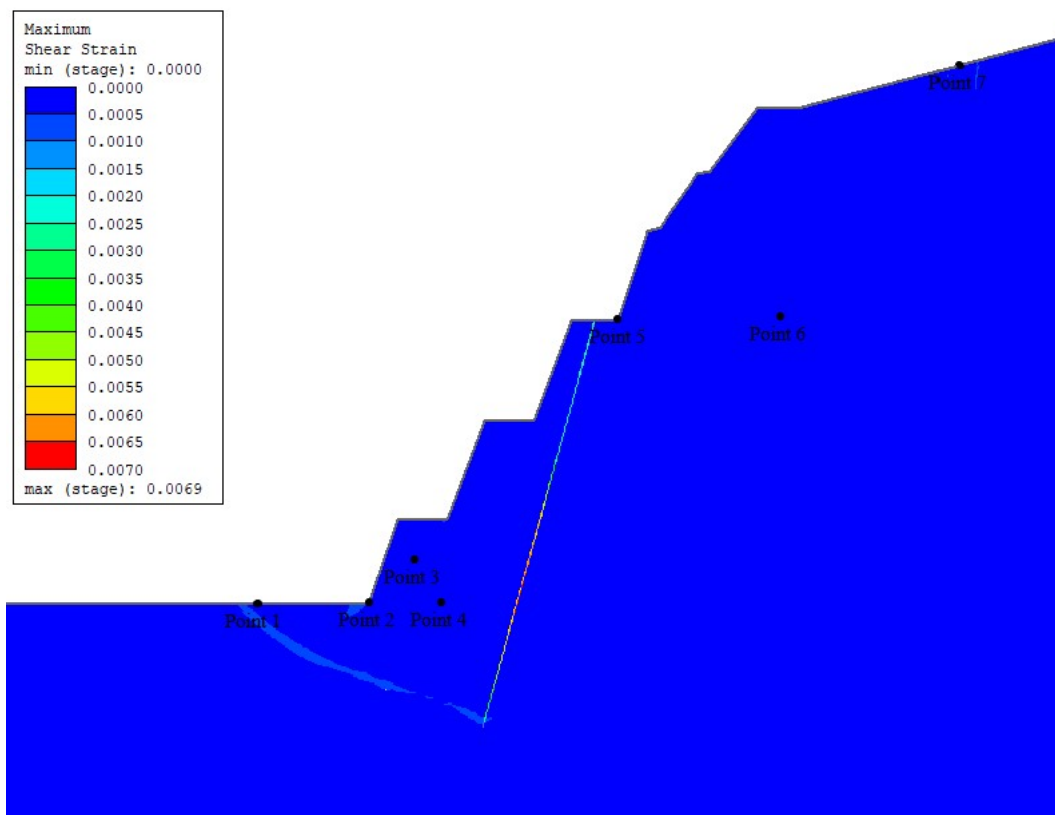


Figure 5.20: The figure indicates the points used to examine the deformation of the rock mass at different places in the back wall.

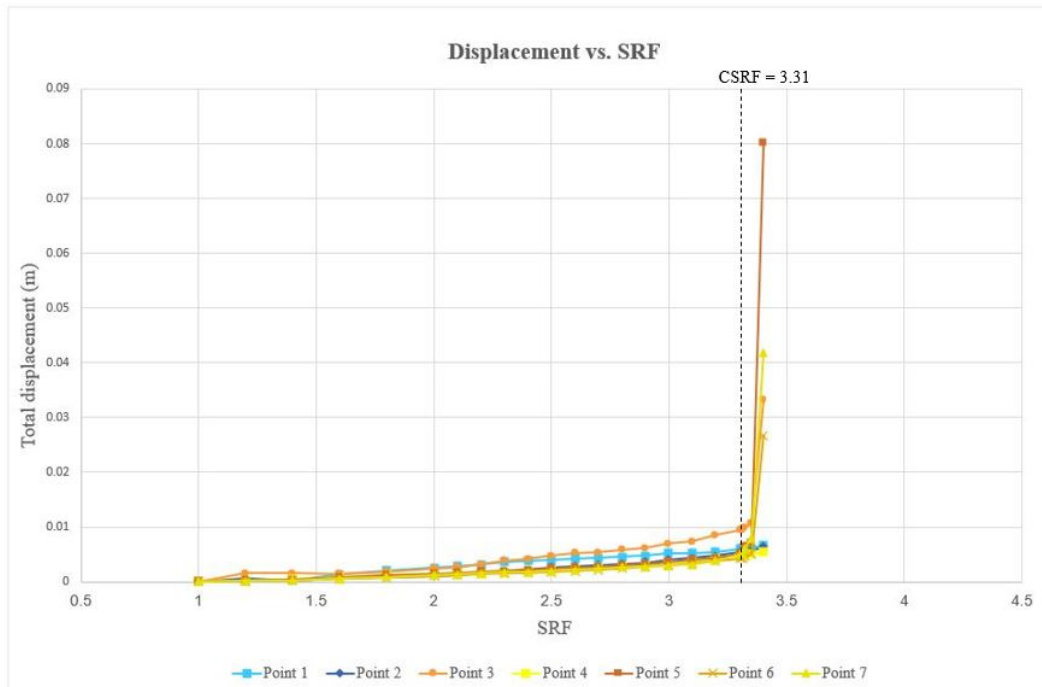


Figure 5.21: Graph showing the maximum displacement for increasing SRF at different places in the back wall. Blue curves are used for points located in rock mass typical for area section 2. Brown and yellow curves are used for points located in rock mass typical for area section 1.

Section S3

The location of the analysed points along section S3 is displayed in figure 5.22. The graph in figure 5.23 shows the same trend in displacements in the back wall before the wall becomes unstable as observed along section S1 and S2 . Figure 5.31 displays a concentration of shear strain in the lowermost bench when $SRF = 1$. The graph of point 3, located in the lowermost bench, shows small displacements without abrupt changes. It can therefore be assumed that a failure would not occur in this area when SRF is low. When $SRF > CSRF$ there is abrupt increase in the displacements from the lowest bench to the top of the wall. The displacements at the bottom of the wall and in front of the wall do not increase. This correlate with the location of the max shear strain shown in figure 5.26c. The figure displays low shear strain in front of the wall.

The numerical model used for the analysis of the current back wall along section S3 is shown in figure G.12 and G.13 in appendix G

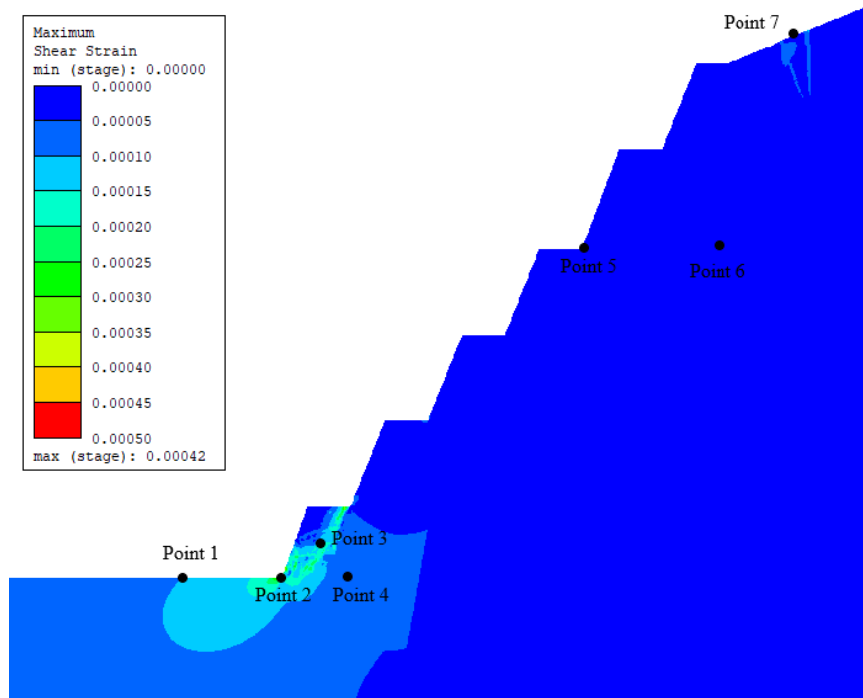


Figure 5.22: The figure indicates the points used to examine the deformation of the rock mass at different places in the back wall.

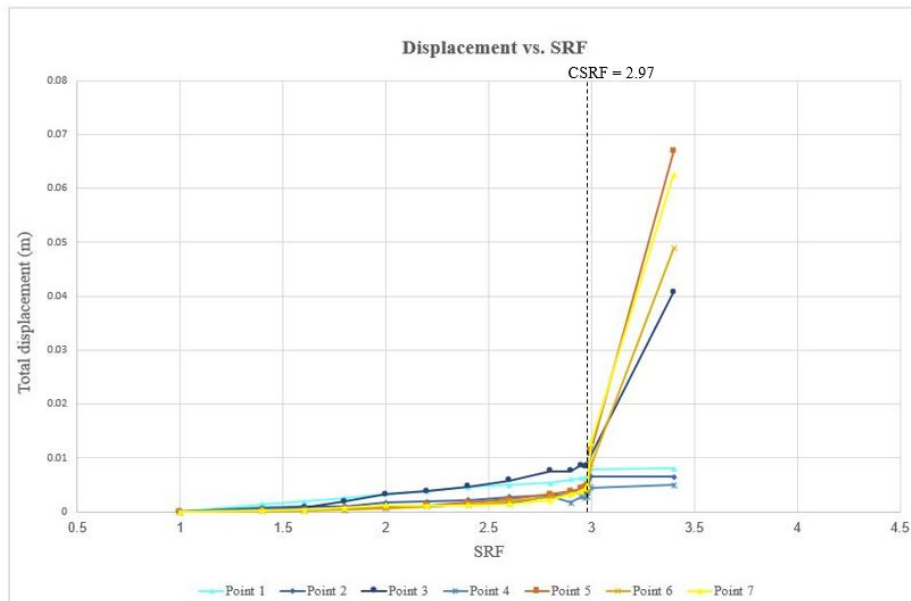


Figure 5.23: Graph showing the maximum displacement for increasing SRF at different places in the rock mass in the back wall. Blue curves are used for points located in rock mass typical for area section 2. Brown and yellow curves are used for points located in rock mass typical for area section 1.

Section S4

The location of the analysed points along section S2 is displayed in figure 5.24. The graph in figure 5.25 show that the curve for point 7 display altering displacements in the front of the wall when SRF is lower than CSRF. The wall stabilises after these deformations. Past CSRF, there is a fast increase in the displacements in the rock mass closest to the surface. The displacements in point 6 show that there is very little movement in the back of the wall. Figure 5.26d indicates that the failure will be deeper at the top of the quarry.

The numerical model used for the analysis of section S4 is shown in figure G.14 and G.15 in appendix G.

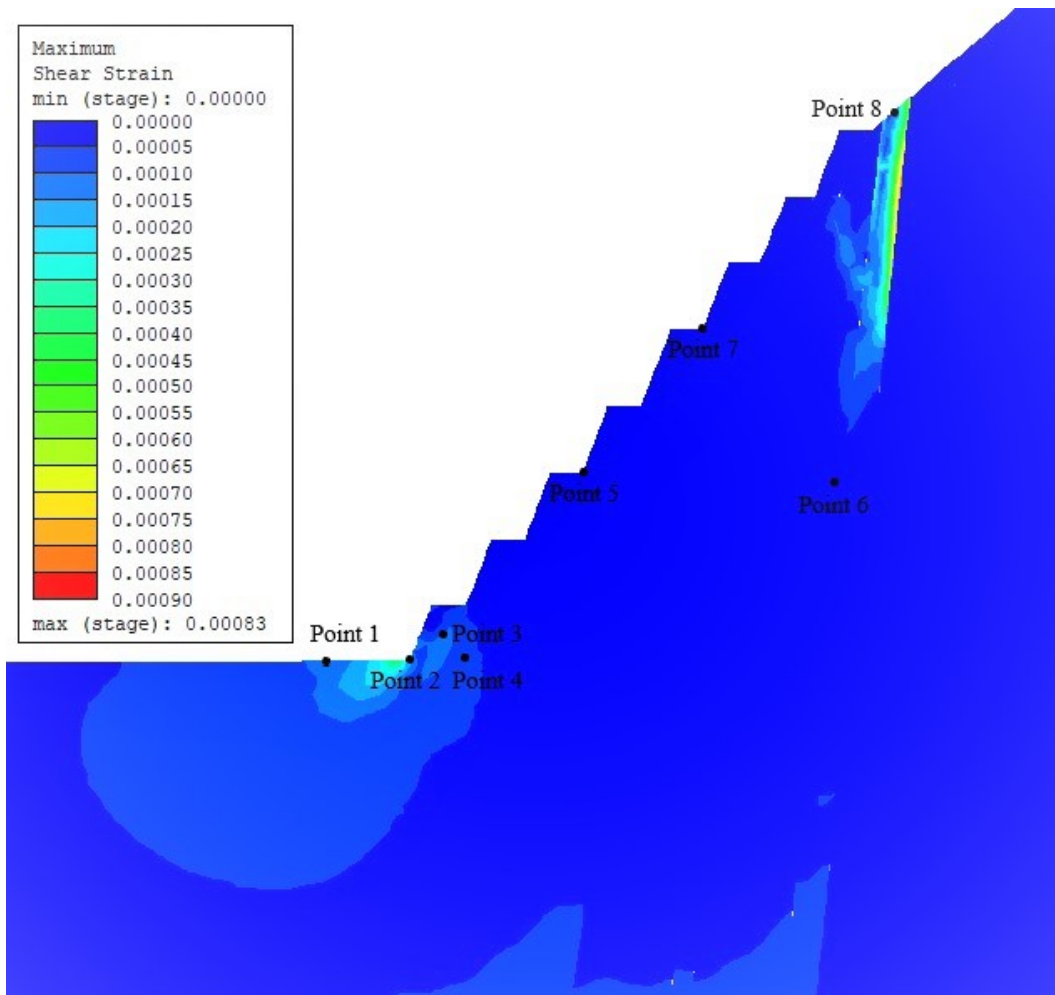


Figure 5.24: The figure indicates the points used to examine the deformation of the rock mass at different places in the back wall.

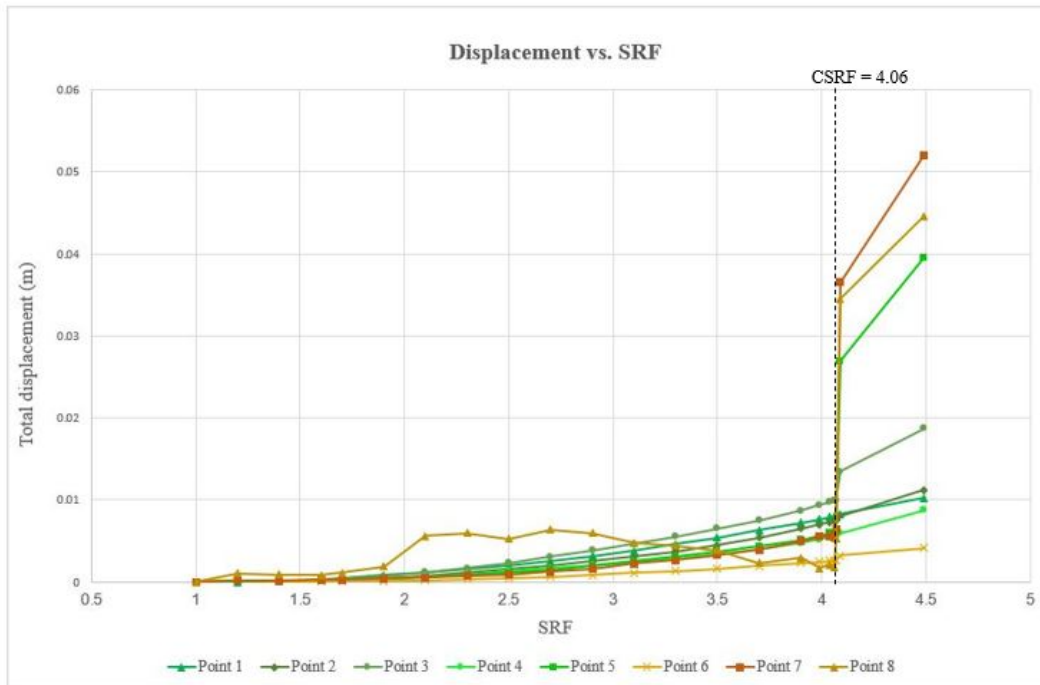
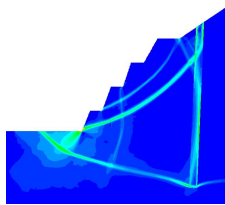
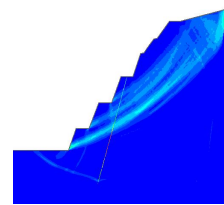


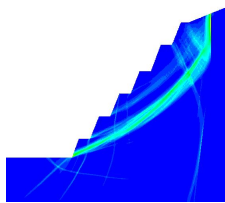
Figure 5.25: Graph showing the maximum displacement for increasing SRF at different places in the rock mass in the back wall. Green curves are used for the points located in rock mass typical for area section 2. Brown and yellow curves are used for the point located in rock mass typical for area section 1.



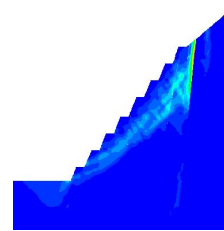
(a) The distribution of the maximal strain along section S1 when SRF = 4.2.



(b) The distribution of the maximal strain along section S1 when SRF = 3.4.



(c) The distribution of the maximal strain along section S1 when SRF = 3.4.



(d) The distribution of the maximal strain along section S1 when SRF = 4.49.

Figure 5.26: The figure shows the contours of maximum strain along the four sections S1, S2, S3, and S4 for the highest SRF values used in the analysis of each section. The colours are used to show the location of the global failure along each section, and the colour of the strain in the different figures should not be compared.

The displacement in the sections is low before the slope suddenly becomes unstable. This indicates that the final back wall will be very stable for much lower rock mass strength than defined in the input parameters, when the movement along joints is not considered. The wall becomes unstable due to a global failure from the bottom of the wall, like observed in the analysis of the current back wall. The analysis indicates that there are no large failures in other places in the back wall before the failure at the bottom occurs. The slope failure has varying depth in the different sections, but along the whole wall, the contact zone by the gneiss boundary will influence the depth of the failure.

5.5.2 Stability analysis using method 2

The numerical analysis of the influence of the foliation on the stability of the final back wall, was performed in the same way as the analysis of the current back wall along section S2. Shear displacement was plotted for joints with the three different surface types along section S1, S2, S3, and S4. The plots and the location of the joints in each section and the distribution of shear strain for $SRF = 1$ are shown in figure 5.27, 5.29, 5.31, and 5.33.

Section S1

The numerical model for the section used in analysing method 2 is displayed in figure G.16 and G.17 in appendix G.

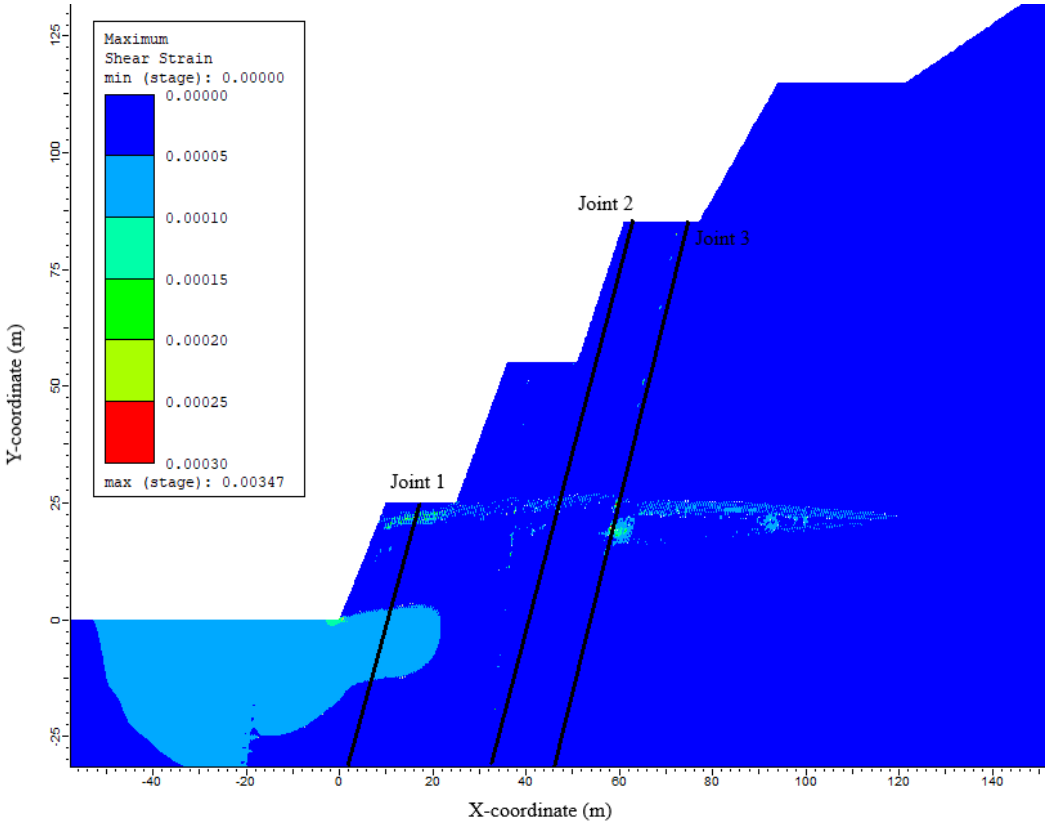


Figure 5.27: The figure indicates the joints used in the analysis of shear displacement. The coordinates are used to show the location of the displacements along the joints given in graph 5.28. The coordinates are defined relative to the location of the bottom of the wall in the numerical model of the section.

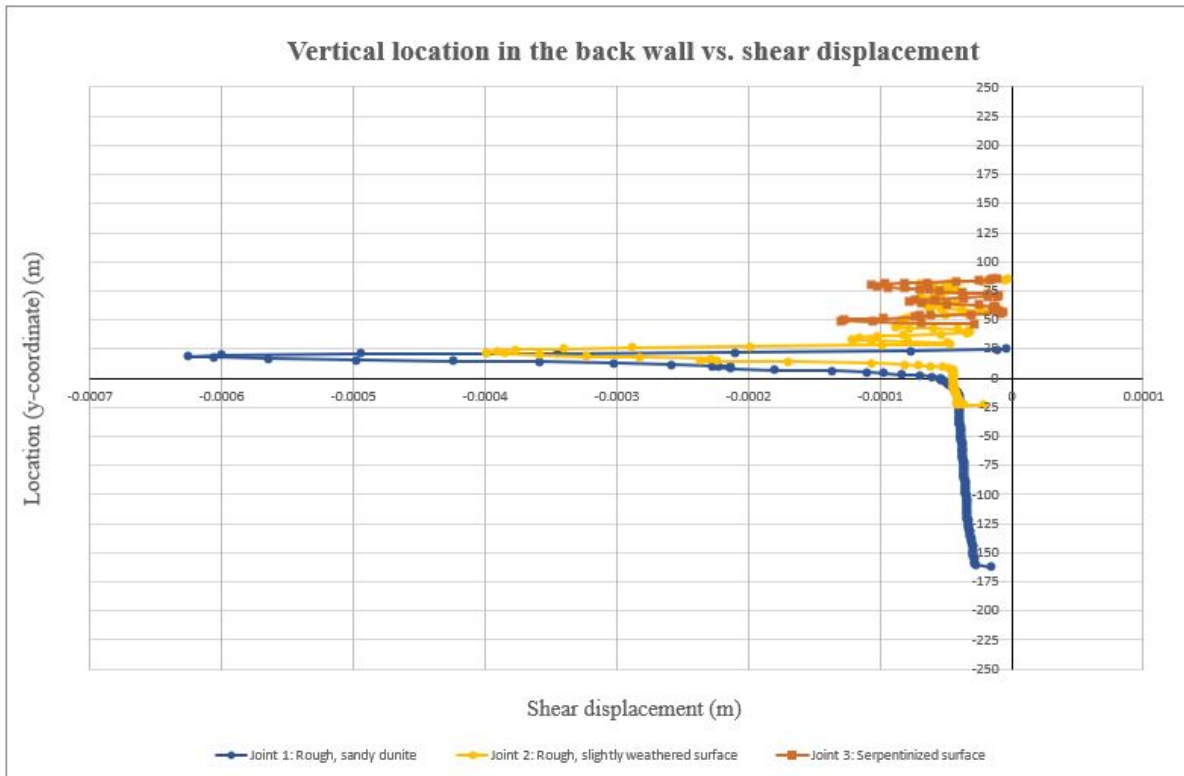


Figure 5.28: The graph displays the shear displacement along three joints with different surface types in the final back wall in section S1. The coordinates give the location of the displacement relative to the bottom of the wall in the numerical model of the section. The location of the joints are shown in figure 5.27.

Section S2

The numerical model for the section used in analysing method 2 is displayed in figure G.18 and G.19 in appendix G.

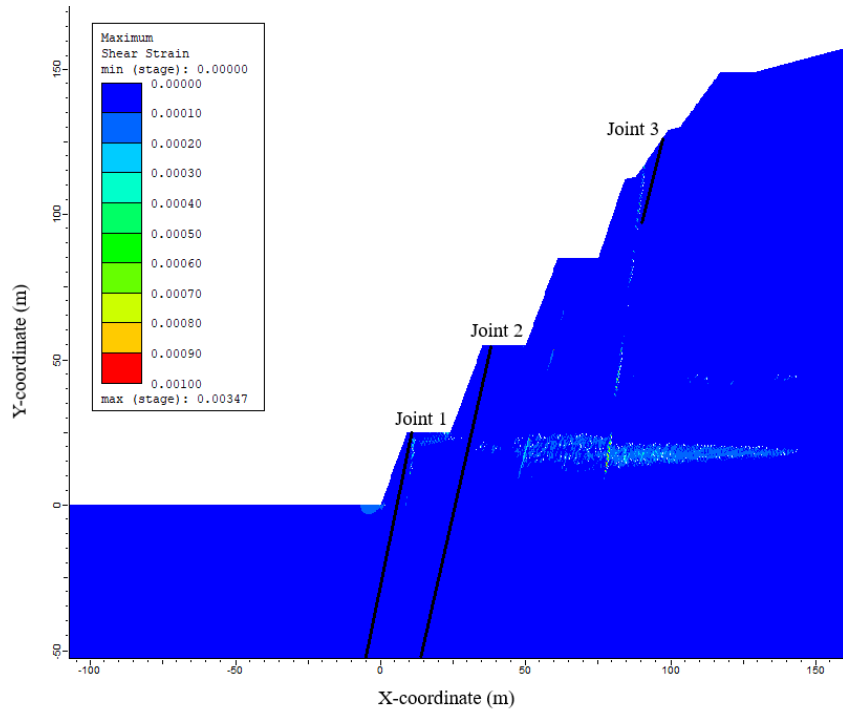


Figure 5.29: The figure indicates the joints used in the analysis of shear displacement. The coordinates are used to show the location of the displacements along the joints given in graph 5.30. The coordinates are defined relative to the location of the bottom of the wall in the numerical model of the section.

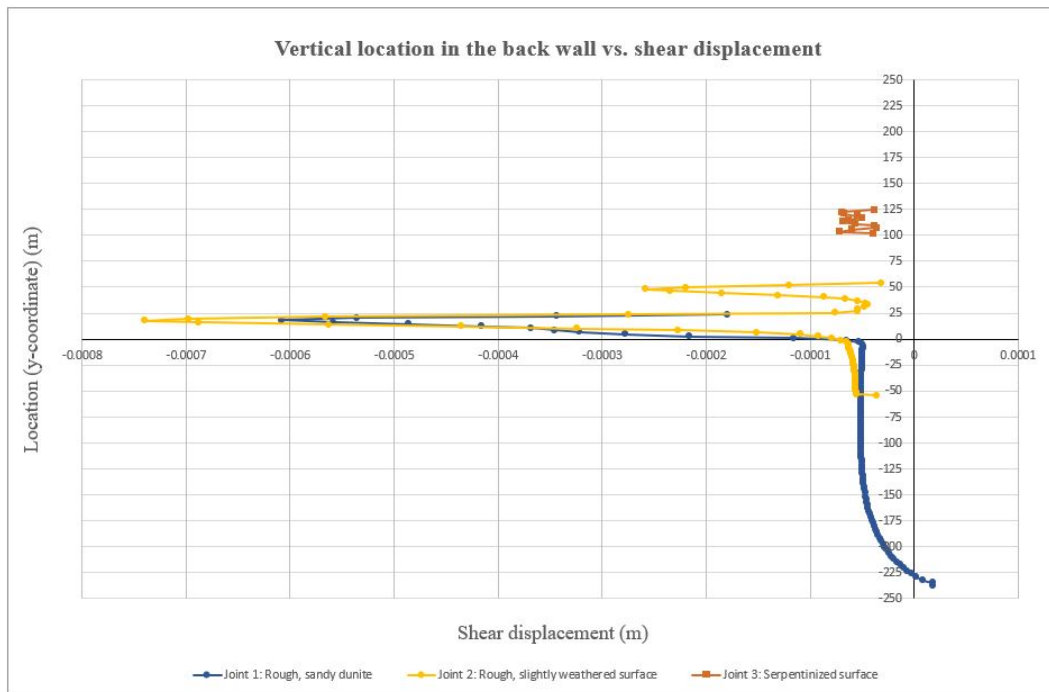


Figure 5.30: The graph displays the shear displacement along three joints with different surface types in the final back wall in section S2. The coordinates give the location of the displacement relative to the bottom of the wall in the numerical model of the section. The location of the joints are shown in figure 5.29.

Section S3

The numerical model for the section used in analysing method 2 is displayed in figure G.20 and G.21 in appendix G.

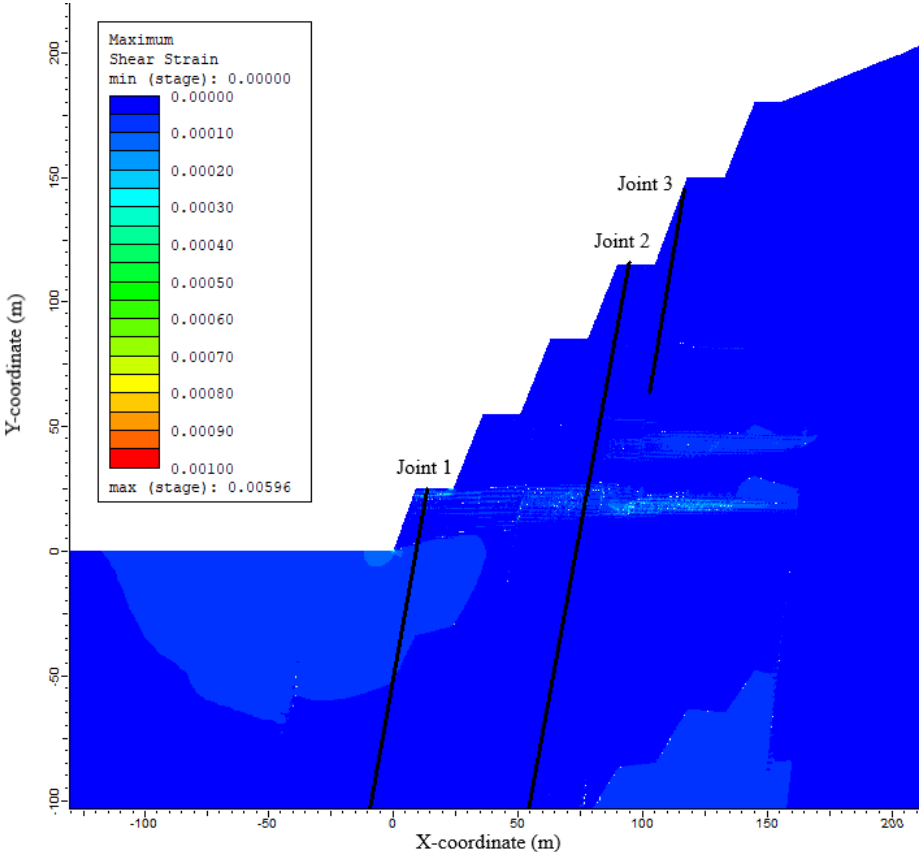


Figure 5.31: The figure indicates the joints used in the analysis of shear displacement. The coordinates are used to show the location of the displacements along the joints given in graph 5.32. The coordinates are defined relative to the location of the bottom of the wall in the numerical model of the section.

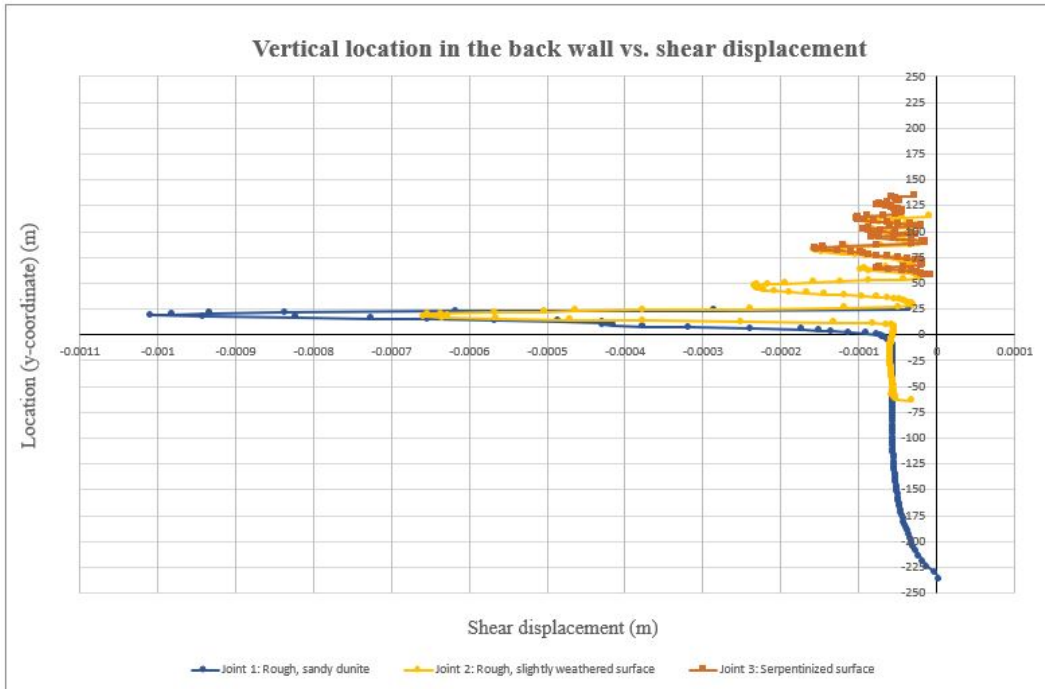


Figure 5.32: The graph displays the shear displacement along three joints with different surface types in the final back wall in section S3. The coordinates give the location of the displacement relative to the bottom of the wall in the numerical model of the section. The location of the joints are shown in figure 5.31.

Section S4

The numerical model for the section used in analysing method 2 is displayed in figure G.22 and G.23 in appendix G.

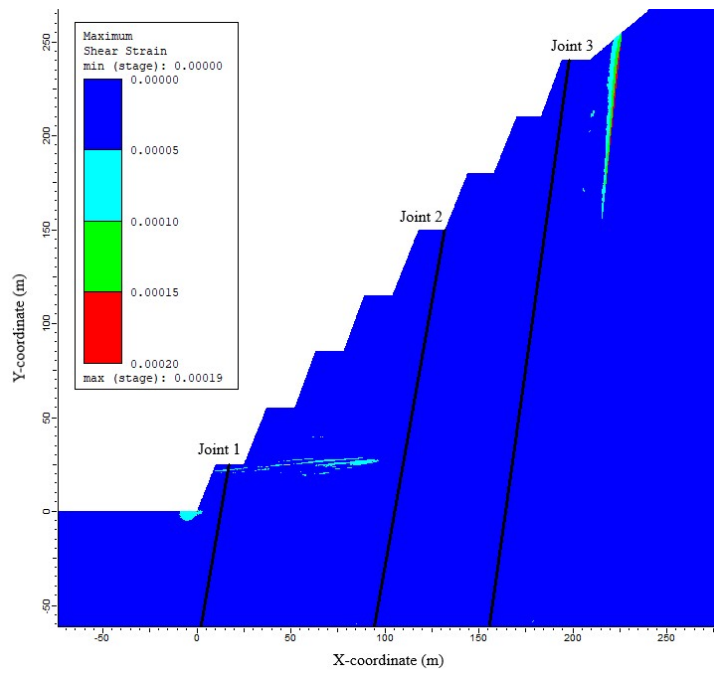


Figure 5.33: The figure indicates the joints used in the analysis of shear displacement. The coordinates are used to show the location of the displacements along the joints given in graph 5.34. The coordinates are defined relative to the location of the bottom of the wall in the numerical model of section S4.

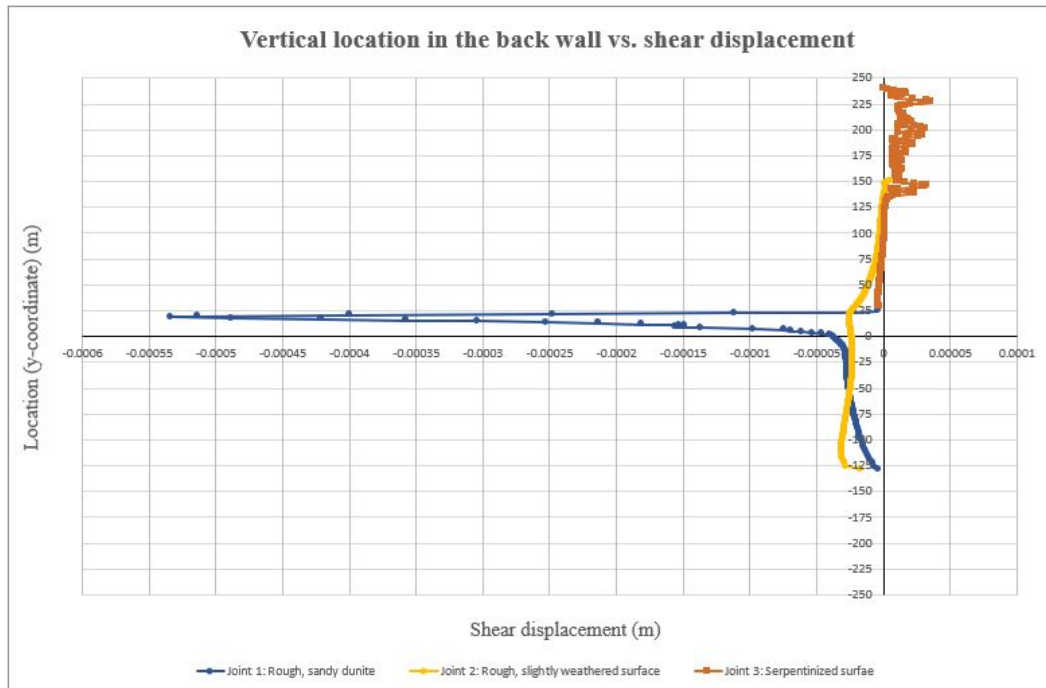


Figure 5.34: The graph displays the shear displacement along three joints with different surface types in the final back wall in section S4. The coordinates give the location of the displacement relative to the bottom of the wall in the numerical model of the section. The location of the joints are shown in figure 5.33

The graphs for the four sections show the same trend in length and the location of the largest shear displacement. The largest shear displacements occur at the height of the top of the lowermost bench in the final back wall. The largest displacements are 1mm. The length of the displacement indicates that a failure does not occur for the given input parameters. The joint with a serpentinized surface has the lowest shear strength, but does not display any larger displacements than along the joints with higher surface strength.

5.6 Discussion - the stability of the current and the final back wall

5.6.1 Global stability

The numerical modelling analysis gives an indication of the global stability of the current and the final back wall. The risk and cause of potential global instability seem to be similar in the walls. From the SSR analysis, the current and the final back wall appear to become unstable due to a failure from the bottom to the top of the quarry. The lower rock mass strength in the contact zone causes the failure plane to go far into the wall at the top of the quarry. The lowest CSRFS must be considered when evaluating the risk of instability in the final back wall due to a global slope failure. The calculated CSRFS of the current back wall is equal to 5.62. The lowest CSRFS in the final back wall is equal to 2.97. The SSR analysis shows that a high reduction of rock mass strength can be accepted along the whole wall before a global failure will occur. The SSR analyses also indicate a low risk of circular failure higher up in the wall. The analysis of displacements in the rock mass showed that movements of about 5cm can occur in the rock mass before it stabilises again. The displacement analysis also showed that there is no visible difference in the behaviour of the different types of rock mass as SRF is reduced. The difference in deformation is related to location in the back wall. The circular failure will cause the largest deformations to happen in the upper part of the wall. Since a potential global failure will be induced by a failure at the bottom of the wall, the strength of the rock mass in this area will be important for the stability. The rock mass in this part of the quarry consist of chlorite banded dunite and blastogranular dunite, rock mass typical for area section 2 and 3. These rock types were observed in the field to have a high weathering rate and disintegrate when exposed to water, see figure 3.9 in section 3.1. The risk of global failures will depend on the depth of the weathering of these rock types.

The weathering of the rock mass of chlorite banded dunite and blastogranular dunite can be considered to have less influence on the stability of the current back wall than on the final back wall. The parts of the current back wall that will be a part of the final back wall consist of serpentized dunite, rock mass typical for area section 1. This type of rock mass was observed to have a much lower weathering rate, and the strength of the intact rock was not visibly reduced. The weathering seemed to mostly occur along the foliation surface. The chlorite banded dunite and blastogranular dunite are located in areas of the current back wall where dunite is regularly produced. As a result, exposed surfaces are weathered for a short period of time, and the strength of the rock mass at the bottom of the slope is less reduced. The high CSRFS for the current back wall can therefore be evaluated to indicate a high global stability of the current back wall. There is a low risk for the rock mass strength to be reduced close to CSRFS.

When the quarry develops further, the bottom of the final back wall will consist of rock mass typical for area section 2 and 3. When the rock is located in the permanent final wall, the rock will be exposed to long term weathering. The observations from field mapping show a high weathering rate of near

surface rock mass. The strength of the rock mass further into the wall will depend on the depth of the weathering. The depth of the weathering and the effect of weathering after long term exposure on the rock mass at depth will determine the stability. It would be valuable to perform an analysis of the depth of weathering in areas where chlorite banded dunite and dunite have been exposed for a long period of time, to determine the long term stability of the wall. The SSR analysis reduced the strength of the rock mass in the entire back wall. Due to the low weathering rate of serpentinized dunite, there will be less strength reduction in this area of the wall. That can result in a more shallow path of the failure if a global failure occurs. The determined CRSF for the final back wall varies from 2.97 to 4.08 for the four analysed sections, and the tolerated weathering will differ along the wall.

The stability of the wall should also be evaluated by taking into account the structurally controlled instability. There is mainly one joint set in the rock mass in the quarry. This joint set is defined by the foliation. The field of application for the Hoek-Brown criterion described by Hoek and Marinos (2007) indicate that the foliation in the quarry can be controlling the risk of rock failure in the back wall. The results from the numerical analysis by method 1 and method 2 did not indicate that the contact zone by the gneiss boundary of the weakness zone by point Z1-Z5 would increase the risk of instability in the current back wall or the final back wall. The results from the free swelling test also indicated that there is a low risk of an added pressure from swelling clay in the weakness zones by point Z1-Z5. The SSR analysis shows that the walls will continue to be stable also for a much lower rock mass strength in the weakness zones than given by the determined input parameters. The results from the numerical analysis using method 2, does not indicate a risk of global failures along the foliation surface with the given input parameters. The displacements along the joint surfaces were less than 0.1cm in the models of the current and the final back wall. This suggest that the joint shear strength defined in the input parameters is higher than the shear stress along the joints, that there is little space for movement, or a combination of these factors. Failure along joints can happen abruptly if the surface strength is reduced. The effect of decreased surface strength was analysed in the calibration analysis. The small movements and the absence of a clear relationship between displacement and surface strength can be a result of the limits of continuum numerical modelling observed in the calibration analysis. To get a better understanding of the influence of the foliation on the stability, an analysis using discontinuum numerical modelling can be carried out.

5.6.2 Local stability

The SSR analysis indicates that the benches are stable in the current and the final back wall, when the influence of the geometry and the location of the foliation are not considered. The analysis also shows that the stability will be preserved with a decrease in strength of the rock mass due the presence of water. Observations in the field imply that the foliation has a high influence on the stability of the benches in area section 1 in the current back wall. The sliding was observed to occur only when the

slabs along the foliation had space to move due to undercutting. This observation can be supported by the registered small displacements in the results from numerical models with the foliation included. Like for the analysis of global stability, evaluations of movements along the foliation using the results from analysing method 2 should be performed with care. The sliding due to undercutting was observed to happen along the serpenized surfaces in area section 1. Most of these failures occurred in rock mass close to the eclogite boudins. To reduce the degree of undercutting, the blasting must be performed carefully. This will influence the blasting operation. To prevent undercutting, the bench angle should also be smaller than or equal to the dip of the foliation. Securing of key blocks by bolting can be used to keep blocks from sliding where undercutting has occurred. Bolts have already been used to secure blocks in risk of sliding in area section 1. The serpenized dunite in these areas was observed to fracture around the bolts due to a brittle behaviour of the rock and small foliation spacing. As a result, the bolts were divided the large slabs into smaller blocks. Based on these considerations, preventing undercutting of the bench will probably be the most effective measure to reduce the risk of instability of the benches close to the eclogite boudins.

In area section 1, the bench faces were observed to often follow the foliation as shown in figure 1.4b in section 1.1. When the foliation is used to define the bench angle, undercutting should be avoided to create a stable wall. If the slope of the bench face is made after a predetermined design, alterations in the design after the dip of the foliation in the area can be considered. In the final back wall, the benches are designed to have a bench angle of 70° . The dip of the foliation was measured to be below 70° in area section 1 by the points marked in figure 5.35. The foliation by the points are between 58° to 66° , and the proposed bench angle will result in undercutting of the foliation in this area. (See table A.1 in appendix A for the dip measured in each point.) The figure shows that the points are located by the eclogite boudins. Due to the observed difficulties in supporting sliding blocks in area section 1, a reduced bench angle should be considered in this area.

There were less observations of plane failure in area section 2 and 3. The foliation in this area has a steeper dip and the bench angle is smaller than the foliation, resulting in less undercutting. The foliation was also measured to have a higher surface strength in these sections, which may keep blocks from sliding (for the strength parameters, see section 5.1.1. The cohesion along the foliation, was after the calibration analysis, evaluated to be the reason why most blocks in section 1 did not slide down, or slid after a long period of time. The blocks slide down when the cohesion is reduced due to weathering. The exposed foliation surfaces in area section 2 and 3 have been exposed to weathering for a shorter period of time since the wall is continuously altered. The cohesion along the foliation in these areas may therefore be higher. The risk of failure by sliding may increase after weathering when the cohesion is reduced.

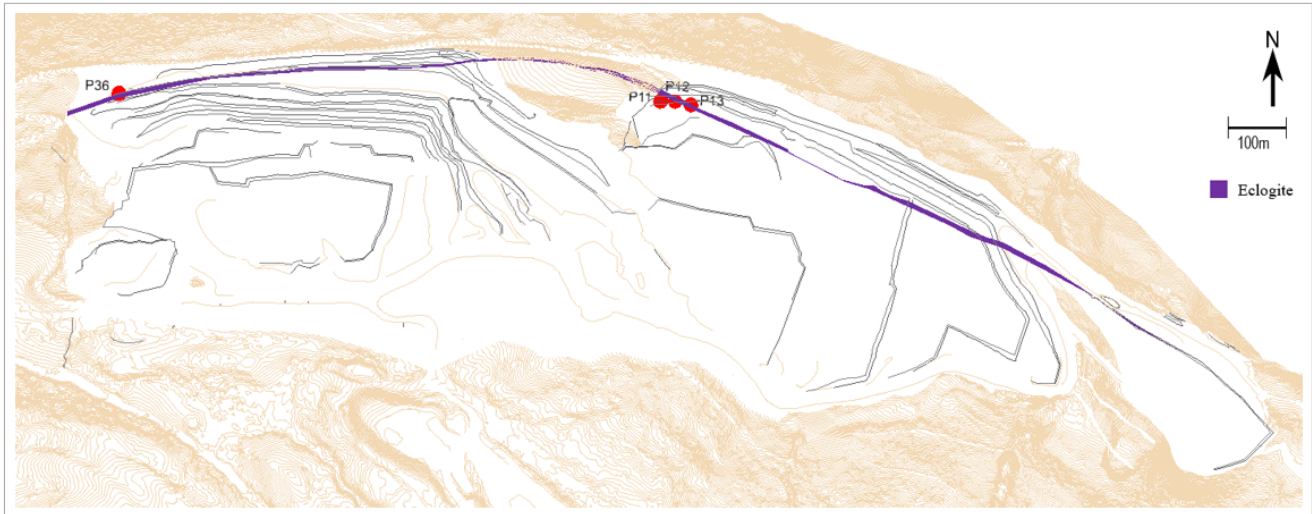


Figure 5.35: The plan of the quarry show the locations where the foliation has been measured to have a dip below 70° (marked in red). The names of the points used in the results from field mapping are indicated. The plan also shows (in purple) the area with eclogite boudins. The plane failure used for calibration occurred by point P12. The plan is modified after a model of the quarry by Sibelco Nordic.

Wedges were only observed and analysed for area section 1. Only the analysis of wedge 2 indicated a risk of instability for the current and the final back wall. The wedge was analysed to be unstable when worst case scenario water pressure was included in the analysis. The wedge was stable when water was not included in the model. There was a large difference between the factor of safety for each of these cases. The rock mass around the joints in wedge 2 was characterised to be dry during estimation of Q-value in the field (see point P17 in table A.3 in appendix A for the value of each parameter from estimation of Q-values). The risk of the worst case scenario water pressure is considered to be small. It should still be noted that the wedge can be unstable during severe conditions.

There are uncertainties related to the dip, dip direction and surface conditions of wedge 3 and 4, and the geometries of the wedges are simplified. During the analysis, the steep dip and the dip directions of the discontinuities were observed to give an intersection line which either had a very small dip towards the slope, or was dipping away from the slope. This gives in general a high stability of the wedges. The discontinuities of wedge 3 and wedge 4 was evaluated to have these features when observed from distance. This indicates that the wedges will be stable, even though the exact value of dip and dip directions are not determined. This feature also indicates that there is a low risk of instability of wedges due to an unregistered tension crack. Since there were no wedges observed in area section 2 and 3, the risk of wedge failure in the current back wall is evaluated to be very small. The risk must arise from unobserved wedges. The current wall in this part of the quarry is far from the final wall, and the risk of wedges in the final back wall in area section 2 and 3 can not be determined.

The risk of structurally controlled failure in the benches due to the foliation has been evaluated by correlating the computer analyses with observations of failures and measurements from field mapping. A

broader understanding of the influence of the foliation on bench stability can be obtained by discontinuum modelling. The risk of toppling failure has not been considered. Toppling failure was not observed in the quarry, but the subvertical dip of the foliation in certain areas can suggest a potential for toppling failure.

5.6.3 Limitations and uncertainties in the analysis

Simplifications, assumptions, and interpretations of parameters, geological conditions, and the geometry of the quarry were carried out to perform the numerical analysis and the analysis of wedges. This results in uncertainties in the analysis and the reliability of the models should be evaluated. The properties of the rock mass which were considered to have high influence on the behaviour of the rock mass in the back wall were included in the numerical models. This causes certain rock mass properties to be better reproduced in the models than others. The software RS2 can not perform an SSR analysis on the joints surface strength when the strength is defined by the Barton-Bandis criterion. As a result, more assumptions about the influence of surface strength for stability must be made in order to capture the consequences of reduced surface strength along the foliation. The consequence of reduction of the surface strength for the stability, when not taking into account the geometry of the foliation, was investigated by the SSR model. The foliation could not be included in the SSR analysis with the demanded finite element sizes. As a consequence, the relationship between the foliation structure and reduction of rock mass strength had to be evaluated based on two different analyses. That increased the uncertainties in the results of the analysis.

The SSR analysis allowed the stability to be investigated for rock mass strength that deviates from the given input parameters. The consequence of reduced rock mass strength was used to investigate the effect of water. The flow of the ground water was not included in the models even though it would have increased the driving forces in the slope and influenced the computed risk of structurally controlled failure. That was evident in the analysis of wedges. The use of worst case scenario modelling will decrease the probability of an underestimated risk. It can also indicate a too large risk of failure. The analysis must therefore be evaluated with the assumptions in the modelling in mind. Observations from the field can be used to evaluate the results from the computer analysis. Observations can also be valuable to evaluate rock mass conditions that were not registered in the computer analysis. This type of evaluation will also be influenced by assumptions and simplification.

6. Conclusion and further investigations

The stability analysis of the current and the final back wall was carried out by numerical modelling and wedge analyses. The results from the analyses were evaluated and interpreted by measurements and observations from field mapping. The analysis gave the following conclusions on the stability of the current and the final back wall, and the performance of the stability analysis:

- The risk of global instability in the current back wall due to a failure in the rock mass or a structural failure is considered to be very low. The SSR analysis of section S2 located in the most developed part of the quarry give a CSRF of 5.62. The SRR analyses did not display any risk of structural failure due to the weakness zone by point Z1-Z5, or the contact zone by the gneiss boundary before the strength was reduced to CSRF. It should be considered that these analysis did not take into account the location and the geometry of the foliation.
- The global stability of the final back wall is depending on the depth of the weathering of chlorite banded dunite and dunite at the bottom of the wall. The SSR analysis calculated the lowest CSRF in the final back wall to be 2.97. If this strength reduction occurs at the bottom of the wall, a global failure can be induced. Long term weathering of the rock mass of chlorite banded dunite and dunite in the final back wall was considered to be able to result in a strength reduction of the rock mass close to CSRF. An investigation on the depth of weathering is recommended to determine the possible strength reduction of the rock mass at the bottom of the back wall. Weathering of the rock mass was evaluated to not cause a risk of instability in the current back wall since the back wall in this area is regularly moved.
- The benches are considered to be stable in the current and the final back wall apart from in area section 1. The numerical analyses displayed very small movements in the rock mass and along the foliation in the benches. The SSR analyses did not display any circular failure in the benches before a global failure will occur. Still, local instability caused by plane failure along the foliation was observed in area section 1. The largest risk of plane failure in this area was evaluated to be along serpentinized foliation surfaces near the location of eclogite boudins. The risk of plane failure in the benches in area section 2 and 3 are considered to be low in the current back wall. There can be a risk of plane failure in these sections in the final back wall if weathering reduces the strength of the foliation surface and undercutting occurs. The best measure to reduce the risk of instability is reduction of undercutting by careful blasting and by keeping the bench angle smaller than the angle of the foliation.

- The planned geometry of the benches in the final back wall with a width of 15m and a height of 30m can be kept where the foliation has a dip equal to or greater than 70° . The bench angle should be reduced when the foliation has a smaller dip to avoid undercutting. The foliation was measured to have a dip below 70° in parts of area section 1. The bench angle should be considered reduced in this area.
- There is a possibility of wedge failure in the current and the final back wall by wedge 2 in area section 1. The safety factor of the wedge is above 5 for dry conditions and below 0.2 in the current back wall when the joints are completely filled with water. The risk of instability of the wedge can be determined by examination of the drainage of the joints forming the wedge after heavy rainfall.
- The foliation in parts of the quarry has a subvertical dip. The steep dip can indicate a risk of toppling failure. An analysis of the risk of toppling failure can be considered to give a better understanding of the risk of structural failure in the back wall.
- The numerical analysis of the stability along the foliation is close to the limits of the continuum numerical modelling. An analysis using discontinuum numerical modelling is recommended to get more information about the influence of the foliation on the stability of the back wall.
- Computer analysis is not sufficient to carry out a stability analysis. The influence of assumptions, simplifications, and limitations of computer analysis on the calculated results should be evaluated by observations in the field and mechanical measurements.
- The computer resources available will have high influence on the number of simplifications in the numerical model and the accuracy of the model. This will further influence how the analysis can be performed and the results of the analysis.

Based on these evaluations, two instability risk zones were defined for the current and the final back wall.

- Risk zone 1: A zone defined by the location of eclogite boudins. The zone presents an area with local instability in the current quarry and can continue to cause instability as the quarry is developed further.
- Risk zone 2: A zone defined by the benches in the final back wall that will consist of chlorite banded dunite and blastogranular dunite. The zone defines an area where extra attention should be paid to the behaviour of the rock mass. The zone is stable in the current quarry, but weathering of the rock mass in this area can induce global stability in the final back wall.

The zones with instability in the current back wall are displayed in figure 6.1. The zones with potential instability in the final back wall are displayed in figure 6.2.

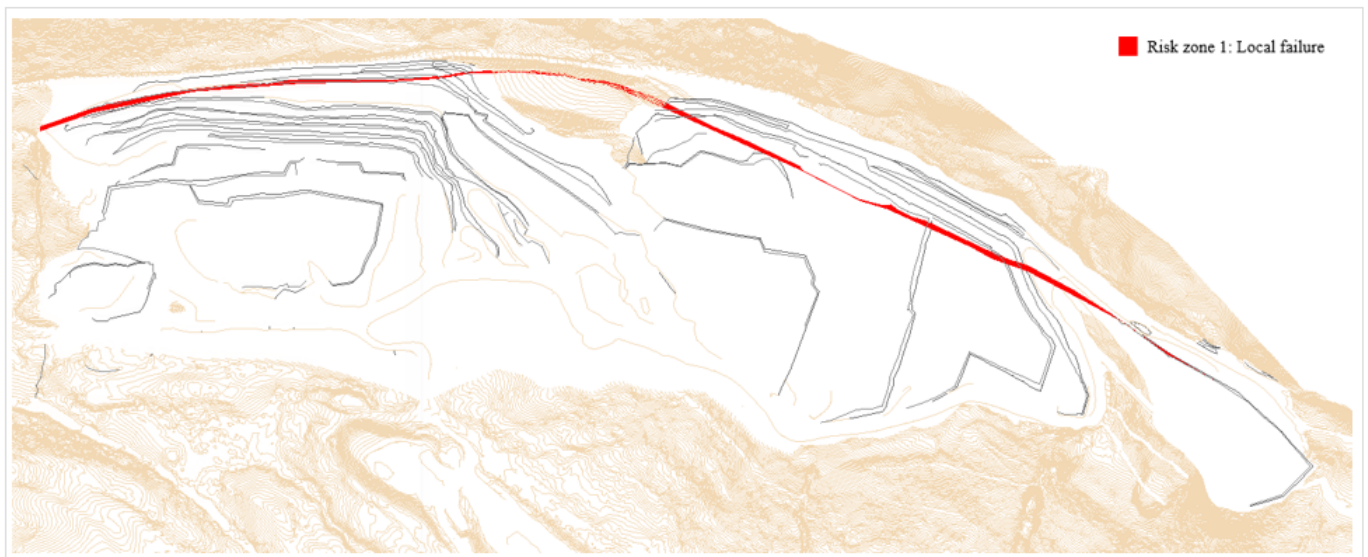


Figure 6.1: The figure shows a plan of the current quarry with the location of risk zone 1. The zone is drawn after a map of geology from Sibelco Nordic (see fig 1.3) and observations of eclogite boudins during field mapping. The plan of the quarry is modified after a model of the quarry by Sibelco Nordic.

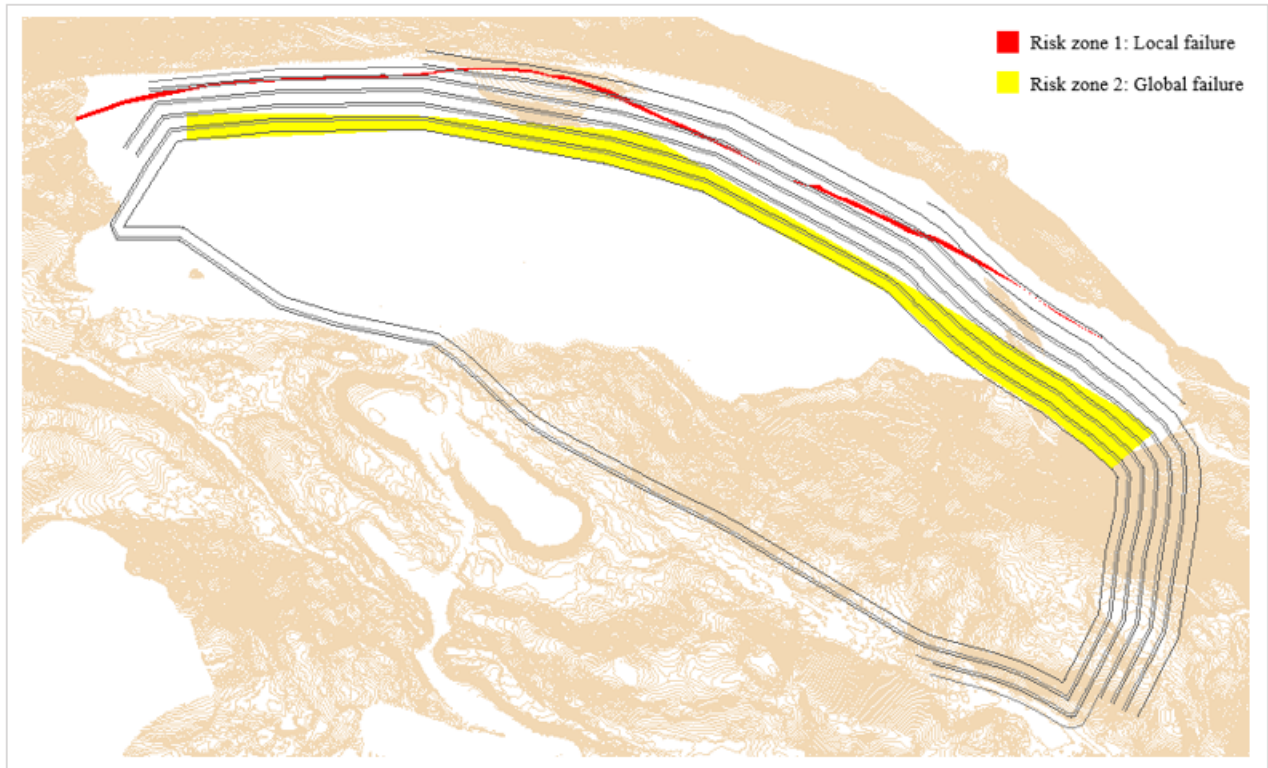


Figure 6.2: The figure shows a plan of the quarry at life of mine with location of risk zone 1 and 2. Risk zone 1 is drawn after map of geology from Sibelco Nordic (see fig 1.3) and observations from field mapping. Risk zone 2 is drawn as an approximation of the area in the final back wall that will consist of chlorite banded dunite and blastogranular dunite after geology sections of S1, S2, S3, and S4. The plan of the quarry is modified after a model of the quarry by Sibelco Nordic.

Bibliography

- Aasteboel, H. (2019), Olivin quarry, Åheim: Field mapping and laboratory testing of parameters influencing the rock mass stability.
- Alejano, L. R., Muralha, J., Li, C., Pérez-Rey, I., Karakul, H., Chryssanthakis, P. and Aydan, (2018), 'Isrm suggested methods for determining the basic friction angle of planar rock surfaces by means of tilt tests', *Rock Mechanics and Rock Engineering* **51**(12), 3853–3859.
- Barton, N. (1972), 'A model study of rock-joint deformation', *International Journal of Rock Mechanics and Mining Science Geomechanics Abstracts* **9**, 597–602.
- Barton, N. (1973), 'Review of a new shear-strength criterion for rock joints', *Engineering Geology* **7**(4), 287–332.
- Barton, N. (2012), 'Shear strength criteria for rock, rock joints, rockfill and rock masses: Problems and some solutions', *Journal of Rock Mechanics and Geotechnical Engineering* **5**, 249–261.
- Barton, N. and Bandis, S. (1990), Review of predictive capabilities of jrc-jcs model in engineering practice, A. A. Balkema, Rotterdam, pp. 603–610.
- Barton, N. and Choubey, V. (1977), 'The shear strength of rock joints in theory and practice', *Rock Mechanics* (10), 1–54.
- Barton, N., Lien, R. and Lunde, J. (1974), 'Engineering classification of rock masses for the design of tunnel support', *Springer-Verlag* **6**, 189–236.
- Barton, N. R. (1976), 'The shear strength of rock and rock joints', *International Journal of Rock Mechanics and Mining Science and Geomechanics Abstracts* **13**(9), 255–279.
- Bentley Systems (2018), 'Microstation connect edition update 9 (version 10.09.01.01)'.
URL: <https://www.bentley.com/en/products/brands/microstation>
- Chugh, A. (2003), 'On the boundary conditions in slope stability analysis', *International Journal for Numerical and Analytical Methods in Geomechanics* **27**, 905–926.
- Contreras, L. (2015), 'An economic risk evaluation approach for pit slope optimization', *Journal of the Southern African Institute of Mining and Metallurgy* **115**(7).
- Cordellier, F., Boudier, F. and Boullier, A. (1981), 'Structural study of the almklovdalen peridotite massif (southern norway)', *Tectonophysics* **77**(3-4), 257–281.

- Coulson, J. (1970), The Effects of Surface Roughness on The Shear Strength of Joints in Rock, PhD thesis, University of Illinois.
- Deere, D. and Deere, D. (1988), The rock quality designation (rqd) index in practice, *in* L. Kikaldie, ed., 'Rock Classification Systems for Engineering Purposes', American Society for Testing and Materials, Philadelphia, pp. 91–101.
- Deere, D., Hendron, A., Patton, J. F. and Cording, E. (1967), Design of surface and near-surface construction in rock, *in* C. Fairhurst, ed., 'Failure and Breakage of Rock: Proceedings of the Eighth Symposium on Rock Mechanics Held at the University of Minnesota September 15-17th 1966', American Institute of Mining, Metallurgical, and Petroleum Engineers, New York, chapter 11, pp. 237–302.
- Deere, D. U. and Miller, R. P. (1966), *Engineering Classification and Index Properties for Intact Rock*, University of Illinois, Urbana, Illinois.
- Deliveris, A., Zevgolis, I. and Koukoulas, N. (2016), Numerical modelling of slope stability in open pit lignite mines: a comparative study, Thessaloniki.
- Dorren, L. and Seijmonsbergen, A. (2003), 'Comparison of three gis-based models for predicting rockfall runout zones at a regional scale', *Geomorphology* **56**(1), 49–64.
- GCTS Testing Systems (n.d.), 'Gcts cats-adv'.
URL: https://www.gcts.com/?s=prod_verp = productsID = 117
- Goodman, R. (2013), Toppling - - a fundamental failure mode in discontinuous materials — description and analysis, San Diego.
- Hammah, R., Yacoub, T. and Corkum, B. (2008), The practical modelling of discontinuous rock masses with finite element analysis, San Fransisco.
- Hammah, R., Yacoub, T., Corkum, B. and Curran, J. (2005), The shear strength reduction method for the generalized hoek-brown criterion.
- Harrison, J. and Hudson, J. (2000), *Engineering Rock Mechanics Part II*, Pergamon.
- Hoek, E. (1994), 'Strength of rock and rock masses', *ISRM News Journal* **2**(2), 4–16.
- Hoek, E. (2007), *Practical Rock Engineering*, Rocscience.
URL: <https://www.rocscience.com/learning/hoeks-corner/course-notes-books>
- Hoek, E. and Bray, J. (1977), *Rock Slope Engineering*, 2 edn, Stephen Austin and Sons Limited, Hertford.
- Hoek, E. and Brown, E. (1980), 'Empirical strength criterion for rock masses', *Journal of The Geotechnical Engineering Division* **106**(9), 1013–1035.

- Hoek, E. and Brown, E. (1988), The hoek-brown criterion - a 1988 update, University of Toronto, Toronto, pp. 31–38.
- Hoek, E., Carranza-Torres, C. and Corkum, B. (1973), ‘Hoek-brown failure criterion - 2002 edition’, *Engineering Geology* **7**(4), 287–332.
- Hoek, E. and Diederichs, M. (2006), ‘Empirical estimation of rock mass modulus’, *International Journal of Rock Mechanics and Mining Sciences* **43**, 203–215.
- Hoek, E., Kaiser, P. and Bawden, W. (1995), *Support of Underground Excavations in Hard Rock*, A.A. Balkema.
- Hoek, E. and Marinos, P. (2007), ‘A brief history of the development of the hoek-brown failure criterion’, *Soils and Rocks* .
- International Society for Rock Mechanics (1978), ‘Suggested methods for determining sound velocity’, *International Journal of Rock Mechanics and Mining Sciences and Geomechanics Abstracts* **15**(2), 53–58.
- International Society for Rock Mechanics (1979), ‘Suggested methods for determining the uniaxial compressive strength and deformability of rock materials’, *International Journal of Rock Mechanics and Mining Sciences and Geomechanics Abstracts* **16**(2), 137.
- Jaeger, J., Cook, N. and Zimmermann, R. (2007), *Fundamentals of Rock Mechanics*, 4 edn, Blackwell Publishing Ltd.
- Jings, L. and Hudson, J. (2002), ‘Numerical methods in rock mechanics’, *International Journal of Rock Mechanics and Mining Sciences* **39**(4), 409–427.
- Jones, D. and Brischke, C. (2017), *Performance of Bio-based Building Materials*, Woodhead Publishing.
- Joughin, W. (2018), Dealing with uncertainty and risk in rock engineering design.
- Kartverket (2020). [accessed 18.03.2020].
URL: <https://hoydedata.no/LaserInnsyn/>
- Khatik, V. and Nandi, A. (2018), ‘A generic method for rock mass classification’, *Journal of Rock Mechanics and Geotechnical Engineering* **10**(1), 102–116.
- Kliche, C. (2018), *Rock Slope Stability*, 2 edn, Society for Mining, Metallurgy Exploration, Colorado.
- Lappin, M. A. (1966), ‘The field relationships of basic and ultrabasic masses in the basal complex of stadlandet and almklovdalen, nordfjord, southwestern norway’, *Norsk Geologisk Tidsskrift* **46**(4), 439–495.
- Li, C., ed. (2018), *TGB 4210 Rock Mechanics*, NTNU, Trondheim.

- Maps, G. (2009). [GeoBasis-DE/BKG, viewed 30.05.2020].
URL: <https://www.google.com/maps/@61.2319068,7.5673286,6.75z>
- Marinos, P. and Hoek, E. (2000), Gsi: A geologically friendly tool for rock mass strength estimation, Melbourne, Australia.
- Myrvang, A. (2001), *Bergmekanikk*, NTNU, Trondheim.
- Nikolić, M., Roje-Bonacci, T. and Ibrahimbegović, A. (2016), ‘Overview of the numerical methods for the modelling of rock mechanics problems’, *Technical gazette* **23**(2), 627–637.
- Nilsen, B. (2000), ‘New trends in rock slope stability analyses’, *Bulletin of Engineering Geology and the Environment* **58**, 173–178.
- Nilsen, B. (2016), *Ingeniørgeologi-Berg grunnkurskompendium*, NTNU, Trondheim.
- Norges Geotekniske Institutt (2015), *Bruk av Q-systemet Bergmasseklassifisering og bergforsterkning*, Norges Geotekniske Institutt, Oslo.
- Osland, R. (1998), Modelling of variations in Norwegian olivine deposits: causes of variation and estimation of key quality factors, PhD thesis, NTNU, Trondheim.
- Raghuvanshi, T. K. (2019), ‘Plane failure in rock slopes - a review on stability analysis techniques’, *ScienceDirect* **31**(1), 101–109.
- Rocscience (2019a), ‘Rs2’. [accessed 15.11.2019].
URL: <https://www.rocscience.com/software/rs2>
- Rocscience (2019b), ‘Rs2 (version 10.006)’.
URL: <https://www.rocscience.com>
- Rocscience (2019c), *SWedge Surface Wedge Analysis for Slopes*, rocscience.
- Rocscience (n.d.a), ‘Convergence criteria’. [accessed 15.04.2020].
URL: https://www.rocscience.com/help/rs2/pdf_files/theory/Convergence_criteria.pdf
- Rocscience (n.d.b), ‘Define joint properties’. [accessed 14.04.2020].
URL: https://www.rocscience.com/help/rs2/phase2_model/Define_joint_properties.htm
- Rocscience (n.d.c), ‘Equivalent mohr-coulomb parameters’. [accessed 11.05.2020].
URL: https://www.rocscience.com/help/rocddata/rocddata/Equivalent_Mohr_Coulomb_parameters.htm —
- Rocscience (n.d.d), ‘Estimating joint stiffness’. [accessed 25.01.2020].
URL: https://www.rocscience.com/help/rs2/theory/Estimating_joint_stiffness.htm

- Rocscience (n.d.e), ‘Joint water pressure’. [accessed 27.05.2020].
URL: <https://www.rocscience.com/help/swedge/swedge/JointWaterPressure.htm>
- Rocscience (n.d.f), ‘Mesh overview’. [accessed 15.04.2020].
URL: https://www.rocscience.com/help/rs2/phase2_model/MeshOverview.htm
- Rocscience (n.d.g), ‘Rs2 interpret’. [accessed 15.04.2020].
URL: https://www.rocscience.com/help/rs2/phase2_interpret/phase2_interpreter.htm
- Rocscience (n.d.h), ‘Shear strength reduction analysis’. [accessed 26.05.2020].
URL: https://www.rocscience.com/help/rs2/tutorials/03_shear_strength_reduction_analysis.htm
- Rocscience (n.d.i), ‘Ssr’. [accessed 24.04.2020].
URL: <https://www.rocscience.com/help/rs2/index.htmlt=KnowledgeBase%2FSSRKB.htm>
- Rocscience (n.d.j), ‘Strength parameters’. [accessed 08.04.2020].
URL: https://www.rocscience.com/help/rs2/phase2_model/StrengthParameters.htm
- Rocscience (n.d.k), ‘Stress analysis settings’. [accessed 14.04.2020].
URL: https://www.rocscience.com/help/rs2/phase2_model/StressAnalysis.htm
- Rocscience (n.d.l), ‘Tutorial 06 - joint persistence analysis in swedge’. [accessed 06.05.2020].
URL: https://www.rocscience.com/help/swedge/tutorials/06_joint_persistence_analysis_tutorial.htm
- Rocscience Inc (2019a), ‘Dips7.0 (version 7.016)’.
URL: <https://www.rocscience.com>
- Rocscience Inc (2019b), ‘Rocdata (version 5.009)’.
URL: <https://www.rocscience.com>
- Rocscience Inc (2019c), ‘Swedge (version 6.019 64-bit)’.
URL: <https://www.rocscience.com>
- Savage, J., Byerlee, J. and Lockner, D. (1996), ‘Is internal friction friction?’, *Geophysical research letters* **23**(5), 487–490.
- Schmidt, E. (1978), ‘Commission on standardization of laboratory and field tests suggested methods for the quantitative description of discontinuities in rock mass’, *International Journal of Rock Mechanics and Mining Sciences Geomechanics Abstracts* **15**(6), 95–97.
- Schönborn, t. (1995), Stability analysis of the gusdal open pit mine - western norway, Master’s thesis, NTNU and RWTH Aachen.
- Sinha, S. and Walton, G. (2019), ‘Understanding continuum and discontinuum models of rock-support interaction for excavations undergoing stress-induced spalling’, *International Journal of Rock Mechanics and Mining Sciences* **123**.

- Souza, M. and Nelson, M. (2018), A comparison of the shear strength reduction technique and limit equilibrium method for slope stability.
- Varnes, D. (1978), Slope movement types and processes, in R. Schuster and R. Krizek, eds, 'Landslides: Analysis and Control Special report 176', National Academy of Sciences, Washington, D.C., chapter 2, pp. 11–33.
- Vegdirektoratet (2016), *Laboratorieundersøkelser Retningslinje Håndbok R210*, Statens Vegvesen.
- Wyllie, D. and Mah, C. (2004), *Rock Slope Engineering Civil and Mining*, 4 edn, Spon Press, New York.
- You, G., Mandalawi, M., Soliman, A., Dowling, K. and Dahlhaus, P. (2017), Finite element analysis of rock slope stability using shear strength reduction method, in W. Frikha, S. Varaksin and A. Viana da Fonseca, eds, 'Soil Testing, Soil Stability and Ground Improvement Proceedings of the 1st GeoMEast International Congress and Exhibition, Egypt 2017 on Sustainable Civil Infrastructures', Springer, Cham.

Appendix

A. Field Mapping

A.1 Measurements of dip and dip direction

Area section 1			Area section 2			Area section 3		
Location	Dip (°)	Dip direction (°)	Location	Dip (°)	Dip direction (°)	Location	Dip (°)	Dip direction (°)
P3	75	166	P26	76	174	P30	9	11
P3	80	258	P26	75	175	P30	72	201
P3	50	68	P26	21	236	P30	74	232
P3	20	262	P28	75	186	P30	72	254
P4	60	297	P37	81	167	P31	52	292
P5	70	100	P45	72	159	P32	31	347
P6	72	92	P45	55	207	P32	14	336
P6	74	187	P45	15	84	P33	87	2
P7	75	167	P45	13	76	P33	81	221
P7	86	182	P45	45	299	P33	84	235
P7	80	262	P45	70	170	P34	85	246
P9	72	92	P46	65	191	P34	25	206
P10	75	167				P34	74	311
P10	72	164				P34	81	346
P10	88	254				P46	89	341
P11	60	172				P49	73	344
P12	58	177				P49	81	346
P12	75	88						
P13	60	206						
P13	54	96						
P13	15	352						
P13	65	189						
P13	70	194						
P13	74	192						
P16	49	111						
P17	59	138						
P17	58	122						
P17	76	111						
P18	75	211						
P19	5	314						
P19	88	229						
P19	84	229						
P19	5	305						
P21	85	218						
P21	82	214						
P21	89	186						
P22	72	211						
P22	7	109						
P22	15	133						
P23	30	116						
P23	73	133						
P23	82	291						

Area section 1			Area section 2			Area section 3		
P24	87	247						
P24	73	224						
P24	83	190						
P24	88	283						
P35	71	152						
P36	77	202						
P36	66	164						
P36	21	211						
P36	41	239						
P40	80	299						
P40	74	291						
P40	5	291						
P40	13	117						
P40	76	239						
P40	86	159						
P40	58	120						
P40	32	136						
P44	89	211						
P50	49	129						
P50	59	121						
P50	39	285						
P51	84	203						
P53	69	331						
P54	80	69						
P55	81	195						

Table A.1: All results from measurements of dip and dip direction for area section 1, 2, 3, and 4. The locations indicated in the table are shown in the map in figure 3.2.

A.1.1 Data of dip and dip direction from Sibelco Nordic

Area section 1			Area section 2		
Name of measurement	Dip (°)	Dip direction (°)	Name of measurement	Dip (°)	Dip direction (°)
GU-190087	56	82	GU-190080	64	270
GU-190086	72	182	GU-190277	79	269
GU-190088	79	88	GU-190288	64	89
GU-190089	76	88	GU-190167	65	89
GU-190090	80	86	GU-190289	65	88
GU-190091	67	175	GU-190170	6	85
GU-190092	19	311	GU-190160	60	85
GU-190094	50	76	GU-190177	84	262
GU-190093	83	171	GU-190279	38	81
GU-190096	77	182	GU-190165	80	80
GU-190095	65	100	GU-190172	47	253
GU-190098	65	85	GU-190179	47	71
GU-190099	74	179	GU-190169	16	68
GU-190097	11	308	GU-190290	21	67
GU-190100	81	85	GU-190192	89	65
GU-190103	80	177	GU-190074	19	61
GU-190101	65	276	GU-190264	32	61
GU-190102	80	94	GU-190201	41	61
GU-190105	79	175	GU-190202	75	238
GU-190106	11	286	GU-190190	85	236
GU-190104	83	92	GU-190181	60	226
GU-190109	80	88	GU-190081	27	46
GU-190108	36	80	GU-190180	44	46
GU-190107	81	184	GU-190205	26	42
GU-190110	70	277	GU-190196	61	219
GU-190112	75	176	GU-190194	25	35
GU-190111	70	98	GU-190200	24	34
GU-190113	5	178	GU-190173	16	213
GU-190115	70	272	GU-190199	72	211
GU-190114	76	92	GU-190208	26	30
GU-190119	36	80	GU-190206	65	206
GU-190118	76	79	GU-190204	70	205
GU-190117	15	64	GU-190166	15	25
GU-190116	79	180	GU-190261	70	204
GU-190121	75	266	GU-190078	20	24
GU-190120	43	85	GU-190271	85	203
GU-190122	74	178	GU-190198	80	203
GU-190124	52	70	GU-190207	70	198
GU-190123	66	271	GU-190082	79	195
GU-190125	60	76	GU-190163	70	195
GU-190126	70	173	GU-190287	75	194
GU-190127	61	81	GU-190183	74	194
GU-190128	71	183	GU-190175	75	186
GU-190257	61	73	GU-190274	70	184
GU-190256	65	170	GU-190171	89	182
GU-190255	59	185	GU-190278	75	182
GU-190254	66	185	GU-190266	73	177
GU-190253	70	172	GU-190275	80	177
GU-190252	67	272	GU-190164	75	174
GU-190251	84	172	GU-190191	12	348
GU-190250	20	249	GU-190079	17	168
GU-190249	71	175	GU-190265	69	168

GU-190248	72	191	GU-190280	73	166
GU-190247	85	94	GU-190203	68	338
GU-190286	75	206	GU-190176	19	333
GU-190285	30	152	GU-190182	86	141
GU-190284	67	75	GU-190197	70	140
GU-190246	86	100	GU-190262	7	311
GU-190245	73	199	GU-190273	45	303
GU-190244	70	92	GU-190195	79	121
GU-190243	72	196	GU-190168	80	111
GU-190242	29	4	GU-190174	52	287
GU-190283	22	59	GU-190158	15	287
GU-190282	87	180	GU-190159	49	287
GU-190281	89	284	GU-190077	79	106
GU-190241	90	91	GU-190267	65	285
GU-190240	70	175	GU-190178	15	283
GU-190239	81	273	GU-190263	47	282
GU-190238	52	87	GU-190270	89	99
GU-190237	15	260	GU-190193	66	277
GU-190236	90	174	GU-190076	77	97
GU-190235	75	85	GU-190075	65	97
GU-190234	17	219	GU-190276	48	275
GU-190232	39	288	GU-190272	60	273
GU-190231	32	247			
GU-190233	84	193			
GU-190230	35	271			
GU-190229	59	68			
GU-190228	12	262			
GU-190227	30	217			
GU-190226	76	184			
GU-190225	74	9			
GU-190224	20	205			
GU-190223	65	58			
GU-190222	80	163			
GU-190221	35	228			
GU-190220	35	116			
GU-190219	87	174			
GU-190216	75	288			
GU-190217	37	292			
GU-190218	71	203			
GU-190214	89	295			
GU-190215	12	320			
GU-190212	54	75			
GU-190211	9	132			
GU-190213	74	197			
GU-190210	76	202			
GU-190209	40	73			
GU-190189	24	201			
GU-190188	46	196			
GU-190186	84	185			
GU-190187	40	119			
GU-190184	55	88			
GU-190185	40	258			
GU-190073	35	92			
GU-190073	35	92			
GU-190072	55	112			
GU-190071	10	297			

GU-190070	85	98			
GU-190069	54	102			
GU-190068	80	216			
GU-190067	84	212			
GU-190066	70	308			
GU-190065	30	116			
GU-190064	75	224			
GU-190063	89	228			
GU-190062	31	116			
GU-190061	88	224			
GU-190060	35	125			
GU-190059	30	118			
GU-190058	82	208			
GU-190057	88	36			
GU-190056	28	146			
GU-190055	35	292			
GU-190054	40	135			
GU-190053	85	243			
GU-190052	64	340			
GU-190051	84	246			
GU-190050	88	3			
GU-190049	70	250			
GU-190047	90	28			
GU-190048	70	322			
GU-190046	82	340			
GU-190045	80	102			
GU-190041	25	193			
GU-190040	85	198			
GU-190039	80	205			
GU-190157	76	64			
GU-190038	84	200			
GU-190156	84	212			
GU-190037	5	6			
GU-190034	86	235			
GU-190036	84	188			
GU-190035	48	109			
GU-190033	10	215			
GU-190032	81	198			
GU-190031	79	200			
GU-190154	84	197			
GU-190155	17	193			
GU-190151	36	61			
GU-190153	77	295			
GU-190152	77	108			
GU-190029	85	4			
GU-190030	20	343			
GU-190028	77	203			
GU-190027	85	212			
GU-190026	70	255			
GU-190025	15	253			
GU-190148	35	13			
GU-190150	10	166			
GU-190149	75	104			
GU-190129	90	260			
GU-190130	69	150			
GU-190024	85	195			

GU-190023	70	298			
GU-190022	15	185			
GU-190021	73	303			
GU-190020	85	207			
GU-190147	72	112			
GU-190131	71	203			
GU-190133	60	155			
GU-190132	74	102			
GU-190019	80	220			
GU-190143	84	201			
GU-190146	67	108			
GU-190145	70	272			
GU-190144	30	90			
GU-190018	65	262			
GU-190017	60	70			
GU-190016	80	213			
GU-190134	80	210			
GU-190136	25	11			
GU-190135	69	292			
GU-190138	14	17			
GU-190139	84	203			
GU-190015	70	283			
GU-190140	85	205			
GU-190141	27	320			
GU-190142	19	105			
GU-190014	40	50			
GU-190013	70	194			
GU-190011	78	190			
GU-190010	75	110			
GU-190009	77	200			
GU-190008	64	77			
GU-190007	30	102			
GU-190006	50	28			
GU-190005	20	60			
GU-190004	20	58			
GU-190003	25	55			
GU-190002	51	97			
GU-190001	80	290			

Table A.2: Measurements of dip and dip direction in area section 1 and 2 from Sibelco Nordic. The measurements were used to make the rose diagrams in section 3.2.1. The names of the measurements are given by the names used by Sibelco Nordic.

A.2 Q-value

A.2.1 Area section 1

Location	Rock	RQD	J_n	J_r	J_a	J_w	SRF	Q-value
P5	Chlorite Amphibole Dunite	80	9	3	4	1	2.5	2.7
P5	Chlorite Amphibole Dunite	83	3	3	6	1	2.5	5.6
P6	Chlorite Amphibole Dunite	77	9	2.5	3	1	2.5	2.8
P6	Chlorite Amphibole Dunite	83	3	2.5	4	1	2.5	6.9
P7	Chlorite Amphibole Dunite	77	3	2.5	3	1	2.5	8.5
P9	Chlorite Amphibole Dunite	80	3	3	5	1	2.5	6.4
P10	Chlorite Amphibole Dunite	83	6	2.25	4	1	2.5	3.1
P11	Chlorite Amphibole Dunite	80	3	3	4	1	2.5	8.0
P12	Chlorite Amphibole Dunite	97	3	2	4	1	2.5	6.4
P13	Chlorite Amphibole Dunite	83	9	2.5	4	1	2.5	2.3
P13	Chlorite Amphibole Dunite	80	4	2.5	4	1	2.5	5.0
P14	Chlorite Amphibole Dunite	83	3	2.5	4	1	2.5	6.9
P15	Chlorite Amphibole Dunite	83	6	2	4	1	2.5	2.8
P16	Chlorite Amphibole Dunite	73	3	2.5	4	1	2.5	6.1
P17	Chlorite Amphibole Dunite	87	3	3	4	1	2.5	8.7
P18	Chlorite Amphibole Dunite	80	6	3	4	1	2.5	4.0

Location	Rock	RQD	J_n	J_r	J_a	J_w	SRF	Q-value
P19	Chlorite Amphibole Dunite	70	6	3	4	1	2.5	3.5
P19	Chlorite Amphibole Dunite	78	6	3	3	1	2.5	5.2
P20	Chlorite Amphibole Dunite	68	6	3	4	1	2.5	3.4
P21	Chlorite Amphibole Dunite	72	3	2.5	6	1	2.5	4.0
P21	Serpentinised dunite	75	3	3	3	1	2.5	10
P22	Chlorite Amphibole Dunite	60	6	3	3.5	1	2.5	3.4
P23	Massive dunite	77	4	3	3	1	2.5	7.7
P23	Massive dunite	88	3	2.5	3	1	2.5	9.8
P24	Massive dunite	68	3	2.5	3	1	2.5	7.6
P25	Chlorite Amphibole Dunite	73	1.5	3	3	1	2.5	19.6
P35	Chlorite Amphibole Dunite	50	6	3	4	0.66	2.5	1.7
P36	Chlorite Amphibole Dunite	85	9	0.75	4	1	2.5	0.7
P55	Gneiss	80	6	3	1.5	0.66	2.5	7
P55	Gneiss	70	3	2.5	3.5	1	2.5	6.7

Table A.3: Values of the estimated parameters for calculation of Q-value in area section 1. The locations for estimation indicated in the table are shown in the map in figure 3.3.

A.2.2 Section 2

Location	Rock	RQD	J_n	J_r	J_a	J_w	SRF	Q-value
P26	Chlorite Banded Dunite	77	6	3	4	0.66	1	6.3
P26	Chlorite Banded Dunite	73	3	3	4	1	1	18.3
P27	Chlorite Banded Dunite	57	6	2.5	3	1	1	7.9
P28	Chlorite Banded Dunite	80	3	3	6	0.66	1	8.8

Location	Rock	RQD	J_n	J_r	J_a	J_w	SRF	Q-value
P29	Chlorite Banded Dunite	83	3	2.5	3.5	0.66	1	13.1
P37	Chlorite Banded Dunite	80	3	3	3.5	1	1	22.9

Table A.4: Values of the estimated parameters for calculation of Q-value in area section 2. The locations for estimation indicated in the table are shown in the map in figure 3.3.

A.2.3 Section 3

Location	Rock	RQD	J_n	J_r	J_a	J_w	SRF	Q-value
P30	Dunite	83	6	3	3	0.66	2.5	3.7
P31	Dunite	87	1	3	3	0.66	2.5	22.9
P32	Dunite	87	3	3	3	0.66	2.5	7.6
P33	Dunite	70	3	3	3	0.66	2.5	6.2
P33	Dunite	73	3	1	3	0.66	2.5	2.2
P34	Dunite	70	3	2.5	3	1	2.5	7.8

Table A.5: Values of the estimated parameters for calculation of Q-value in area section 3. The locations for estimation indicated in the table are shown in the map in figure 3.3.

A.3 Shear strength of joints

A.3.1 Tilttesting

Location	Surface	Test conditions	Test 1 (°)	Test 2 (°)	Test 3 (°)	Test 4 (°)	Test 5 (°)	Median (°)
T1	Rough, slightly weathered surface	Rain	34.6	29.2	32.3	36.1	35.4	34.6
T2	Rough, slightly weathered surface	Rain	42.6	35.3	33.3	39.4	34.7	35.3
T3	Rough, slightly weathered surface	Rain	32.3	29.1	28	26.5	28.3	28.3
T4	Rough, slightly weathered surface	Dry	29.9	28.8	34.4	30.4	34.7	30.4
T5	Rough, sandy surface	Dry	24.1	40.2	37.1	34.3	33.6	34.3

Location	Surface	Test conditions	Test 1 (°)	Test 2 (°)	Test 3 (°)	Test 4 (°)	Test 5 (°)	Median (°)
T6	Rough, sandy surface	Dry	27.2	31.2	38.3	40.1	33.2	33.2
T7	Rough, sandy surface	Rain	29.6	39.5	36.5	36.3	34.3	36.3
T8	Rough, sandy surface	Rain	29.6	32.1	33.3	36.2	31.3	32.1
T9	Rough, sandy surface	Rain	36.5	35.3	45.7	29.5	40.9	36.5
T10	Rough, sandy surface	Dry	33.7	33.6	33.8	32.5	33.6	33.6
T11	Rough, sandy surface	Dry	43.1	44.5	44.5	44.7	43.2	44.5
T12	Rough, sandy surface	Rain	42.2	42.2	32.6	39.7	36.5	39.7
T13	Serpentized	Dry	29.1	29	29.3	41	29.5	29.3
T14	Serpentized	Dry	18.2	21.2	25.7	28.3	26.1	25.7
T15	Serpentized	Rain	24.3	27.2	23.9	25.7	27.5	25.7
T16	Serpentized	Dry	29.9	28.8	28.9	28.5	28.4	28.8
T17	Slickensided	Dry	28.4	31.1	30.2	28.1	30.4	30.2
T18	Slickensided	Dry	20.1	34.3	28.2	24.3	25.7	25.7
T19	Slickensided	Rain	20.7	16.5	18.3	17.4	17.8	17.8
T20	Talk, chlorite and mica coated surface	Dry	30.6	32.1	25	23.4	24.6	25
T21	Talk, chlorite and mica coated surface	mica	19.5	27.5	22.1	28.2	20.4	22.1
T22	Talk, chlorite and mica coated surface	surface	33.7	29.3	27.7	34.9	34.4	33.7
T23	Talk, chlorite and mica coated surface	Rain	28.6	23.8	23.3	27.4	25.5	25.5

Table A.6: The measured apparent friction angle for tilt tested blocks. The locations for testing indicated in the table are shown in the map in figure 3.5.

A.3.2 Joint Roughness Coefficient (JRC)

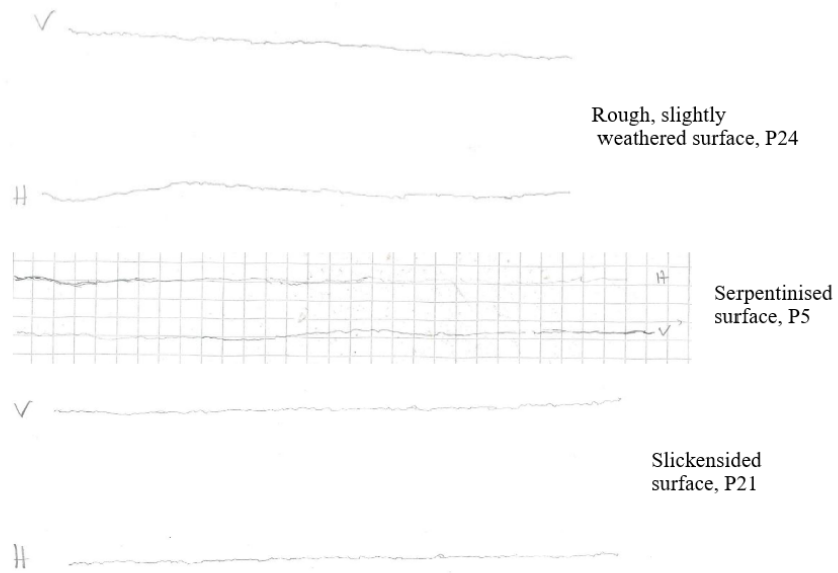


Figure A.1: Roughness profiles drawn during field mapping to estimate JRC.



Figure A.2: Roughness profiles drawn during field mapping to estimate JRC.

Location	Section	Rock	Surface Category	Horizontal value	Vertical value	Final value
P1	1	Chlorite Amphibole Dunite	Talk, chlorite and mica coated surface	10	12	11
P2	1	Chlorite Amphibole Dunite	Slickensided	10	12	11
P3	1	Chlorite Amphibole Dunite	Rough, sandy surface	4	8	6
P4	1	Chlorite Amphibole Dunite	Serpentized	8	6	7
P5	1	Chlorite Amphibole Dunite	Serpentized	4	8	6
P5	1	Chlorite Amphibole Dunite	Serpentized	4	8	6
P6	1	Chlorite Amphibole Dunite	Serpentized	2	5	3.5
P6	1	Chlorite Amphibole Dunite	Serpentized	2	5	3.5
P7	1	Chlorite Amphibole Dunite	Rough, slightly weathered surface	8	6	7
P7	1	Chlorite Amphibole Dunite	Rough, slightly weathered surface	8	6	7
P8	1	Chlorite Amphibole Dunite	Rough, slightly weathered surface	12	8	10
P8	1	Chlorite Amphibole Dunite	Rough, slightly weathered surface	12	8	10
P9	1	Chlorite Amphibole Dunite	Serpentized	2	5	3.5
P9	1	Chlorite Amphibole Dunite	Serpentized	2	5	3.5

Location	Section	Rock	Surface Category	Horizontal value	Vertical value	Final value
P10	1	Chlorite Amphibole Dunite	Rough, slightly weathered surface	14	9	11.5
P10	1	Chlorite Amphibole Dunite	Rough, slightly weathered surface	14	9	11.5
P11	1	Chlorite Amphibole Dunite	Rough, slightly weathered surface	12	8	10
P12	1	Chlorite Amphibole Dunite	Serpentized	12	8	10
P13	1	Chlorite Amphibole Dunite	Rough, slightly weathered surface	13	11	12
P13	1	Chlorite Amphibole Dunite	Rough, slightly weathered surface	12	8	10
P14	1	Chlorite Amphibole Dunite	Talk, chlorite and mica coated surface	7	7	7
P14	1	Chlorite Amphibole Dunite	Rough, slightly weathered surface	8	7	7.5
P15	1	Chlorite Amphibole Dunite	Rough, slightly weathered surface	12	8	10
P15	1	Chlorite Amphibole Dunite	Rough, slightly weathered surface	8	7	7.5
P16	1	Chlorite Amphibole Dunite	Rough, slightly weathered surface	3	2	2.5
P17	1	Chlorite Amphibole Dunite	Rough, slightly weathered surface	3	2	2.5
P17	1	Chlorite Amphibole Dunite	Talk, chlorite and mica coated surface	12	10	11
P18	1	Chlorite Amphibole Dunite	Slickensided	6	12	9

Location	Section	Rock	Surface Category	Horizontal value	Vertical value	Final value
P19	1	Chlorite Amphibole Dunite	Rough, slightly weathered surface	8	7	7.5
P20	1	Chlorite Amphibole Dunite	Talk, chlorite and mica coated surface	8	7	7.5
P21	1	Chlorite Amphibole Dunite	Talk, chlorite and mica coated surface	8	8	8
P21	1	Chlorite Amphibole Dunite	Slickensided	8	8	8
P22	1	Chlorite Amphibole Dunite	Rough, slightly weathered surface	8	7	7.5
P22	1	Chlorite Amphibole Dunite	Rough, slightly weathered surface	6	6	6
P23	1	Massiv Dunite	Rough, slightly weathered surface	12	8	10
P24	1	Massiv Dunite	Rough, slightly weathered surface	8	7	7.5
P24	1	Massiv Dunite	Rough, slightly weathered surface	5	6	5.5
P25	1	Chlorite Amphibole Dunite	Slickensided	6	4	5
P25	1	Chlorite Amphibole Dunite	Slickensided	6	4	5
P26	2	Chlorite Banded Dunite	Talk, chlorite and mica coated surface	6	6	6
P27	2	Chlorite Banded Dunite	Serpentized	6	6	6
P28	2	Chlorite Banded Dunite	Rough, sandy surface	6	4	5
P28	2	Chlorite Banded Dunite	Rough, sandy surface	6	4	5
P29	2	Chlorite Banded Dunite	Rough, sandy surface	6	4	5

Location	Section	Rock	Surface Category	Horizontal value	Vertical value	Final value
P29	2	Chlorite Banded Dunite	Rough, sandy surface	6	4	5
P30	3	Dunite	Rough, sandy surface	12	6	9
P30	3	Dunite	Rough, sandy surface	8	6	7
P31	3	Dunite	Rough, sandy surface	8	6	7
P32	3	Dunite	Rough, sandy surface	8	6	7
P33	3	Dunite	Rough, sandy surface	6	4	5
P34	3	Dunite	Rough, sandy surface	6	6	6

Table A.7: Estimated JRC-values for different surfaces in the quarry. The locations for testing indicated in the table are shown in the map in figure 3.6.

A.3.3 Joint Compressive Strength (JCS)

Point	Section	Rock	Surface Category	Direction	Rebound value											Mean value	Density (kN/m^3)	JCS (MPa)
					1	2	3	4	5	6	7	8	9	10	11			
P1	1	Chlorite Amphibole Dunite	Talk, chlorite and mica coated surface	Horizontal	12	22	14	18	17	13	12	12	14	17	15	28.1	20	
P2	1	Chlorite Amphibole Dunite	Slickensided	Horizontal	18	19	35	18	26	26	20	27	28	22	23	28.1	33	
P3	1	Chlorite Amphibole Dunite	Rough, sandy surface	Horizontal	27	25	40	42	26	30	20	35	34	30	31	28.1	50	
P4	1	Chlorite Amphibole Dunite	Serpentinised	Horizontal	20	15	20	17	24	24	21	25	22	20	21	28.1	28	
P5	1	Chlorite Amphibole Dunite	Serpentinised	Horizontal	40	40	30	38	43	29	33	36	31	30	36	28.1	67	
P5	1	Chlorite Amphibole Dunite	Serpentinised	Horizontal	38	33	26	30	36	37	49	35	36	49	36	28.1	67	
P6	1	Chlorite Amphibole Dunite	Serpentinised	Horizontal	26	29	23	30	33	35	35	38	31	39	32	28.1	53	
P6	1	Chlorite Amphibole Dunite	Serpentinised	Horizontal	27	31	23	21	24	26	30	34	30	24	27	28.1	40	
P7	1	Chlorite Amphibole Dunite	Rough, slightly weathered surface	Horizontal	32	25	35	33	28	35	31	29	26	28	30	28.1	48	
P7	1	Chlorite Amphibole Dunite	Rough, slightly weathered surface	Horizontal	25	25	32	27	37	26	23	26	28	40	29	28.1	44	

Point	Section	Rock	Surface Category	Direction	Rebound value								Mean value	Density (kN/m^3)	JCS (MPa)		
P8	1	Chlorite Amphibole Dunite	Rough, slightly weathered surface	Horizontal	22	39	27	42	40	35	36	40	41	39	37	28.1	71
P8	1	Chlorite Amphibole Dunite	Rough, slightly weathered surface	Horizontal	35	34	34	25	34	34	44	32	40	41	36	28.1	67
P9	1	Chlorite Amphibole Dunite	Serpentinised	Horizontal	33	21	27	31	23	29	28	27	24	40	28	28.1	42
P9	1	Chlorite Amphibole Dunite	Serpentinised	Horizontal	15	21	17	31	26	22	33	24	29	22	24	28.1	34
P10	1	Chlorite Amphibole Dunite	Rough, slightly weathered surface	Horizontal	25	35	34	20	35	29	21	34	19	34	28	28.1	42
P10	1	Chlorite Amphibole Dunite	Rough, slightly weathered surface	Horizontal	23	24	20	33	24	28	36	32	32	34	29	28.1	44
P11	1	Chlorite Amphibole Dunite	Rough, slightly weathered surface	Horizontal	37	26	34	33	20	34	21	31	29	37	30	28.1	48
P12	1	Chlorite Amphibole Dunite	Serpentinised	Horizontal	27	27	25	35	30	33	25	32	25	20	28	28.1	42
P13	1	Chlorite Amphibole Dunite	Rough, slightly weathered surface	Horizontal	28	23	25	27	26	20	30	20	25	23	25	28.1	35
P13	1	Chlorite Amphibole Dunite	Rough, slightly weathered surface	Horizontal	38	26	26	46	31	32	30	28	27	31	30	28.1	48

Point	Section	Rock	Surface Category	Direction	Rebound value										Mean value	Density (kN/m^3)	JCS (MPa)
P14	1	Chlorite Amphibole Dunite	Talk, chlorite and mica coated surface	Horizontal	38	38	38	46	47	45	29	37	41	38	39	28.1	82
P14	1	Chlorite Amphibole Dunite	Rough, slightly weathered surface	Horizontal	29	36	29	27	36	30	36	41	41	26	33	28.1	55
P15	1	Chlorite Amphibole Dunite	Rough, slightly weathered surface	Horizontal	43	40	38	53	46	47	44	39	42	54	44	28.1	108
P15	1	Chlorite Amphibole Dunite	Rough, slightly weathered surface	Horizontal	43	27	31	24	28	34	42	26	36	31	32	28.1	53
P16	1	Chlorite Amphibole Dunite	Rough, slightly weathered surface	Vertical down	43	39	37	38	37	44	42	48	45	45	42	28.1	108
P17	1	Chlorite Amphibole Dunite	Rough, slightly weathered surface	Vertical down	51	47	38	39	44	31	35	45	47	45	43	28.1	120
P18	1	Chlorite Amphibole Dunite	Talk, chlorite and mica coated surface	Horizontal	38	37	47	42	30	33	46	36	43	39	39	28.1	82
P19	1	Chlorite Amphibole Dunite	Slickensided	Horizontal	35	39	21	39	39	39	33	39	44	43	38	28.1	77
P20	1	Chlorite Amphibole Dunite	Rough, slightly weathered surface	Horizontal	33	21	21	22	20	18	22	29	17	37	23	28.1	33
P21	1	Chlorite Amphibole Dunite	Talk, chlorite and mica coated surface	Horizontal	31	31	36	37	28	29	31	21	28	30	31	28.1	50

Point	Section	Rock	Surface Category	Direction	Rebound value										Mean value	Density (kN/m^3)	JCS (MPa)	
P22	1	Chlorite Amphibole Dunite	Talk, chlorite and mica coated surface	Horizontal	37	48	36	36	18	31	35	25	32	26	41	34	28.1	61
P22	1	Chlorite Amphibole Dunite	Slickensided	Vertical down	56	39	58	52	40	56	51	50	58	38		50	28.1	170
P23	1	Chlorite Amphibole Dunite	Rough, slightly weathered surface	Vertical down	47	22	41	39	34	36	32	34	29	37	25	34	28.1	67
P23	1	Chlorite Amphibole Dunite	Rough, slightly weathered surface	Vertical down	31	36	32	35	31	39	29	29	29	42		33	28.1	64
P24	1	Massive dunite	Rough, slightly weathered surface	Horizontal	40	40	38	37	36	26	39	34	43	34		37	25.8	68
P25	1	Massive dunite	Rough, slightly weathered surface	Horizontal	35	38	41	34	30	41	41	41	38	43	44	39	25.8	65
P25	1	Massive dunite	Rough, slightly weathered surface	Horizontal	35	42	33	40	41	43	43	45	43			41	25.8	75
P26	1	Chlorite Amphibole Dunite	Slickensided	Horizontal	59	52	52	51	51	51	49	44	54	56	56	52	28.1	170
P26	1	Chlorite Amphibole Dunite	Slickensided	Horizontal	57	57	61	49	58	59	56	43	59	61	61	57	0.0	235
P27	2	Chlorite Banded Dunite	Talk, chlorite and mica coated surface	Horizontal	23	19	29	34	32	35	31	28	26	32	36	30	31.1	60

Point	Section	Rock	Surface Category	Direction	Rebound value										Mean value	Density (kN/m^3)	JCS (MPa)	
P28	2	Chlorite Banded Dunite	Serpentinised	Horizontal	37	36	31	39	31	32	36	31	31	13	13	31	31.1	50
P29	2	Chlorite Banded Dunite	Rough, sandy surface	Horizontal	16	21	14	13	20	15	13	17	14	26		16	31.1	23
P29	2	Chlorite Banded Dunite	Rough, sandy surface	Vertical down	21	26	19	21	22	21	26	21	25	38	39	25	31.1	49
P30	2	Chlorite Banded Dunite	Rough, sandy surface	Horizontal	34	34	37	34	36	34	38	41	33	35		35	31.1	80
P30	2	Chlorite Banded Dunite	Rough, sandy surface	Horizontal	38	34	41	41	39	31	39	44	39	38		38	31.1	99
P31	3	Dunite	Rough, sandy surface	Horizontal	24	23	17	19	21	18	17	27	22	24		21	31.7	31
P31	3	Dunite	Rough, sandy surface	Vertical down	35	33	29	33	38	31	33	37	33	34		34	31.7	90
P32	3	Dunite	Rough, sandy surface	Vertical down	19	21	17	16	17	21	23	24	26	20	24	21	31.7	38
P32	3	Dunite	Rough, sandy surface	Vertical down	29	28	26	18	24	24	20	25	27	24		25	31.7	49
P33	3	Dunite	Rough, sandy surface	Horizontal	21	16	28	27	26	28	37	33	37	31	32	29	31.7	52
P34	3	Dunite	Rough, sandy surface	Horizontal	36	26	44	34	43	40	47	21	29	44	42	38	31.7	98

Table A.8: Measured rebound values, and the corresponding JCS-values for surfaces in the quarry. The locations for testing indicated in the table are shown in the map in figure 3.6.

B. Lab testing

B.1 Uniaxial Compressive Strength (UCS) Testing

B.1.1 Typical failure modes of UCS-tested cores

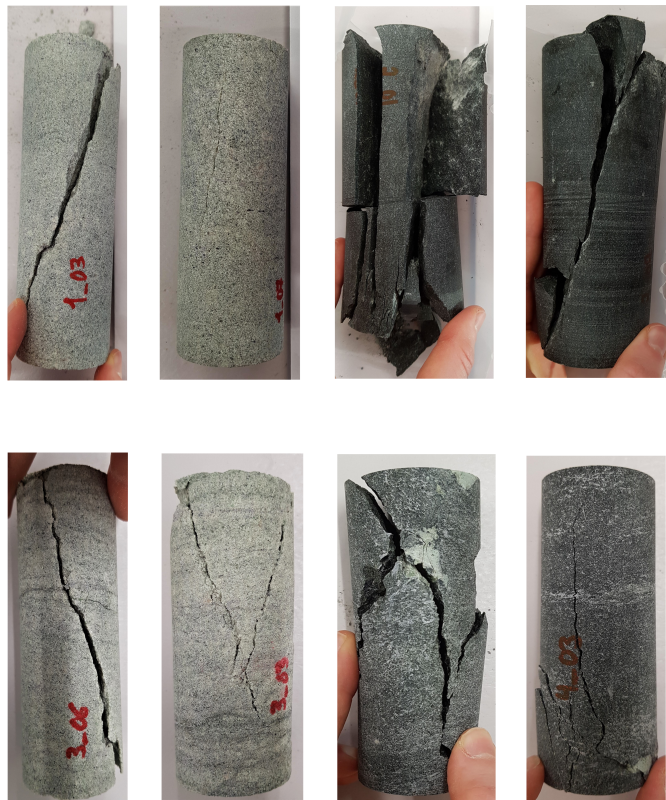


Figure B.1: The photos by Aasteboel (2019) show typical failure modes of cores from block No.1, 2, 3 and 4 during UCS-testing.

B.1.2 The complete data from UCS-testing

Block No.	Core number	Rock	Average diameter (mm)	Length (mm)	UCS (MPa)	Young's modulus E (GPa)	Poisson's ratio ν	Failure mode	Fracture angle θ ($^{\circ}$)
B1	1	Dunite	50.04	134.21	88.7	62.6	0.53	Shear failure	21.1

Block No.	Core number	Rock	Average diameter (mm)	Length (mm)	UCS (MPa)	Young's modulus E (GPa)	Poisson's ratio ν	Failure mode	Fracture angle θ (°)
B1	2	Dunite	49.95	134.21	82.7	55.8	0.30	Shear failure	20.9
B1	3	Dunite	50.09	134.22	85.2	55.4	0.45	Shear failure	20.8
B1	4	Dunite	50.04	127.69	84.5	51.5	0.50	Shear failure	18.8
B1	7	Dunite	49.95	128.53	84.6	53.6	0.46	Shear failure	18.3
B2	1	Massive Dunite	50.14	135.11	165.5	56.4	0.35	Complex failure	
B2	2	Massive Dunite	50.04	135.09	74.3	60.3	0.40	Complex failure	
B2	3	Massive Dunite	50.02	135.07	163.9	57.6	0.35	Complex failure	
B2	4	Massive Dunite	50.12	135.08	112.5	61.8	0.33	Complex failure	
B2	5	Massive Dunite	50.11	135.1	132.4	62.3	0.28	Complex failure	
B2	6	Massive Dunite	50.00	133.43	131.9	61.4	0.37	Complex failure	
B3	1	Chlorite Banded Dunite	40.67	110.19	83.6	40.7	0.39	Shear failure	23.3
B3	2	Chlorite Banded Dunite	40.66	108.82	79.1	30.9	0.26	Shear failure	19.9
B3	3	Chlorite Banded Dunite	40.67	110.2	73.4	27.5	0.41	Shear failure	22.3
B3	4	Chlorite Banded Dunite	40.67	110.21	87.8	38.2	0.35	Shear failure	22.6
B3	5	Chlorite Banded Dunite	40.68	110.24	83.4	40.3	0.37	Shear failure	25.9
B3	6	Chlorite Banded Dunite	40.72	110.49	87.1	39.8	0.31	Shear failure	20.2
B3	7	Chlorite Banded Dunite	40.67	108.67	78.1	30.8	0.36	Shear failure	18.3
B4	1	Serpentinised dunite	40.68	110.37	79.4	53.4	0.28	Complex failure	

Block No.	Core number	Rock	Average diameter (mm)	Length (mm)	UCS (MPa)	Young's modulus E (GPa)	Poisson's ratio ν	Failure mode	Fracture angle θ ($^{\circ}$)
B4	2	Serpentinised dunite	40.67	110.43	85.8	56.2	0.28	Complex failure	
B4	3	Serpentinised dunite	40.66	110.36	95	53.0	0.22	Complex failure	
B4	4	Serpentinised dunite	40.68	110.74	85.5	51.7	0.27	Complex failure	
B4	5	Serpentinised dunite	40.67	110.71	93.2	55.6	0.30	Complex failure	

Table B.1: Results from UCS-testing of the cores from block No. 1, 2, 3 and 4., after Aasteboel (2019).

B.1.3 Graphical representation of the results from UCS-testing

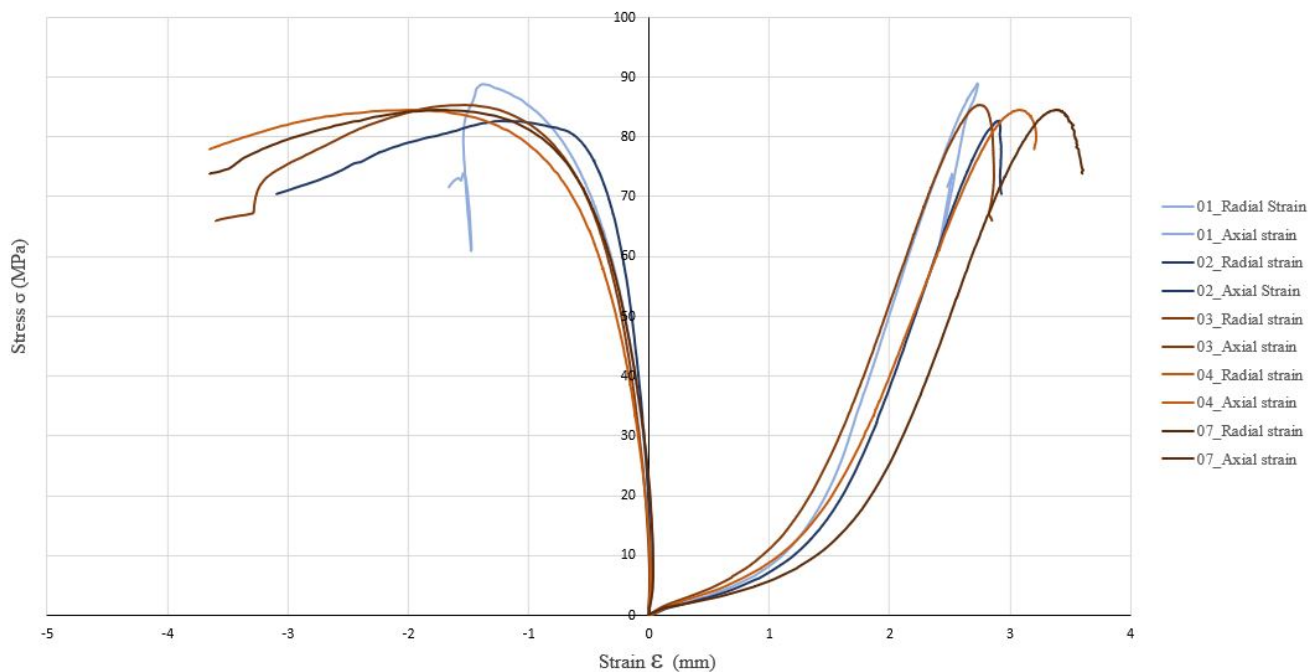


Figure B.2: Graphical representation, after Aasteboel (2019), of the relationship between stress and strain during UCS-testing of five cores from block No. 1.

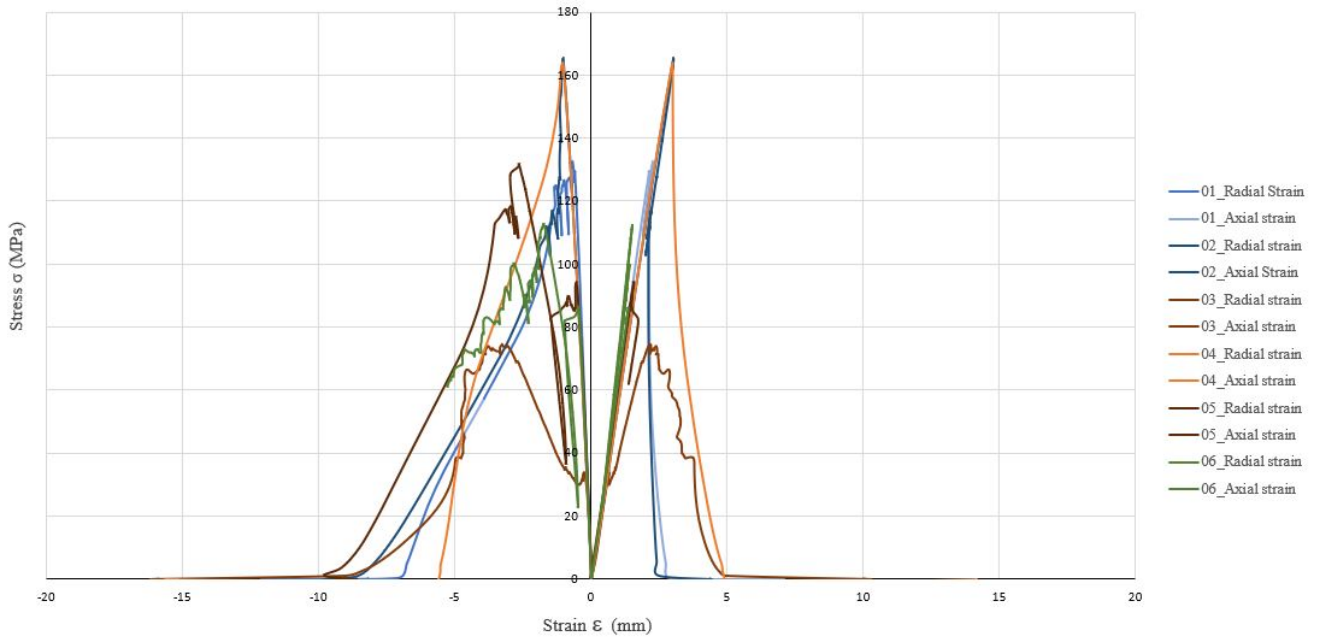


Figure B.3: Graphical representation, after Aasteboel (2019), of the relationship between stress and strain during UCS-testing of six cores from block No. 2.

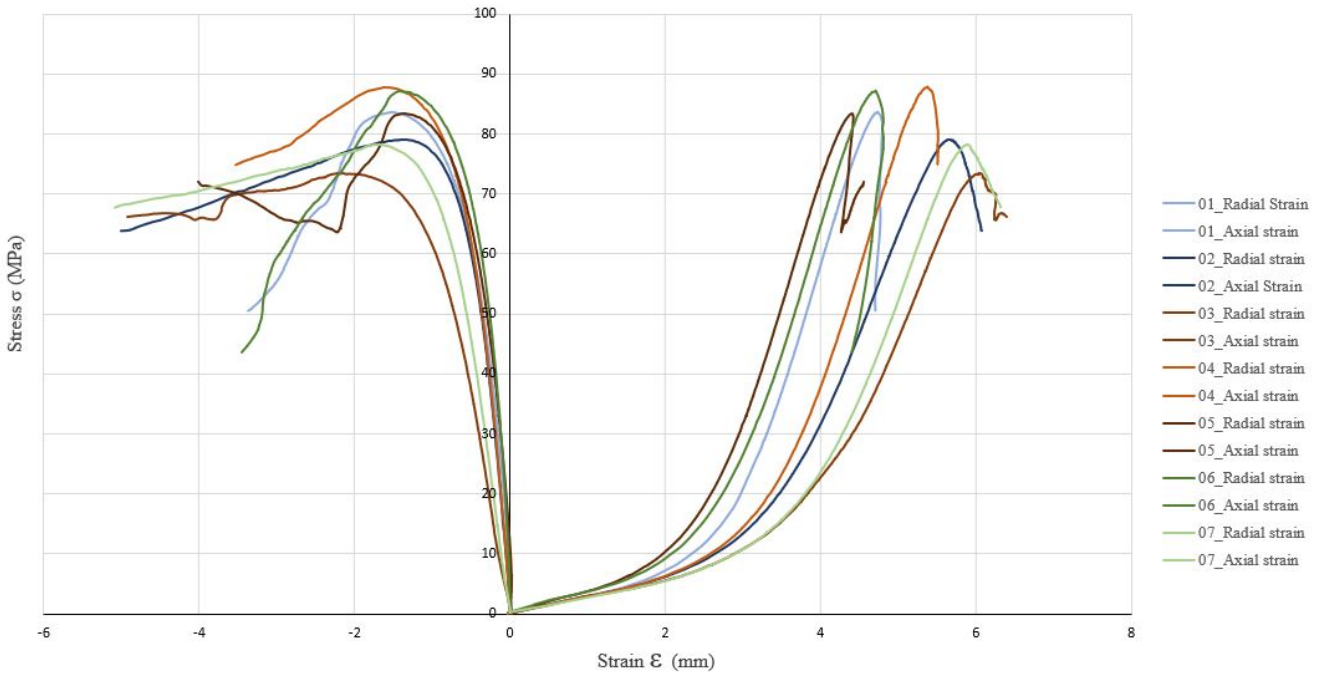


Figure B.4: Graphical representation, after Aasteboel (2019), of the relationship between stress and strain during UCS-testing of seven cores from block No. 3.

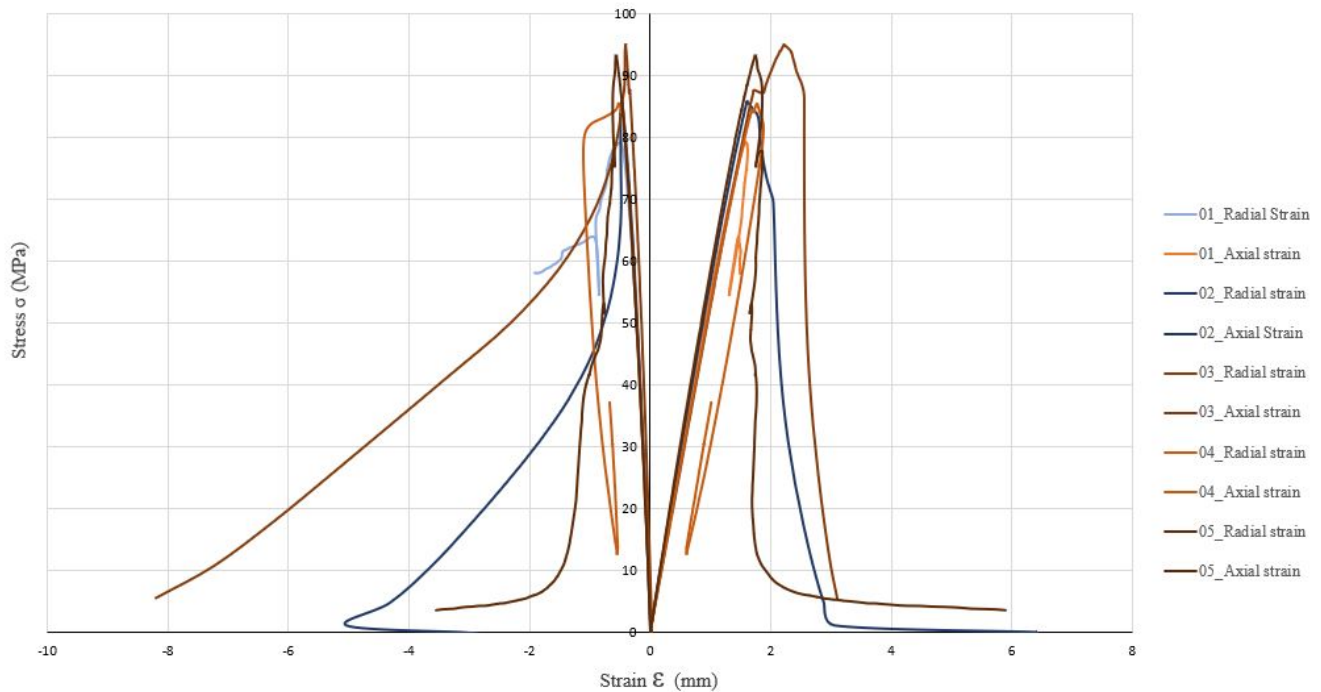


Figure B.5: Graphical representation, after Aasteboel (2019), of the relationship between stress and strain during UCS-testing of five cores from block No. 4.

B.2 P-wave velocity testing

Block No.	Core number	Rock	Average diameter (mm)	Length (mm)	Weight (g)	time	Density	p-wave velocity
B1	1	Dunite	50.04	134.21	854.53	49	3.24	2739.0
B1	2	Dunite	49.95	134.21	851.24	50.6	3.24	2652.4
B1	3	Dunite	50.09	134.22	855.83	51	3.24	2631.8
B1	4	Dunite	50.04	127.69	810.02	51.1	3.23	2498.8
B1	5	Dunite	50.10	135.11	859.13	54.9	3.23	2461.0
B1	6	Dunite	50.09	134.01	849.64	57.4	3.22	2334.7
B1	7	Dunite	49.95	128.53	811.97	54.5	3.22	2358.3
B2	1	Massive Dunite	50.14	135.11	707.21	23.4	2.65	5773.9
B2	2	Massive Dunite	50.04	135.09	694.58	24	2.61	5628.8
B2	3	Massive Dunite	50.02	135.07	695.57	23.9	2.62	5651.5
B2	4	Massive Dunite	50.12	135.08	697.81	23.4	2.62	5772.6
B2	5	Massive Dunite	50.11	135.1	708.46	23.4	2.66	5773.5

Block No.	Core number	Rock	Average diameter (mm)	Length (mm)	Weight (g)	time	Density	p-wave velocity
B2	6	Massive Dunite	50.00	133.43	690.59	23.4	2.64	5702.1
B3	1	Chlorite Banded Dunite	40.67	110.19	455.92	96.3	3.18	1144.2
B3	2	Chlorite Banded Dunite	40.66	108.82	447.72	98.7	3.17	1102.5
B3	3	Chlorite Banded Dunite	40.67	110.2	453.28	97.5	3.17	1130.3
B3	4	Chlorite Banded Dunite	40.67	110.21	455.06	91.4	3.18	1205.8
B3	5	Chlorite Banded Dunite	40.68	110.24	455.24	86.4	3.18	1275.9
B3	6	Chlorite Banded Dunite	40.72	110.49	456.75	87.2	3.17	1267.1
B3	7	Chlorite Banded Dunite	40.67	108.67	446.95	96.4	3.17	1127.3
B4	1	Serpentinised	40.68	110.37	411.93	20	2.87	5518.5
B4	2	Serpentinised	40.67	110.43	412.6	19.9	2.88	5549.2
B4	3	Serpentinised	40.66	110.36	409.95	20.4	2.86	5409.8
B4	4	Serpentinised	40.68	110.74	410.58	20.4	2.85	5428.4
B4	5	Serpentinised	40.67	110.71	413.25	19.9	2.87	5563.3
B4	6	Serpentinised	40.67	110.72	413.24	20.4	2.87	5427.5
B4	7	Serpentinised	40.66	110.71	413.06	20.4	2.87	5427.0

Table B.2: Results from p-wave velocity test of the cores from block No. 1,2, 3 and 4., after Aasteboel (2019).

B.3 Free Swelling Test



Figure B.6: Photo, after Aasteboel (2019), of clay from weakness zones Z4 after 24 hours of swelling in free swelling test.

C. Core logging

C.1 Weakness zone Z1-Z5



Figure C.1: Photo of the core with the weakness zones evaluated to be related to the weakness zone Z1-Z5 observed in the quarry.

C.2 Contact zone at the gneiss boundary



(a) Photo of contact zone in drill core GU-D2010-039.



(b) Photo of contact zone in drill core GU-D2010-040.



(c) Photo of contact zone in drill core GU-D2010-040.



(d) Photo of contact zone in drill core GU-D2010-040.

Figure C.2: Photos of the areas in the studied cores evaluated to correspond to the contact zone at the gneiss boundary observed in the quarry at point Z8.



(e) Photo of contact zone in drill core GU-D2010-041.



(f) Photo of contact zone in drill core GU-D2010-041.



(g) Photo of contact zone in drill core GU-D2010-042.



(h) Photo of contact zone in drill core GU-D2010-042.

Figure C.2: Photos of the areas in the studied cores evaluated to correspond to the contact zone at the gneiss boundary observed in the quarry at point Z8.



(i) Photo of contact zone in drill core GU-D2010-043.



(j) Photo of contact zone in drill core GU-D2010-043.



(k) Photo of contact zone in drill core GU-D2010-043.

Figure C.2: Photos of the areas in the studied cores evaluated to correspond to the contact zone at the gneiss boundary observed in the quarry at point Z8.

C.3 Eclogite and amphibolite zones



(a) Photo of the widest eclogite and amphibolite zone in drill core GU-D2010-039.



(b) Photo of two eclogite zones in drill core GU-D2010-040.



(c) Photo of an eclogite zone in drill core GU-D2010-040.



(d) Photo of parts of the widest eclogite and amphibolite zone in drill core GU-D2010-042.



(e) Photo of the rest of the widest eclogite and amphibolite zone and another eclogite zone in drill core GU-2010-042.



(f) Photos of the areas in the studied cores with eclogite and amphibolite zones.

Figure C.3: Photos of weathering of chlorite banded dunite.

C.4 Data from core logs by Sibelco Nordic

C.4.1 Drill core GU-D2010-039

GU-D2010-039		
Depth from (m)	Depth to (m)	Rock type *
0	1	DUN
1	5.12	DUN
5.12	5.13	SERP
5.13	5.25	DUN
5.25	5.28	SERP
5.28	5.53	DUN
5.53	5.55	SERP
5.55	5.8	DUN
5.8	6	DUN
6	6.2	DUN
6.2	9.5	DUN
9.5	10	DUN
10	15.25	DUN
15.25	16.75	DUN
16.75	21.67	DUN
21.67	35.25	CHBDUN
35.25	46.25	DUN
46.25	51.2	DUN
51.2	70.75	DUN
70.75	79	DUN
79	80.7	DUN
80.7	83.3	SERP
83.3	124.4	DUN
124.4	125.66	ECLO
125.66	125.75	ECLO
125.75	126.3	ECLO
126.3	127.15	DUN
127.15	129	DUN
129	132.6	DUN
132.6	132.8	DUN
132.8	136	DUN
136	136.3	DUN
136.3	138.5	DUN
138.5	138.65	UKJENT
138.65	144.3	DUN
144.3	144.6	ECLO
144.6	145.6	DUN
145.6	155.8	DUN
155.8	156.5	ECLO
156.5	157.3	DUN
157.3	157.6	SERPDUN
157.6	158.1	DUN
158.1	160.9	SERPDUN
160.9	161	SERP
161	178.8	SERPDUN
178.8	202.65	SERP
202.65	202.8	UKJENT
202.8	205.8	TAP
205.8	206.15	SERPDUN
206.15	208.3	GNEISS
208.3	220.4	SERP

*The geology is described by abbreviations for the different rock types. The abbreviations has the following meaning:
DUN = Dunite, SERP = Serpentine, CHBDUN = Chlorite banded dunite, ECLO = Eclogite, SERPDUN = Serpentinized dunite,
TAP = Loss of core, UKJENT = Unknown rock type

Table C.1: The data of drill core GU-D2010-039 from the core logs by Sibelco Nordic used to study the core.

C.4.2 Drill core GU-D2010-040

GU-D2010-040		
Depth from (m)	Depth to (m)	Geology *
0	12.8	CHBDUN
12.8	14.4	CHBDUN
14.4	21.4	DUN
21.4	33.5	DUN
33.5	50.4	DUN
50.4	50.5	DUN
50.5	59.3	DUN
59.3	62.5	DUN
62.5	68	DUN
68	71.8	DUN
71.8	87	DUN
87	91.85	DUN
91.85	106	DUN
106	115.1	SERPDUN
115.1	116	SERPDUN
116	126.5	SERPDUN
126.5	126.6	ECLO
126.6	127.2	SERPDUN
127.2	127.45	ECLO
127.45	145.5	SERPDUN
145.5	146.3	ECLO
146.3	189	SERPDUN
189	214.25	SERP
214.25	231	GNEISS

*The geology is described by abbreviations for the different rock types. The abbreviations has the following meaning:
DUN = Dunite, SERP = Serpentinite, CHBDUN = Chlorite banded dunite, ECLO = Eclogite, SERPDUN = Serpentinized dunite
TAP = Loss of core, UKJENT = Unknown rock type

Table C.2: The data of drill core GU-D2010-040 from the core logs by Sibelco Nordic used to study the core.

C.4.3 Drill core GU-D2010-041

GU-D2010-041		
Depth from (m)	Depth to (m)	Geology *
0	0.9	TAP
0.9	18	CHBDUN
18	30	CHBDUN
30	52.63	DUN
52.63	71.1	DUN
71.1	81.5	DUN
81.5	81.7	SERP
81.7	82.5	DUN
82.54	110.5	DUN
110.5	114	DUN
114	125.53	DUN
125.53	130.8	DUN
130.8	131.1	ECLO
131.1	141.05	DUN
141.05	166.1	SERPDUN
166.1	180.9	DUN
180.9	182.7	SERPDUN
182.7	211.28	SERP
211.28	217.25	GNEISS
217.25	217.5	GNEISS
217.5	222	GNEISS
222	237.8	GNEISS
*The geology is described by abbreviations for the different rock types. The abbreviations has the following meaning: DUN = Dunite, SERP = Serpentine, CHBDUN = Chlorite banded dunite, ECLO = Eclogite, SERPDUN = Serpentinized dunite TAP = Loss of core, UKJENT = Unknown rock type		

Table C.3: The data of drill core GU-D2010-041 from the core logs by Sibelco Nordic used to study the core.

C.4.4 Drill core GU-D2010-042

GU-D2010-042		
Depth from (m)	Depth to (m)	Geology *
0	0.1	TAP
0.1	5	DUN
5	5.8	DUN
5.8	6.75	DUN
6.75	6.94	DUN
6.94	12.15	DUN
12.15	14.1	SERPBRUC
14.1	19.1	DUN
19.1	20.2	SERPBRUC
20.2	21.11	DUN
21.11	21.2	SERPBRUC
21.2	30.1	DUN
30.1	30.17	SERPBRUC
30.17	40.25	DUN
40.25	42.8	DUN
42.8	49.63	DUN
49.63	49.67	UKJENT
49.67	57.92	DUN
57.92	62.8	DUN
62.8	63.5	DUN
63.5	82.34	DUN
82.34	82.7	DUN
82.7	98.25	DUN
98.25	98.6	DUN
98.6	105.7	DUN
105.7	110.8	DUN
110.8	115	DUN
115	130.9	DUN
130.9	132.4	ECLO
132.4	132.8	ECLO
132.8	136.2	DUN
136.2	136.7	ECLO
136.7	136.95	UKJENT
136.95	141.15	SERPBRUC
141.15	175.9	SERPBRUC
175.9	175.95	ECLO
175.95	176	SERPBRUC
176	176.2	ECLO
176.2	186.5	SERPBRUC
186.5	196.5	GNEISS
196.5	221.5	GNEISS

*The geology is described by abbreviations for the different rock types. The abbreviations have the following meaning:
DUN = Dunite, SERP = Serpentinite, CHBDUN = Chlorite banded dunite, ECLO = Eclogite, SERPBRUC = Serpentinized dunite,
SERPBRUC = Serpentinized shear zone

TAP = Loss of core, UKJENT = Unknown rock

Table C.4: The data of drill core GU-D2010-042 from the core logs by Sibelco Nordic used to study the core.

C.4.5 Drill core GU-D2010-043

GU-D2010-043		
Depth from (m)	Depth to (m)	Geology *
0	0.1	TAP
0.1	29.7	CHBDUN
29.7	42.5	DUN
42.5	52.35	CHBDUN
52.35	52.55	SERPBRZC
52.55	53.05	CHBDUN
53.05	58.3	CHBDUN
58.3	62.15	DUN
62.15	67.9	DUN
67.9	68.7	DUN
68.7	69	DUN
69	72.6	DUN
72.6	75.1	DUN
75.1	115.15	DUN
115.15	125.75	DUN
125.75	127.6	SERPDUN
127.6	131.2	DUN
131.2	131.35	UKJENT
131.35	133.85	DUN
133.85	134.6	SERPDUN
134.6	139.8	DUN
139.8	163.2	DUN
163.2	181.4	DUN
181.4	188.9	DUN
188.9	190.9	ECLO
190.9	192.3	SERPDUN
192.3	193.1	DUN
193.1	211	SERP
211	219.85	GNEISS
219.85	220.3	GNEISS
220.3	227.05	GNEISS
227.05	235.8	GNEISS

*The geology is described by abbreviations for the different rock types. The abbreviations has the following meaning:
DUN = Dunite, SERP = Serpentine, CHBDUN = Chlorite banded dunite, ECLO = Eclogite, SERPDUN = Serpentinized dunite,
SERPBREC = Serpentinized shear zone

TAP = Loss of core, UKJENT = Unknown rock

Table C.5: The data of drill core GU-D2010-043 from the core logs by Sibelco Nordic used to study the core.

C.4.6 Drill core GU-D2010-047

GU-D2010-047		
Depth from (m)	Depth to (m)	Geology *
0	1.4	JORD
1.4	11.45	DUN
11.45	14.3	DUN
14.3	18.4	DUN
18.4	21.2	DUN
21.2	24	SERPDUN
24	26	DUN
26	36.65	DUN
36.65	45.6	DUN
45.6	48	DUN
48	49	ECLD
49	55	DUN
55	60.7	SERPDUN
60.7	78.5	DUN
78.5	83	DUN
83	84.3	SERPDUN
84.3	89	DUN
89	90	SERPDUN
90	91.9	DUN
91.9	98.7	DUN
98.7	107	DUN
107	115.35	DUN
115.35	116	SERP
116	120	SERPDUN
120	135.8	SERP
135.8	137.4	GNEISS
137.4	142	GNEISS
142	144.1	GNEISS
144.1	152.8	GNEISS
152.8	155.3	GNEISS
*The geology is described by abbreviations for the different rock types. The abbreviations has the following meaning: DUN = Dunite, SERP = Serpentinite, CHBDUN = Chlorite banded dunite, ECLD = Eclogite, SERPDUN = Serpentinized dunite TAP = Loss of core, UKJENT = Unknown rock		

Table C.6: The data of drill core GU-D2010-047 from the core logs by Sibelco Nordic used to study the core.

C.4.7 Drill core GU-D2013-054

GU-D2010-054		
Depth from (m)	Depth to (m)	Geology *
0	5.65	DUN
5.65	6.8	DUN
6.8	7.4	DUN
7.4	7.44	DUN
7.44	11.36	DUN
11.36	29.55	DUN
29.55	36.1	DUN
36.1	49	DUN
49	69.24	DUN
69.24	69.7	SERPDUN
69.7	86.8	SERPDUN
86.8	87.75	SERPDUN
87.75	88	SERP
88	88.1	GNEISS

*The geology is described by abbreviations for the different rock types. The abbreviations has the following meaning:
DUN = Dunite, SERP = Serpentine, SERPDUN = Serpentinized dunite
TAP = Loss of core, UKJENT = Unknown rock

Table C.7: The data of drill core GU-D2010-054 from the core logs by Sibelco Nordic used to study the core.

D. Rock Mass Classification

D.1 Barton-Bandis failure criterion

D.1.1 Determination of JCS from rebound value

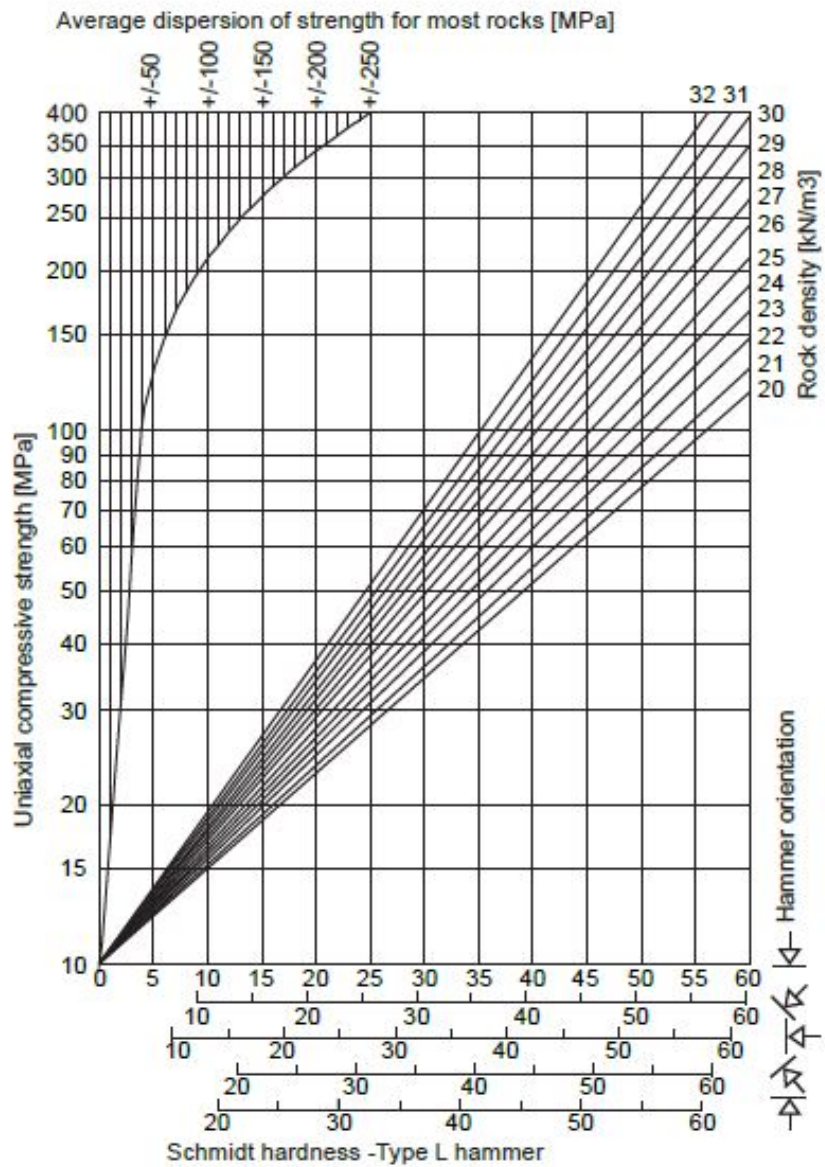


Figure D.1: Chart by Deere and Miller (1966) used to determine JCS based on measured Schmidtness hardness SH and the density of measured rock.

D.1.2 Determination of JRC from roughness profiles

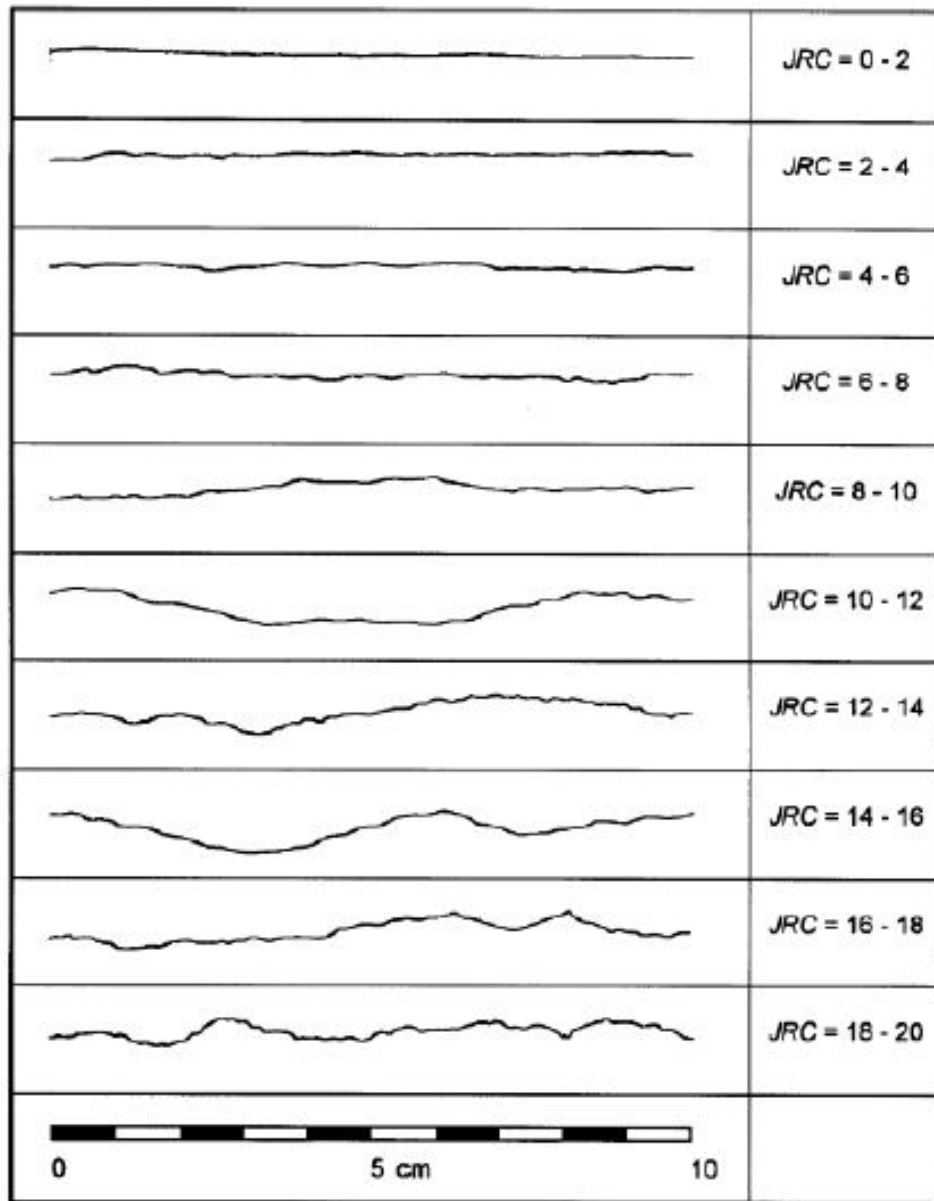


Figure D.2: Chart of roughness profiles used to determine the JRC value after Barton and Choubey (1977).

D.2 Geological Strength Index







<p>GEOLOGICAL STRENGTH INDEX FOR JOINTED ROCKS</p> <p>From the lithology, structure and surface conditions of the discontinuities, estimate the average value of GSI. Do not try to be too precise. Quoting a range from 33 to 37 is more realistic than stating that GSI = 35. Note that the table does not apply to structurally controlled failures. Where weak planar structural planes are present in an unfavourable orientation with respect to the excavation face, these will dominate the rock mass behaviour. The shear strength of surfaces in rocks that are prone to deterioration as a result of changes in moisture content will be reduced if water is present. When working with rocks in the fair to very poor categories, a shift to the right may be made for wet conditions. Water pressure is dealt with by effective stress analysis</p> <p>STRUCTURE</p>		<p>SURFACE CONDITIONS</p> <p>VERY GOOD Very rough, fresh, unweathered surfaces</p> <p>GOOD Rough, slightly weathered, iron stained surfaces</p> <p>FAIR Smooth, moderately weathered and altered surfaces</p> <p>POOR Slickensided, highly weathered surfaces with compact coating or fillings of angular fragments</p> <p>VERY POOR Slickensided, highly weathered surfaces with soft clay coatings or fillings</p> <p>DECREASING SURFACE QUALITY →</p>				
 <p>INTACT OR MASSIVE- Intact rock specimens or massive in-situ rock with few widely spaced discontinuities</p>	90			N/A	N/A	
 <p>BLOCKY - Well interlocked undisturbed rock mass consisting of cubical blocks formed by three intersecting discontinuity sets</p>	80	70	60			
 <p>VERY BLOCKY - Interlocked, partially disturbed mass with multi-faceted angular blocks formed by 4 or more joint sets</p>			50			
 <p>BLOCKY/DISTURBED/SEAMY - Folded with angular blocks formed by many intersecting discontinuity sets. Persistence of bedding planes or schistosity</p>			40	30		
 <p>DISINTEGRATED - Poorly interlocked, heavily broken rock mass with mixture of angular and rounded rock pieces</p>				20		
 <p>LAMINATED/SHEARED - Lack of blockiness due to close spacing of the weak schistosity or shear planes</p>	N/A	N/A			10	

Figure D.3: Chart after Marinos and Hoek (2000) for determination of the Geological Strength Index (GSI).

D.3 Q-value

1 RQD = Oppsprekkingsfaktor (Rock Quality Designation)			RQD
A	Svært dårlig	(> 27 sprekker per m ²)	0-25
B	Dårlig	(20-27 sprekker per m ²)	25-50
C	Middels	(13-19 sprekker per m ²)	50-75
D	God	(8-12 sprekker per m ²)	75-90
E	Utmerket	(0-7 sprekker per m ²)	90-100
Merk: i) Der RQD er rapportert eller målt til ≤ 10 (inklusive 0), brukes verdien 10 for å bestemme Q-verdien ii) RQD-intervaller på 5, dvs. 100, 95, 90, osv., er tilstrekkelig nøyaktige			

Figure D.4: Table after Norges Geotekniske Institutt (2015) for determination of RQD.

2 J _n = Tall for sprekkesett		J _n
A	Massivt. Ingen eller få sprekker	0,5-1,0
B	Ett sprekkesett	2
C	Ett sprekkesett pluss tilfeldige sprekker	3
D	To sprekkesett	4
E	To sprekkesett pluss tilfeldige sprekker	6
F	Tre sprekkesett	9
G	Tre sprekkesett pluss tilfeldige sprekker	12
H	Fire eller flere sprekkesett, tilfeldig og sterkt oppsprukket "sukkerbitberg", osv.	15
J	Knust berg, jordaktig	20
Merk: i) For tunnelkruss, bruk 3 x J _n ii) For påhug, bruk 2 x J _n		

Figure D.5: Table after Norges Geotekniske Institutt (2015) for determination of J_n.

3 $J_r =$ Sprekkeruhetstall		J_r
a) Bergveggkontakt, og b) Bergveggkontakt før skjærbevegelsen har gått 10 cm		
A	Diskontinuerlige sprekker	4
B	Ru eller ujevn, bølgete	3
C	Glatt, bølgete	2
D	Glidespeil, bølgete	1,5
E	Ru, ujevn, plan	1,5
F	Glatt, plan	1
G	Glidespeil, plan	0,5
Merk: i) Beskrivelse henviser til småskalaegenskaper og mellomskalaegenskaper, i den rekkefølgen		
c) Ingen bergkontakt ved skjærbevegelse		
H	Sone som inneholder leirfylling tykk nok til å forhindre bergkontakt ved skjærdeformasjon	1
Merk: ii) Legg til 1 hvis gjennomsnittlig avstand i det relevante sprekkesettet er mer enn 3 m (avhenger av størrelsen på tunnelåpningen) iii) $J_r = 0,5$ kan brukes for plane glidespeil med lineasjon, forutsatt at lineasjonen er orientert i sannsynlig bevegelsesretning		

Figure D.6: Table after Norges Geotekniske Institutt (2015) for determination of J_r .

4 $J_a =$ Tall for sprekkefylling		Φ_r	J_a
a) Bergkontakt (ingen mineralfylling, bare belegg)			
A	Sammenvokste sprekker med harde mineraler som kvarts eller epidot.		0,75
B	Uomvandlede sprekkeflater, bare overflateoksidasjon.	25-35°	1
C	Svakt omvandlede sprekkeflater. Uoppbløtellig mineralbelegg, sandpartikler, oppknust berg uten leir.	25-30°	2
D	Siltig eller sandig sprekkebelegg, litt leir (ikke svellende).	20-25°	3
E	Oppbløtellig leirbelegg med lav friksjon, f.eks. kaolinit eller glimmer. Også kloritt, talk gips, grafitt osv. og små mengder svelleleire.	8-16°	4
b) Bergkontakt før 10 cm skjærdeformasjon (tynn mineralfylling)			
F	Sandige partikler, oppknust berg, ikke leir.	25-30°	4
G	Sterkt overkonsolidert, uoppbløtellig fylling av leirmineraler (kontinuerlig, men <5 mm tykkelse).	16-24°	6
H	Middels eller litt overkonsolidert fylling av oppbløtellig leirmateriale (kontinuerlig, men <5 mm tykkelse).	12-16°	8
J	Fylling av svelleleire, dvs. montmorillonitt (kontinuerlig, men <5 mm tykkelse). J_a -verdien avhenger av prosentvis innhold av svelleleire.	6-12°	8-12
c) Ingen bergkontakt ved skjærdeformasjon (tykk mineralfylling)			
K	Soner og bånd av desintegret eller knust berg. Sterkt overkonsolidert, uoppbløtellig fylling.	16-24°	6
L	Soner og bånd av knust eller desintegret berg og leir. Middels til litt overkonsolidert uoppbløtellig fylling.	12-16°	8
M	Soner og bånd av leir eller knust eller desintegret berg. J_a -verdien avhenger av prosentvis innhold av svelleleire.	6-12°	8-12
N	Tykke kontinuerlige soner eller bånd med leir. Sterkt overkonsolidert.	12-16°	10
O	Tykke kontinuerlige soner eller bånd med leir. Middels-til-lav overkonsolidering	12-16°	13
P	Tykke kontinuerlige soner eller bånd med leir. Svelleleire. J_a avhenger av prosentvis innhold av svelleleire.	6-12°	13-20

Figure D.7: Table after Norges Geotekniske Institutt (2015) for determination of J_a .

5 $J_w =$ Sprekkevannstall		J_w
A	Tørre bergrom eller mindre innsig (fuktig eller noen få drypp)	1,0
B	Middels innsig, av og til utfasking av sprekefyllinger (mange drypp/"regn")	0,66
C	Vannstråler eller høyt trykk i kompetent berg med ufylte sprekker	0,5
D	Stort tilsig eller høyt trykk, betydelig utfasking av sprekefyllinger	0,33
E	Usedvanlig høy innstrømming eller vanntrykket avtar med tid. Forårsaker utfasking av materialer og kanskje utrasinger	0,2-0,1
F	Usedvanlig høy innstrømming eller vanntrykket fortsetter uten merkbar reduksjon. Forårsaker utfasking av materialer og kanskje utrasinger	0,1-0,05
Merk: i) Faktorene C til F er grove estimater. Øk J_w hvis berget dreneres eller det utføres injeksjon ii) Spesielle problemer forårsaket av isdannelse er ikke tatt med i betraktning		

Figure D.8: Table after Norges Geotekniske Institutt (2015) for determination of J_w .

6 SRF = Spenningsfaktor (Stress Reduction Factor)			SRF	
a) Svakhetssoner som krysser tunnelen eller bergrommet, som kan føre til at bergmasse løsner				
A	Hyppig opptreden av svakhetssoner som inneholder leire eller kjemisk forvitret berg, avspent berg (uansett dybde), eller lange seksjoner med inkompetent (svakt) berg (uansett dybde). For skvising, se δL og δM		10	
B	Flere skjærsoner innenfor en kort seksjon i kompetent avspent sideberg (uansett dybde)		7,5	
C	Enkeltstående svakhetssoner med eller uten leire eller kjemisk forvitret berg (dybde ≤ 50 m)		5	
D	Ukonsoliderte, åpne sprekker, mange sprekker eller "sukkerbit", osv. (uansett dybde)		5	
E	Enkeltstående svakhetssoner med eller uten leire eller kjemisk forvitret berg (dybde > 50 m)		2,5	
Merk: 1) Reduser disse SRF-verdiene med 25-50 % hvis svakhetssonene bare påvirker men ikke krysser den underjordiske åpningen				
b) Kompetent, hovedsakelig massivt berg, spenningsproblemer				
		σ_o / σ_1	σ_s / σ_o	SRF
F	Lave spenninger, nær overflaten, åpne sprekker	>200	<0,01	2,5
G	Middels spenninger, gunstige spenningsforhold	200-10	0,01-0,3	1
H	Høye spenninger, svært tett struktur. Vanligvis gunstig for stabiliteten. Kan også være ugunstig for stabiliteten, avhengig av retningen på spenningene sammenliknet med sprekke dannelse/svakhetsplan*	10-5	0,3-0,4	0,5-2 2-5*
J	Moderat avskalling etter > 1 time i massivt berg	5-3	0,5-0,65	5-50
K	Avskalling og bergslag etter noen minutter i massivt berg	3-2	0,65-1	50-200
L	Intens bergslag og umiddelbar dynamisk deformasjon i massivt berg	<2	>1	200-400

Figure D.9: Table after Norges Geotekniske Institutt (2015) for determination of SRF.

<p>Merk: ii) For sterkt anisotropiske urørte spenningsfelt (om målt): når $5 \leq \sigma_1 / \sigma_3 \leq 10$, reduser σ_c til $0,75 \sigma_c$. Når $\sigma_1 / \sigma_3 > 10$, reduser σ_c til $0,5 \sigma_c$ der σ_c = fri trykkfasthet, σ_1 og σ_3 er de primære og sekundære spenningene, og σ_s = maksimum tangential spenning (estimert fra elastisk teori)</p> <p>iii) Når dybden av hengenget under overflaten er mindre enn spennet; foreslås det at SRF økes fra 2,5 til 5 for slike tilfeller (se F)</p>			
c) Skvisende berg: plastisk deformasjon i ikke kompetent berg under påvirkning av høyt trykk		σ_s / σ_c	SRF
M	Moderat skvisende bergtrykk	1-5	5-10
N	Intens skvisende bergtrykk	>5	10-20
<p>Merk: iv) For bestemmelse av skvisende bergforhold henvises til relevant litteratur (dvs. Singh et al., 1992 og Bhasin og Grimstad, 1996)</p>			
d) Svellende berg: kjemisk svelleaktivitet ved tilgang på vann			SRF
O	Moderat svelling		5-10
P	Intens svelling		10-15

Figure D.10: Continuation of table after Norges Geotekniske Institutt (2015) for determination of SRF.

E. Input parameters for numerical modelling

E.1 Input rock mass parameters

E.1.1 Calculation of Q'-value and GSI

Dunite						Serpentinized dunite 1						Chlorite banded dunite						Serpentinized dunite 2						Gneiss					
Location	RQD	Jn	Jr	Ja	Q'	Location	RQD	Jn	Jr	Ja	Q'	Location	RQD	Jn	Jr	Ja	Q'	Location	RQD	Jn	Jr	Ja	Q'	Location	RQD	Jn	Jr	Ja	Q'
P30	83	6	3	3	14	P5	80	9	3	4	7	P27	77	6	3	4	10	P21	72	3	2.5	6	10	P55	80	6	3	1.5	27
P31	87	1	3	3	87	P5	83	3	3	6	14	P27	73	3	3	4	18	P21	75	3	3	3	25	P55	70	3	2.5	3.5	17
P32	87	3	3	3	29	P6	77	9	2.5	3	7	P27	57	6	2.5	3	8	P22	60	6	3	3.5	9						13
P33	70	3	3	3	23	P6	83	3	2.5	4	17	P28	80	3	3	6	13	P23	77	4	3	3	19						67
P33	73	3	1	3	8	P7	77	3	2.5	3	21	P29	83	3	2.5	3.5	20	P23	88	3	2.5	3	25						
P34	70	3	2.5	3	19	P9	80	3	3	5	16	P37	80	3	3	3.5	23	P24	68	3	2.5	3	19						
					21	P10	83	6	2.25	4	8						16	P25	73	1.5	3	3	49						
					72	P11	80	3	3	4	20						69						19						
						P12	97	3	2	4	16												71						
						P13	83	9	2.5	4	6																		
						P13	80	4	2.5	4	13																		
						P14	83	3	2.5	4	17																		
						P15	83	6	2	4	7																		
						P16	73	3	2.5	4	15																		
						P17	87	3	3	4	22																		
						P19	70	6	3	4	9																		
						P19	78	6	3	3	13																		
						P20	68	6	3	4	9																		
						P35	50	6	3	4	6																		
						P36	85	9	0.75	4	2																		
Median	21					13					16					19					13								
GSI	72					67					69					71					67								

Table E.1: Values of parameters used for calculation of Q'-value and GSI, and the final GSI value. The locations for estimation indicated in the table are shown in the map in figure 3.3.

E.2 Input joints strength parameters

E.2.1 Input parameters for calculation of joint stiffness

Area section 1							
Rock	Surface type	Rock mass Modulus, E_m (MPa)	Intact rock shear modulus, G_i (MPa)	Rock mass shear modulus, G_m (MPa)	Spacing, L (m)	Normal stiffness, k_n (MPa/m)	Shear stiffness, k_s (MPa/m)
Serpentinized dunite 1	Rough, slightly weathered surface	12863	20971	4997	0.2	84435	32803
Serpentinized dunite 1	Serpentinized	12863	20971	4997	0.2	84435	32803
Serpentinized dunite 2	Rough, slightly weathered surface	19369	22219	7174	0.2	143023	52971

Table E.2: The input parameters used to calculate the joint stiffness for joints in area section 1.

Area section 2							
Rock	Surface type	Rock mass Modulus, E_m (MPa)	Intact rock shear modulus, G_i (MPa)	Rock mass shear modulus, G_m (MPa)	Spacing, L (m)	Normal stiffness, k_n (MPa/m)	Shear stiffness, k_s (MPa/m)
Chlorite banded dunite	Rough, sandy surface	12492	13130	4627	0.2	96446	35721

Table E.3: The input parameters used to calculate the joint stiffness for the joints in area section 2.

Area section 3							
Rock	Surface type	Rock mass Modulus, E_m (MPa)	Intact rock shear modulus, G_i (MPa)	Rock mass shear modulus, G_m (MPa)	Spacing, L (m)	Normal stiffness, k_n (MPa/m)	Shear stiffness, k_s (MPa/m)
Dunite	Rough, sandy surface	20478	19234	7961	0.2	161784	55788

Table E.4: The input parameters used to calculate the joint stiffness for the joints in area section 3.

F. Wedges

F.1 Determination of the geometry defining the wedges



(a) Figure of the photo used to measure the dip of the western joint defining wedge 1. The value of the measured dip is indicated.



(b) Geometry of the current slope and the slope defined in the life of mine model, by wedge 1.

Figure F.1: Wedge 1

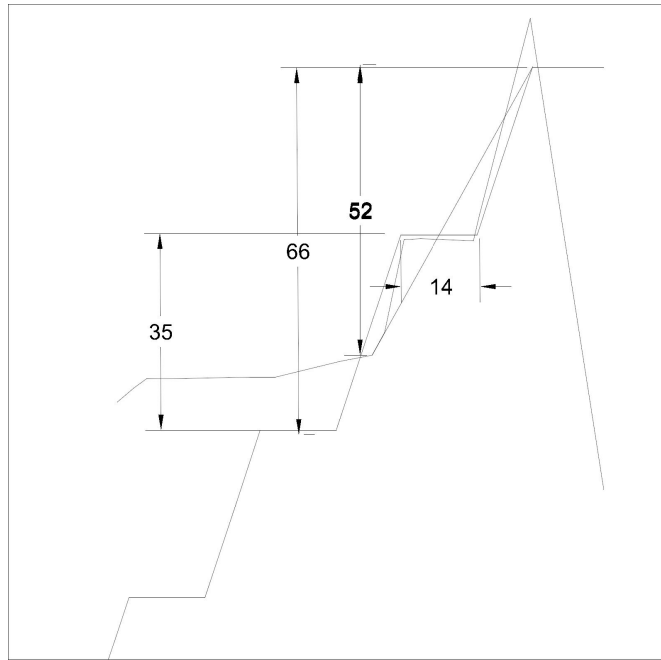
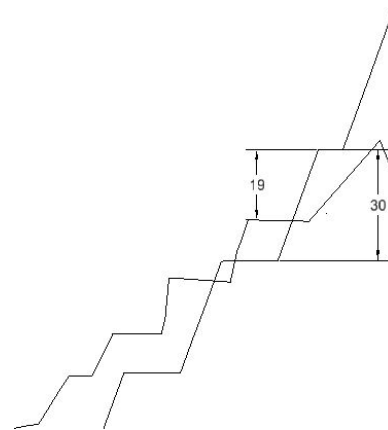


Figure F.2: Geometry of the current slope and the slope defined in the life of mine model, by wedge 2.

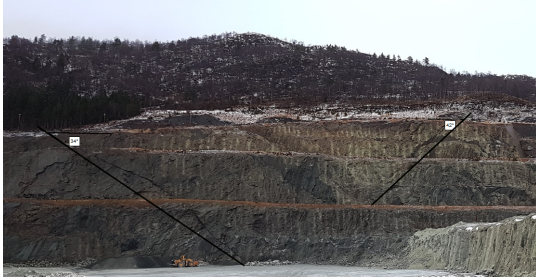


(a) Photo used to measure the dip of the western and eastern joints defining wedge 3.

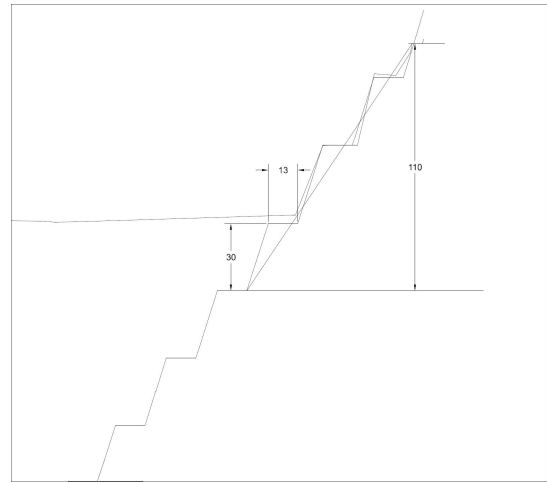


(b) Geometry of the current slope and the slope defined by the life of mine, by wedge 3. The bench face of the current slope is determined from observations to have the same dip as the bench defined in the life of mine model.

Figure F.3: Wedge 3



(a) Photo used to measure the dip of the western and eastern joints defining wedge 4. The photo show that the whole wedge won't be exposed before the quarry is developed to lower levels.

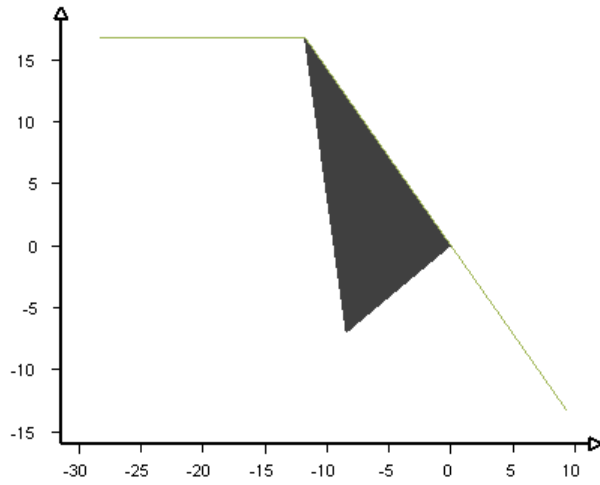


(b) Geometry of the current slope and the slope defined in the life of mine, by wedge 4. The current slope has the same geometry as the slope defined in the life of mine model.

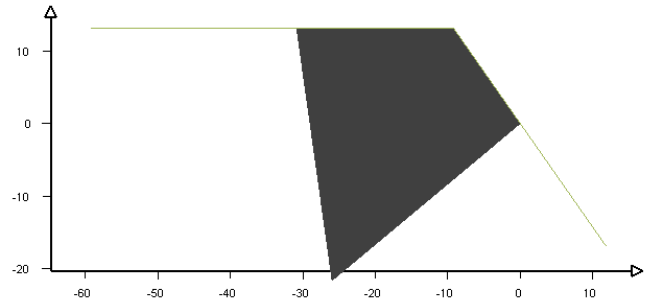
Figure F.4: Wedge 4

F.1.1 Sections of identified wedges in the current back wall

Wedge 1



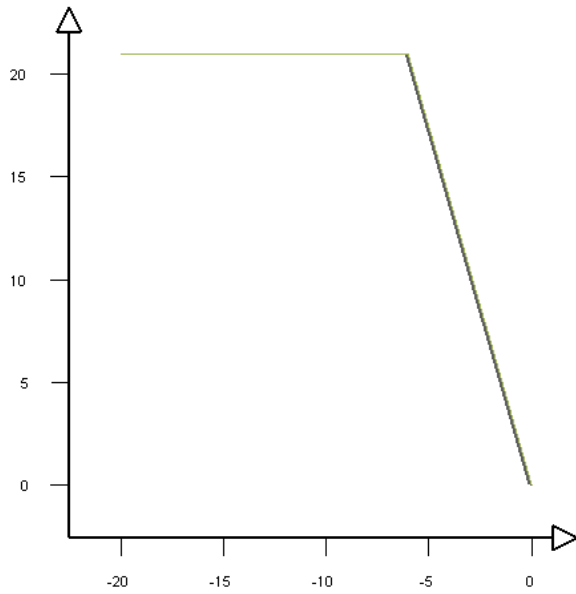
(a) Section of the wedge formed when the tension crack is defined by the closest foliation joint.



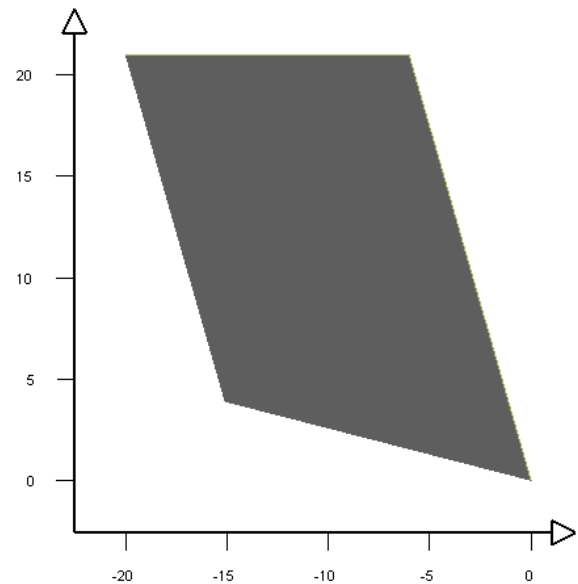
(b) Section of the wedge formed when the tension crack is defined by the foliation located at the innermost part of the bench.

Figure F.5: Sections of the identified wedges in the final back wall formed by the discontinuities in wedge 1. The sections are constructed by the software Swedge (Rocscience Inc, 2019c).

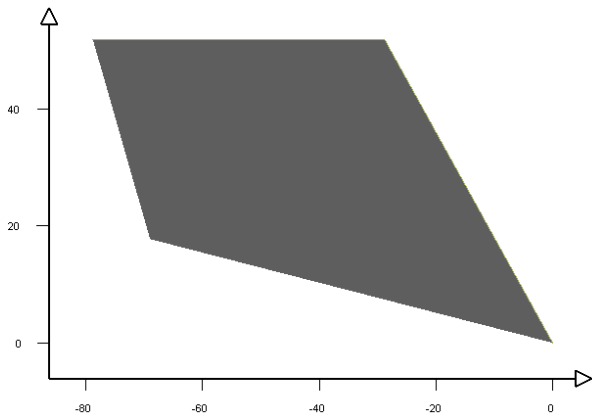
Section 2



(a) Section of the wedge formed when the tension crack is defined by the closest foliation joint.



(b) Section of the wedge formed when the tension crack is defined by the foliation located at the innermost part of the bench.



(c) Section of the wedge formed when the discontinuities extend up to the top of the quarry and there is no tension crack.

Figure E.6: Sections of the identified wedges in the final back wall formed by the discontinuities in wedge 2. The sections are constructed by the software Swedge (Rocscience Inc, 2019c).

Section 3

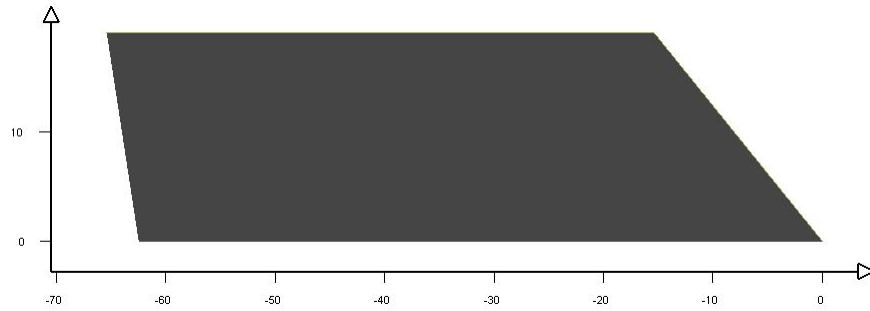
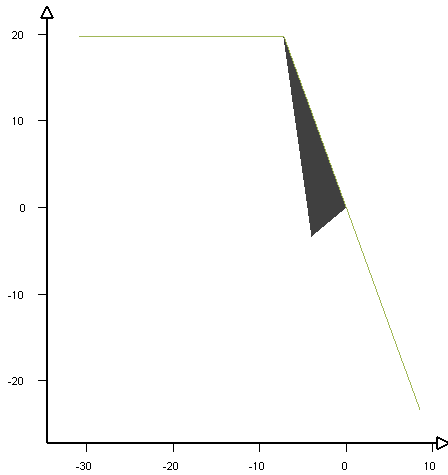


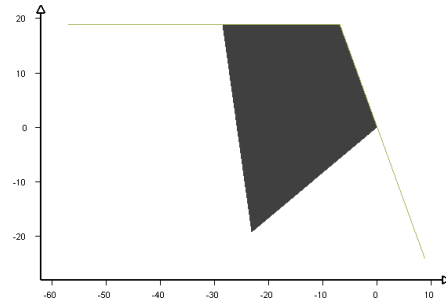
Figure F.7: Section of the wedge formed when the tension crack is defined by a foliation crack and bench width. The wedge is located in the uppermost bench, and the bench top is the surface at the top of the quarry. The section are constructed by the software Swedge (Rocscience Inc, 2019c).

F.1.2 Sections of identified wedges in the final back wall

Wedge 1



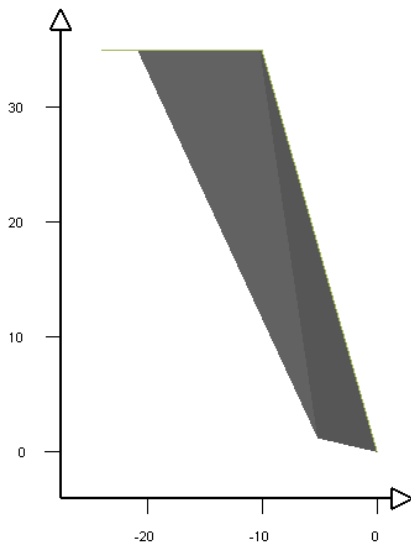
(a) Section of the wedge formed when the tension crack is defined by the closest foliation joint.



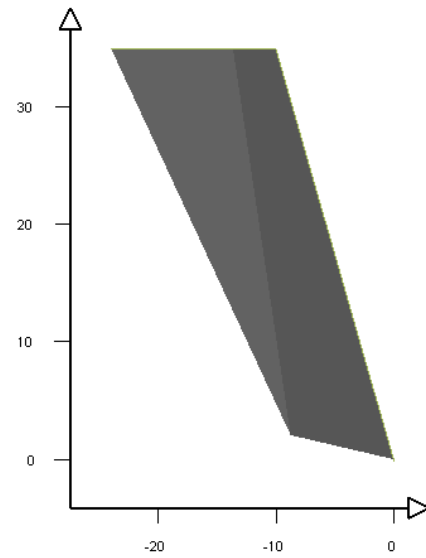
(b) Section of the wedge formed when the tension crack is defined by the foliation located at the innermost part of the bench.

Figure F.8: Sections of the identified wedges in the final back wall formed by the discontinuities in wedge 1. The sections are constructed by the software Swedge (Rocscience Inc, 2019c).

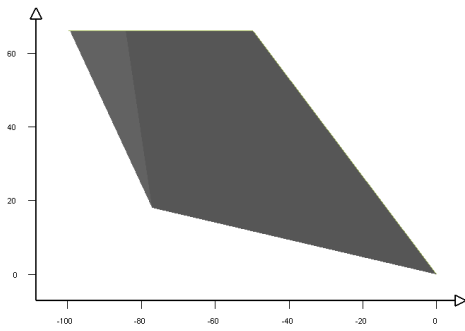
Wedge 2



(a) Section of the wedge formed when the tension crack is defined by the closest foliation joint.



(b) Section of the wedge formed when the tension crack is defined by the foliation located at the innermost part of the bench.



(c) Section of the wedge formed when the discontinuities extend up to the top of the quarry and there is no tension crack.

Figure F.9: Sections of the identified wedges in the final back wall formed by the discontinuities in wedge 2. The sections are constructed by the software Swedge (Rocscience Inc, 2019c).

Wedge 3

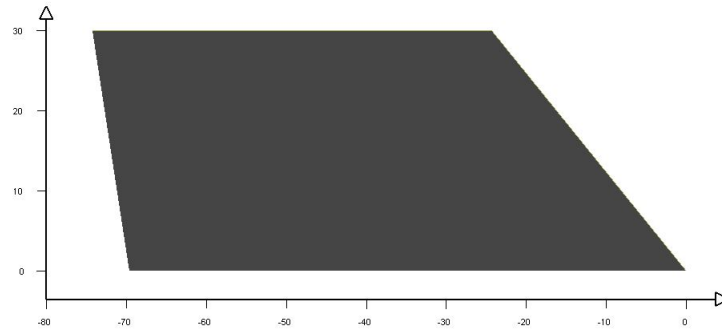
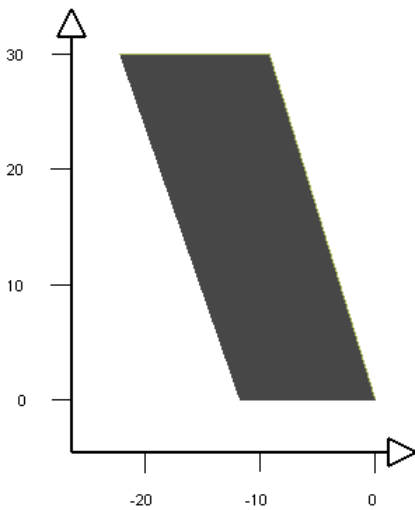
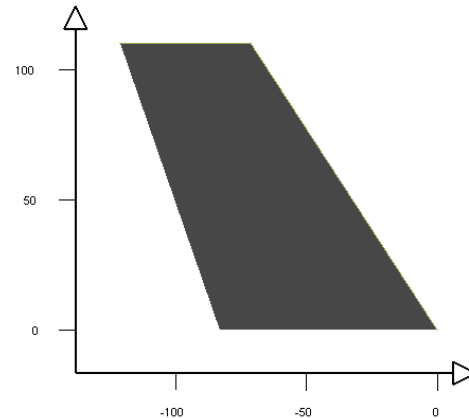


Figure F.10: Section of the wedge formed when the tension crack is defined by a foliation crack and bench width. The wedge is located in the uppermost bench, and the bench top is the surface at the top of the quarry. The sections are constructed by the software Swedge (Rocscience Inc, 2019c).

Wedge 4



(a) Section of the wedge formed when the tension crack is defined by the foliation located at the innermost part of the bench at the bottom of the wedge.



(b) Section of the wedge formed when the discontinuities extend up to the top of the quarry and the foliation crack is located 50m from the crest of the wall.

Figure F.11: Sections of the identified wedges in the final back wall formed by the discontinuities in wedge 2. The sections are constructed by the software Swedge (Rocscience Inc, 2019c).

G. Numerical modelling

G.1 Calibration

G.1.1 The numerical model used for calibration

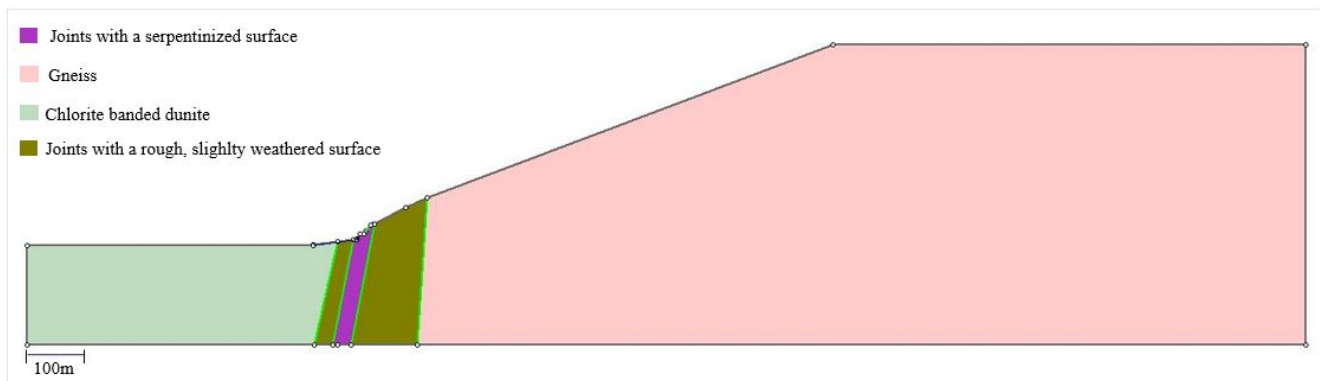


Figure G.1: The numerical model used to perform the calibration of joint strength parameters for the serpentinized surface.

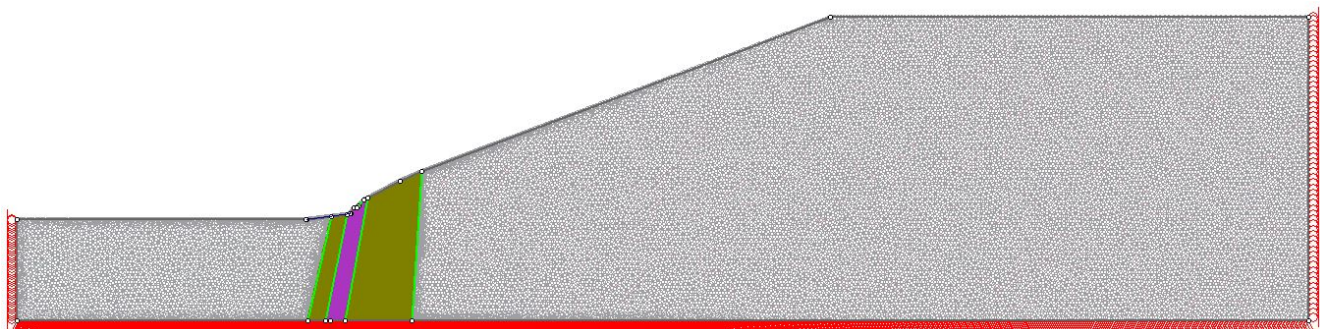


Figure G.2: The numerical model used to perform the calibration divided into finite elements.

Total displacement in the numerical model

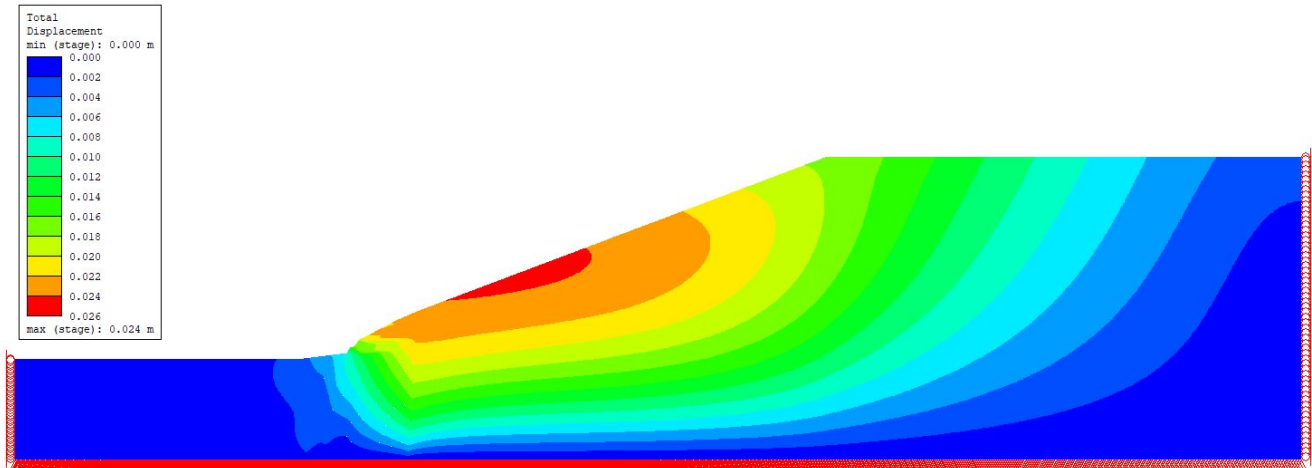


Figure G.3: The figure show the calculated total displacement in the numerical model used for calibration in Round 1.

G.1.2 Data used for plotting of displacement along joint surface

Location (y-coordinate) (m)	Shear displacement (m)				
	Round 1	Round 2	Round 3	Round 4	Round 5
40.28	0.000271	0.000225	0.000213	0.000215	0.000120
40.31	0.000273	0.000225	0.000214	0.000216	0.000122
40.35	0.000272	0.000224	0.000213	0.000215	0.000123
40.44	0.000271	0.000223	0.000209	0.000211	0.000123
40.61	0.000267	0.000220	0.000201	0.000200	0.000121
40.95	0.000259	0.000213	0.000189	0.000184	0.000116
41.54	0.000234	0.000196	0.000165	0.000161	0.000107
42.34	0.000192	0.000167	0.000128	0.000127	0.000095
43.18	0.000143	0.000129	0.000089	0.000085	0.000083
44.03	0.000092	0.000086	0.000054	0.000042	0.000067
44.81	0.000042	0.000049	0.000023	0.000006	0.000044
45.59	-0.000015	0.000015	-0.000005	-0.000020	0.000013
46.44	-0.000054	-0.000018	-0.000028	-0.000040	-0.000025
47.29	-0.000059	-0.000039	-0.000039	-0.000049	-0.000065
48.10	-0.000047	-0.000044	-0.000035	-0.000040	-0.000098
48.77	-0.000036	-0.000042	-0.000024	-0.000027	-0.000117
49.31	-0.000030	-0.000040	-0.000016	-0.000019	-0.000122

Table G.1: The data used to create the graphs in figure 5.10 showing the shear displacement along the joints used for calibration at different locations (given by the y-coordinate).

G.2 Stability analysis of the current back wall along section S2

G.2.1 Analysis using method 1

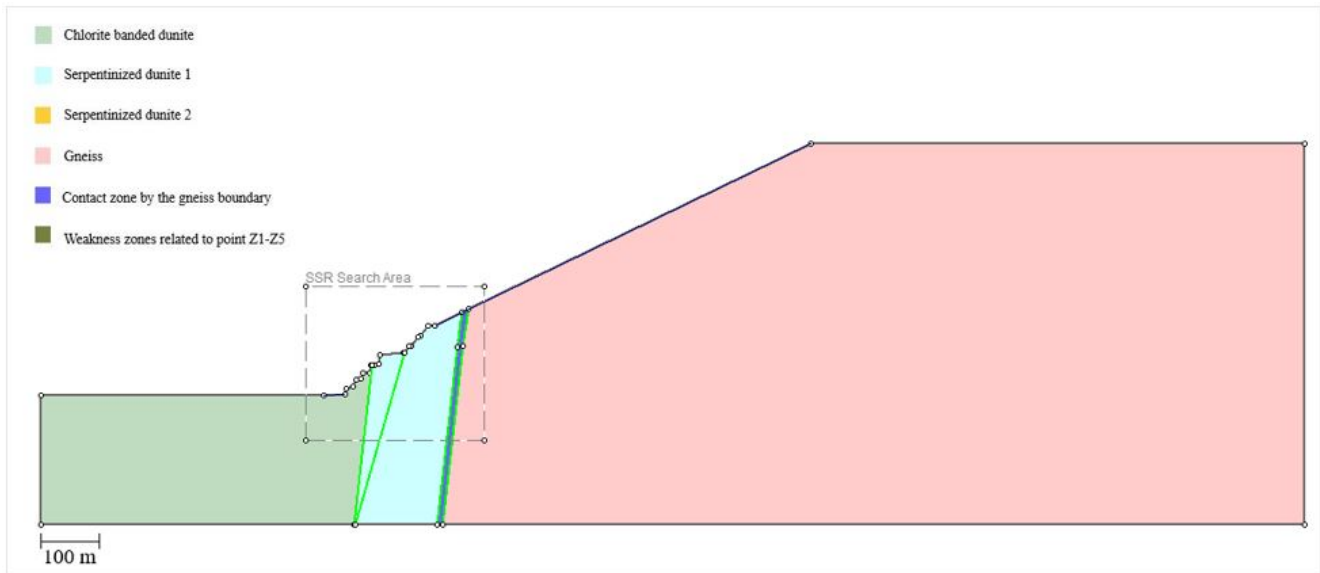


Figure G.4: The numerical model of section S2 used to perform the stability analysis of the current back wall using method 1.

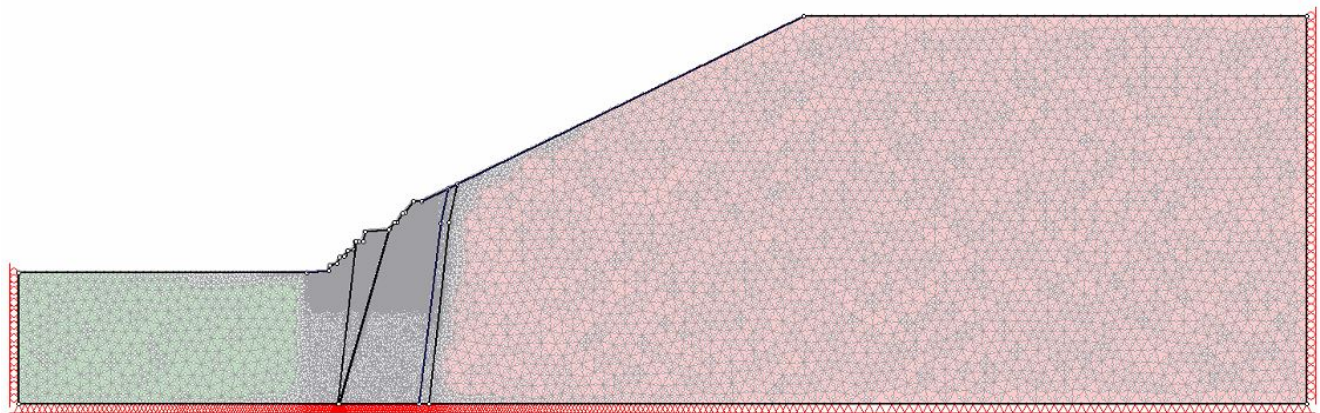


Figure G.5: The numerical model of section S2 showing the division of the model into finite elements. The model was used to perform the stability analysis of the current back wall using method 1.

G.2.2 Analysis using method 2

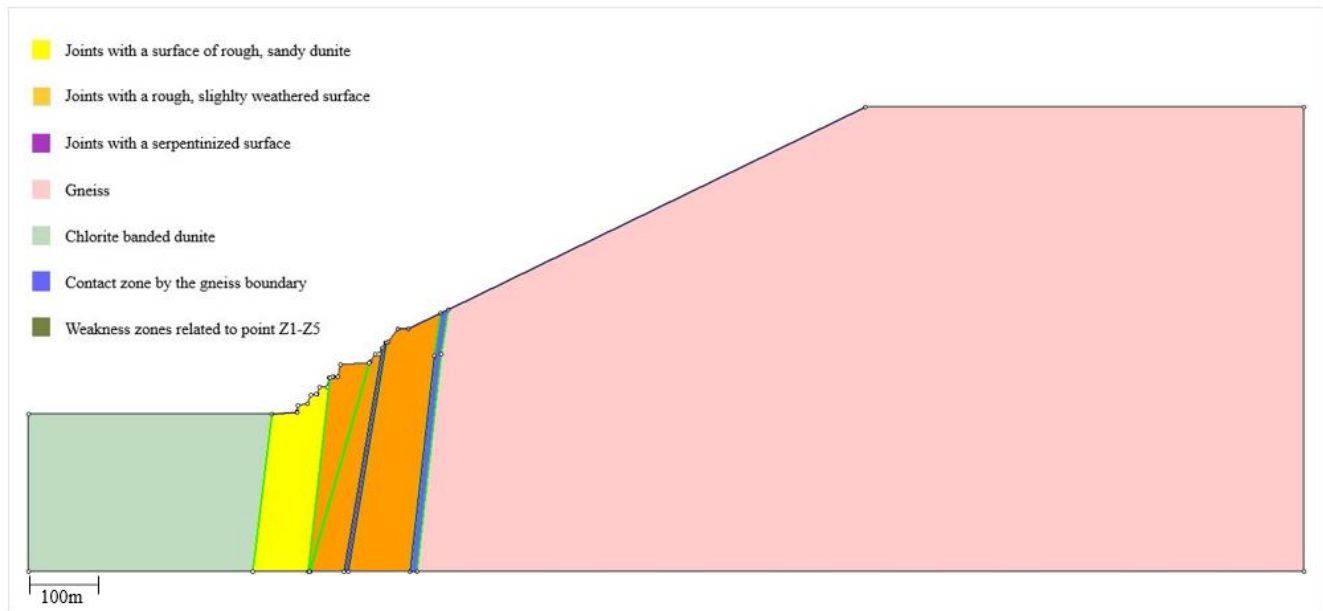


Figure G.6: The numerical model of section S2 used to perform the stability analysis of the current back wall using method 2 with the division of the model into finite elements.

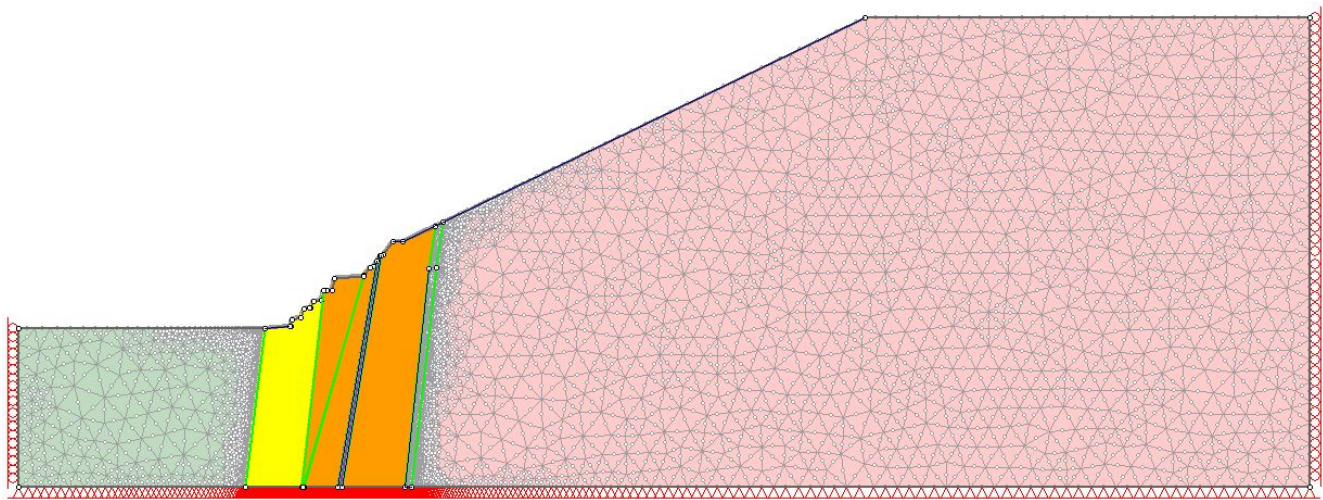


Figure G.7: The numerical model of section S2 showing the division of the model into finite elements. The model was used to perform the stability analysis of the current back wall using method 2.

G.3 Stability analysis of the final back wall

G.3.1 Analysis using method 1

Section S1

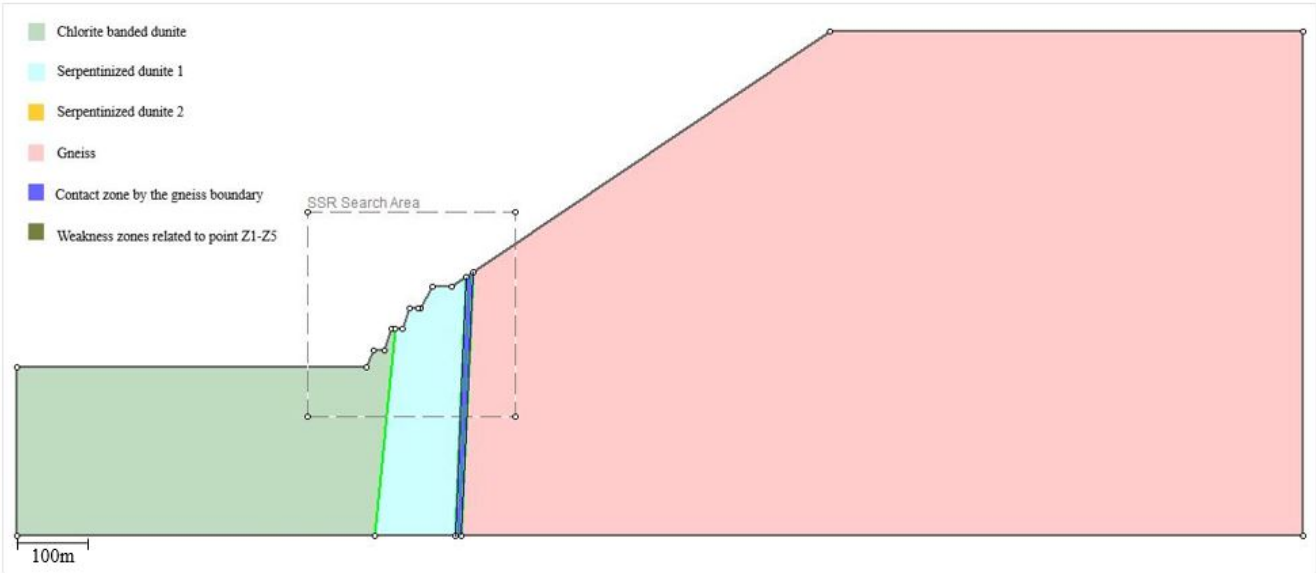


Figure G.8: The numerical model of section S1 used to perform the stability analysis of the final back wall using method 1.

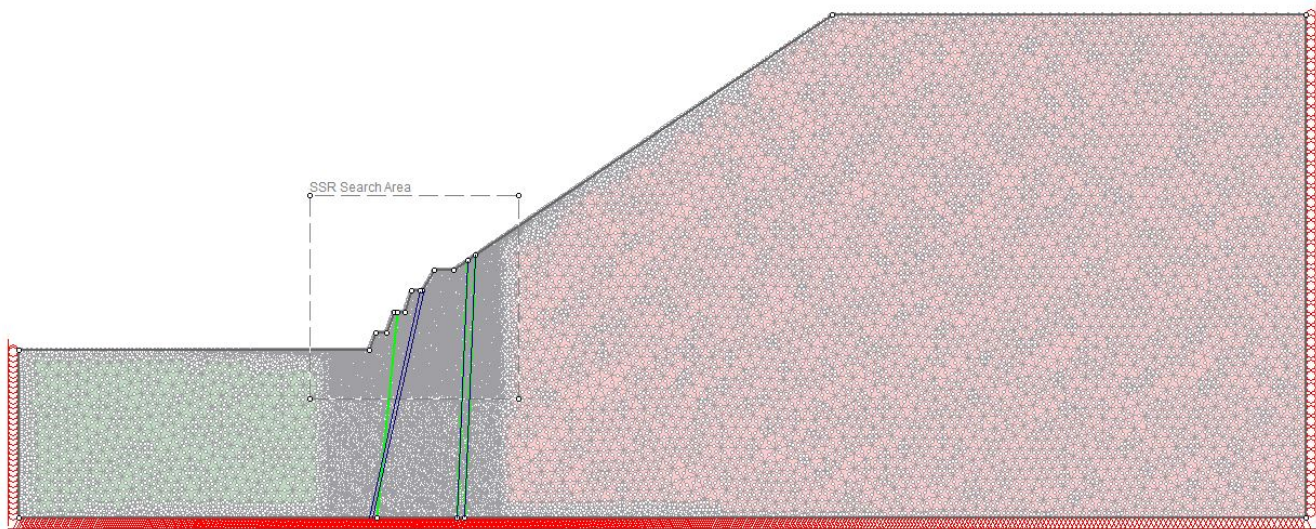


Figure G.9: The numerical model of section S1 showing the division of the model into finite elements. The model was used to perform the stability analysis of the current back wall using method 1.

Section S2

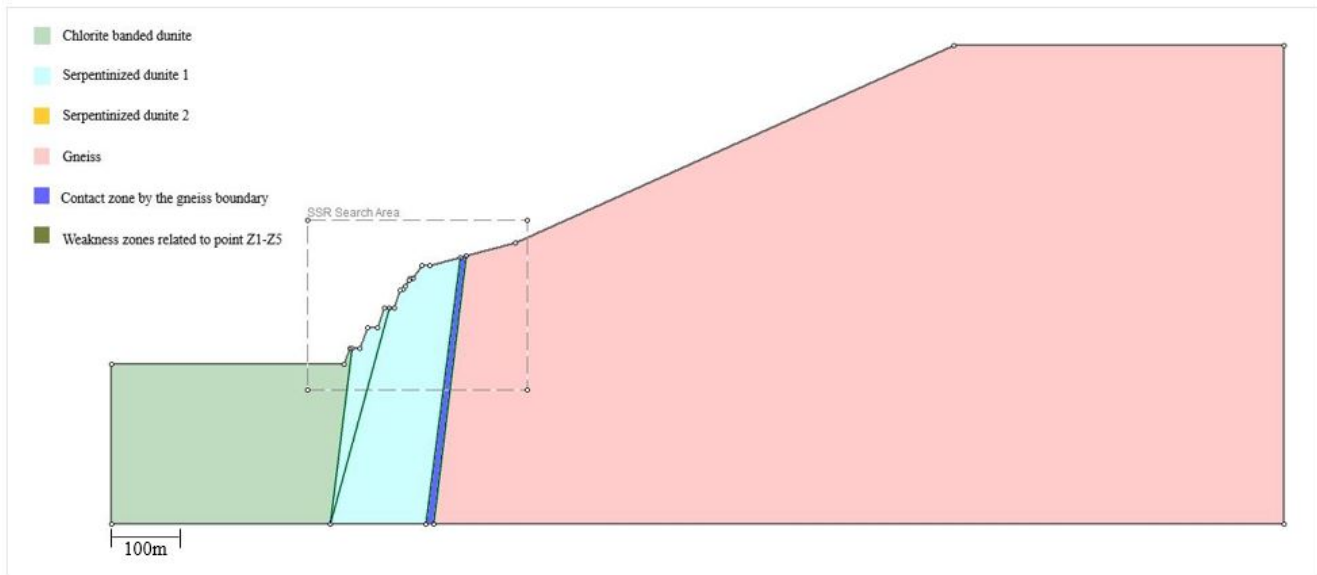


Figure G.10: The numerical model of section S2 used to perform the stability analysis of the final back wall using method 1.

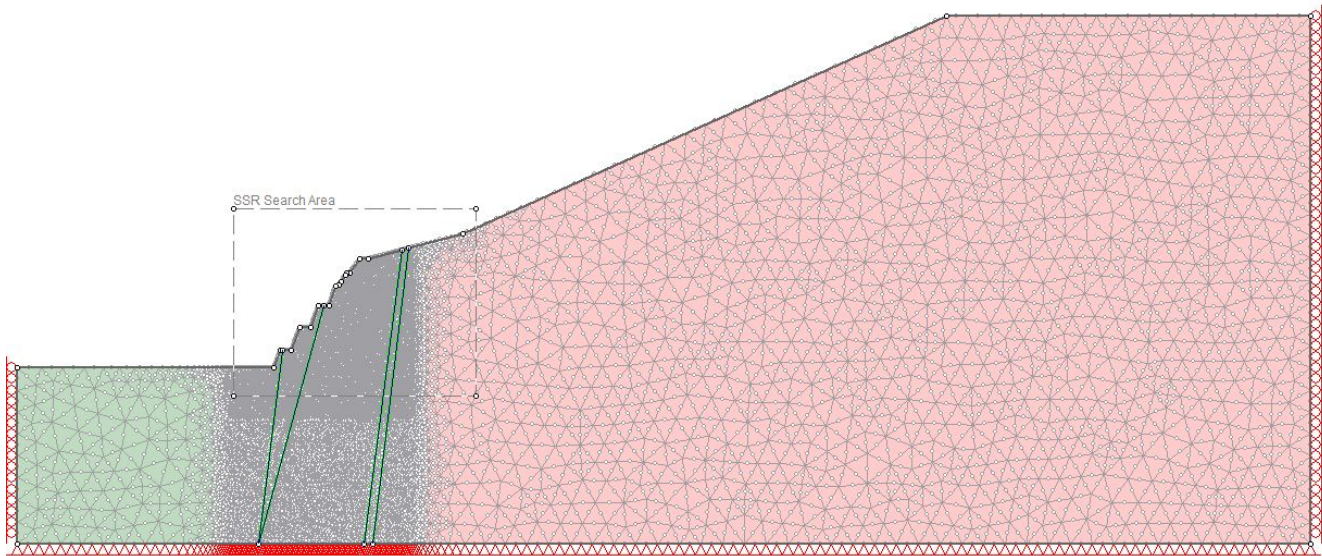


Figure G.11: The numerical model of section S2 showing the division of the model into finite elements. The model was used to perform the stability analysis of the current back wall using method 1.

Section S3

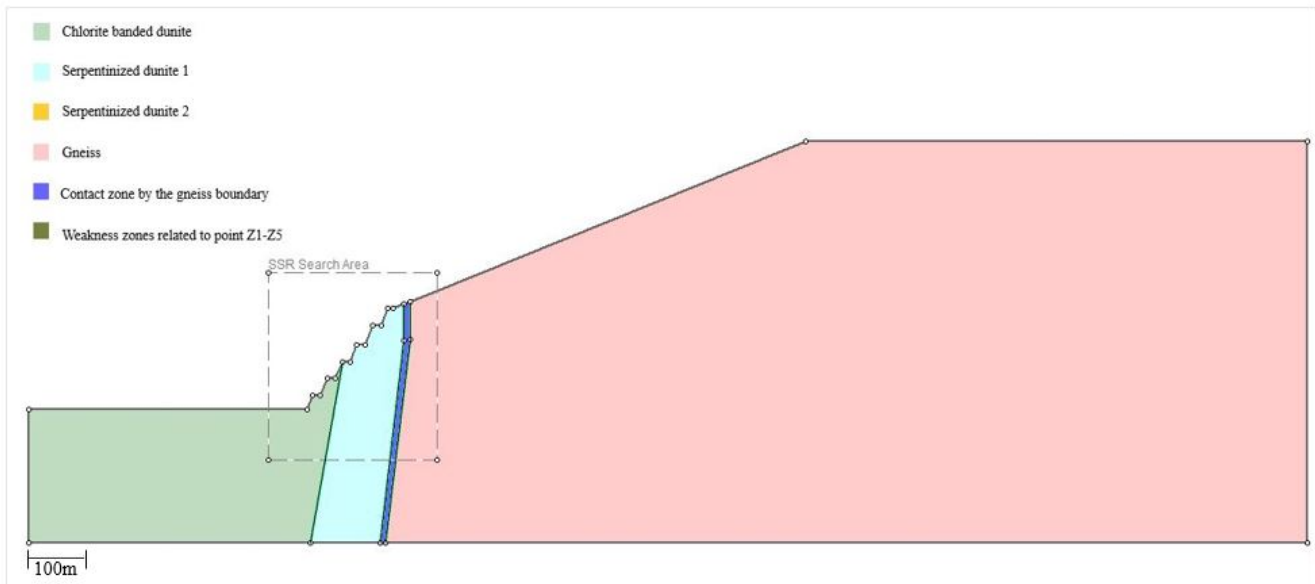


Figure G.12: The numerical model of section S3 showing the division of the model into finite elements. The model was used to perform the stability analysis of the current back wall using method 1.

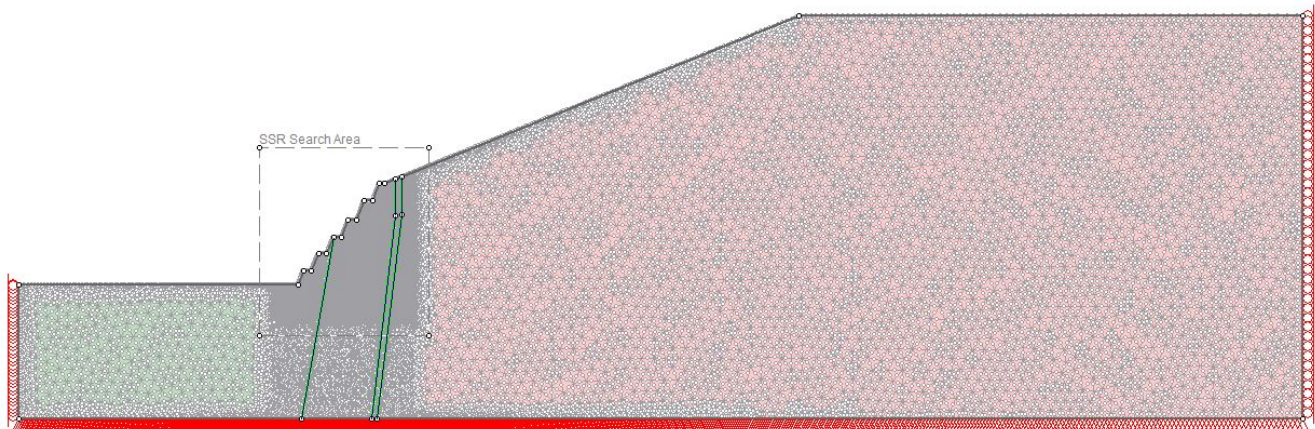


Figure G.13: The numerical model of section S3 showing the division of the model into finite elements. The model was used to perform the stability analysis of the current back wall using method 1.

Section S4

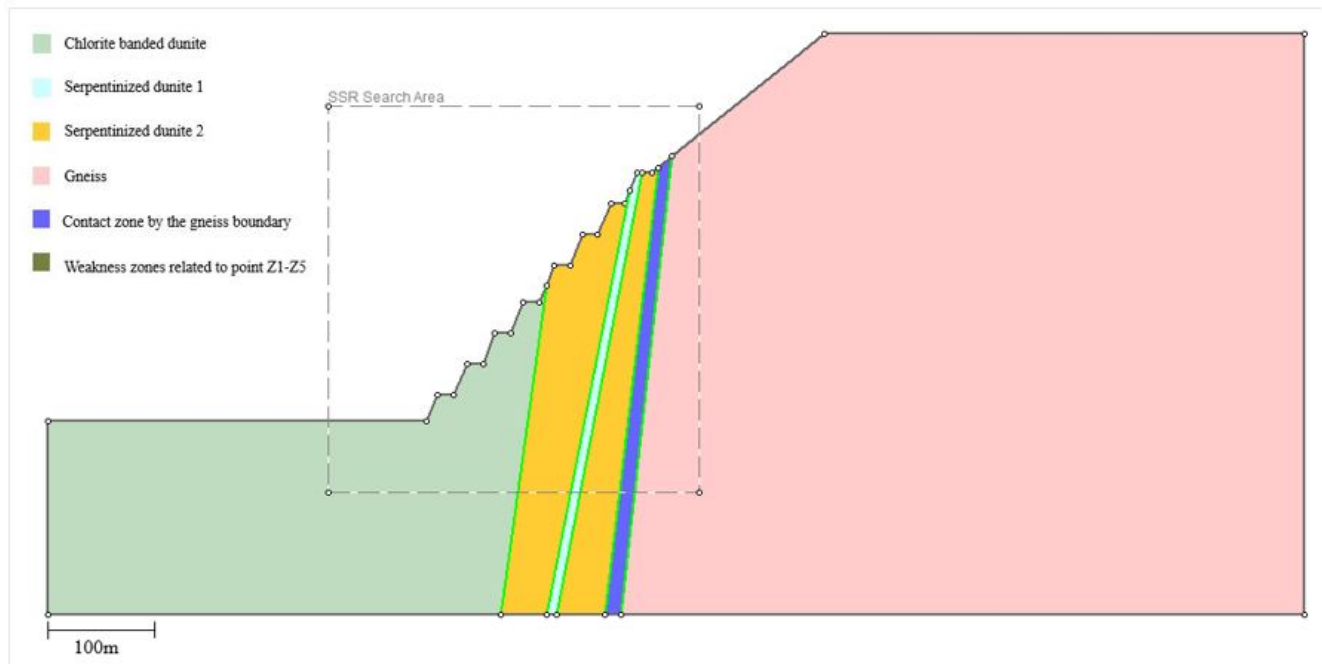


Figure G.14: The numerical model of section S4 used to perform the stability analysis of the final back wall using method 1.

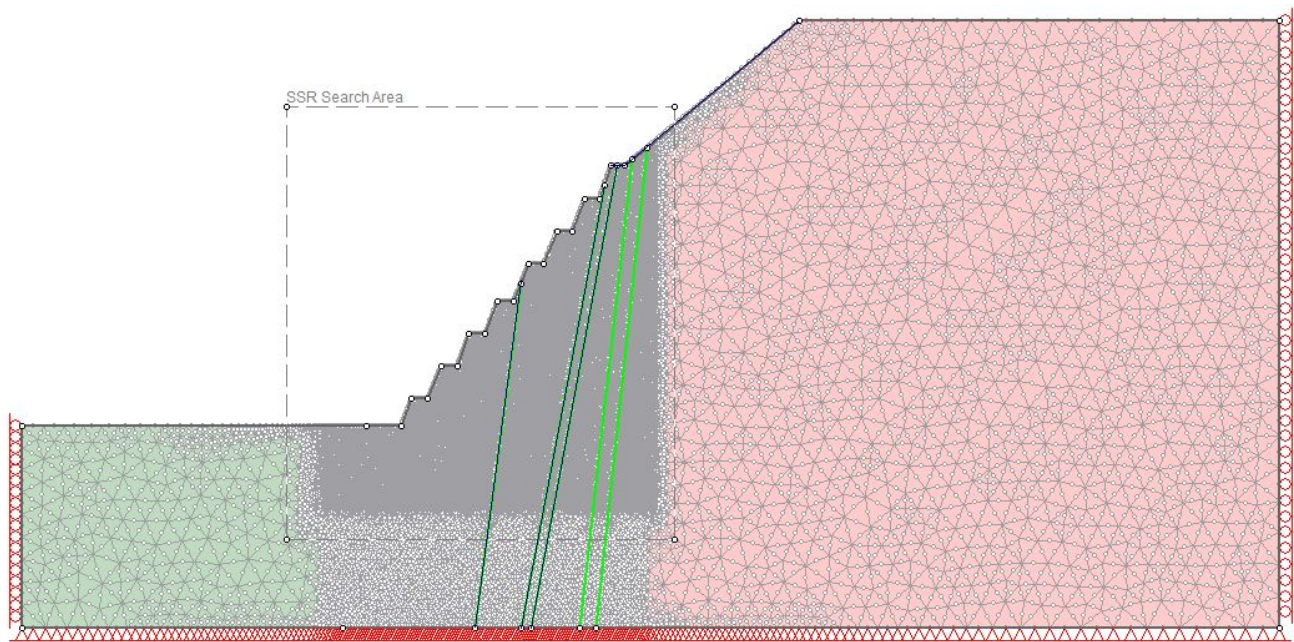


Figure G.15: The numerical model of section S4 showing the division of the model into finite elements. The model was used to perform the stability analysis of the current back wall using method 1.

G.3.2 Analysis using method 2

Section S1

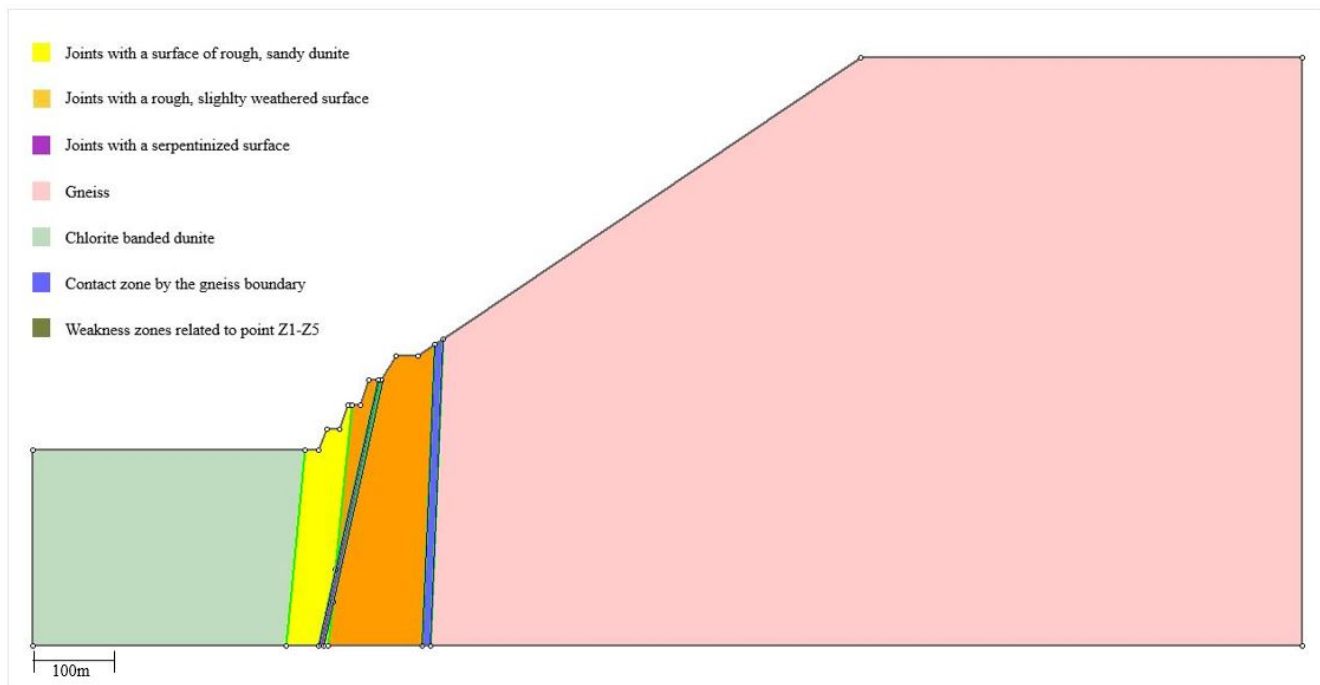


Figure G.16: The numerical model of section S1 used to perform the stability analysis of the final back wall using method 2.

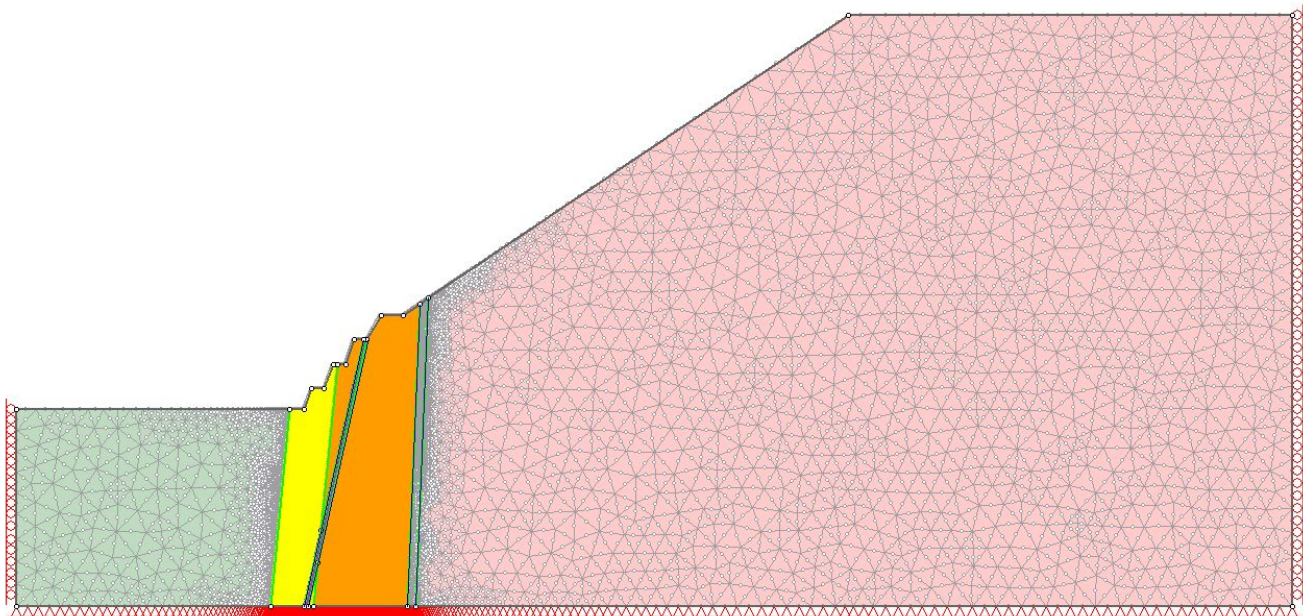


Figure G.17: The numerical model of section S1 showing the division of the model into finite elements. The model was used to perform the stability analysis of the current back wall using method 1.

Section S2

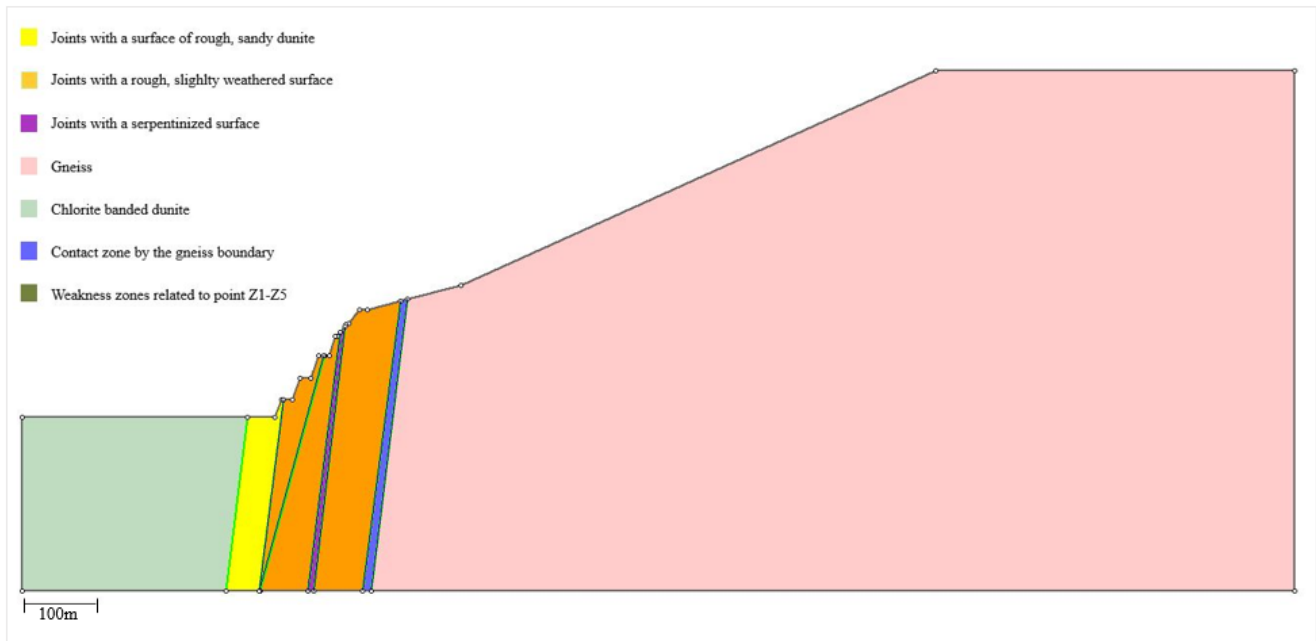


Figure G.18: The numerical model of section S2 used to perform the stability analysis of the final back wall using method 2.

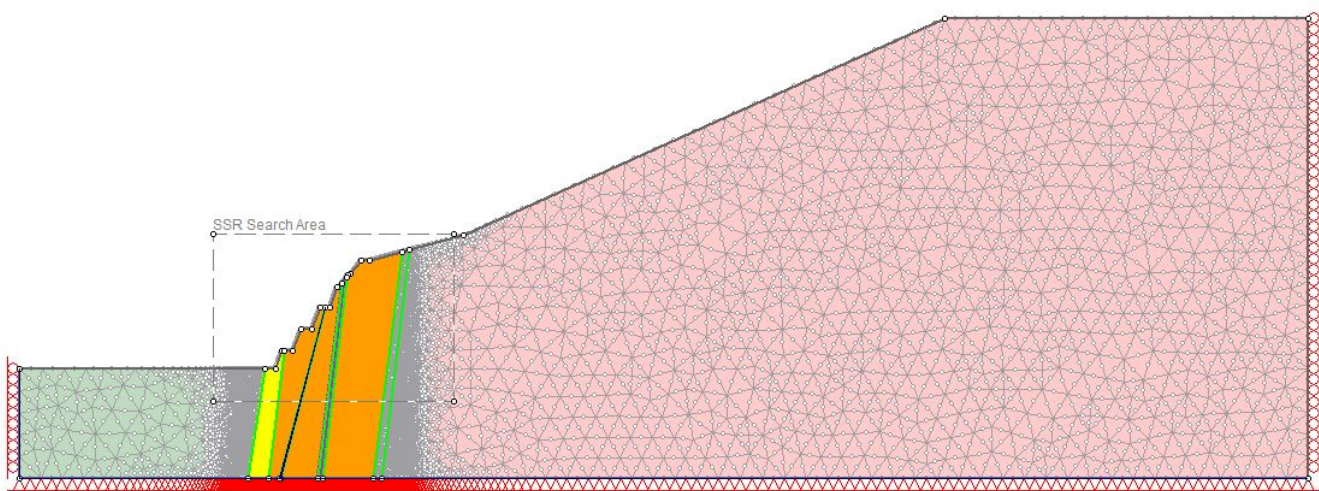


Figure G.19: The numerical model of section S2 showing the division of the model into finite elements. The model was used to perform the stability analysis of the current back wall using method 2.

Section S3

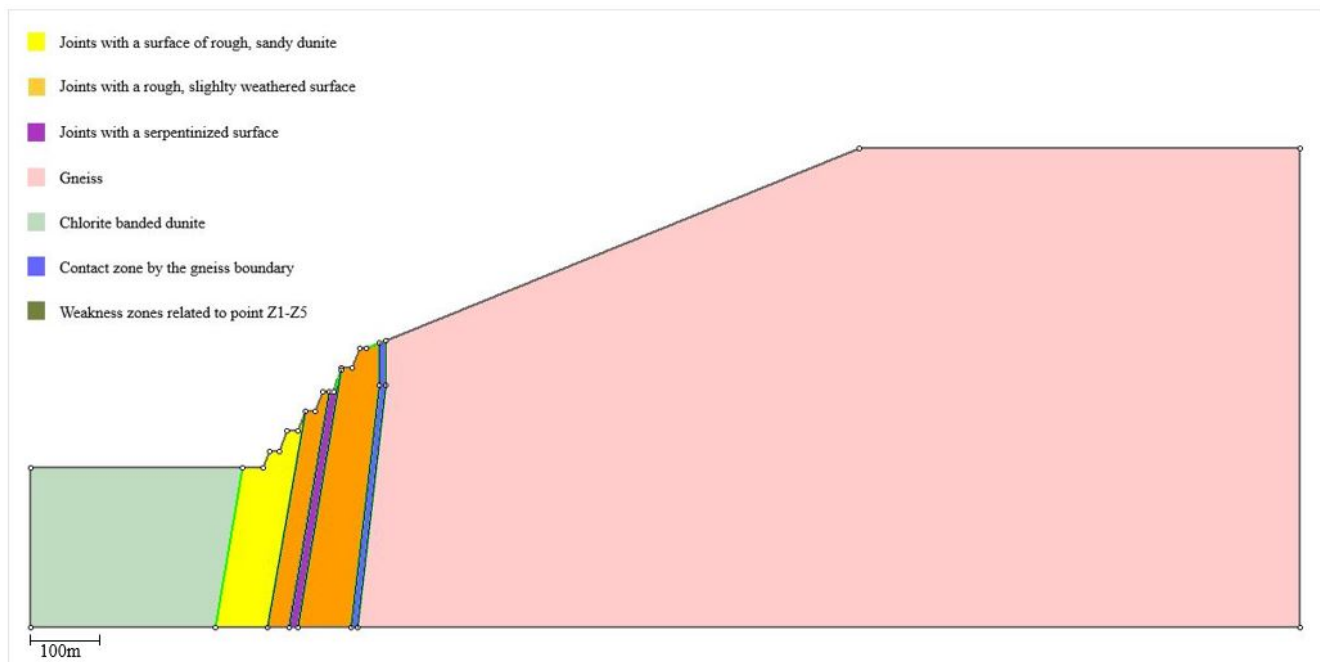


Figure G.20: The numerical model of section S3 used to perform the stability analysis of the final back wall using method 2.

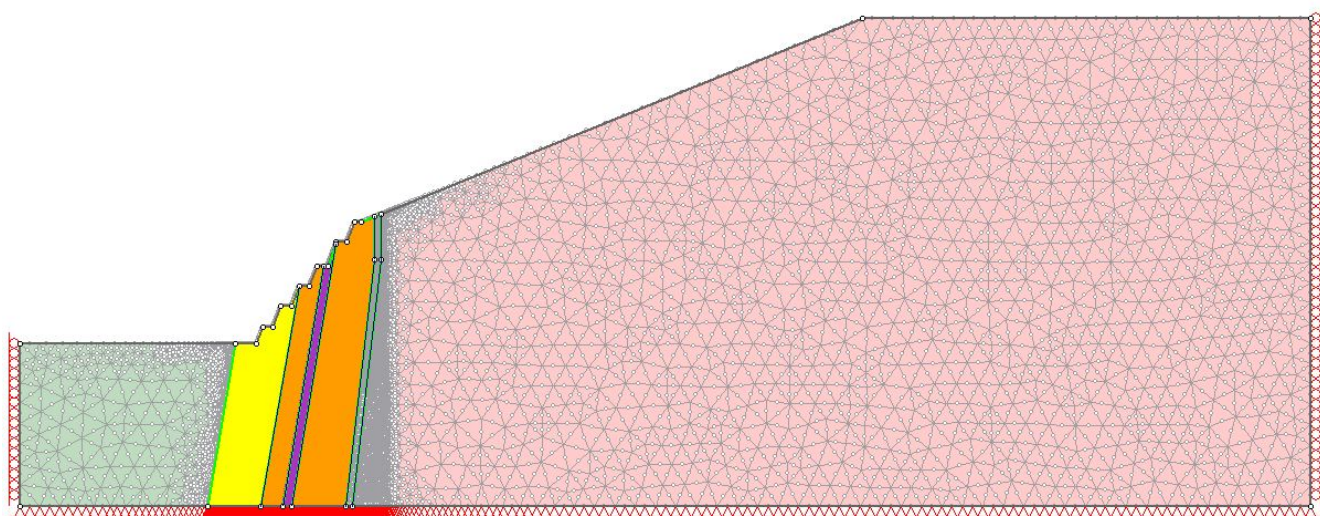


Figure G.21: The numerical model of section S3 showing the division of the model into finite elements. The model was used to perform the stability analysis of the current back wall using method 2.

Section S4

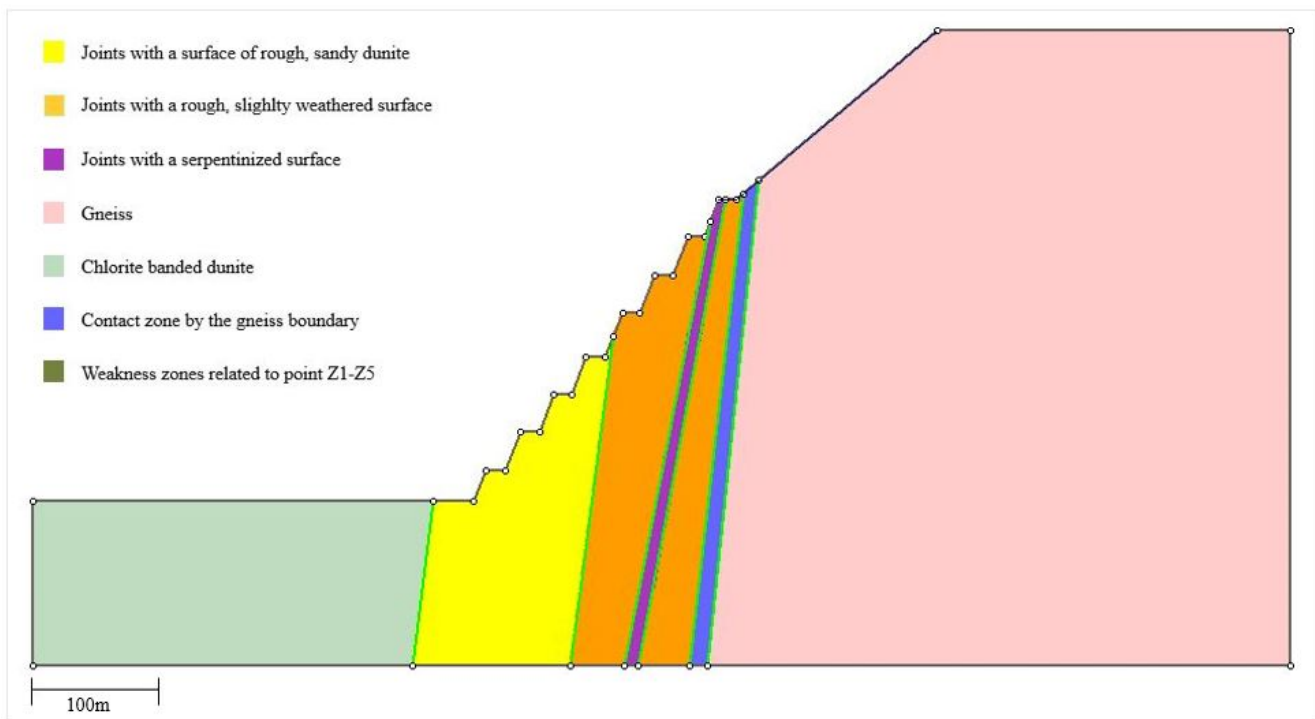


Figure G.22: The numerical model of section S4 used to perform the stability analysis of the final back wall using method 2.

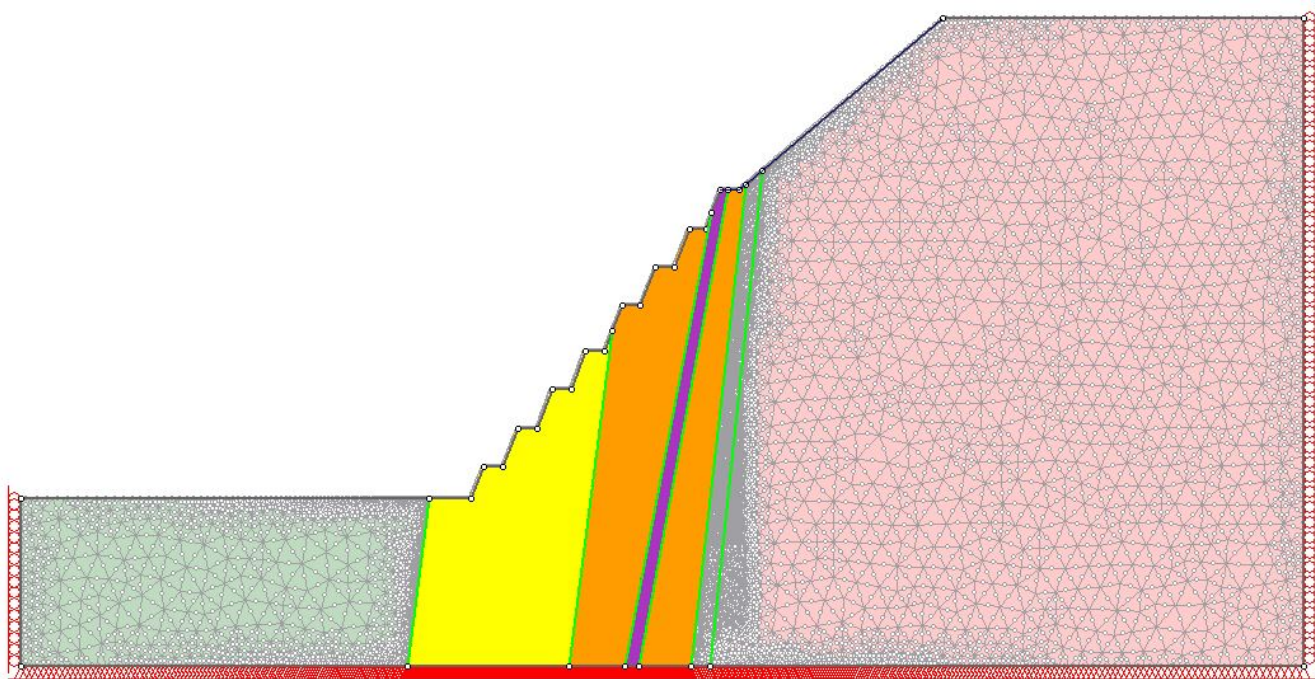


Figure G.23: The numerical model of section S2 showing the division of the model into finite elements. The model was used to perform the stability analysis of the current back wall using method 2.

G.3.3 Elevation profiles

Section S1

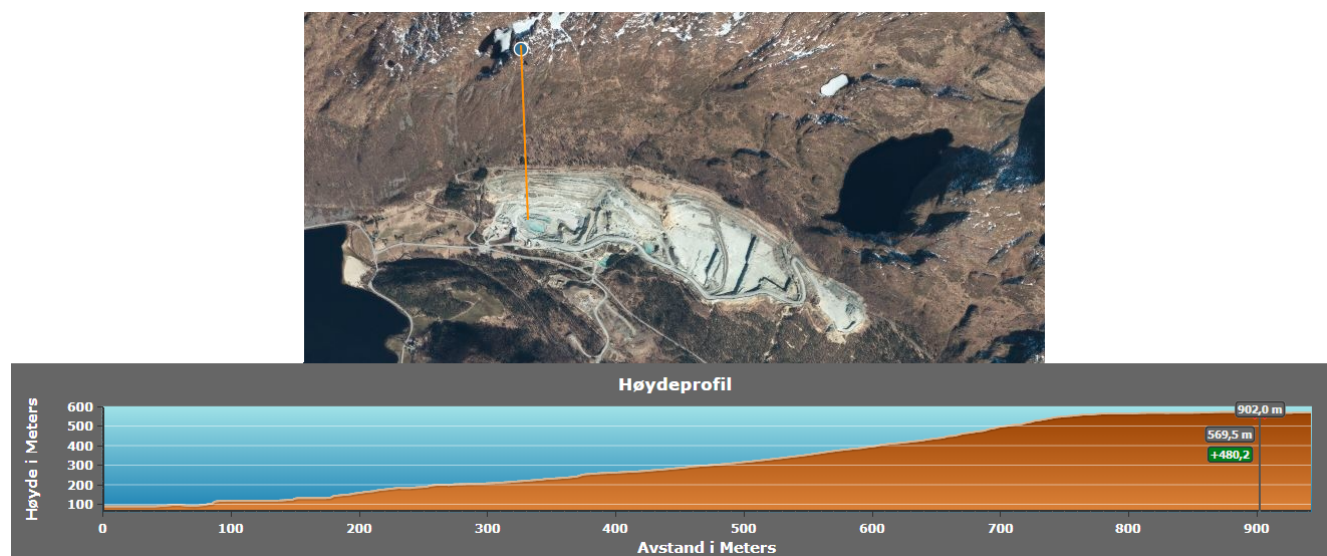


Figure G.24: The figure show the elevation profile used to draw the hill slope above the quarry in the numerical model of section S1. The profile show the elevation along the orange line. "Høyde i Meters" define meters above sea level. "Avstand in Meters" define the distance from the start of the line in meters The elevation profile is made by Høydedata (Kartverket, 2020).

Section S2

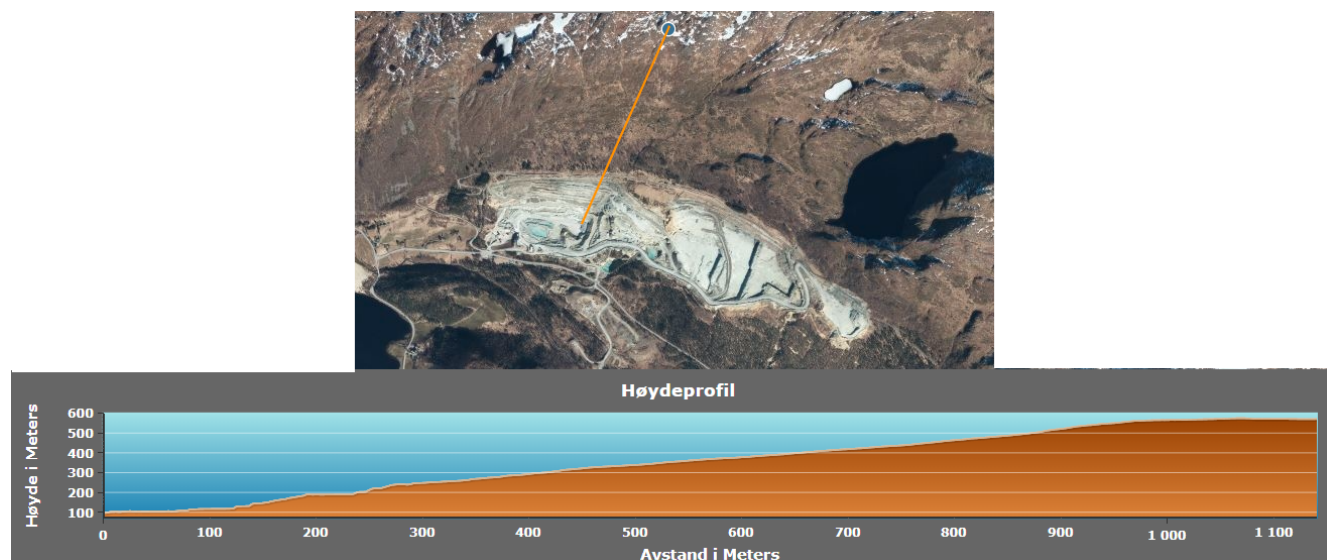


Figure G.25: The figure show the elevation profile used to draw the hill slope above the quarry in the numerical model of section S2. The profile show the elevation along the orange line. "Høyde i Meters" define meters above sea level. "Avstand in Meters" define the distance from the start of the line in meters The elevation profile is made by Høydedata (Kartverket, 2020).

Section S3

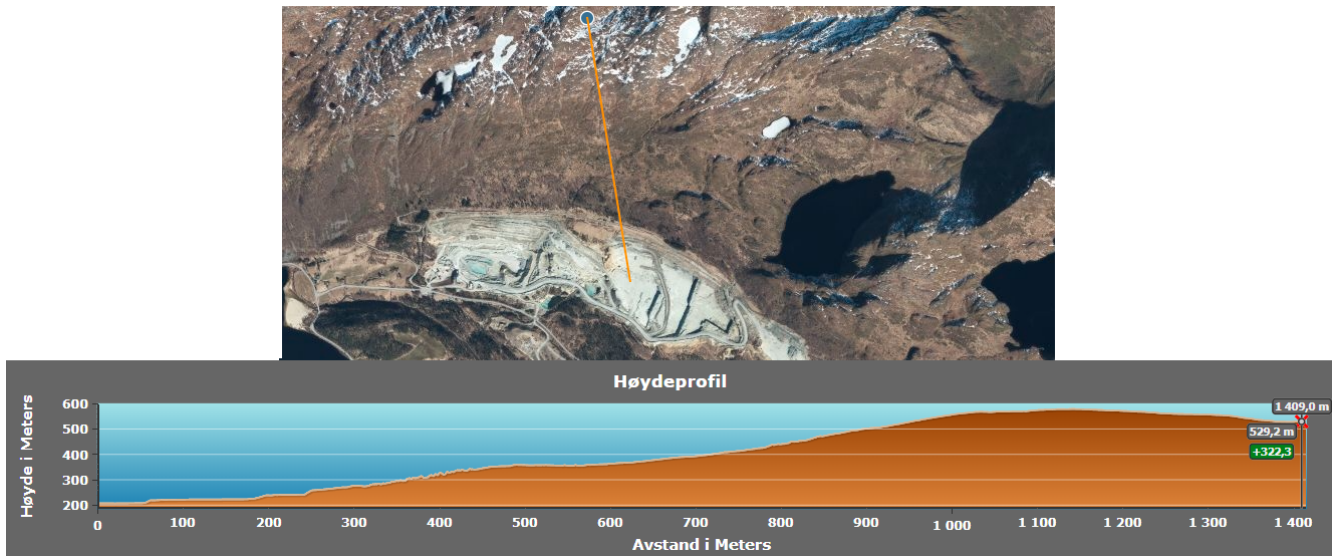


Figure G.26: The figure show the elevation profile used to draw the hill slope above the quarry in the numerical model of section S3. The profile show the elevation along the orange line. "Høyde i Meters" define meters above sea level. "Avstand in Meters" define the distance from the start of the line in meters The elevation profile is made by Høydedata (Kartverket, 2020).

Section S4

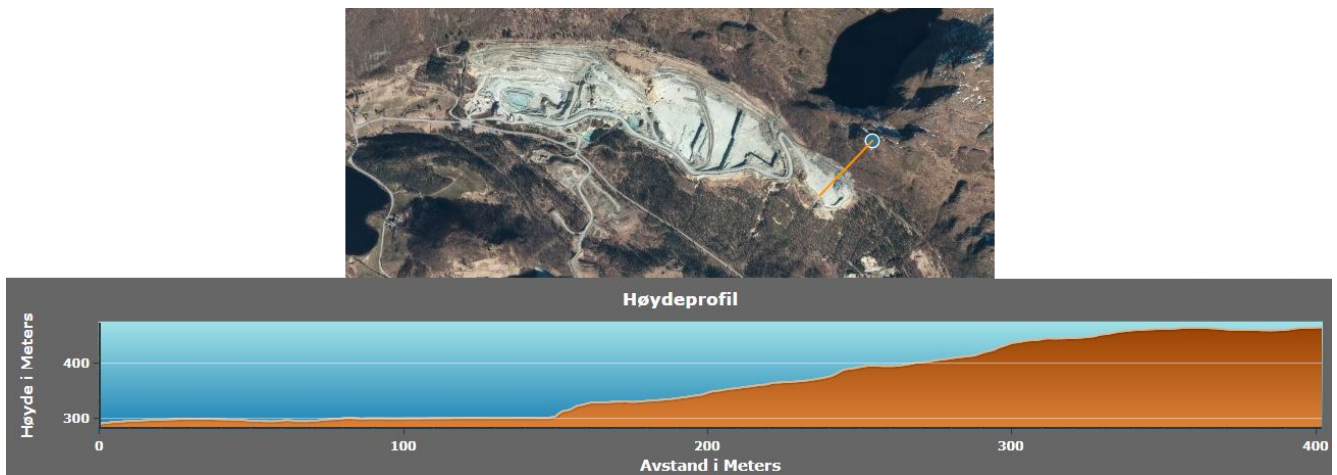


Figure G.27: The figure show the elevation profile used to draw the hill slope above the quarry in the numerical model of section S4. The profile show the elevation along the orange line. "Høyde i Meters" define meters above sea level. "Avstand in Meters" define the distance from the start of the line in meters The elevation profile is made by Høydedata (Kartverket, 2020).

G.3.4 Data for plotting from the numerical models for analysing method 1

Section S1

	Punkt 1	Punkt 2	Punkt 3	Punkt 4	Punkt 5	Punkt 6	Punkt 7
SRF	Total displacement (m)	Total displacement (m)	Total displacement (m)	Total displacement (m)	Total displacement (m)	Total displacement (m)	Total displacement (m)
1	0	0	0	0	0	0	0
2	0.0030	0.0013	0.0017	0.0006	0.0007	0.0001	0.0017
2.2	0.0035	0.0016	0.0021	0.0007	0.0011	0.0002	0.0023
2.4	0.0044	0.0019	0.0027	0.0012	0.0018	0.0005	0.0040
2.6	0.0049	0.0025	0.0031	0.0018	0.0026	0.0008	0.0049
2.8	0.0056	0.0034	0.0038	0.0031	0.0036	0.0014	0.0061
3	0.0062	0.0048	0.0048	0.0043	0.0046	0.0029	0.0078
3.2	0.0067	0.0056	0.0056	0.0049	0.0054	0.0039	0.0089
3.4	0.0074	0.0063	0.0064	0.0053	0.0062	0.0052	0.0096
3.6	0.0084	0.0074	0.0073	0.0057	0.0069	0.0065	0.0109
3.8	0.0100	0.0088	0.0082	0.0061	0.0074	0.0079	0.0125
4	0.0114	0.0100	0.0094	0.0065	0.0081	0.0092	0.0140
4.03	0.0118	0.0103	0.0096	0.0066	0.0082	0.0094	0.0142
4.06	0.0121	0.0106	0.0099	0.0068	0.0083	0.0097	0.0146
4.07	0.0122	0.0107	0.0100	0.0069	0.0084	0.0098	0.0147
4.08	0.0122	0.0107	0.0101	0.0070	0.0084	0.0098	0.0148
4.09	0.0124	0.0108	0.0105	0.0078	0.0085	0.0099	0.0151
4.2	0.0130	0.0114	0.0141	0.0123	0.0089	0.0105	0.0180

Table G.2: Data of displacement in point 1-7 for increasing SRF. The data was used to create the graph in section 5.5.1 for stability analysis of the final back wall along section S1.

Section S2: Current back wall

	Punkt 1	Punkt 2	Punkt 3	Punkt 4	Punkt 5	Punkt 6	Punkt 7	Punkt 8
SRF	Total displacement (m)	Total displacement (m)	Total displacement (m)	Total displacement (m)	Total displacement (m)	Total displacement (m)	Total displacement (m)	Total displacement (m)
1	0	0	0	0	0	0	0	0
1.75	0.00081	0.00049	0.00044	0.00033	0.00092	0.00060	0.00113	0.00079
1.95	0.00128	0.00081	0.00084	0.00068	0.00170	0.00101	0.00174	0.00126
2.15	0.00184	0.00125	0.00129	0.00099	0.00240	0.00142	0.00226	0.00164
2.35	0.00241	0.00169	0.00186	0.00126	0.00309	0.00186	0.00280	0.00200
2.45	0.00271	0.00198	0.00214	0.00142	0.00339	0.00208	0.00306	0.00220
2.55	0.00299	0.00230	0.00248	0.00161	0.00369	0.00229	0.00332	0.00245
2.65	0.00329	0.00260	0.00284	0.00184	0.00397	0.00250	0.00353	0.00270
2.75	0.00356	0.00296	0.00318	0.00210	0.00424	0.00273	0.00374	0.00297
2.85	0.00382	0.00333	0.00356	0.00239	0.00449	0.00298	0.00395	0.00324
2.95	0.00409	0.00368	0.00395	0.00272	0.00474	0.00324	0.00417	0.00352
3.05	0.00435	0.00402	0.00435	0.00309	0.00499	0.00350	0.00441	0.00382
3.15	0.00461	0.00442	0.00478	0.00343	0.00522	0.00377	0.00464	0.00413
3.25	0.00486	0.00483	0.00518	0.00381	0.00546	0.00403	0.00488	0.00444
3.35	0.00511	0.00523	0.00559	0.00419	0.00569	0.00430	0.00511	0.00476
3.45	0.00538	0.00572	0.00605	0.00460	0.00592	0.00456	0.00536	0.00508
3.55	0.00562	0.00621	0.00650	0.00501	0.00615	0.00482	0.00559	0.00539
3.65	0.00585	0.00665	0.00693	0.00542	0.00638	0.00507	0.00583	0.00570
3.75	0.00608	0.00712	0.00738	0.00584	0.00662	0.00532	0.00606	0.00600
3.85	0.00628	0.00765	0.00786	0.00627	0.00686	0.00556	0.00626	0.00626
3.95	0.00646	0.00820	0.00833	0.00674	0.00713	0.00579	0.00648	0.00653
4.05	0.00666	0.00875	0.00882	0.00720	0.00744	0.00603	0.00671	0.00678
4.14	0.00681	0.00930	0.00932	0.00766	0.00771	0.00623	0.00690	0.00698
4.23	0.00698	0.00987	0.00984	0.00817	0.00800	0.00645	0.00709	0.00717
4.33	0.00716	0.01057	0.01047	0.00877	0.00841	0.00672	0.00735	0.00741
4.42	0.00732	0.01119	0.01107	0.00933	0.00874	0.00696	0.00757	0.00761
4.51	0.00747	0.01177	0.01164	0.00987	0.00911	0.00720	0.00780	0.00781
4.6	0.00761	0.01238	0.01221	0.01039	0.00944	0.00744	0.00801	0.00800
4.7	0.00776	0.01300	0.01283	0.01097	0.00984	0.00771	0.00827	0.00823
4.8	0.00791	0.01370	0.01346	0.01156	0.01023	0.00798	0.00854	0.00849
4.89	0.00802	0.01422	0.01398	0.01204	0.01060	0.00824	0.00879	0.00873
4.98	0.00814	0.01476	0.01450	0.01252	0.01099	0.00851	0.00907	0.00898
5.08	0.00828	0.01533	0.01511	0.01301	0.01143	0.00882	0.00940	0.00928
5.18	0.00841	0.01593	0.01571	0.01359	0.01193	0.00913	0.00975	0.00953
5.27	0.00852	0.01640	0.01626	0.01408	0.01238	0.00942	0.01008	0.00969
5.37	0.00864	0.01701	0.01686	0.01460	0.01296	0.00979	0.01055	0.00988
5.47	0.00877	0.01761	0.01752	0.01518	0.01364	0.01020	0.01117	0.01016
5.56	0.00887	0.01812	0.01818	0.01565	0.01443	0.01061	0.01188	0.01050
5.61	0.00893	0.01849	0.01860	0.01597	0.01494	0.01085	0.01235	0.01073
5.63	0.00894	0.01851	0.01871	0.01603	0.01504	0.01089	0.01243	0.01076
5.66	0.00896	0.01864	0.01881	0.01611	0.01513	0.01095	0.01255	0.01083
6.11	0.00980	0.08929	0.16132	0.09902	0.18984	0.07072	0.18145	0.17382

Table G.3: Data of displacement in point 1-7 for increasing SRF. The data was used to create the graph in section 5.5.1 for stability analysis of the current back wall along section S2.

Section S2: Final back wall

	Punkt 1	Punkt 2	Punkt 3	Punkt 4	Punkt 5	Punkt 6	Punkt 7
SRF	Total displacement (m)	Total displacement (m)	Total displacement (m)	Total displacement (m)	Total displacement (m)	Total displacement (m)	Total displacement (m)
1	0.00000	0.00000	0.00000	0.00000	0.00000	0.00000	0.00000
1.2	0.00021	0.00062	0.00029	0.00018	0.00018	0.00019	0.00155
1.4	0.00031	0.00023	0.00044	0.00027	0.00028	0.00051	0.00156
1.6	0.00136	0.00063	0.00089	0.00063	0.00062	0.00087	0.00151
1.8	0.00210	0.00080	0.00119	0.00087	0.00085	0.00115	0.00191
2	0.00254	0.00097	0.00150	0.00117	0.00109	0.00134	0.00248
2.1	0.00289	0.00129	0.00170	0.00138	0.00125	0.00148	0.00266
2.2	0.00314	0.00156	0.00187	0.00152	0.00139	0.00153	0.00317
2.3	0.00358	0.00190	0.00208	0.00175	0.00156	0.00175	0.00382
2.4	0.00376	0.00231	0.00223	0.00183	0.00170	0.00198	0.00415
2.5	0.00392	0.00264	0.00239	0.00199	0.00184	0.00221	0.00472
2.6	0.00428	0.00286	0.00257	0.00214	0.00204	0.00242	0.00512
2.7	0.00437	0.00302	0.00271	0.00235	0.00224	0.00261	0.00533
2.8	0.00457	0.00327	0.00305	0.00262	0.00250	0.00286	0.00585
2.9	0.00486	0.00351	0.00329	0.00275	0.00273	0.00307	0.00623
3	0.00512	0.00397	0.00368	0.00296	0.00304	0.00320	0.00692
3.1	0.00516	0.00435	0.00404	0.00324	0.00335	0.00368	0.00740
3.2	0.00548	0.00487	0.00433	0.00379	0.00374	0.00426	0.00853
3.3	0.00609	0.00539	0.00502	0.00496	0.00430	0.00479	0.00948
3.31	0.00608	0.00539	0.00508	0.00513	0.00432	0.00483	0.00943
3.32	0.00620	0.00554	0.00628	0.00609	0.00467	0.00500	0.00987
3.35	0.00626	0.00566	0.00713	0.00785	0.00505	0.00504	0.01052
3.4	0.00658	0.00632	0.08028	0.04185	0.02673	0.00535	0.03318

Table G.4: Data of displacement in point 1-7 for increasing SRF. The data was used to create the graph in section 5.5.1 for stability analysis of the final back wall along section S2.

Section S3

	Punkt 1	Punkt 2	Punkt 3	Punkt 4	Punkt 5	Punkt 6	Punkt 7
SRF	Total displacement (m)	Total displacement (m)	Total displacement (m)	Total displacement (m)	Total displacement (m)	Total displacement (m)	Total displacement (m)
1	0	0	0	0	0	0	0
1.4	0.00147	0.00088	0.00014	0.00025	0.00012	0.00051	0.00039
1.6	0.00188	0.00107	0.00022	0.00036	0.00018	0.00067	0.00082
1.8	0.00257	0.00092	0.00055	0.00074	0.00043	0.00042	0.00198
2	0.00339	0.00172	0.00088	0.00113	0.00069	0.00072	0.00324
2.2	0.00386	0.00196	0.00119	0.00111	0.00096	0.00093	0.00390
2.4	0.00457	0.00223	0.00172	0.00118	0.00139	0.00133	0.00463
2.6	0.00494	0.00268	0.00241	0.00138	0.00201	0.00150	0.00576
2.8	0.00546	0.00309	0.00323	0.00207	0.00278	0.00292	0.00748
2.9	0.00593	0.00335	0.00384	0.00329	0.00325	0.00168	0.00760
2.95	0.00614	0.00440	0.00424	0.00383	0.00361	0.00274	0.00859
2.97	0.00614	0.00372	0.00459	0.00417	0.00402	0.00244	0.00841
2.98	0.00633	0.00427	0.00482	0.00470	0.00432	0.00267	0.00869
3	0.00789	0.00656	0.01152	0.01285	0.00874	0.00454	0.01049
3.4	0.00804	0.00649	0.06684	0.06258	0.04878	0.00496	0.04071

Table G.5: Data of displacement in point 1-7 for increasing SRF. The data was used to create the graph in section 5.5.1 for stability analysis of the final back wall along section S3.

Section S4

	Punkt 1	Punkt 2	Punkt 3	Punkt 4	Punkt 5	Punkt 6	Punkt 7	Punkt 8
SRF	Total displacement (m)	Total displacement (m)	Total displacement (m)	Total displacement (m)	Total displacement (m)	Total displacement (m)	Total displacement (m)	Total displacement (m)
1	0.000000	0.000000	0.000000	0.000000	0.000000	0.000000	0.000000	0.000000
1.2	0.000014	0.000026	0.000118	0.001038	0.000203	0.000063	0.000006	0.000181
1.4	0.000059	0.000048	0.000074	0.000903	0.000042	0.000056	0.000007	0.000112
1.6	0.000273	0.000167	0.000196	0.000801	0.000080	0.000168	0.000022	0.000251
1.7	0.000464	0.000275	0.000263	0.001102	0.000101	0.000232	0.000034	0.000237
1.9	0.000812	0.000490	0.000388	0.001891	0.000146	0.000373	0.000068	0.000379
2.1	0.001122	0.000767	0.000578	0.005627	0.000222	0.000599	0.00116	0.000545
2.3	0.001493	0.001144	0.000825	0.005970	0.000335	0.000923	0.00170	0.000783
2.5	0.001975	0.001576	0.001086	0.005250	0.000456	0.001288	0.00233	0.000906
2.7	0.002535	0.002029	0.001484	0.006335	0.000640	0.001648	0.00305	0.001233
2.9	0.003118	0.002494	0.001933	0.005916	0.000846	0.002022	0.00381	0.001590
3.1	0.003798	0.003056	0.002509	0.004723	0.001101	0.002457	0.00463	0.002203
3.3	0.004585	0.003704	0.003051	0.004429	0.001338	0.002882	0.00550	0.002635
3.5	0.005375	0.004483	0.003712	0.003856	0.001626	0.003345	0.00648	0.003277
3.7	0.006274	0.005400	0.004328	0.002300	0.001916	0.003952	0.00748	0.003937
3.9	0.007186	0.006501	0.005132	0.002938	0.002276	0.004772	0.00871	0.004932
3.99	0.007651	0.007015	0.005592	0.001645	0.002467	0.005194	0.00935	0.005528
4.04	0.007894	0.007304	0.005978	0.002063	0.002592	0.005430	0.00976	0.005591
4.06	0.007988	0.007439	0.005977	0.001733	0.002610	0.005543	0.00987	0.005487
4.07	0.008041	0.007480	0.006191	0.005212	0.002646	0.005575	0.00998	0.006433
4.09	0.008291	0.008077	0.026939	0.034514	0.003211	0.005961	0.01346	0.036571
4.49	0.010233	0.011178	0.039581	0.044575	0.004156	0.008756	0.01869	0.052075

Table G.6: Data of displacement in point 1-7 for increasing SRF. The data was used to create the graph in section 5.5.1 for stability analysis of the current back wall along section S4.

G.3.5 Data used in graphs from analysing method 2

Section S1

Joint 1		Joint 2		Joint 3	
Location (y-coordinate) (m)	Shear displacement (m)	Location (y-coordinate) (m)	Shear displacement (m)	Location (y-coordinate) (m)	Shear displacement (m)
-162.07	-0.0000163	-23.57	-0.0000219	46.48	-0.0000280
-160.51	-0.0000275	-22.75	-0.0000365	47.43	-0.0000686
-158.97	-0.0000280	-21.97	-0.0000416	48.38	-0.0001051
-157.44	-0.0000278	-21.16	-0.0000424	49.33	-0.0001296
-155.91	-0.0000283	-20.26	-0.0000398	50.28	-0.0001274
-154.40	-0.0000283	-19.31	-0.0000402	51.23	-0.0000974
-152.89	-0.0000287	-18.36	-0.0000410	52.19	-0.0000735
-151.40	-0.0000289	-17.41	-0.0000411	53.14	-0.0000697
-149.91	-0.0000292	-16.45	-0.0000411	54.09	-0.0000612
-148.44	-0.0000295	-15.50	-0.0000416	55.04	-0.0000307
-146.98	-0.0000297	-14.55	-0.0000419	55.99	-0.0000084
-145.52	-0.0000300	-13.60	-0.0000420	56.94	-0.0000065
-144.08	-0.0000302	-12.65	-0.0000425	57.89	-0.0000104
-142.64	-0.0000304	-11.70	-0.0000428	58.84	-0.0000136
-141.21	-0.0000307	-10.75	-0.0000430	59.79	-0.0000140
-139.80	-0.0000309	-9.80	-0.0000432	60.74	-0.0000120
-138.39	-0.0000311	-8.85	-0.0000434	61.70	-0.0000128
-136.99	-0.0000313	-7.89	-0.0000436	62.65	-0.0000258
-135.60	-0.0000315	-6.94	-0.0000437	63.60	-0.0000489
-134.22	-0.0000317	-5.99	-0.0000439	64.67	-0.0000692
-132.85	-0.0000319	-5.04	-0.0000441	65.84	-0.0000787
-131.49	-0.0000321	-4.09	-0.0000442	66.90	-0.0000740
-130.14	-0.0000322	-3.14	-0.0000443	67.85	-0.0000589
-128.80	-0.0000324	-2.19	-0.0000443	68.80	-0.0000364
-127.46	-0.0000326	-1.24	-0.0000443	69.75	-0.0000181
-126.13	-0.0000327	-0.29	-0.0000443	70.70	-0.0000118
-124.82	-0.0000329	0.66	-0.0000442	71.65	-0.0000109
-123.51	-0.0000330	1.62	-0.0000441	72.61	-0.0000180
-122.21	-0.0000332	2.57	-0.0000439	73.56	-0.0000376
-120.92	-0.0000333	3.52	-0.0000438	74.51	-0.0000551
-119.63	-0.0000334	4.47	-0.0000438	75.46	-0.0000628
-118.36	-0.0000335	5.42	-0.0000438	76.41	-0.0000697
-117.09	-0.0000337	6.37	-0.0000440	77.36	-0.0000814
-115.83	-0.0000338	7.32	-0.0000447	78.31	-0.0000940
-114.58	-0.0000339	8.27	-0.0000472	79.26	-0.0001028
-113.34	-0.0000340	9.22	-0.0000527	80.21	-0.0001060
-112.11	-0.0000341	10.18	-0.0000614	81.09	-0.0000958
-110.88	-0.0000343	11.13	-0.0000711	81.72	-0.0000810
-109.66	-0.0000344	12.08	-0.0000807	82.31	-0.0000648
-108.45	-0.0000345	13.03	-0.0001062	83.02	-0.0000423
-107.25	-0.0000346	13.98	-0.0001695	83.76	-0.0000248
-106.06	-0.0000347	14.93	-0.0002360	84.36	-0.0000173
-104.87	-0.0000348	15.88	-0.0002240	84.69	-0.0000140
-103.69	-0.0000349	16.83	-0.0002293	84.90	-0.0000113
-102.52	-0.0000349	17.78	-0.0002825		
-101.35	-0.0000350	18.73	-0.0003232		
-100.20	-0.0000351	19.69	-0.0003579		
-99.05	-0.0000352	20.64	-0.0003854		

Joint 1		Joint 2		Joint 3	
Location (y-coordinate) (m)	Shear displacement (m)	Location (y-coordinate) (m)	Shear displacement (m)	Location (y-coordinate) (m)	Shear displacement (m)
-97.91	-0.0000353	21.59	-0.0003994		
-96.77	-0.0000354	22.54	-0.0003989		
-95.65	-0.0000354	23.49	-0.0003906		
-94.53	-0.0000355	24.44	-0.0003765		
-93.41	-0.0000356	25.39	-0.0003394		
-92.31	-0.0000357	26.34	-0.0002881		
-91.21	-0.0000357	27.29	-0.0001981		
-90.12	-0.0000358	28.25	-0.0000990		
-89.03	-0.0000359	29.20	-0.0000466		
-87.96	-0.0000360	30.14	-0.0000498		
-86.89	-0.0000360	31.14	-0.0000796		
-85.82	-0.0000361	32.14	-0.0001076		
-84.77	-0.0000362	33.09	-0.0001206		
-83.72	-0.0000362	34.05	-0.0001222		
-82.68	-0.0000363	35.00	-0.0001156		
-81.64	-0.0000363	35.95	-0.0001029		
-80.61	-0.0000364	36.90	-0.0000821		
-79.59	-0.0000365	37.85	-0.0000535		
-78.57	-0.0000365	38.80	-0.0000340		
-77.56	-0.0000366	39.75	-0.0000318		
-76.56	-0.0000366	40.70	-0.0000332		
-75.56	-0.0000367	41.65	-0.0000410		
-74.57	-0.0000367	42.61	-0.0000594		
-73.59	-0.0000368	43.56	-0.0000778		
-72.61	-0.0000369	44.51	-0.0000873		
-71.64	-0.0000369	45.46	-0.0000859		
-70.67	-0.0000370	46.41	-0.0000859		
-69.59	-0.0000370	47.36	-0.0000858		
-68.39	-0.0000371	48.31	-0.0000836		
-67.31	-0.0000371	49.26	-0.0000838		
-66.34	-0.0000372	50.21	-0.0000836		
-65.37	-0.0000373	51.16	-0.0000804		
-64.41	-0.0000373	52.12	-0.0000754		
-63.44	-0.0000374	53.07	-0.0000691		
-62.48	-0.0000374	54.02	-0.0000606		
-61.51	-0.0000375	54.97	-0.0000501		
-60.54	-0.0000375	55.92	-0.0000337		
-59.58	-0.0000376	56.87	-0.0000202		
-58.61	-0.0000376	57.82	-0.0000235		
-57.65	-0.0000377	58.77	-0.0000378		
-56.68	-0.0000377	59.72	-0.0000528		
-55.71	-0.0000378	60.68	-0.0000619		
-54.75	-0.0000379	61.63	-0.0000643		
-53.78	-0.0000379	62.58	-0.0000605		
-52.82	-0.0000380	63.53	-0.0000495		
-51.85	-0.0000380	64.48	-0.0000420		
-50.89	-0.0000381	65.43	-0.0000488		
-49.92	-0.0000382	66.38	-0.0000590		
-48.95	-0.0000382	67.33	-0.0000671		
-47.99	-0.0000383	68.28	-0.0000705		
-47.02	-0.0000383	69.24	-0.0000684		
-46.06	-0.0000384	70.19	-0.0000600		
-45.09	-0.0000385	71.14	-0.0000530		

Joint 1		Joint 2		Joint 3	
Location (y-coordinate) (m)	Shear displacement (m)	Location (y-coordinate) (m)	Shear displacement (m)	Location (y-coordinate) (m)	Shear displacement (m)
-44.12	-0.0000385	72.09	-0.0000529		
-43.16	-0.0000386	73.04	-0.0000544		
-42.19	-0.0000387	73.99	-0.0000546		
-41.23	-0.0000388	74.94	-0.0000500		
-40.26	-0.0000388	75.89	-0.0000431		
-39.29	-0.0000389	76.84	-0.0000436		
-38.33	-0.0000389	77.79	-0.0000510		
-37.36	-0.0000389	78.75	-0.0000594		
-36.40	-0.0000389	79.70	-0.0000660		
-35.43	-0.0000389	80.65	-0.0000696		
-34.46	-0.0000390	81.60	-0.0000640		
-33.50	-0.0000390	82.55	-0.0000473		
-32.53	-0.0000390	83.46	-0.0000227		
-31.57	-0.0000391	84.19	-0.0000056		
-30.60	-0.0000391	84.75	-0.0000030		
-29.63	-0.0000391				
-28.67	-0.0000391				
-27.70	-0.0000392				
-26.74	-0.0000392				
-25.77	-0.0000393				
-24.81	-0.0000393				
-23.84	-0.0000394				
-22.87	-0.0000394				
-21.91	-0.0000395				
-20.94	-0.0000395				
-19.98	-0.0000396				
-19.01	-0.0000397				
-18.04	-0.0000398				
-17.08	-0.0000399				
-16.11	-0.0000401				
-15.15	-0.0000403				
-14.18	-0.0000405				
-13.21	-0.0000408				
-12.25	-0.0000412				
-11.28	-0.0000416				
-10.32	-0.0000422				
-9.35	-0.0000429				
-8.38	-0.0000438				
-7.42	-0.0000448				
-6.45	-0.0000461				
-5.49	-0.0000475				
-4.52	-0.0000490				
-3.55	-0.0000505				
-2.59	-0.0000519				
-1.62	-0.0000530				
-0.66	-0.0000536				
0.31	-0.0000551				
1.27	-0.0000605				
2.24	-0.0000704				
3.21	-0.0000837				
4.17	-0.0000970				
5.14	-0.0001095				
6.10	-0.0001363				

Joint 1		Joint 2		Joint 3	
Location (y-coordinate) (m)	Shear displacement (m)	Location (y-coordinate) (m)	Shear displacement (m)	Location (y-coordinate) (m)	Shear displacement (m)
7.07	-0.0001795				
8.04	-0.0002144				
9.00	-0.0002222				
9.97	-0.0002137				
10.93	-0.0002270				
11.90	-0.0002588				
12.87	-0.0003020				
13.83	-0.0003590				
14.80	-0.0004244				
15.76	-0.0004973				
16.73	-0.0005646				
17.70	-0.0006062				
18.66	-0.0006262				
19.63	-0.0005999				
20.59	-0.0004946				
21.56	-0.0003449				
22.53	-0.0002103				
23.45	-0.0000767				
24.19	-0.0000117				
24.75	-0.0000043				

Table G.7: Data of shear displacement along joint 1,2, and 3 for increasing SRF. The data was used to create the graph in section 5.5.2 for stability analysis of the final back wall along section S1.

Section S2: Current back wall

Joint 1		Joint 2		Joint 3	
Location (y-coordinate) (m)	Shear displacement (m)	Location (y-coordinate) (m)	Shear displacement (m)	Location (y-coordinate) (m)	Shear displacement (m)
-217.8	0.0000138	-148.7	-0.0000225	86.0	-0.000008
-217.2	0.0000236	-146.8	-0.0000353	86.9	-0.000020
-216.4	0.0000229	-144.9	-0.0000397	87.9	-0.000028
-214.8	0.0000182	-143.0	-0.0000405	88.8	-0.000039
-211.8	0.0000102	-141.1	-0.0000410	89.8	-0.000056
-207.5	0.0000016	-139.2	-0.0000414	90.7	-0.000073
-203.1	-0.0000049	-137.3	-0.0000431	91.7	-0.000088
-198.7	-0.0000097	-135.4	-0.0000428	92.6	-0.000102
-194.5	-0.0000135	-133.5	-0.0000390	93.6	-0.000119
-190.5	-0.0000166	-131.6	-0.0000407	94.5	-0.000132
-186.6	-0.0000192	-129.7	-0.0000431	95.5	-0.000139
-182.8	-0.0000215	-127.8	-0.0000433	96.4	-0.000133
-179.1	-0.0000234	-125.9	-0.0000432	97.4	-0.000107
-175.6	-0.0000252	-124.0	-0.0000442	98.3	-0.000064
-172.1	-0.0000267	-122.0	-0.0000449	99.4	-0.000035
-168.8	-0.0000281	-120.1	-0.0000422	100.5	-0.000032
-165.6	-0.0000294	-118.2	-0.0000418	101.5	-0.000037
-162.5	-0.0000305	-116.3	-0.0000436	102.5	-0.000043
-159.5	-0.0000315	-114.4	-0.0000446	103.4	-0.000046
-156.6	-0.0000325	-112.5	-0.0000447	104.4	-0.000044
-153.8	-0.0000333	-110.6	-0.0000457	105.3	-0.000035
-151.0	-0.0000341	-108.7	-0.0000466	106.3	-0.000027

Joint 1		Joint 2		Joint 3	
Location (y-coordinate) (m)	Shear displacement (m)	Location (y-coordinate) (m)	Shear displacement (m)	Location (y-coordinate) (m)	Shear displacement (m)
-148.4	-0.0000349	-106.8	-0.0000449	107.2	-0.000028
-145.9	-0.0000355	-104.9	-0.0000437	108.2	-0.000034
-143.4	-0.0000361	-103.0	-0.0000442	109.1	-0.000042
-141.0	-0.0000367	-101.1	-0.0000455	110.1	-0.000050
-138.7	-0.0000372	-99.2	-0.0000458	111.0	-0.000055
-136.5	-0.0000376	-97.3	-0.0000468	112.0	-0.000055
-134.3	-0.0000381	-95.4	-0.0000476	112.8	-0.000053
-132.2	-0.0000385	-93.5	-0.0000466	113.4	-0.000051
-130.2	-0.0000388	-91.6	-0.0000454	113.8	-0.000050
-128.2	-0.0000391	-89.7	-0.0000451	114.1	-0.000050
-126.3	-0.0000395	-87.8	-0.0000460		
-124.3	-0.0000398	-85.9	-0.0000466		
-122.4	-0.0000400	-84.0	-0.0000476		
-120.5	-0.0000403	-82.1	-0.0000482		
-118.5	-0.0000406	-80.2	-0.0000471		
-116.6	-0.0000408	-78.3	-0.0000460		
-114.7	-0.0000410	-76.4	-0.0000450		
-112.7	-0.0000412	-74.5	-0.0000450		
-110.8	-0.0000414	-72.6	-0.0000457		
-108.9	-0.0000416	-70.7	-0.0000467		
-106.9	-0.0000418	-68.8	-0.0000474		
-105.0	-0.0000420	-67.0	-0.0000469		
-103.1	-0.0000421	-65.3	-0.0000464		
-101.2	-0.0000423	-63.7	-0.0000459		
-99.2	-0.0000424	-62.2	-0.0000454		
-97.2	-0.0000426	-60.8	-0.0000455		
-95.0	-0.0000427	-59.5	-0.0000459		
-92.9	-0.0000428	-58.2	-0.0000465		
-90.9	-0.0000429	-57.1	-0.0000471		
-89.0	-0.0000430	-56.0	-0.0000476		
-87.1	-0.0000431	-54.9	-0.0000476		
-85.1	-0.0000431	-53.9	-0.0000474		
-83.2	-0.0000432	-53.0	-0.0000471		
-81.3	-0.0000433	-52.0	-0.0000470		
-79.3	-0.0000433	-51.1	-0.0000468		
-77.4	-0.0000434	-50.1	-0.0000465		
-75.5	-0.0000434	-49.2	-0.0000463		
-73.5	-0.0000434	-48.2	-0.0000460		
-71.6	-0.0000435	-47.3	-0.0000459		
-69.7	-0.0000435	-46.3	-0.0000461		
-67.8	-0.0000435	-45.4	-0.0000465		
-66.1	-0.0000435	-44.4	-0.0000470		
-64.4	-0.0000435	-43.5	-0.0000475		
-62.8	-0.0000435	-42.5	-0.0000478		
-61.4	-0.0000435	-41.6	-0.0000479		
-60.0	-0.0000435	-40.6	-0.0000478		
-58.7	-0.0000435	-39.7	-0.0000476		
-57.5	-0.0000435	-38.7	-0.0000475		
-56.3	-0.0000435	-37.8	-0.0000473		
-55.2	-0.0000435	-36.8	-0.0000472		
-54.2	-0.0000435	-35.9	-0.0000470		
-53.2	-0.0000435	-34.9	-0.0000468		
-52.3	-0.0000435	-34.0	-0.0000466		

Joint 1		Joint 2		Joint 3	
Location (y-coordinate) (m)	Shear displacement (m)	Location (y-coordinate) (m)	Shear displacement (m)	Location (y-coordinate) (m)	Shear displacement (m)
-51.3	-0.0000435	-33.0	-0.0000466		
-50.3	-0.0000435	-32.0	-0.0000469		
-49.4	-0.0000435	-31.1	-0.0000473		
-48.4	-0.0000435	-30.1	-0.0000477		
-47.4	-0.0000435	-29.2	-0.0000481		
-46.5	-0.0000435	-28.2	-0.0000482		
-45.5	-0.0000435	-27.3	-0.0000481		
-44.5	-0.0000435	-26.3	-0.0000480		
-43.6	-0.0000435	-25.6	-0.0000480		
-42.6	-0.0000435	-24.8	-0.0000479		
-41.7	-0.0000435	-23.9	-0.0000478		
-40.7	-0.0000435	-22.9	-0.0000477		
-39.7	-0.0000435	-22.0	-0.0000476		
-38.8	-0.0000435	-21.0	-0.0000474		
-37.8	-0.0000435	-20.1	-0.0000473		
-36.8	-0.0000435	-19.1	-0.0000473		
-35.9	-0.0000435	-18.2	-0.0000475		
-34.9	-0.0000435	-17.2	-0.0000478		
-33.9	-0.0000435	-16.3	-0.0000482		
-33.0	-0.0000435	-15.3	-0.0000484		
-32.0	-0.0000435	-14.4	-0.0000484		
-31.0	-0.0000435	-13.4	-0.0000484		
-30.1	-0.0000435	-12.5	-0.0000483		
-29.1	-0.0000435	-11.5	-0.0000483		
-28.1	-0.0000435	-10.6	-0.0000482		
-27.2	-0.0000436	-9.6	-0.0000481		
-26.2	-0.0000436	-8.7	-0.0000480		
-25.2	-0.0000436	-7.7	-0.0000479		
-24.3	-0.0000436	-6.8	-0.0000477		
-23.3	-0.0000436	-5.8	-0.0000477		
-22.3	-0.0000436	-4.9	-0.0000477		
-21.4	-0.0000436	-3.9	-0.0000479		
-20.4	-0.0000436	-3.0	-0.0000480		
-19.4	-0.0000436	-2.0	-0.0000482		
-18.5	-0.0000436	-1.1	-0.0000482		
-17.5	-0.0000437	-0.1	-0.0000481		
-16.5	-0.0000437	0.8	-0.0000480		
-15.6	-0.0000437	1.8	-0.0000479		
-14.6	-0.0000437	2.7	-0.0000477		
-13.6	-0.0000437	3.7	-0.0000476		
-12.7	-0.0000437	4.6	-0.0000474		
-11.7	-0.0000437	5.6	-0.0000472		
-10.7	-0.0000437	6.5	-0.0000470		
-9.8	-0.0000437	7.5	-0.0000468		
-8.8	-0.0000437	8.5	-0.0000467		
-7.8	-0.0000436	9.4	-0.0000466		
-6.9	-0.0000436	10.4	-0.0000465		
-5.9	-0.0000436	11.3	-0.0000465		
-4.9	-0.0000435	12.3	-0.0000464		
-4.0	-0.0000435	13.2	-0.0000462		
-3.0	-0.0000434	14.2	-0.0000460		
-2.0	-0.0000434	15.1	-0.0000457		
-1.1	-0.0000434	16.1	-0.0000455		

Joint 1		Joint 2		Joint 3	
Location (y-coordinate) (m)	Shear displacement (m)	Location (y-coordinate) (m)	Shear displacement (m)	Location (y-coordinate) (m)	Shear displacement (m)
-0.1	-0.0000434	17.0	-0.0000453		
0.8	-0.0000434	18.0	-0.0000450		
1.8	-0.0000434	18.9	-0.0000448		
2.8	-0.0000435	19.9	-0.0000445		
3.7	-0.0000437	20.8	-0.0000443		
4.7	-0.0000439	21.8	-0.0000441		
5.7	-0.0000444	22.7	-0.0000440		
6.6	-0.0000450	23.7	-0.0000439		
7.6	-0.0000459	24.6	-0.0000438		
8.6	-0.0000473	25.6	-0.0000438		
9.5	-0.0000490	26.5	-0.0000438		
10.5	-0.0000508	27.5	-0.0000453		
11.5	-0.0000522	28.4	-0.0000532		
12.4	-0.0000560	29.4	-0.0000719		
13.4	-0.0000655	30.3	-0.0001259		
14.4	-0.0000780	31.3	-0.0002708		
15.3	-0.0001560	32.2	-0.0004285		
16.3	-0.0002961	33.2	-0.0005389		
17.3	-0.0003721	34.1	-0.0006205		
18.2	-0.0004009	35.1	-0.0006753		
19.2	-0.0004136	36.0	-0.0006816		
20.2	-0.0003666	37.0	-0.0006237		
21.1	-0.0003208	37.9	-0.0005093		
22.1	-0.0003204	38.9	-0.0003440		
23.0	-0.0002579	39.8	-0.0001473		
23.8	-0.0001154	40.8	-0.0000347		
24.4	-0.0000233	41.7	-0.0000214		
		42.7	-0.0000211		
		43.6	-0.0000207		
		44.6	-0.0000204		
		45.5	-0.0000202		
		46.5	-0.0000206		
		47.4	-0.0000218		
		48.4	-0.0000237		
		49.3	-0.0000266		
		50.3	-0.0000310		
		51.2	-0.0000387		
		52.2	-0.0000539		
		53.2	-0.0000894		
		54.1	-0.0001335		
		55.1	-0.0001600		
		56.0	-0.0001660		
		57.0	-0.0001476		
		57.9	-0.0001005		
		58.9	-0.0000477		
		59.8	-0.0000287		
		60.8	-0.0000285		
		61.7	-0.0000298		
		62.7	-0.0000322		
		63.6	-0.0000379		
		64.6	-0.0000582		
		65.5	-0.0000895		
		66.5	-0.0001221		

Joint 1		Joint 2		Joint 3	
Location (y-coordinate) (m)	Shear displacement (m)	Location (y-coordinate) (m)	Shear displacement (m)	Location (y-coordinate) (m)	Shear displacement (m)
		67.4	-0.0001538		
		68.4	-0.0001827		
		69.3	-0.0002067		
		70.3	-0.0002264		
		71.2	-0.0002482		
		72.2	-0.0002680		
		73.1	-0.0002792		
		74.1	-0.0002748		
		75.0	-0.0002407		
		76.0	-0.0001790		
		76.9	-0.0000966		
		77.9	-0.0000303		
		78.8	-0.0000123		
		79.8	-0.0000118		
		80.7	-0.0000119		
		81.7	-0.0000121		
		82.6	-0.0000127		
		83.6	-0.0000148		
		84.5	-0.0000192		
		85.5	-0.0000264		
		86.4	-0.0000362		
		87.4	-0.0000463		
		88.3	-0.0000546		
		89.3	-0.0000659		
		90.2	-0.0000816		
		91.2	-0.0000972		
		92.1	-0.0001104		
		93.1	-0.0001270		
		94.0	-0.0001431		
		95.0	-0.0001485		
		95.9	-0.0001411		
		96.8	-0.0001261		
		97.4	-0.0001136		
		97.7	-0.0001083		
		97.8	-0.0001068		
		97.9	-0.0001060		

Table G.8: Data of shear displacement along joint 1,2, and 3 for increasing SRF. The data was used to create the graph in section 5.5.2 for stability analysis of the current back wall along section S2.

Section S2: Final back wall

Joint 1		Joint 2		Joint 3	
Location (y-coordinate) (m)	Shear displacement (m)	Location (y-coordinate) (m)	Shear displacement (m)	Location (y-coordinate) (m)	Shear displacement (m)
-238.5	0.0000179	-54.7	-0.0000360	101.8	-0.0000393
-235.6	0.0000178	-52.8	-0.0000556	103.7	-0.0000721
-232.7	0.0000092	-50.9	-0.0000556	105.6	-0.0000598
-229.8	0.0000028	-49.0	-0.0000567	107.5	-0.0000362
-226.9	-0.0000023	-47.1	-0.0000565	109.4	-0.0000375
-224.0	-0.0000064	-45.2	-0.0000567	111.2	-0.0000569

Joint 1		Joint 2		Joint 3	
Location (y-coordinate) (m)	Shear displacement (m)	Location (y-coordinate) (m)	Shear displacement (m)	Location (y-coordinate) (m)	Shear displacement (m)
-221.1	-0.0000101	-43.3	-0.0000566	113.1	-0.0000686
-218.2	-0.0000133	-41.3	-0.0000566	115.0	-0.0000625
-215.3	-0.0000162	-39.4	-0.0000567	116.9	-0.0000500
-212.4	-0.0000188	-37.5	-0.0000568	118.8	-0.0000547
-209.5	-0.0000213	-35.6	-0.0000569	120.7	-0.0000674
-206.6	-0.0000235	-33.7	-0.0000569	122.6	-0.0000693
-203.7	-0.0000257	-31.8	-0.0000571	124.5	-0.0000377
-200.8	-0.0000276	-29.9	-0.0000574		
-197.9	-0.0000295	-28.0	-0.0000576		
-195.0	-0.0000312	-26.1	-0.0000579		
-192.1	-0.0000328	-24.2	-0.0000582		
-189.2	-0.0000343	-22.3	-0.0000586		
-186.3	-0.0000357	-20.4	-0.0000590		
-183.4	-0.0000370	-18.4	-0.0000595		
-180.5	-0.0000383	-16.5	-0.0000601		
-177.5	-0.0000394	-14.6	-0.0000607		
-174.6	-0.0000404	-12.7	-0.0000613		
-171.7	-0.0000414	-10.8	-0.0000620		
-168.8	-0.0000423	-8.9	-0.0000624		
-165.9	-0.0000432	-7.0	-0.0000626		
-163.0	-0.0000439	-5.1	-0.0000627		
-160.1	-0.0000447	-3.2	-0.0000650		
-157.2	-0.0000453	-1.3	-0.0000706		
-154.3	-0.0000459	0.6	-0.0000794		
-151.5	-0.0000465	2.5	-0.0000921		
-148.6	-0.0000470	4.4	-0.0001092		
-145.8	-0.0000475	6.4	-0.0001517		
-143.1	-0.0000479	8.3	-0.0002262		
-140.3	-0.0000483	10.2	-0.0003239		
-137.6	-0.0000486	12.1	-0.0004354		
-134.9	-0.0000489	14.0	-0.0005624		
-132.3	-0.0000492	15.9	-0.0006878		
-129.7	-0.0000494	17.8	-0.0007398		
-127.1	-0.0000497	19.7	-0.0006975		
-124.5	-0.0000499	21.6	-0.0005663		
-122.0	-0.0000501	23.5	-0.0002742		
-119.5	-0.0000502	25.4	-0.0000761		
-117.0	-0.0000504	27.3	-0.0000545		
-114.5	-0.0000505	29.2	-0.0000539		
-112.1	-0.0000506	31.2	-0.0000474		
-109.7	-0.0000507	33.1	-0.0000447		
-107.4	-0.0000508	35.0	-0.0000462		
-105.0	-0.0000509	36.9	-0.0000547		
-102.7	-0.0000509	38.8	-0.0000662		
-100.4	-0.0000510	40.7	-0.0000874		
-98.1	-0.0000510	42.6	-0.0001303		
-95.9	-0.0000510	44.5	-0.0001851		
-93.7	-0.0000511	46.4	-0.0002342		
-91.5	-0.0000511	48.3	-0.0002587		
-89.3	-0.0000511	50.2	-0.0002186		
-87.2	-0.0000511	52.1	-0.0001193		
-85.1	-0.0000511	54.0	-0.0000316		
-83.0	-0.0000511				

Joint 1		Joint 2		Joint 3	
Location (y-coordinate) (m)	Shear displacement (m)	Location (y-coordinate) (m)	Shear displacement (m)	Location (y-coordinate) (m)	Shear displacement (m)
-80.9	-0.0000511				
-78.8	-0.0000511				
-76.8	-0.0000511				
-74.8	-0.0000511				
-72.8	-0.0000511				
-70.9	-0.0000511				
-68.9	-0.0000510				
-67.0	-0.0000510				
-65.0	-0.0000510				
-63.1	-0.0000510				
-61.2	-0.0000509				
-59.2	-0.0000509				
-57.3	-0.0000509				
-55.4	-0.0000509				
-53.4	-0.0000508				
-51.5	-0.0000508				
-49.6	-0.0000508				
-47.6	-0.0000508				
-45.7	-0.0000507				
-43.7	-0.0000507				
-41.8	-0.0000507				
-39.9	-0.0000506				
-37.9	-0.0000506				
-36.0	-0.0000506				
-34.1	-0.0000505				
-32.1	-0.0000505				
-30.2	-0.0000504				
-28.3	-0.0000504				
-26.3	-0.0000503				
-24.4	-0.0000502				
-22.4	-0.0000501				
-20.5	-0.0000500				
-18.6	-0.0000499				
-16.6	-0.0000498				
-14.7	-0.0000497				
-12.8	-0.0000495				
-10.8	-0.0000494				
-8.9	-0.0000492				
-7.0	-0.0000492				
-5.0	-0.0000499				
-3.1	-0.0000536				
-1.1	-0.0000650				
0.8	-0.0001155				
2.7	-0.0002161				
4.7	-0.0002781				
6.6	-0.0003213				
8.5	-0.0003455				
10.5	-0.0003685				
12.4	-0.0004150				
14.3	-0.0004860				
16.3	-0.0005580				
18.2	-0.0006089				
20.2	-0.0005351				

Joint 1		Joint 2		Joint 3	
Location (y-coordinate) (m)	Shear displacement (m)	Location (y-coordinate) (m)	Shear displacement (m)	Location (y-coordinate) (m)	Shear displacement (m)
22.1	-0.0003436				
24.0	-0.0001797				

Table G.9: Data of shear displacement along joint 1,2, and 3 for increasing SRF. The data was used to create the graph in section 5.5.2 for stability analysis of the final back wall along section S2.

Section S3

Joint 1		Joint 2		Joint 3	
Location (y-coordinate) (m)	Shear displacement (m)	Location (y-coordinate) (m)	Shear displacement (m)	Location (y-coordinate) (m)	Shear displacement (m)
-236.8	0.0000039	-63.9	-0.0000319	57.3	-0.0000071
-230.7	-0.0000016	-62.5	-0.0000514	58.2	-0.0000151
-225.0	-0.0000117	-61.2	-0.0000539	59.2	-0.0000192
-219.6	-0.0000175	-60.0	-0.0000523	60.1	-0.0000239
-214.6	-0.0000221	-58.8	-0.0000543	61.1	-0.0000313
-209.9	-0.0000258	-57.8	-0.0000564	62.1	-0.0000431
-205.5	-0.0000289	-56.8	-0.0000559	63.0	-0.0000615
-201.4	-0.0000315	-55.9	-0.0000535	64.0	-0.0000771
-197.6	-0.0000337	-54.9	-0.0000530	64.9	-0.0000727
-194.0	-0.0000356	-54.0	-0.0000551	65.9	-0.0000419
-190.6	-0.0000373	-53.0	-0.0000555	66.8	-0.0000200
-187.4	-0.0000388	-52.1	-0.0000554	67.8	-0.0000178
-184.4	-0.0000401	-51.1	-0.0000558	68.7	-0.0000176
-181.5	-0.0000413	-50.2	-0.0000553	69.7	-0.0000179
-178.6	-0.0000424	-49.2	-0.0000546	70.6	-0.0000198
-175.6	-0.0000434	-48.3	-0.0000553	71.6	-0.0000224
-172.7	-0.0000444	-47.3	-0.0000562	72.5	-0.0000265
-169.8	-0.0000453	-46.4	-0.0000564	73.5	-0.0000359
-166.9	-0.0000462	-45.4	-0.0000561	74.4	-0.0000484
-163.9	-0.0000470	-44.5	-0.0000559	75.4	-0.0000620
-161.0	-0.0000478	-43.5	-0.0000560	76.4	-0.0000761
-158.1	-0.0000485	-42.6	-0.0000563	77.3	-0.0000874
-155.2	-0.0000492	-41.6	-0.0000567	78.3	-0.0000929
-152.2	-0.0000498	-40.7	-0.0000569	79.2	-0.0000970
-149.3	-0.0000504	-39.7	-0.0000568	80.2	-0.0001092
-146.4	-0.0000509	-38.8	-0.0000567	81.1	-0.0001261
-143.4	-0.0000514	-37.8	-0.0000569	82.1	-0.0001433
-140.5	-0.0000519	-36.8	-0.0000573	83.0	-0.0001535
-137.6	-0.0000523	-35.9	-0.0000575	84.0	-0.0001557
-134.7	-0.0000528	-34.9	-0.0000576	84.9	-0.0001459
-131.7	-0.0000531	-34.0	-0.0000577	85.9	-0.0001202
-128.8	-0.0000535	-33.0	-0.0000577	86.8	-0.0000761
-125.9	-0.0000538	-32.1	-0.0000579	87.8	-0.0000315
-123.0	-0.0000541	-31.1	-0.0000581	88.7	-0.0000145
-120.0	-0.0000543	-30.2	-0.0000583	89.7	-0.0000144
-117.1	-0.0000546	-29.2	-0.0000584	90.7	-0.0000182
-114.2	-0.0000548	-28.3	-0.0000584	91.6	-0.0000317
-111.2	-0.0000550	-27.3	-0.0000585	92.6	-0.0000542
-108.3	-0.0000552	-26.4	-0.0000587	93.5	-0.0000732
-105.4	-0.0000554	-25.4	-0.0000588	94.5	-0.0000832

Joint 1		Joint 2		Joint 3	
Location (y-coordinate) (m)	Shear displacement (m)	Location (y-coordinate) (m)	Shear displacement (m)	Location (y-coordinate) (m)	Shear displacement (m)
-102.5	-0.0000555	-24.5	-0.0000590	95.4	-0.0000784
-99.5	-0.0000556	-23.5	-0.0000590	96.4	-0.0000532
-96.6	-0.0000558	-22.6	-0.0000591	97.3	-0.0000269
-93.7	-0.0000559	-21.6	-0.0000592	98.3	-0.0000312
-90.7	-0.0000560	-20.7	-0.0000593	99.2	-0.0000513
-87.8	-0.0000560	-19.7	-0.0000593	100.2	-0.0000708
-84.9	-0.0000561	-18.8	-0.0000593	101.1	-0.0000863
-82.0	-0.0000562	-17.8	-0.0000592	102.1	-0.0000933
-79.2	-0.0000562	-16.9	-0.0000592	103.1	-0.0000868
-76.6	-0.0000562	-15.9	-0.0000591	104.0	-0.0000594
-74.2	-0.0000563	-15.0	-0.0000590	105.0	-0.0000246
-72.0	-0.0000563	-14.0	-0.0000589	105.9	-0.0000198
-69.9	-0.0000563	-13.0	-0.0000588	106.9	-0.0000336
-68.1	-0.0000563	-12.1	-0.0000587	107.8	-0.0000480
-66.3	-0.0000563	-11.1	-0.0000585	108.8	-0.0000631
-64.7	-0.0000563	-10.2	-0.0000583	109.7	-0.0000789
-63.3	-0.0000563	-9.2	-0.0000582	110.7	-0.0000921
-61.9	-0.0000563	-8.3	-0.0000579	111.6	-0.0000996
-60.7	-0.0000563	-7.3	-0.0000577	112.6	-0.0001023
-59.5	-0.0000563	-6.4	-0.0000574	113.5	-0.0001001
-58.5	-0.0000564	-5.4	-0.0000571	114.5	-0.0000884
-57.5	-0.0000564	-4.5	-0.0000568	115.4	-0.0000679
-56.5	-0.0000564	-3.5	-0.0000565	116.4	-0.0000520
-55.5	-0.0000564	-2.6	-0.0000562	117.4	-0.0000447
-54.5	-0.0000564	-1.6	-0.0000558	118.3	-0.0000426
-53.6	-0.0000563	-0.7	-0.0000554	119.3	-0.0000427
-52.6	-0.0000563	0.3	-0.0000551	120.2	-0.0000438
-51.6	-0.0000563	1.2	-0.0000548	121.2	-0.0000480
-50.6	-0.0000563	2.2	-0.0000544	122.1	-0.0000532
-49.7	-0.0000563	3.1	-0.0000542	123.1	-0.0000579
-48.7	-0.0000563	4.1	-0.0000539	124.0	-0.0000641
-47.7	-0.0000563	5.0	-0.0000538	125.0	-0.0000716
-46.7	-0.0000563	6.0	-0.0000537	125.9	-0.0000758
-45.7	-0.0000563	6.9	-0.0000537	126.9	-0.0000729
-44.8	-0.0000563	7.9	-0.0000540	127.8	-0.0000628
-43.8	-0.0000563	8.9	-0.0000565	128.8	-0.0000509
-42.8	-0.0000563	9.8	-0.0000648	129.8	-0.0000466
-41.8	-0.0000562	10.8	-0.0000820	130.7	-0.0000477
-40.9	-0.0000562	11.7	-0.0001316	131.7	-0.0000523
-39.9	-0.0000562	12.7	-0.0002501	132.6	-0.0000576
-38.9	-0.0000562	13.6	-0.0003769	133.6	-0.0000564
-37.9	-0.0000562	14.6	-0.0004703	134.5	-0.0000274
-37.0	-0.0000562	15.5	-0.0005645		
-36.0	-0.0000561	16.5	-0.0006338		
-35.0	-0.0000561	17.4	-0.0006577		
-34.0	-0.0000561	18.4	-0.0006264		
-33.1	-0.0000560	19.3	-0.0006364		
-32.1	-0.0000560	20.3	-0.0006528		
-31.1	-0.0000560	21.2	-0.0005664		
-30.1	-0.0000559	22.2	-0.0005029		
-29.2	-0.0000558	23.1	-0.0004622		
-28.2	-0.0000558	24.1	-0.0003760		
-27.2	-0.0000557	25.0	-0.0002385		

Joint 1		Joint 2		Joint 3	
Location (y-coordinate) (m)	Shear displacement (m)	Location (y-coordinate) (m)	Shear displacement (m)	Location (y-coordinate) (m)	Shear displacement (m)
-26.2	-0.000556	26.0	-0.0001182		
-25.3	-0.000555	26.9	-0.0000489		
-24.3	-0.000555	27.9	-0.0000301		
-23.3	-0.000554	28.8	-0.0000301		
-22.3	-0.000553	29.8	-0.0000322		
-21.4	-0.000552	30.7	-0.0000350		
-20.4	-0.000551	31.7	-0.0000385		
-19.4	-0.000550	32.7	-0.0000424		
-18.4	-0.000550	33.6	-0.0000472		
-17.4	-0.000549	34.6	-0.0000538		
-16.5	-0.000549	35.5	-0.0000619		
-15.5	-0.000548	36.5	-0.0000755		
-14.5	-0.000549	37.4	-0.0000953		
-13.5	-0.000549	38.4	-0.0001183		
-12.6	-0.000550	39.3	-0.0001428		
-11.6	-0.000553	40.3	-0.0001668		
-10.6	-0.000556	41.2	-0.0001889		
-9.6	-0.000561	42.2	-0.0002077		
-8.7	-0.000568	43.1	-0.0002214		
-7.7	-0.000578	44.1	-0.0002289		
-6.7	-0.000591	45.0	-0.0002302		
-5.7	-0.000607	46.0	-0.0002315		
-4.8	-0.000627	46.9	-0.0002328		
-3.8	-0.000650	47.9	-0.0002297		
-2.8	-0.000672	48.8	-0.0002165		
-1.8	-0.000691	49.8	-0.0001937		
-0.9	-0.000705	50.7	-0.0001574		
0.1	-0.000757	51.7	-0.0001228		
1.1	-0.000901	52.6	-0.0000866		
2.1	-0.0001124	53.6	-0.0000410		
3.0	-0.0001357	54.5	-0.0000210		
4.0	-0.0001501	55.5	-0.0000215		
5.0	-0.0001729	56.5	-0.0000234		
6.0	-0.0002389	57.4	-0.0000253		
6.9	-0.0003180	58.4	-0.0000272		
7.9	-0.0003765	59.3	-0.0000293		
8.9	-0.0004151	60.3	-0.0000380		
9.9	-0.0004291	61.2	-0.0000614		
10.9	-0.0004198	62.2	-0.0000861		
11.8	-0.0004284	63.1	-0.0000976		
12.8	-0.0004848	64.1	-0.0000910		
13.8	-0.0005671	65.0	-0.0000645		
14.8	-0.0006522	66.0	-0.0000370		
15.7	-0.0007260	66.9	-0.0000305		
16.7	-0.0008222	67.9	-0.0000304		
17.7	-0.0009419	68.8	-0.0000304		
18.7	-0.0010087	69.8	-0.0000322		
19.6	-0.0009811	70.7	-0.0000373		
20.6	-0.0009325	71.7	-0.0000429		
21.6	-0.0008367	72.6	-0.0000476		
22.6	-0.0006167	73.6	-0.0000544		
23.5	-0.0002853	74.5	-0.0000648		
24.5	-0.0000355	75.5	-0.0000775		

Joint 1		Joint 2		Joint 3	
Location (y-coordinate) (m)	Shear displacement (m)	Location (y-coordinate) (m)	Shear displacement (m)	Location (y-coordinate) (m)	Shear displacement (m)
		76.4	-0.0000904		
		77.4	-0.0001046		
		78.3	-0.0001191		
		79.3	-0.0001333		
		80.3	-0.0001473		
		81.2	-0.0001538		
		82.2	-0.0001567		
		83.1	-0.0001562		
		84.1	-0.0001434		
		85.0	-0.0001160		
		86.0	-0.0000712		
		86.9	-0.0000326		
		87.9	-0.0000227		
		88.8	-0.0000258		
		89.8	-0.0000328		
		90.7	-0.0000406		
		91.7	-0.0000491		
		92.6	-0.0000568		
		93.6	-0.0000608		
		94.5	-0.0000583		
		95.5	-0.0000459		
		96.4	-0.0000335		
		97.4	-0.0000377		
		98.3	-0.0000520		
		99.3	-0.0000677		
		100.2	-0.0000812		
		101.2	-0.0000876		
		102.1	-0.0000807		
		103.1	-0.0000599		
		104.1	-0.0000315		
		105.0	-0.0000185		
		106.0	-0.0000254		
		106.9	-0.0000386		
		107.9	-0.0000558		
		108.8	-0.0000723		
		109.8	-0.0000866		
		110.7	-0.0000979		
		111.7	-0.0000989		
		112.6	-0.0000809		
		113.6	-0.0000431		
		114.5	-0.0000088		

Table G.10: Data of shear displacement along joint 1,2, and 3 for increasing SRF. The data was used to create the graph in section 5.5.2 for stability analysis of the final back wall along section S3.

Section S4

Joint 1		Joint 2		Joint 3	
Location (y coordinate) (m)	Shear displacement (m)	Location (y coordinate) (m)	Shear displacement (m)	Location (y coordinate) (m)	Shear displacement (m)
-128.8	-0.0000035	-128.7	-0.0000166	29.5	-0.00000256

Joint 1		Joint 2		Joint 3	
Location (y coordinate) (m)	Shear displacement (m)	Location (y coordinate) (m)	Shear displacement (m)	Location (y coordinate) (m)	Shear displacement (m)
-125.6	-0.0000066	-125.6	-0.0000275	30.5	-0.00000389
-122.6	-0.0000080	-122.4	-0.0000285	31.5	-0.00000393
-119.6	-0.0000093	-119.4	-0.0000295	32.4	-0.00000386
-116.7	-0.0000106	-116.4	-0.0000303	33.4	-0.00000377
-113.9	-0.0000117	-113.6	-0.0000307	34.4	-0.00000369
-111.3	-0.0000126	-110.9	-0.0000308	35.4	-0.00000360
-108.8	-0.0000135	-108.3	-0.0000307	36.4	-0.00000351
-106.4	-0.0000143	-105.9	-0.0000306	37.4	-0.00000342
-104.1	-0.0000149	-103.5	-0.0000305	38.4	-0.00000333
-101.9	-0.0000156	-101.3	-0.0000303	39.4	-0.00000325
-99.8	-0.0000161	-99.2	-0.0000300	40.3	-0.00000316
-97.8	-0.0000167	-97.1	-0.0000297	41.3	-0.00000307
-95.9	-0.0000171	-95.1	-0.0000294	42.3	-0.00000299
-93.9	-0.0000176	-93.2	-0.0000292	43.3	-0.00000290
-92.0	-0.0000180	-91.2	-0.0000290	44.3	-0.00000282
-90.1	-0.0000185	-89.3	-0.0000288	45.3	-0.00000274
-88.1	-0.0000189	-87.3	-0.0000285	46.3	-0.00000265
-86.2	-0.0000193	-85.3	-0.0000282	47.2	-0.00000257
-84.3	-0.0000197	-83.4	-0.0000280	48.2	-0.00000249
-82.3	-0.0000201	-81.4	-0.0000278	49.2	-0.00000240
-80.4	-0.0000205	-79.4	-0.0000275	50.2	-0.00000231
-78.5	-0.0000208	-77.5	-0.0000273	51.2	-0.00000222
-76.6	-0.0000212	-75.5	-0.0000269	52.2	-0.00000213
-74.6	-0.0000215	-73.6	-0.0000267	53.2	-0.00000203
-72.7	-0.0000218	-71.7	-0.0000264	54.1	-0.00000194
-70.9	-0.0000222	-69.8	-0.0000262	55.1	-0.00000185
-69.1	-0.0000225	-68.0	-0.0000260	56.1	-0.00000176
-67.3	-0.0000228	-66.2	-0.0000258	57.1	-0.00000167
-65.6	-0.0000230	-64.5	-0.0000255	58.1	-0.00000158
-63.9	-0.0000233	-62.8	-0.0000253	59.1	-0.00000149
-62.3	-0.0000236	-61.1	-0.0000251	60.1	-0.00000140
-60.7	-0.0000238	-59.5	-0.0000249	61.0	-0.00000131
-59.1	-0.0000240	-57.9	-0.0000247	62.0	-0.00000123
-57.6	-0.0000243	-56.4	-0.0000246	63.0	-0.00000114
-56.1	-0.0000245	-54.9	-0.0000244	64.0	-0.00000104
-54.7	-0.0000247	-53.4	-0.0000242	65.0	-0.00000094
-53.2	-0.0000249	-52.0	-0.0000240	66.0	-0.00000082
-51.8	-0.0000251	-50.6	-0.0000239	67.0	-0.00000104
-50.5	-0.0000253	-49.2	-0.0000238	67.9	-0.00000099
-49.1	-0.0000255	-47.9	-0.0000237	68.9	-0.00000067
-47.8	-0.0000256	-46.6	-0.0000235	69.9	-0.00000061
-46.6	-0.0000258	-45.3	-0.0000234	70.9	-0.00000053
-45.3	-0.0000260	-44.1	-0.0000233	71.9	-0.00000045
-44.1	-0.0000261	-42.8	-0.0000232	72.9	-0.00000038
-42.9	-0.0000262	-41.7	-0.0000231	73.9	-0.00000030
-41.8	-0.0000263	-40.5	-0.0000230	74.8	-0.00000023
-40.7	-0.0000263	-39.4	-0.0000229	75.8	-0.00000016
-39.6	-0.0000264	-38.3	-0.0000228	76.8	-0.00000010
-38.5	-0.0000265	-37.2	-0.0000228	77.8	0.00000005
-37.4	-0.0000265	-36.1	-0.0000227	78.8	0.00000009
-36.4	-0.0000266	-35.1	-0.0000227	79.8	0.00000013
-35.4	-0.0000266	-34.1	-0.0000226	80.8	0.00000020
-34.4	-0.0000267	-33.1	-0.0000225	81.7	0.00000027

Joint 1		Joint 2		Joint 3	
Location (y coordinate) (m)	Shear displacement (m)	Location (y coordinate) (m)	Shear displacement (m)	Location (y coordinate) (m)	Shear displacement (m)
-33.4	-0.0000267	-32.1	-0.0000225	82.7	0.00000034
-32.5	-0.0000268	-31.2	-0.0000224	83.7	0.00000042
-31.5	-0.0000268	-30.2	-0.0000224	84.7	0.00000049
-30.5	-0.0000269	-29.2	-0.0000224	85.7	0.00000056
-29.6	-0.0000269	-28.2	-0.0000223	86.7	0.00000061
-28.6	-0.0000269	-27.2	-0.0000223	87.7	0.00000067
-27.6	-0.0000270	-26.2	-0.0000223	88.7	0.00000072
-26.7	-0.0000270	-25.3	-0.0000223	89.6	0.00000078
-25.7	-0.0000271	-24.3	-0.0000223	90.6	0.00000083
-24.8	-0.0000271	-23.3	-0.0000222	91.6	0.00000088
-23.8	-0.0000272	-22.3	-0.0000222	92.6	0.00000093
-22.8	-0.0000272	-21.3	-0.0000222	93.6	0.00000097
-21.9	-0.0000272	-20.4	-0.0000222	94.6	0.00000102
-20.9	-0.0000273	-19.4	-0.0000222	95.6	0.00000106
-19.9	-0.0000274	-18.4	-0.0000222	96.5	0.00000110
-19.0	-0.0000274	-17.4	-0.0000222	97.5	0.00000114
-18.0	-0.0000275	-16.4	-0.0000223	98.5	0.00000118
-17.0	-0.0000276	-15.4	-0.0000223	99.5	0.00000121
-16.1	-0.0000277	-14.5	-0.0000223	100.5	0.00000124
-15.1	-0.0000279	-13.5	-0.0000224	101.5	0.00000127
-14.1	-0.0000281	-12.5	-0.0000224	102.5	0.00000130
-13.2	-0.0000283	-11.5	-0.0000225	103.4	0.00000132
-12.2	-0.0000286	-10.5	-0.0000225	104.4	0.00000134
-11.2	-0.0000290	-9.6	-0.0000226	105.4	0.00000136
-10.3	-0.0000294	-8.6	-0.0000227	106.4	0.00000138
-9.3	-0.0000299	-7.6	-0.0000227	107.4	0.00000140
-8.3	-0.0000306	-6.6	-0.0000227	108.4	0.00000141
-7.4	-0.0000313	-5.6	-0.0000228	109.4	0.00000143
-6.4	-0.0000321	-4.6	-0.0000229	110.3	0.00000144
-5.4	-0.0000331	-3.7	-0.0000229	111.3	0.00000145
-4.5	-0.0000341	-2.7	-0.0000230	112.3	0.00000147
-3.5	-0.0000351	-1.7	-0.0000231	113.3	0.00000149
-2.5	-0.0000360	-0.7	-0.0000232	114.3	0.00000152
-1.6	-0.0000366	0.3	-0.0000233	115.3	0.00000155
-0.6	-0.0000370	1.2	-0.0000233	116.3	0.00000149
0.4	-0.0000377	2.2	-0.0000234	117.2	0.00000158
1.3	-0.0000403	3.2	-0.0000235	118.2	0.00000167
2.3	-0.0000455	4.2	-0.0000236	119.2	0.00000170
3.3	-0.0000529	5.2	-0.0000238	120.2	0.00000171
4.2	-0.0000612	6.2	-0.0000239	121.2	0.00000172
5.2	-0.0000685	7.1	-0.0000240	122.2	0.00000176
6.2	-0.0000745	8.1	-0.0000241	123.2	0.00000184
7.1	-0.0000968	9.1	-0.0000242	124.1	0.00000196
8.1	-0.0001366	10.1	-0.0000243	125.1	0.00000207
9.1	-0.0001553	11.1	-0.0000244	126.1	0.00000214
10.0	-0.0001482	12.0	-0.0000245	127.1	0.00000229
11.0	-0.0001531	13.0	-0.0000246	128.1	0.00000247
12.0	-0.0001809	14.0	-0.0000246	129.1	0.00000258
12.9	-0.0002128	15.0	-0.0000247	130.1	0.00000273
13.9	-0.0002528	16.0	-0.0000247	131.0	0.00000296
14.9	-0.0003040	17.0	-0.0000247	132.0	0.00000332
15.8	-0.0003575	17.9	-0.0000247	133.0	0.00000387
16.8	-0.0004207	18.9	-0.0000246	134.0	0.00000461

Joint 1		Joint 2		Joint 3	
Location (y coordinate) (m)	Shear displacement (m)	Location (y coordinate) (m)	Shear displacement (m)	Location (y coordinate) (m)	Shear displacement (m)
17.8	-0.0004884	19.9	-0.0000245	135.0	0.00000559
18.7	-0.0005332	20.9	-0.0000243	136.0	0.00000711
19.7	-0.0005139	21.9	-0.0000240	137.0	0.00001114
20.7	-0.0003993	22.8	-0.0000237	138.0	0.00001947
21.6	-0.0002472	23.8	-0.0000232	138.9	0.00002383
22.6	-0.0001115	24.8	-0.0000227	139.9	0.00001924
23.6	-0.0000213	25.8	-0.0000221	140.9	0.00001043
24.5	-0.0000038	26.8	-0.0000214	141.9	0.00000672
		27.8	-0.0000207	142.9	0.00001159
		28.7	-0.0000199	143.9	0.00002241
		29.7	-0.0000192	144.9	0.00003108
		30.7	-0.0000185	145.8	0.00003319
		31.7	-0.0000179	146.8	0.00002951
		32.7	-0.0000173	147.8	0.00002327
		33.6	-0.0000167	148.8	0.00001691
		34.6	-0.0000162	149.8	0.00001154
		35.6	-0.0000157	150.8	0.00001098
		36.6	-0.0000152	151.8	0.00001226
		37.6	-0.0000148	152.7	0.00001275
		38.6	-0.0000144	153.7	0.00001211
		39.5	-0.0000140	154.7	0.00001062
		40.5	-0.0000136	155.7	0.00000994
		41.5	-0.0000133	156.7	0.00000996
		42.5	-0.0000129	157.7	0.00001021
		43.5	-0.0000126	158.7	0.00001067
		44.4	-0.0000123	159.6	0.00001161
		45.4	-0.0000120	160.6	0.00001343
		46.4	-0.0000116	161.6	0.00001462
		47.4	-0.0000113	162.6	0.00001241
		48.4	-0.0000110	163.6	0.00000984
		49.4	-0.0000107	164.6	0.00000904
		50.3	-0.0000104	165.6	0.00000792
		51.3	-0.0000101	166.5	0.00000739
		52.3	-0.0000098	167.5	0.00000833
		53.3	-0.0000095	168.5	0.00001088
		54.3	-0.0000092	169.5	0.00001411
		55.2	-0.0000089	170.5	0.00001366
		56.2	-0.0000086	171.5	0.00000954
		57.2	-0.0000083	172.5	0.00000764
		58.2	-0.0000081	173.4	0.00000785
		59.2	-0.0000078	174.4	0.00000822
		60.2	-0.0000075	175.4	0.00000931
		61.1	-0.0000073	176.4	0.00001298
		62.1	-0.0000070	177.4	0.00001780
		63.1	-0.0000068	178.4	0.00001698
		64.1	-0.0000065	179.4	0.00001087
		65.1	-0.0000063	180.3	0.00000752
		66.1	-0.0000061	181.3	0.00000784
		67.0	-0.0000059	182.3	0.00000847
		68.0	-0.0000056	183.3	0.00001039
		69.0	-0.0000054	184.3	0.00001713
		70.0	-0.0000052	185.3	0.00002295
		71.0	-0.0000050	186.3	0.00002277

Joint 1		Joint 2		Joint 3	
Location (y coordinate) (m)	Shear displacement (m)	Location (y coordinate) (m)	Shear displacement (m)	Location (y coordinate) (m)	Shear displacement (m)
		71.9	-0.0000049	187.2	0.00001879
		72.9	-0.0000047	188.2	0.00001236
		73.9	-0.0000046	189.2	0.00000775
		74.9	-0.0000044	190.2	0.00000743
		75.9	-0.0000043	191.2	0.00000951
		76.9	-0.0000041	192.2	0.00001764
		77.8	-0.0000040	193.2	0.00002679
		78.8	-0.0000039	194.2	0.00003007
		79.8	-0.0000037	195.1	0.00002745
		80.8	-0.0000036	196.1	0.00002003
		81.8	-0.0000035	197.1	0.00001165
		82.7	-0.0000034	198.1	0.00001206
		83.7	-0.0000032	199.1	0.00002167
		84.7	-0.0000031	200.1	0.00002936
		85.7	-0.0000030	201.1	0.00003139
		86.7	-0.0000029	202.0	0.00002890
		87.7	-0.0000028	203.0	0.00002349
		88.6	-0.0000027	204.0	0.00001655
		89.6	-0.0000026	205.0	0.00001188
		90.6	-0.0000025	206.0	0.00001353
		91.6	-0.0000024	207.0	0.00001935
		92.6	-0.0000024	208.0	0.00002178
		93.5	-0.0000023	208.9	0.00001996
		94.5	-0.0000022	209.9	0.00001870
		95.5	-0.0000021	210.9	0.00001705
		96.5	-0.0000020	211.9	0.00001456
		97.5	-0.0000020	212.9	0.00001349
		98.5	-0.0000019	213.9	0.00001484
		99.4	-0.0000018	214.9	0.00001599
		100.4	-0.0000017	215.8	0.00001482
		101.4	-0.0000017	216.8	0.00001299
		102.4	-0.0000016	217.8	0.00001228
		103.4	-0.0000016	218.8	0.00001200
		104.3	-0.0000015	219.8	0.00001148
		105.3	-0.0000014	220.8	0.00001135
		106.3	-0.0000014	221.8	0.00001178
		107.3	-0.0000013	222.7	0.00001330
		108.3	-0.0000013	223.7	0.00001676
		109.3	-0.0000012	224.7	0.00002099
		110.2	-0.0000012	225.7	0.00002872
		111.2	-0.0000011	226.7	0.00003516
		112.2	-0.0000011	227.7	0.00003534
		113.2	-0.0000010	228.7	0.00003250
		114.2	-0.0000009	229.6	0.00002314
		115.1	-0.0000009	230.6	0.00001135
		116.1	-0.0000008	231.6	0.00000624
		117.1	-0.0000008	232.6	0.00000907
		118.1	-0.0000007	233.6	0.00001458
		119.1	-0.0000006	234.6	0.00001714
		120.1	-0.0000006	235.6	0.00001643
		121.0	-0.0000005	236.5	0.00001328
		122.0	-0.0000004	237.5	0.00000852
		123.0	-0.0000004	238.5	0.00000352

Joint 1		Joint 2		Joint 3	
Location (y coordinate) (m)	Shear displacement (m)	Location (y coordinate) (m)	Shear displacement (m)	Location (y coordinate) (m)	Shear displacement (m)
		124.0	-0.0000003	239.5	0.00000071
		125.0	-0.0000002		
		125.9	0.0000000		
		126.9	0.0000001		
		127.9	0.0000003		
		128.9	0.0000004		
		129.9	0.0000005		
		130.9	0.0000007		
		131.8	0.0000008		
		132.8	0.0000009		
		133.8	0.0000010		
		134.8	0.0000011		
		135.8	0.0000012		
		136.7	0.0000013		
		137.7	0.0000015		
		138.7	0.0000017		
		139.7	0.0000020		
		140.7	0.0000023		
		141.7	0.0000026		
		142.6	0.0000028		
		143.6	0.0000029		
		144.6	0.0000028		
		145.6	0.0000025		
		146.6	0.0000021		
		147.5	0.0000017		
		148.5	0.0000024		
		149.5	0.0000052		

Table G.11: Data of shear displacement along joint 1,2, and 3 for increasing SRF. The data was used to create the graph in section 5.5.2 for stability analysis of the final back wall along section S4.

H. Risk analysis

Risk Analysis for field work					
Risk	Description	Probability	Consequence	Classification	Measures
1	Block fall from benches	Possible	High	Major	Look out for loose blocks. Reduce time by the bench face. Stay away from the bench face on days with heavy rainfall.
2	Trucks in the quarry	Possible	Very high	Major	Keep distance to trucks. Have eye contact with the driver before passing the truck.
3	Falling from a bench	Unlikely	Very high	Major	Keep distance to the edge of the bench.
Risk analysis for laboratory work					
Risk	Description	Probability	Consequence	Classification	Measures
1	Sawing of cores	Possible	Medium	Moderate	Get proper instructions before use
2	Dust and water in eye	Probable	Medium	Major	Use safety glasses
3	Noise	Probable	Medium	Moderate	Use earmuffs
4	Inhalation of mineral fines	Probable	Medium	Moderate	Use exhaust fan when handling dry mineral fines.
5	Falling objects	Probable	Medium	Major	Use safety shoes.

Table H.1: Risk analysis of potential risks during field mapping and laboratory testing based on risk matrix by Aasteboel (2019) used for the field work in the quarry and the laboratory testing.

